Design of Electrode for Electrochemical Energy Storage and Conversion Devices using Multiwall Carbon Nanotubes

by

Seung Woo Lee

Bachelor of Science, Chemical Engineering
Seoul National University, Seoul, Republic of Korea, 2004

MASSACHUSETTS INSTITUTE OF TECHNOLOGY
JUN 30 2010
LIBRARIES

SUBMITTED TO THE DEPARTMENT OF CHEMICAL ENGINEERING
IN PARTIAL FULFUILLMENT OF THE REQUIREMENTS FOR THE DEGREE OF

DOCTOR OF PHILOSOPHY IN CHEMICAL ENGINEERING
AT THE
MASSACHUSETTS INSTITUTE OF TECHNOLOGY

ARCHIVES

JUNE 2010

© 2010 Massachusetts Institute of Technology. All rights reserved

Signature of Author:_____
Department of Chemical Engineering
February 25, 2010

Certified by:_____
Yang Shao-Horn
Associate Professor of Mechanical Engineering
Thesis Supervisor

Certified by:_____
Paula T. Hammond
Bayer Chair Professor of Chemical Engineering
Thesis Supervisor

Accepted by:_____
William M. Deen
Professor of Chemical Engineering
Chairman, Committee for Graduate Student

Design of Electrode for Electrochemical Energy Storage and Conversion Devices using Multiwall Carbon Nanotubes

by

Seung Woo Lee

Submitted to the Department of Chemical Engineering
on February 25, 2010 in partial fulfillment of the requirements for the degree of
Doctor of Philosophy in Chemical Engineering
At the Massachusetts Institute of Technology

Abstract

All-multiwall carbon nanotube (MWNT) thin films are created by layer-by-layer (LbL) assembly of surface functionalized MWNTs. Negatively and positively charged MWNTs were prepared by surface functionalization, allowing the incorporation of MWNTs into highly tunable thin films via the LbL technique. The pH dependent surface charge on the MWNTs gives this system the unique characteristics of LbL assembly of weak polyelectrolytes, controlling thickness and morphology with assembly pH conditions. We demonstrate that these MWNT thin films have randomly oriented interpenetrating network structure with well developed nanopores using SEM, which is an ideal structure of functional materials for various applications. LbL-MWNT electrodes show high electronic conductivity in comparison with polymer composites with single wall nanotubes, and high capacitive behavior in aqueous electrolyte with precise control of capacity.

Of significance, additive-free LbL-MWNT electrodes with thicknesses of several microns can deliver high energy density (200 Wh/kg) at an exceptionally high power of 100 kW/kg in lithium nonaqueous cells. Utilizing the redox reactions on the surface functional groups in a wide voltage window (1.5 – 4.5 V vs. lithium) in nonaqueous electrolytes, asymmetric electrochemical capacitors consisting of LbL-MWNT and either lithium or a lithium titanium oxide negative electrode exhibit gravimetric energy density ~5 times higher than conventional electrochemical capacitors with comparable gravimetric power and cycle life. Thin-film LbL-MWNT electrodes could potentially lead to breakthrough power sources for microsystems and flexible electronic devices such as smart cards and e-book readers, while thicker LbL-MWNT electrodes could expand the application of electrochemical capacitors into heavy vehicle and industrial systems, where the ability to deliver high energy at high power will be an enabling technological development.

Furthermore, nanoscale pseuduocapactive oxides and electrocatalysts were incorporated into LbL-MWNT electrodes for energy storage and conversion. Inorganic oxides such as MnO_2 and RuO_2 are incorporated to increase volumetric capacitance in LbL-MWNT electrodes using electroless deposition and square wave pulse potential deposition methods. Preliminary results show that we can increase volumetric capacitance of LbL-MWNT/MnO_2 and LbL-MWNT/RuO_2 composite up to 1000 F/cm^3 in aqueous electrolytes. In addition, Pt and Pt/Ru alloy electrocatalysts are introduced into LbL-MWNT electrodes using square wave pulse potential deposition, which show higher CO and methanol oxidation activities. Tailored incorporation of metal and oxide nanoparticles into LbL-MWNT electrodes by square wave pulse potential opens a new strategy for novel energy storage and conversion electrodes with superior electrochemical properties.

Thesis Supervisors: Paula T. Hammond, Bayer Chair Professor of Chemical Engineering
Yang Shao-Horn, Associate Professor of Mechanical Engineering

Dedicated to My Loving Family:

Hyang Hee, Sang Won, & Chang Woo

Acknowledgements

This thesis would not have been a reality without the advice, encouragement, and support of many great researchers. First of all, I thank my two research advisors, Professors Paula T. Hammond and Yang Shao-Horn. I am the first fortunate student to begin this collaborative research. Co-advised students sometimes struggle to find contact points between the different research groups, and have difficulty in combining the strong points of each advisor. In the beginning stage of this thesis project, they gave me the freedom and encouragement to develop my own abilities as an independent researcher. Paula and Yang have built up a good working relationship, thus allowing me to make progress in the project on the great synergies between the two research groups. I thank Paula for her generous nature and constant encouragement. Paula's perspective on the self-assembly of nano-materials inspired me to design nano-structured electrode materials. I thank Yang for her enthusiasm and consistent support; I was always impressed with her passion for science. She brought me into the wonderful world of electrochemistry and physical chemistry. The complementing characteristics of the two advisors have shown me the importance of collaboration in research. Finally, both of them have always been reliable mentors who have guided me into right direction trough the sailing on Ph.D. course at MIT.

I also thank my thesis committee members, Professors. Robert E. Cohen and Nicola Marzari, for constructive and insightful comments. In particular, Prof. Cohen always has encouraged me to pursue an academic career. In addition, I have benefited from discussion with Prof. Nicola Marzari on the understanding of electronic properties for nano-scale electrocatalysts.

My undergraduate advisor, Professor Kookheon Char at Seoul National University, has also been a great mentor in my life. It was very fortunate that he was always with me when I made the most important decisions in my life. I believe that the only way to return his favors is to become a great scientist like many other his students.

I would like to thank all former and current group members in the Paula and Yang groups whom I have greatly learned from and enjoyed interacting with. From the Paula group: Prof. Juhyun Park, Prof. Pil Jin Yoo, Prof. Jodie Lutkenhaus, Prof. Nicole Zacharia, Prof. Hyung-il Lee, Dr. Jung Ah Lee, Dr. Avni Argun, Dr. Fevzi Cebeci, Dr. Nathan Ashcraft, Dr. Kevin Krogman, Daniel Schmidt, Dr. Rebekah Miller, and Prof. Byeong-Su Kim for his advice on layer-by-layer assembly of MWNTs. From the Yang group: Prof. Yong-Tae Kim for the functionalization of MWNTs, Dr. Shuo-Chen for all electron microscopy imaging, Prof. Naoaki Yaubuuchi, Tadashi Kawaguchi, and Betar Gallant for electrochemical measurements, Prof. Hubert Gasteiger and Prof. Robert F. Savinell for electrochemistry and electrochemical measurements, Dr. Gerardo Jose la O', Dr. Robert McGuire Jr., Dr. Christopher Earl Carlton, Dr. Susumu Imashuku, Dr. Zhichuan Xu, Wenchao Sheng, Yi-Chun Lu, Jin Suntivich, and Marjorie A. Joss, special thanks for my English teachers including Theodore Golfinopoulos, Ethan Crumlin, and Betar Gallant.

In particular, I would like thank Korean friends, so called "Korean Mafia", at MIT. I thank my Korean seniors at MIT: Junsang Doh, Dayeon Lee, Juhyun Park, Eunjee Lee, Youjin Lee, Baobae Lee, Taeho Shin, Yoon Sung Nam, Chang Hoon Lim, Sung Gap Im, Ju Jin Ahn, Sunyoung Lee, Tae Seok Moon, Jumin Kim, and Gwang Gyu Kim for their help and support during my thesis. I am very thankful for my lab/room/coffee mates: Jungik Kim, Yang-Hyo Kim, Yongjin Sung, Tairin Hahn, Jingee Hong, Sangwook Kang, Jeong Gon Son, Sungjin Ahn, Hye Ryung Byon, Dongkyu Lee, Tek Hyung Lee, Seok Joon Kwon, Hye Kyung Noh, Ki Wan Bong, Su Kyung Suh, Hyewon Kim, Juhyun Song (Joe), Eun-Suk Lee, and Junhyung Kim to share their valuable time with me.

Financial support of the research projects described in this thesis was provided by the DuPont-MIT Alliance, Masdar Institute, and Samsung Foundation of Culture.

Finally, I would like to thank my parents, Hyang Hee Lee and Sang Won Lee, and brother, Chang Woo Lee, for their endless support and love.

Table of Contents

Abstract.....2

Acknowledgements.....5

Table of Contents.....7

List of Figures and Schemes.....10

List of Tables.....23

Chapter 1. Introduction and Background.....24

1.1 Introductory Remarks and Technical Summary.....24

1.2 Electrochemical Systems: Batteries, Electrochemical Capacitors, and Fuel Cells.....26

1.3 Comparison between Secondary Batteries and Electrochemical Capacitors.....28

1.4 Electrode materials for electrochemical capacitors.....32

1.5 Layer-by-Layer Assembly.....35

1.5.1 Layer-by-Layer Assembly with Functionalized Carbon Nanotubes.....37

1.6 Thesis Overview.....40

1.7 References.....44

Chapter 2. Layer-by-Layer Assembly of All Carbon Nanotube Ultrathin Films for Electrochemical Applications.....47

Abstract.....47

2.1 Introduction.....47

2.2 Experimental Section.....50

2.3 Results and Discussion.....52

2.3.1 XPS Results of Surface Functionalized MWNTs.....53

2.3.2 Surface Charge and LBL Assembly of Functionalized MWNTs.....56

2.3.3 Microstructure of LBL Assembled, Surface Functionalized MWNT Thin Film..59

2.3.4 Swelling Behavior and Mechanical Integrity of LBL Assembled, Surface Functionalized MWNT Thin Films.....64

2.3.5 Electrochemical Properties of LBL Assembled, Surface Functionalized MWNT Thin Films.....67
2.4 Conclusions.....71
2.5 References.....72

Chapter 3. Functionalized Carbon Nanotube Electrodes for High-Power Energy Storage Applications.....75
Abstract.....75
3.1 Introduction.....75
3.2 Experimental Section.....76
3.3 Results and Discussion.....80
3.3.1 Physical characteristics and surface chemistry of LBL-MWNT electrodes.....80
3.3.2 Electrochemical characteristics of LBL-MWNT electrodes.....86
3.3.3 Gravimetric energy and power densities, and cycle life of LBL-MWNT.....95
3.4 Conclusions.....104
3.5 References.....107

Chapter 4. Carbon Nanotube/Manganese Oxide Ultrathin Film Electrodes for Electrochemical Capacitors.....110
Abstract.....110
4.1 Introduction.....110
4.2 Experimental Section.....113
4.3 Results and Discussion.....115
4.3.1 Microstructure of LbL-MWNT/MnO_2 composite electrodes.....116
4.3.2 Electrochemical properties of LbL-MWNT/MnO_2 composite electrodes.....121
4.4 Conclusions.....127
4.5 References.....129

Chapter 5. Square-Wave Potential Electrodeposition of Nanoparticles into Carbon

Nanotube Framework for Electrochemical Applications.....131
Abstract.....131
5.1 Introduction.....132
5.2 Experimental Section.....133
5.3 Results and Discussion.....135
5.3.1 Incorporation of RuO_2 nanoparticles into the LbL-MWNT electrodes.....137
5.3.2 Incorporation of Pt and Pt/Ru nanoparticles into the LbL-MWNT electrodes.....141
5.4 Conclusions.....146
5.5 References.....147

Chapter 6. Roles of Surface Steps on Pt Nanoparticles on the Electrochemical Activity for Electro-Oxidation of Carbon Monoxide and Methanol, and Oxygen Reduction Reaction.....148
Abstract.....148
6.1 Introduction.....149
6.2 Experimental Section.....150
6.3 Results and Discussion Part 1: Roles of Surface Steps on Pt Nanoparticles in Electro-Oxidation of Carbon Monoxide and Methanol.....153
6.3.1 Surface Atomic Structure Characteristics of Pt Nanoparticles.....155
6.3.2 Intrinsic Activity of Pt Nanoparticles for CO Electro-Oxidation.....158
6.3.3 Intrinsic Activity of Pt Nanoparticles for Methanol Electro-Oxidation.....166
6.4 Results and Discuss Part 2: Comparing the Role of Surface Steps of Pt Nanoparticles on the Electrochemical Activity for Oxygen Reduction and Methanol Oxidation....172
6.5 Conclusions.....181
6.6 References.....183

Chapter 7. Conclusion and Perspective.....186

List of Figures and Schemes

Figure 1-1. Electrochemical cell structure of batteries, electrochemical capacitors, and fuel cells.....27

Figure 1-2. A Ragone plot of the various electrochemical energy systems compared to an internal combustion engine and turbines. Adapted from Ref 1 (*Chem. Rev.* 104, 4245-4269 (2004)).....28

Figure 1-3. Schematic illustration of charging and discharging process of lithium ion batteries. Adapted from Prof. Yang Shao-Horn's course (2.625) materials.....29

Figure 1-4. Schematic illustration of charging and discharging process of electrochemical capacitors.....30

Figure 1-5. A Ragone plot for batteries and electrochemical capacitors. Adapted from Ref 2 (*Nat. Mater.* 7, 845-854 (2008)).....31

Figure 1-6. A typical cyclic voltammogram of double layer capacitive materials, which has a rectangular shape.....33

Figure 1-7. Specific capacitance of various materials for ECs in the Literature. Adapted from reference 7 (*The Electrochemical Society Interface* 17, 34-37 (2008)).....34

Figure 1-8. Strategy to improve both energy and power densities of electrochemical capacitors. Nano-scale conformal coating of pseudo-capacitive materials on nano-structured carbon matrix.....35

Figure 1-9. A schematic of alternating layer-by-layer assembly to create thin films on the substrates.....36

Figure 1-10. Degree of ionization of PAA (upper left) and PAH (upper right) in solution as a function of pH. Adapted from reference 46 (*Macromolecules* 38, 116-124 (2005)). pH-dependent zeta potential of functionalized MWNTs (below). Adapted from reference 44 (*Journal of the American Chemical Society* 131, 671-679 (2009)).....38

Figure 1-11. Complete pH matrix (Left) showing the average incremental thickness contributed by a PAH/PAA as a function of pH. Adapted from reference 45 (*Macromolecules* 38, 116-124 (2005)). pH dependent average bilayer thicknesses of MWNT-NH_3^+/MWNT-COO^-. Adapted from reference 44 (*Journal of the American Chemical Society* 131, 671-679 (2009)).....39

Figure 1-12. A schematic of layer-by-layer assembly of functionalized MWNTs. Modified from reference 44 (*Journal of the American Chemical Society* 131, 671-679 (2009))……40

Scheme 2-1. Layer-by-layer assembled MWNT thin film with positively and negatively charged MWNTs……50

Scheme 2-2. Synthesis scheme of (a) COOH and (b) NH_2 functionalized MWNTs…52

Figure 2-1. X-ray photoelectron spectroscopy (XPS) spectra of functionalized MWNTs. (a) Wide scan survey, (b) raw MWNTs C_{1s} spectra, (c) MWNT-COOH (1hr oxidation) C_{1s} spectra, (d) MWNT-COOH (2hr oxidation) C_{1s} spectra, (e) MWNT-NH_2 C_{1s} spectra, (f) MWNT-NH_2 N_{1s} spectra……54

Figure 2-2. Optical images of (a) COOH(COO^-) functionalized MWNT solutions (1hr vs. 2hr oxidation). This picture was taken after 12 hours from sonication. (b) COOH(COO^-) functionalized MWNT solution (0.5 mg/ml) at pH 3.5 and NH_2(NH_3^+) functionalized MWNT solution (0.5 mg/ml) at pH 2.5 in water. This picture was taken after 1 month from the pH adjustment……55

Figure 2-3. pH-dependent zeta potential of functionalized MWNTs. Each point of zeta potential value was obtained by more than 10 measurements and error bars show standard deviations……57

Figure 2-4. (a) Thickness of MWNT thin films under varying assembly pH conditions. The dashed lines are linear fit with standard deviations as error bars. pH 2.5 (+) / 2.5 (-) indicates MWNT thin films assembled from MWNT-NH_2 at pH 2.5 and MWNT-COOH at pH 2.5. (b) pH dependent average bilayer thicknesses. (c) Representative digital picture image of assembled MWNT thin films on Si wafer from pH 2.5 (+) / 4.5 (-). Number on image indicates the number of bilayer (n) in (MWNT-NH_2 / MWNT-COOH)$_n$……57

Figure 2-5. Atomic force microscopy (AFM) height images of (MWNT-NH_2/MWNT-COOH)n thin films deposited at different pH conditions. (a) pH 2.5 (+) / 2.5 (-), (b) pH 2.5 (+) / 4.5 (-). Size of each image is 4 μm × 4 μm……59

Figure 2-6. Representative atomic force microscopy (AFM) phase image of a MWNT thin film of 9 bilayers deposited at pH 2.5 (+) / 3.5 (-). Size of image is 4 μm × 4 μm……60

Figure 2-7. Comparison of the topology of MWNTs using scanning electron microscopy (SEM) images. (a) Deposition of raw MWNT solution on silicone wafer after 2 hr sonication. (b) LBL assembled MWNT thin film at (pH 2.5 (+) / 2.5 (-))$_{20}$……62

Figure 2-8. Scanning electron microscopy (SEM) images of MWNT thin films. (a) A cross-section view of 15 bilayers of MWNT film (pH 2.5 (+) / 3.5 (-)), and (b) a titled cross-

sectional view of a 20 bilayer MWNT film (pH 2.5 (+) / 4.5 (-)). White arrows indicate the interface between silicone substrate and MWNT thin films.....62

Figure 2-9. Representative refractive indices of MWNT thin films assembled at pH 2.5 (+) / 3.5 (-) in air and ethanol, and the porosity calculated from equation 2-2.....63

Figure 2-10. (a)-(d) Time-dependent water swelling behavior of MWNT thin film assembled at pH 2.5 / 4.5, (e) Free-standing film collected on a glass slide tip. (f) Thermally cross-linked film immersed after 24 hr in water. Note the structural integrity is maintained after cross-linking of the MWNT film at 150 °C in vacuum during overnight.....66

Figure 2-11. XPS spectra of the N1s region of a MWNT film of 10 bilayers assembled at pH 2.5 (+) / 3.5 (-) before (a) and after (b) heating at 150 °C under vacuum for 12 hour...67

Figure 2-12. (a) Sheet resistance of the MWNT thin films. (square) as-assembled MWNT thin films assembled at pH 2.5 (+) / 3.5 (-). (circle) MWNT films after a thermal treatment at 150 ^{o}C in vacuum during overnight. (triangle) MWNT films after a second heat-treatment at 300 ^{o}C in H_2 for 2 hours. (b) Corresponding electrical conductivity of the MWNT thin films in S/cm obtained from the data in (a), electrode thickness and area...68

Figure 2-13. (a) Cyclic voltammograms obtained from MWNT thin films on ITO-coated glass electrode (after the second heat-treatment) in 1.0 M H_2SO_4 at room temperature. A scan rate of 50 mV/s was used. (b) Integrated charge from cyclic voltammograms vs. thickness of film measured from profilometer.....69

Figure 2-14. An optical image of a MWNT thin film of 10 bilayers assembled at pH 2.5 (+) / 3.5 (-) on PAH coated PDMS substrate.....70

Figure 3-1. Physical characteristics of LBL-MWNT electrodes. **a,** A digital picture of representative MWNT electrodes on ITO coated glass slides. The number on each image indicates the number of bilayers (n) in $(MWNT\text{-}NH_2 / MWNT\text{-}COOH)_n$. **b,** Thickness of LBL-MWNT electrodes as a function of the number of bilayers. A linear relationship was shown for LBL-MWNT electrodes with thicknesses from 20 nm to 3 μm. Error bars show the standard deviation of thickness computed from 3 samples for each thickness. Transmittance measured at 550 nm as a function of the number of bilayers is shown in the figure inset. Error bars show the standard deviation of transmittance computed from 3 measurements. **c,** A SEM cross-sectional image of an LBL-MWNT electrode on ITO coated glass slide after the heat-treatments. A higher magnification image is shown in the figure inset, which reveals that MWNTs are inter-tangled in the direction perpendicular to the electrode surface. **d,** A TEM image of an LBL-MWNT electrode slice, which shows pore sizes on the order of ~20 nm.....81

Figure 3-2. A plot of deposited area mass density (μg/cm^2) vs. thickness for LBL-MWNT electrodes on quartz crystal microbalance (QCM) substrates. The slope gives the mass

density (0.83 g/cm^3) of MWNT electrodes. Each area mass density value was obtained by 3 measurements using QCM and error bars represent the standard deviations. 5-8 thickness measurements were taken at different positions of each sample using the profilometer...82

Figure 3-3. Surface chemistry of LBL-MWNT electrodes. **a,** XPS O 1s and **b,** N 1s spectra of a representative LBL-MWNT electrode after the heat-treatments. Two peaks (531.7 and 533.4 eV) were fitted in the O 1s spectrum, which could be attributed to oxygen atoms in the carbonyl groups and various other groups bound to the MWNT surface. The nitrogen atoms were mostly in the form of amide groups centered at 400.1 eV. Two small additional peaks suggest that some nitrogen atoms are pyridinic N-6 (398.5 eV) and tied in oxidized-nitrogen-containing functional groups (402.3 eV).....83

Figure 3-4. XPS O 1s spectra of a representative LBL-MWNT electrode after the heat-treatments. **a,** O 1s peaks were analyzed as following groups: carbonyl oxygen atoms in amide, ester, and anhydride groups at 531.7 eV (group 1), oxygen atoms in ether and hydroxyl groups at 532.4 eV (group 2), ether oxygen atoms in anhydride groups at 533.4 eV (group 3), and oxygen atoms in carboxylic acid groups at 534.2 eV (group 4). **b,** A schematic identifying possible surface functional groups on functionalized MWNTs.....84

Figure 3-5. TEM images of the exterior wall structures of **a,** as-received MWNTs, and MWNTs functionalized with **b,** MWNT-COOH and **c,** MWNT-NH_2. Amorphous regions were observed on the surfaces of MWNT-COOH and MWNT-NH_2.....85

Figure 3-6. Potential-dependent electrochemical behavior of LBL-MWNT and functionalized MWNT composite electrodes measured in two-electrode lithium cells. **a,** Cyclic voltammogram data of an LBL-MWNT electrode obtained with different upper- and lower-potential limits. Reducing the lower-potential limit from 3 V to 1.5 V vs. Li resulted in increased current and gravimetric capacitance. **b,** Cyclic voltammogram data of an LBL-MWNT electrode before and after the 500 °C H_2-treatment in 4% H_2 and 96% Ar by volume for 10 hours. **c,** XPS C 1s spectra of an LBL-MWNT electrode before and after this additional heat-treatment, which is shown to remove a considerable amount of surface oxygen and nitrogen functional groups on the MWNT surface. **d,** Cyclic voltammogram data of an LBL-MWNT electrode and composite electrodes of MWNT-COOH and MWNT-NH_2, where the LBL-MWNT electrode has higher current and capacitance normalized to the MWNT weight than composite electrodes. The composite electrodes consisted of 20 wt% PVDF and 80 wt% MWNT-COOH or MWNT-NH_2. Composite MWNT electrodes were prepared from slurry casting and dried at 100 °C for 12 hours under vacuum. The thickness of the LBL-MWNT electrode was 0.3 μm, and those of MWNT-COOH and MWNT-NH_2 composite electrodes are 50 and 30 μm, respectively. The density of composite electrodes was ~0.45 g/cm^3.....88

Figure 3-7. Cyclic voltammograms of conventional PVdF composite electrodes consisting of **a,** MWNT-COOH powder and **b,** MWNT-NH_2 powder collected at 1 mV/s with different lower- and upper-potential limits. Similar to LBL-MWNT electrodes,

narrowing the voltage window to 3.0 – 4.2 V vs. Li resulted in lower specific currents and capacitance values for composite MWNT-COOH and MWNT-NH_2 electrodes.....89

Figure 3-8. Electrochemical characteristics of LBL-MWNT electrodes in two-electrode lithium cells with 1 M $LiPF_6$ in a mixture of ethylene carbonate and dimethyl carbonate (volume ratio 3:7). **a,** Cyclic voltammogram data from electrodes with different thicknesses collected at a scanning rate of 1 mV/s in the voltage range from 1.5 to 4.5 V vs. Li. The integrated charge increases linearly with electrode thickness, as shown in the figure inset. **b,** Cyclic voltammogram data of a 0.3 μm LBL-MWNT electrode over a range of scan rates. **c,** Charge and discharge profiles of an electrode of 0.3 μm obtained over a wide range of gravimetric current densities between 1.5 V and 4.5 V vs. Li. Before each charge and discharge measurement for the data in Fig. 3-8c, cells were held at 1.5 V and 4.5 V for 30 min, respectively. It should be mentioned that the background current from the cell apparatus and ITO coated glass was found to be negligible in comparison to LBL-MWNT electrodes of 0.2 μm thick and greater (Fig. 3-10).....92

Figure 3-9. Charge and discharge voltages for **a,** 1.5 μm and **b,** 3.0 μm LBL-MWNT electrodes, respectively, obtained over a wide range of specific current densities in the voltage range from 1.5 V to 4.5 V vs. Li. Before each charge and discharge measurement, cells were held at 1.5 V and 4.5 V for 30 min, respectively. Cyclic voltammogram data of **c,** 1.5 μm and **d,** 3.0 μm LBL-MWNT electrodes, respectively, over a range of scan rate.....93

Figure 3-10. Background current of the cells with and without LBL-MWNT samples. **a,** Cyclic voltammogram data of ITO coated glass with and without an LBL-MWNT electrode (0.2 μm) collected at 1 mV/s, where significantly higher currents were noted for the LBL-MWNT electrode. **b,** Background current of the Li/ITO-coated-on-glass cell was found to reduce during cycling at 1 mV/s. The data in orange are identical to the ITO-background current shown in Figure S8a. **c,** Electrochemical stability of ITO-coated glass measured in a two-electrode lithium cell with a Li foil as the counter electrode. The electrolyte was 1 M $LiPF_6$ in a mixture of EC and DMC (3:7 volume ratio). ITO can be reduced below 1.5 V vs. Li, and then be reversibly oxidized. In all of the electrochemical testing performed in this work, the lowest voltage has been set to be 1.5 V vs. Li to eliminate the reduction current from ITO substrate.....94

Figure 3-11. Gravimetric energy and power densities, and cycle life of LBL-MWNT electrodes obtained from measurements of two-electrode cells. **a,** A Ragone plot for Li/LBL-MWNT cells with different thicknesses (0.3 ~ 3.0 μm). Corresponding loading density of LBL-MWNT electrodes ranges from 0.025 ~ 0.25 mg/cm^2. Only the LBL-MWNT weight was considered in the gravimetric energy and power density calculations. Gravimetric energy and maximum power densities were reduced for the LTO/LBL-MWNT cells subjected to the same testing conditions due to a lower cell voltage. **b,** Gravimetric capacities of a Li/LBL-MWNT cell as a function of cycle number, which were measured at a current density (~0.25 A/g) once every 100 cycles after voltage holds at the end of charge and discharge for 30 min. Within each 100 cycles, these cells were cycled under an

accelerated rate of ~2.5 A/g. **c,** The voltage profiles of a 1.5 μm electrode in the 1st and 1000th cycles, where negligible changes were noted. **d,** A Ragone plot for Lithium/LBL-MWNT (black squares), LTO/LBL-MWNT (green circles), LTO/$LiNi_{0.5}Mn_{1.5}O_4$ (gray circles), and LBL-MWNT/LBL-MWNT (orange triangles) cells having 4.5 V vs. Li as the upper-potential limit. The thickness of the LBL-MWNT electrode was 0.3 μm for asymmetric Lithium/LBL-MWNT, LTO/LBL-MWNT, and 0.4 μm for symmetric LBL-MWNT/LBL-MWNT.....97

Figure 3-12. Ragone plot based on the unit volume of LBL-MWNT electrodes. The samples used in the graph are the same shown in Fig. 3-11a. It should be noted that the volumetric energy density of LBL-MWNT electrodes, is 2 to 5 times smaller than $LiFePO_4$ and $LiCoO_2$ electrodes due to a lower mass density (~0.8 g/cm^3 for LBL-MWNTs vs. ~4.0 g/cm^3 for composite $LiCoO_2$ electrodes).....98

Figure 3-13. **a,** Cycling of a 1.48 μm LBL-MWNT electrode show that cycling is stable up to 2500 cycles, with no capacity loss even after the cell had been sitting for 30 days unused. **b,** Corresponding Faradaic efficiency (discharge capacity / charge capacity) as a function of cycle number. Capacities were measured at a current density (~0.25 A/g) once every 100 cycles after voltage holds at the end of charge and discharge for 30 min. Within each 100 cycles, these cells were cycled under an accelerated rate of ~2.5 A/g.....99

Figure 3-14. The change in the voltage profiles due to accelerated cycling at 2.5 A/g. Charge and discharge voltage curves of LBL-MWNT electrodes upon cycling within the voltage windows of **a,** 1.5 to 4.2 V and **b,** 1.5 to 4.5 V vs. Li. Measurements were obtained at a lower rate of 250 mA/g once every 100 cycles.....100

Figure 3-15. Surface morphology and surface functional groups of LBL-MWNT electrodes after cycling in lithium cells. **a,** TEM image, **b,** XPS N 1s and **c,** O 1s peaks of an LBL-MWNT electrode after 2000 cycles (1000 cycles in the region of 1.5 to 4.5 V, followed by 1000 cycles from 1.5 to 4.7 V vs. Li). No visible change relative to LBL-MWNT electrodes before cycling (Fig. 3-1) was noted.....101

Figure 3-16. Rate capability of LTO/LBL-MWNT hybrid cells. **a,** Charge and discharge voltages were obtained over a wide range of specific current densities for LBL-MWNT electrode thicknesses of 0.3 μm. The voltage range of 0.0 – 3.0 V vs. LTO corresponds to 1.5 – 4.5 V vs. Li. **c,** Specific capacity as a function of cycle number, which was measured at a current density (~0.7 A/g) once every 100 cycles after voltage holds at the end of charge and discharge for 30 min. Within each 100 cycles, these cells were cycled under an accelerated rate of ~2.5 A/g.....102

Figure 3-17. **a,** Charge and discharge profiles of an LTO/$LiNi_{0.5}Mn_{1.5}O_4$ cell obtained at various rates. The specific capacity is normalized to the weight of $LiNi_{0.5}Mn_{1.5}O_4$ as LTO has higher specific capacity (150 mAh/g) than $LiNi_{0.5}Mn_{1.5}O_4$ (~120 mAh/g), and cell capacity is limited by the capacity of $LiNi_{0.5}Mn_{1.5}O_4$. **b,** A Ragone plot for Li/LBL-MWNT

(black squares), LTO/LBL-MWNT (green circles), and LTO/$LiNi_{0.5}Mn_{1.5}O_4$ (orange triangles) electrode. Only positive electrode weight was considered in the specific energy and power density calculations. The $LiNi_{0.5}Mn_{1.5}O_4$ electrode formulation is active material (80 wt%), SUPER-P® carbon black (10 wt%) and polyvinylidene fluoride (PVdF) binder (10 wt%). Specific power and energy is identical to gravimetric power and energy.....103

Figure 3-18. **a,** Charge and discharge voltage profiles of an electrode of 0.3 μm obtained with upper-voltage limits of 4.2 and 4.5 V vs. Li under constant current measurements. **b,** A Ragone plot of electrodes with thickness of 0.5 μm having 4.2 V or 4.5 V vs. Li as the upper-potential limit. Only the LBL-MWNT weight was considered in the specific energy and power calculations. Specific power and energy is identical to gravimetric power and energy.....105

Figure 3-19. Schematic illustration of the energy storage mechanism of LBL-MWNT electrodes. Faradaic reactions between surface oxygen functional species (orange arrows) and Li were schematically illustrated on an HRTEM image of the LBL-MWNT electrodes. XPS C 1s spectra of the LBL-MWNT electrode is shown in the figure inset, which shows various oxygen and nitrogen functional groups on the MWNT surface. Intact graphite layers inside of the MWNTs (white arrows) were indicated as electron conduction channels.....106

Scheme 4-1. Layer-by-layer assembly of MWNT (LbL-MWNT) film via alternative dipping of substrate into positively charged (MWNT-NH_3^+) and negatively charged (MWNT-COO^-) MWNTs, and process of LbL-MWNT/MnO_2 composite electrode though dipping of the LBLLbL-MWNT film into permanganate ion (MnO_4^-) solution.....113

Figure 4-1. SEM images of (a) pristine LbL-MWNT electrode and (b-d) LbL-MWNT/MnO_2 composite electrodes prepared by dipping LbL-MWNT electrodes into 0.1 M $KMnO_4$/0.1 M K_2SO_4 solution at deposition time from 10 min to 60 min. (d) A cross-section view of an LbL-MWNT/MnO_2 composite electrode after 60min dipping. White arrow indicates the interface between the substrate and LbL-MWNT/MnO_2 composite film.....116

Figure 4-2. (a) A cross-section SEM image and (b) elemental mapping of Mn for an LbL-MWNT/MnO_2 composite electrode (60 min). White arrow indicates the interface between the substrate and LbL-MWNT/MnO_2 composite film.....117

Figure 4-3. TEM image with selected-area diffraction pattern (SAED) of (a) an LbL-MWNT and (b) an LbL-MWNT/MnO_2 composite electrode (60 min dipping). (c) High magnification image of an LbL-MWNT/MnO_2 composite electrode (60 min dipping). White arrows indicate nano-size MnO_2 coating on MWNTs.....119

Figure 4-4. (a) TEM image with elemental mapping of (b) C, (c) O, and (d) Mn for an LbL-MWNT/MnO_2 composite electrode (60 min dipping).....120

Figure 4-5. XPS spectra of LbL-MWNT/MnO_2 composite electrodes. (a) Atomic ratio of Mn/C as a function of dipping time, (b) Mn 2p spectra, and (c) Mn 3s spectra.....121

Figure 4-6. (a) Cyclic voltammograms for LbL-MWNT/MnO_2 composite films on ITO-coated glass electrodes in 0.1 K_2SO_4 at room temperature as a function of dipping time. A scan rate of 50 mV/s was used. 0 min indicates a pristine LbL-MWNT electrode (b) Volumetric capacitance as a function of dipping time. Capacitance was estimated from cyclic voltammograms with a scan rate of 50 mV/s (Fig. 4-6a).....122

Figure 4-7. (a) Rate dependent Cyclic voltammograms of LbL-MWNT/MnO_2 composite electrodes at various scan rates (10 mV/s ~ 1,000 mV/s) (b) Volumetric capacitance (F/cm^3) obtained from LbL-MWNT/MnO_2 composite electrodes with dipping time as a function of scan rates (10 mV ~ 1,000 mV/s).....123

Figure 4-8. (a) Cyclic voltammograms obtained from LbL-MWNT/MnO_2 composite electrodes with different cycling numbers in 0.1 M K_2SO_4 at room temperature. A scan rate of 200 mV/s was used. (b) Capacity retention of from LbL-MWNT/MnO_2 composite electrodes as a function of cycling number.....125

Figure 4-9. (a) Thickness of as-assembled MWNT thin films and LbL-MWNT/MnO_2 composite electrodes after 30 min dipping as a function of the number of bilayers. The dashed lines are linear fit with standard deviations as error bars. (b) Cyclic voltammograms obtained from LbL-MWNT/MnO_2 composite electrodes with different thicknesses on ITO-coated glass electrode in 0.1 M K_2SO_4 at room temperature. A scan rate of 50 mV/s was used. (c) Charge density (measured from cyclic voltammograms and electrode area) vs. thickness of films from profilometry measurements.....126

Scheme 5-1. Introduction of the metal oxide and the bimetallic nanoparticles into the layer-by-layer assembled multiwall carbon nanotube (LbL-MWNT) film electrode via square wave potential cycles in the metal precursor solution.....136

Figure 5-1. (a) Potential and time scales of square-wave potential cycles. (b) Representative current versus time plot during square-wave potential cycles.....137

Figure 5-2. (a) A representative low-magnification TEM image of RuO_2 nanoparticles within the LbL-MWNT electrode after 400 cycles. (b) Histogram and high-magnification TEM image (inset) of RuO_2 nanoparticles within the LbL-MWNT film electrode after 400 cycles. Number-averaged diameter (d_n) and standard deviation of RuO_2 nanoparticles is indicated. At least 100 randomly selected nanoparticles were counted to present the histogram and d_n.....138

Figure 5-3. (a) Cyclic voltammograms for the different number of square-wave pulse cycle LbL-MWNT/RuO_2 composite electrodes on ITO-coated glass electrodes in a 0.5 M H_2SO_4

electrolyte at a scan rate of 50 mV/s at room temperature. (b) Comparison of volumetric capacitance as a function of electropulse deposition cycle number. Capacitance was estimated from the cyclic voltammograms at a scan rate of 50 mV/s (Fig. 5-3a).....139

Figure 5-4. (a) Scan rate dependent cyclic voltammograms of the LbL-MWNT/RuO_2 composite electrode (600 cycles) at various scan rates (50 mV/s ~ 500 mV/s) (b) Volumetric capacitance (F/cm^3) obtained from the LbL-MWNT/RuO_2 composite electrode (600 cycles) as a function of scan rates (50 mV ~ 500 mV/s).....140

Figure 5-5. Histograms and representative HRTEM images of (a) Pt and (b) Pt/Ru alloy nanoparticle within the LbL-MWNT electrode after 400 cycles. Number-averaged diameter (d_n) and standard deviation of nanoparticles is indicated. At least 100 randomly selected nanoparticles were used to present histogram and d_n.....142

Figure 5-6. (a) A low-magnification image with an energy dispersive X-ray (EDX) spectroscopy of Pt/Ru nanoparticle within the LbL-MWNT film electrode after 400 cycles. Atomic ratio of Pt:Ru is indicated. (b-d) Pt and Ru EDX spectroscopy maps of randomly selected Pt/Ru nanoparticle using aberration corrected transmission electron microscopy (TEM).....143

Figure 5-7. (a) Cyclic voltammograms of the methanol electro-oxidation on the Pt/Ru alloy nanoparticles within the LbL-MWNT film electrode, where the specific current is normalized by the ESA of Pt nanoparticles. The data were recorded at 50 mV/s from 0.05 to 1.10 V vs. RHE at room temperature. (b) Comparison of the methanol electro-oxidation activity on the Pt, Pt/Ru alloy nanoparticles within the LbL-MWNT film, and commercial carbon supported Pt nanoparticle electorocatalyst (TKK, d_n: 2.1nm). The specific currents normalized by the ESA of Pt nanoparticles were plotted thorough positive-going scan between ~0.3 V and 0.9 V vs. RHE after the subtraction of the double layer current.....145

Figure 6-1. Particle sizes and surface atomic structure of Pt nanoparticles in the Pt/MWNT samples. (a) Histogram and typical TEM micrograph (inset) of a Pt/MWNT sample heat-treated at 548 K. (b) Number-averaged diameter (d_n) of Pt/MWNTs as a function of heat-treatment temperature. Standard deviation in d_n is ~1 nm and error bars in the graph are based on standard deviation of the mean by considering >200 Pt nanoparticles per sample. (c) and (d) Typical HRTEM images and FFT results (inset) of Pt nanoparticles obtained from 573 K and 673 K, respectively. (e) Schematics of high-index planes observed on Pt nanoparticles. (f) Average area fractions of all high-index planes observed in the Pt/MWNT samples as a function of heat-treatment temperatures. The solid circle corresponds to the 573K sample that was cycled from 0.05 to 1.1 V vs. RHE in CO-saturated 0.1 M $HClO_4$ solution (CO annealing). The calculation of error bars can be found in the experimental section.....154

Figure 6-2. (a) to (c), Histograms and representative HRTEM micrographs of Pt/MWNT samples that were heat-treated at 573 K, 673 K, and 773 K, respectively. The histograms

were measured from at least 200 random selected particles of each sample. The number-averaged diameter and its standard deviation of Pt nanoparticles of each sample are shown.....156

Figure 6-3. Fraction of low-index [(111) and (100)] and high-index surface planes as a function of the heat-treatment temperature. The high-index planes are divided into 1) steps on the (111) terrace, which includes n(111)×(100) and n(111)×(111) having n equal or greater than 2; 2) steps on the (100) terrace, which contains n(100)×(111) having n greater than 2.....157

Figure 6-4. CO electro-oxidation activity on Pt/MWNT samples measured at room temperature. (a) Specific oxidation current (normalized to Pt ESA) of CO_{ad} on Pt/MWNT samples in 0.1 M $HClO_4$ with 5 mV/s. (b) Specific current transients (normalized to Pt ESA) of the oxidation of CO_{ad} after the potential was stepped from 0.1 to 0.73 V vs. RHE. (c) RDE current density (normalized to RDE geometric area) of CO bulk oxidation at 1600 rpm, where the specific activity (normalized to Pt ESA) calculated from current in the negative potential sweep with 5 mV/s is shown in the figure inset.....161

Figure 6-5. CO stripping voltammetry of Pt/MWNTs obtained at (a) T_h : 548 K and (b) T_h : 773 K with a scanning rate of 5 mV/s at room temperature. Data include voltammogram of adsorbed CO oxidation (solid line) recorded in 0.1M $HClO_4$ purged after CO adsorption with nitrogen for 30 minutes at 0.1 V vs. RHE, and base voltammogram data (dotted line) after CO oxidation.....161

Figure 6-6. Current transients of the oxidation of CO adlayer obtained at (a) T_h : 548 K, (b) T_h : 573 K, (c) T_h : 773 K. The potential was stepped from 0.1 V vs. RHE to three potentials near the CO stripping peak potential.....162

Figure 6-7. CO bulk oxidation of Pt/MWNTs obtained at 773 K at rotation rates of 100, 400, 900, and 1600 rpm using a rotation disk electrode. The potential region was from 0.5 to 1.1 V vs. RHE at a scanning rate of 5 mV/s in 0.1M $HClO_4$.....163

Figure 6-8. Comparison of CO electro-oxidation activity on Pt/MWNTs of 573 K before and after CO annealing. (a) Specific oxidation current (normalized to Pt ESA) of CO_{ad} on Pt/MWNT sample in 0.1 M $HClO_4$ with 5 mV/s. (b) Specific current transients (normalized to Pt ESA) of the oxidation of CO_{ad} after the potential was stepped from 0.1 to 0.73 V vs. RHE. (c) RDE geometric current density of CO bulk oxidation at 1600 rpm, where the specific activity (normalized to Pt ESA) calculated from current in the negative potential sweep with 5 mV/s is shown in the figure inset.....165

Figure 6-9. Pt particle size distribution (left axis) and area fraction of high-index planes (right axis) in Pt/MWNTs heat treated at 573 K before (a) and after (b) CO annealing, respectively. (c) and (d) Typical HRTEM image and FFT of a Pt nanoparticle in the

Pt/MWNT sample after CO annealing. The calculation of error bars can be found in the Experimental section.....166

Figure 6-10. Methanol electro-oxidation activity on Pt/MWNT samples measured at room temperature. (a) Cyclic voltammograms for methanol electro-oxidation of Pt/MWNT samples, where specific current is normalized to the Pt ESA. The data were recorded with 50 mV/s from 0.05 to 1.1 V vs. RHE. (b) Specific currents (normalized to Pt ESA) at different potentials (RHE) in cyclic voltammograms. (c) Specific current transients (normalized to Pt ESA) of the electro-oxidation of methanol in the first second, and of the long-time response to 900 s in the inset, which were recorded upon imposing a voltage step from 0.1 to 0.7 V vs. RHE. Measurements were conducted in an N_2 saturated solution of 1 M CH_3OH in 0.1 M $HClO_4$. (d) Intrinsic methanol oxidation activity as a function of area fraction of high-index planes normalized to the 548 K sample. Inset compares specific methanol oxidation charge in the positive-going scan of cyclic voltammogram with the area fraction of high-index planes normalized to the 548 K sample. The calculation of error bars can be found in the Experimental section.....168

Figure 6-11. Cyclic voltammograms for methanol oxidation reaction for Pt/MWNTs obtained at 573 K. The potential cycles were recorded at a scan rate of 50 mV/s from 0.05 to 1.1 V (RHE) in N_2 saturated a solution of 1M CH_3OH in 0.1 M $HClO_4$ at room temperature. Steady-state cyclic voltammetry curves are reached typically after ~5 cycle.....169

Figure 6-12. (a) Cyclic voltammograms for methanol electro-oxidation for Pt/MWNTs obtained at 548 K (d_n: 1.9 nm) and a TKK Pt 46 wt% (d_n: 2.1 nm) sample that is commonly used in fuel cells. The potential cycles were recorded at a scan rate of 50 mV/s from 0.05 to 1.1 V (RHE) in N_2 saturated a solution of 1M CH_3OH in 0.1 M $HClO_4$ at room temperature. (b) Methanol electro-oxidation current of Pt/MWNTs of 573 K as a function of cycle number, which were measured at different potentials (RHE) in the postive-going sweep. The currents were recorded during potential cycling with 50 mV/s from 0.05 to 1.1 V vs. RHE in an N_2 saturated solution of 1 M CH_3OH in 0.1 M $HClO_4$ at room temperature.....171

Figure 6-13. (a) ORR polarization curves of a Pt/MWNT sample heat-treated at 773 K (denoted as Pt/MWNT-773 K). Experiments were conducted in O_2 saturated 0.1 M $HClO_4$, with a scan rate of 10 mV/s. (b) Specific ORR activity of Pt/MWNT samples at 0.85 V and 0.9 V vs. RHE as a function of heat-treatment temperature, which was obtained from the positive-going scan at 1600 rotation per minute (rpm).....173

Figure 6-14. Cyclic voltammograms of Pt nanoparticles obtained from different heat-treatment temperature in 0.1M $HClO_4$ at a sweep rate of 20 mV/s at room temperature.....174

Figure 6-15. Specific MOR (left axis) and ORR activity (right axis) as a function of area fraction of stepped surfaces normalized to the 548 K sample. Specific MOR activity was measured at 0.5 V vs. RHE after subtraction of the double layer current. Specific ORR activity was measured at 0.85 V vs. RHE at 1600 rpm.....174

Figure 6-16 (a) Cyclic voltammograms during potential cycling on Pt/MWNT-573 K in a CO-saturated 0.1 M $HClO_4$ solution from 0.1 to 1.1 V vs. RHE at a scan rate of 50 mV/s for 10 minutes (CO annealing) at room temperature. (b) Comparison of cyclic voltammograms on Pt/MWNT-573 K before and after CO annealing. The potential cycles were recorded at a scan rate of 20 mV/s from 0.05 to 1.1 V (RHE) in an N_2 saturated 0.1 M $HClO_4$ at room temperature.....175

Figure 6-17. Comparison of Tafel plots of ORR specific activity on Pt/MWNT-573 K before and after CO annealing at room temperature. Tafel plots were obtained from the polarization curves in the positive-going scans at 1600 rpm, which was normalized to Pt electrochemical surface area (Figure 6-14).....176

Figure 6-18 (a) Comparison of cyclic voltammograms for methanol oxidation activity on Pt/MWNT-548 K before and after CO annealing at room temperature. The potential cycles were recorded at a scan rate of 50 mV/s from 0.05 to 1.1 V (RHE) in N_2 saturated a solution of 1M CH_3OH in 0.1 M $HClO_4$ at room temperature. (b) Specific currents (normalized to Pt ESA) at different potentials (RHE) in cyclic voltammograms.....177

Figure 6-19. (a) XANES spectra obtained with the Pt/MWNT-573 K at the Pt L_3 edge at three different potentials. (b) Comparison of values extracted from the XANES spectra for Pt/MWNT-573 K and 773 K as a function of potential in 1 M $HClO_4$.....179

Figure 6-20 (a) XANES spectra obtained with the Pt/MWNT-773 K at the Pt L_3 edge at four different potentials. (b) Comparison of XANEs spectra for Pt/MWNT-573 K and 773 K at 0.41 V vs. RHE. Data were collected in fluorescence mode with the in-situ electrochemical cell at different electrode potentials in 1.0 M $HClO_4$ at room temperature.....180

Figure 6-21. HRTEM image of a Pt nanoparticle in Pt/MWNT-673 K. Active sites on the nanoparticle terraces dominate ORR activity while active sites involving surface steps governs MOR activity at low potentials.....181

Figure 7-1. Comparison of the volumetric capacitance (F/cm^3) in aqueous electrolytes for various LbL assembled electrodes.....187

Figure 7-2. Blue circular regions show estimated gravimetric energy and power density of an asymmetric EC device assembled with LBL-MWNT for positive and Li or LTO for negative electrode. Higher power density for LBL-MWNT devices are observed over Li-ion batteries at comparable energy density. Red dashed area is expected range of future

development in EC devices using LbL approach. Adapted from Ref. 2 (*Nature Materials* **7**, 845-854 (2008))..... 189

Figure 7-3. Automated mister for constructed for spray-LBL in the Hammond laboratory at MIT capable of fabricating ~100 cm^2 electrodes. Arrows indicate mist jets (right) and target (left)..... 190

Figure 7-4. (a, b) Representative (left) optical microscope and (right) SEM images of patterned MWNT multilayer film on a silicon wafer, (c) photograph of MWNT pattern transferred on a flexible ITO-coated PET film. All are 5 bilayers of MWNT film. Manuscript (Byeong-Su Kim, Seung Woo Lee, Hyeonseok Yoon, Michael S. Strano, Yang Shao-Horn, and Paula T. Hammond) including the Figure was submitted..... 191

List of Tables

Table 1-1. Comparison of characteristics of secondary batteries and electrochemical capacitors.....31

Table 3-1. Relative surface atomic ratio of C, O and N on functionalized MWNTs (MWNT-COOH and MWNT-NH_2) and a representative LBL-MWNT electrode after the heat-treatments, where were obtained from XPS data analysis. The estimated specific capacity based on the chemical formula ($C_{0.85}O_{0.11}N_{0.04}$) of LBL-MWNT and proposed Faradaic reactions betweens oxygen in the surface functional groups and Li ions is in good agreement with experimental results (Fig. 3-8c).....90

Chapter 1. Introduction and Background

1.1 Introductory Remarks and Technical Summary

Development of novel energy conversion and storage devices using nanotechnology and science has been acknowledged as one of the most important technical issues in clean energy applications. Since the efficiency of energy conversion and storage devices primarily depends on the materials and structures utilized, synthesizing unique nanomaterials and designing optimal nanostructures are essential to this research. Potential advantages of nanostructured electrodes for fuel cells, batteries and electrochemical capacitors include higher electrode/electrolyte contact area and faster charge/discharge rates, ultimately leading to higher energy and power density of energy devices.

This thesis focuses on designing novel energy storage and conversion electrodes using layer-by-layer (LbL) assembly with multiwall carbon nanotubes (MWNTs). Layer-by-layer (LbL) assembly is a versatile thin-film fabrication technique which consists of the repeated, sequential immersion of a substrate into aqueous solutions of complementary functionalized materials. This work introduces MWNTs into LbL assembly via surface functionalization of MWNTs, creating all-MWNT thin film electrodes. LbL assembled MWNT (LbL-MWNT) electrodes are unique in that they yield distinct advantages such as 1) water-based or "green" electrode processing at ambient conditions, 2) elimination of polymeric/insulating binding agents, surfactants and electronic carbon supports, and 3) precise control of electrode thickness. In addition, the LbL method can be adapted to virtually any 2D, 3D, or flexible substrate to increase electrode surface area for increased energy and power.

This work examines the electrochemical characteristics of such composite LbL electrodes in aqueous electrolytes, where it could precisely control both the capacity and the electrochemical activity of the electrode. In addition, this work includes the energy and power characteristics of such composite LbL electrodes in lithium nonaqueous cells as the

asymmetric electrochemical capacitors or batteries, where it could increase the energy and power densities of LbL-MWNT electrodes. This thesis first reveals that the Faradaic reactions of surface functional groups on functionalized MWNT electrodes can be accessed in the wider voltage window (1.5 – 4.5 V vs. lithium) of a nonaqueous electrolyte, which renders considerably higher energy and power capabilities than are available in aqueous systems.

Micron-thick LbL-MWNT electrodes exhibit gravimetric energy densities of ~200 Wh/kg at gravimetric power densities of ~100 kW/kg. MWNT electrodes show a significantly higher power capability than conventional and high-power battery electrodes, where obtainable gravimetric energy densities drop sharply at gravimetric power densities in the range from 10 to 100 kW/kg. Therefore, at gravimetric power densities greater than 100 kW/kg, MWNT electrodes provide much higher gravimetric energy densities than conventional and high-power lithium battery materials. Moreover, it is demonstrated that replacing lithium metal with a lithium titanium oxide (LTO) material can render next-generation Li-metal-free electrochemical capacitors with energy densities considerably higher than those of current electrochemical capacitors (1-5 Wh/kg). The gravimetric energy of LTO/MWNT devices can be estimated to be ~30 Wh/kg at ~5 kW/kg assuming packaged gravimetric energy density of practical devices being roughly 1/5 of gravimetric electrode energy.

With these LbL-MWNT electrodes as a nano-framework, we further incorporate nanoscale metal oxides with pseudo-capacitive properties and metal/metal alloy nanoparticles with electrocataltyic properties using electroless redox deposition and square wave pulse potential deposition. LbL-MWNT/MnO_2 nano-composite electrodes, created by redox deposition of MnO_2 on the LbL-MWNT framework, show higher volumetric capacitance of 246 F/cm^3 with good capacity retention up to an extremely fast scan rate of 1,000 mV/s. Furthermore, uniformly distributed nano-size RuO_2, Pt and Pt/Ru alloy were successfully introduced into LbL-MWNT films via square wave pulse potential cycling. Volumetric capacitance of LbL-MWNT/RuO_2 showed remarkable volumetric capacitance over ~1000 F/cm^3 in aqueous electrolytes, Pt/Ru alloy electrocatalysts showed considerably

higher specific activity for methanol oxidation compared to commercial Pt catalyst (Tanaka Kikinzoku International, Inc.) of a comparable particle size and distribution. With all of these distinct advantages and enhanced electrochemical performance, these LbL-MWNT electrodes provide promising electrode materials for energy storage and conversion devices.

1.2 Electrochemical Systems: Batteries, Electrochemical Capacitors, and Fuel Cells

Representative electrochemical energy storage and conversion systems include batteries, electrochemical capacitors (ECs), and fuel cells[1]. Even though fundamental energy storage and conversion mechanisms are different, these electrochemical systems show structural and operational analogies[1]. Figure 1-1 shows the analogies of the three systems. Basically, these electrochemical systems have negative and positive electrodes, and these two electrodes are separated by electrolyte medium. Electrons are conducted from negative to positive electrode through an external circuit, and corresponding ions are separately migrated through electrolyte medium. Because electrochemical reactions - generation and consumption of ions and electrons - only occur at the interface between electrodes/electrolyte, fast electron and ionic transport thorough the electrodes is the key parameter for high energy production.

In contrast to batteries and ECs, fuel cells are open systems where fuels such as hydrogen and oxygen are continuously delivered to the electrodes (energy conversion center) from storage tanks. Therefore, energy conversion in the electrodes and storage in the tank are physically separated, and energy density of the system is determined by the amount of fuels in the tanks. On the other hand, batteries and ECs are closed systems, where both energy storage and conversion occur in the electrodes. In these systems, energy density depends on active mass (batteries) or surface area (ECs) of the electrodes.

A Ragone plot is a chart developed to compare the energy and power performance of various energy storage systems. In this plot, specific power (W/kg) is plotted versus specific energy (Wh/kg) in both logarithmic scales to compare energy storage capacity and

rate capability of different systems. A Ragone plot of various electrochemical devices (Figure 1-2[1]) shows that fuel cells and batteries are considered as high energy electrochemical systems. On the other extreme, conventional capacitors show high power capability with low energy density. ECs, sometimes called a supercapacitor, can bridge the performance gap between high-power capacitors and high-energy batteries. However, the performance of electrochemical systems cannot compete with traditional energy systems including the combustion engine and gas turbine, which have both high energy and power capability. One strategy to increase the performance of electrochemical system is to design hybrid systems connecting batteries/ECs or batteries/air fuel cells, which can combine the advantages of different systems[1-3].

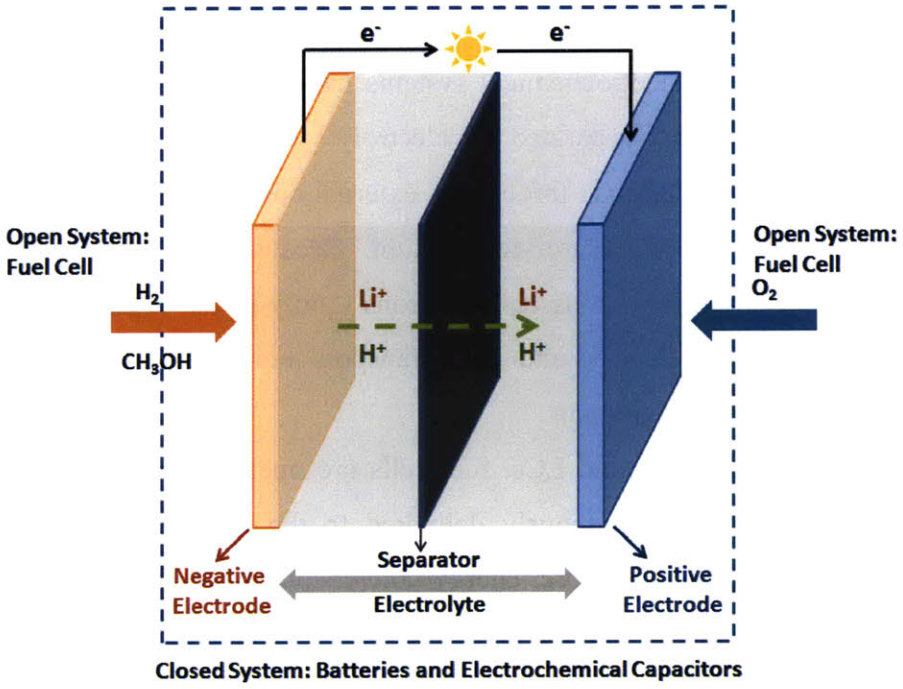

Figure 1-1. Electrochemical cell structure of batteries, electrochemical capacitors, and fuel cells.

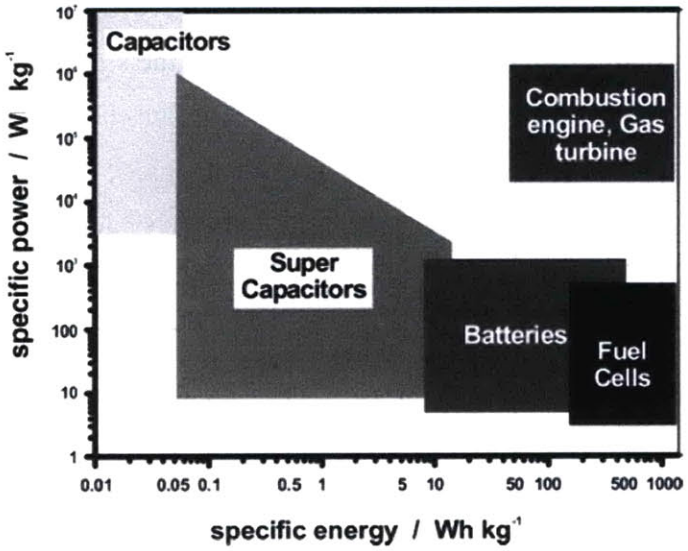

Figure 1-2. A Ragone plot of the various electrochemical energy systems compared to an internal combustion engine and turbines. Adapted from Ref 1 (*Chem. Rev.* **104**, 4245-4269 (2004)).

1.3 Comparison between Secondary Batteries and Electrochemical Capacitors

Secondary (rechargeable) batteries and ECs are both electrochemical energy storage systems for applications such as laptop computers, vehicles, and uninterruptible power supplies (UPS)[2]. Because their energy and power performance are fairly comparable, it is interesting to compare the fundamental differences between electrochemical capacitors and batteries both in their structures and energy storage mechanism. The battery stores energy by using chemical reactions and can store a larger amount of energy than a capacitor can, but it undergoes chemical changes between the charge and discharge process. A representative secondary battery is the lithium-ion battery in which the positive electrode is an oxide material including lithium and the negative electrode is generally graphite carbon materials (Figure 1-3). During the charging process, lithium ions migrate from the positive electrode to the negative electrode, where lithium ions intercalate into the graphite sheets. During discharging, lithium ions are deintercalated from the graphite sheets, and migrate

and inserted into the cathode. On the other hand, the electrochemical capacitor stores its charge physically, and it experiences no major change in the structure of the material in the charged state. The electrodes of the capacitors contain an electrolyte, a fluid containing positive and negative ions; and they store electrical charge at an electrode-electrolyte interface (Figure 1-4)[4]. For this reason, activated carbon, which has an extremely porous structure and a large surface area for storing the ions, is generally used for ECs.

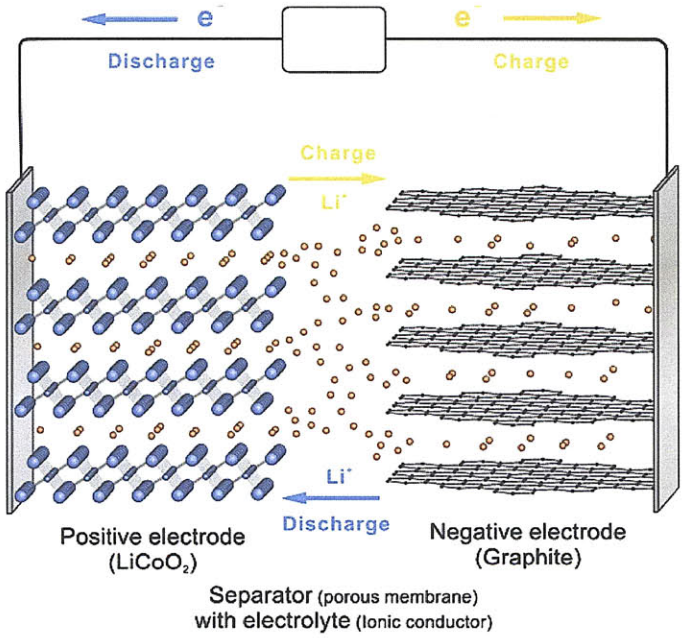

Figure 1-3. Schematic illustration of charging and discharging process of lithium ion batteries. Adapted from Prof. Yang Shao-Horn's course (2.625) materials.

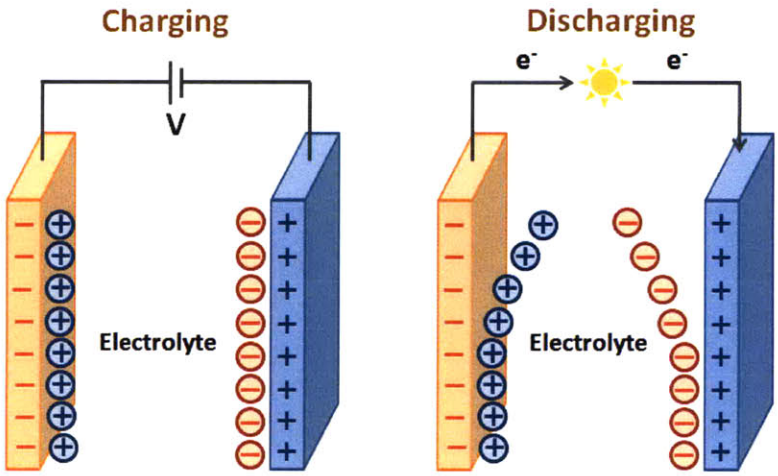

Figure 1-4. Schematic illustration of charging and discharging process of electrochemical capacitors.

Because of their differences in structure, the first fundamental difference between the two technologies is the charge/discharge time. Lithium ion batteries take between several minutes and up to several hours to recharge[4]. In contrast, the charge time for the electrochemical capacitors is on the order of a few seconds or less. The second basic difference caused by the energy storage mechanisms is the life cycle of the two systems. The chemical and mechanical changes during the charge/discharge in the battery system limit their cycle life. For example, we can easily observe that the capacity of a laptop or cell phone battery will decrease as time goes by. On the other hand, the charge/discharge in the capacitor system is highly reversible and the charge/discharge can continue to millions of cycles, because the charge is stored physically, with no chemical changes taking place. Table 1-1[4,5] summarizes these differences between two systems. In addition, ECs and batteries show the gap between the energy and power performance as shown by Ragone plot (Figure 1-5). A major challenge in electrochemical energy storage systems is to bridge the performance gap between ECs and batteries. Consequently, recent research efforts have focused on designing new ECs to improve their energy capacity, and novel batteries to enhance their power density.

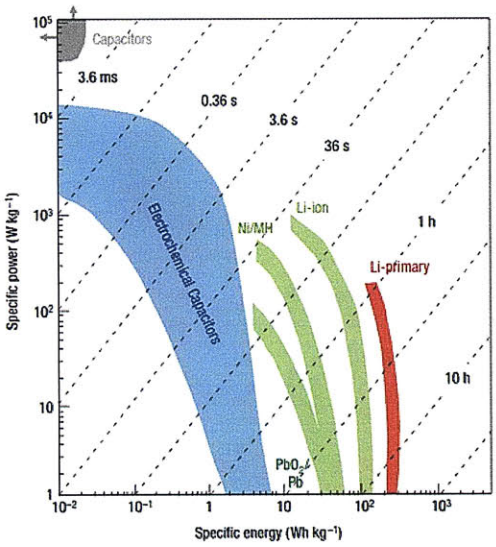

Figure 1-5. A Ragone plot for batteries and electrochemical capacitors. Adapted from Ref 2 (*Nat. Mater.* **7**, 845-854 (2008)).

Characteristic	Battery	Electrochemical Capacitor
Energy storage mechanism	Chemical (intercalation)	Physical (adsorption)
Power limitation	Reaction kinetics, electrical conductivity, ion transport	Electrolyte conductivity
Energy limitation	Electrode mass	Electrode surface area
Cycle life limitation	Mechanical, chemical stability	Side reactions
Charge/discharge time	Several minutes ~ hours	~ Several seconds
Cycle life	<5,000	>500,000
Specific Energy (Wh/kg)	~100	5
Specific Power (kw/kg)	~1	5~10

Table 1-1. Comparison of characteristics of secondary batteries and electrochemical capacitors[4,5].

1.4 Electrode Materials for Electrochemical Capacitors

Electrochemical Capacitors (ECs) store energy at the electrode/electrolyte interface through ion adsorption onto the electrode surface[4]. Because a high interface area can store higher energy, high surface area activated carbons have been generally used. In addition to surface area, high electrical conductivity, open porosity, and electrochemical stability are important factors to reach high capacitances of ECs. Recently, nano-structured carbon materials including carbon nanotubes, carbon fibers, and carbide-derived carbons have actively been tested, and some of them succeed in showing enhanced performance due to higher surface area and fine tuned pore size[5,6]. Double layer capacitance can be described according to equation 1-1:

$$C = \varepsilon A/d \qquad \text{Equation 1-1}$$

Where ε is the electrolyte dielectric constant, A is the surface area of the electrode accessible to ions, and d is the distance between the electrode surface and the center of the adsorbed plane of ions. The double layer capacitance for carbon materials is 5~20 μF/cm², and 50~150 F/g, depending on the electrolyte[2,6]. A cyclic voltammogram of a double layer capacitive material, which has a characteristic rectangular shape, is presented in Figure 1-6. The capacitance (C) of the electrode can be calculated from cyclic voltammmogram according to equation 1-2:

$$C = \frac{dQ}{dV} = \frac{I}{(dV/dt)} \qquad \text{Equation 1-2}$$

Where Q is the charge on the electrode, V is its potential, I is the current, and, (dV/dt) is the potential scan rate. If we expresses current as current density based on mass or volume of the electrode, then specific capacitance C (F/g) or volumetric capacitance C (F/cm^3) is easily attained.

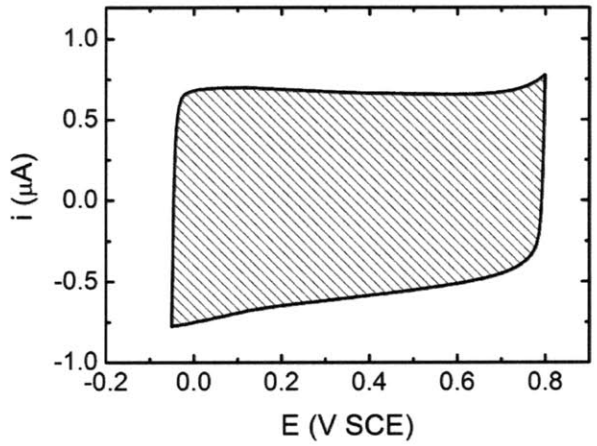

Figure 1-6. A typical cyclic voltammogram of double layer capacitive materials, which has a rectangular shape.

In addition to double layer capacitance from carbon materials, higher capacitance from reversible redox reactions from conducting polymers or metal oxides such as RuO_2 and MnO_2 can be applied for ECs (Figure 1-7)[7]. These fast reversible redox reaction on the surface of active materials was defined as pseudo-capacitive process, which significantly increased specific capacitances[2,7]. Among pseudo-capacitive materials, ruthenium oxides (RuO_2) have been actively studied due to fast mixed proton/electron conducting properties. High theoretical specific capacitance (1358 F /g) and high electrical conductivity (3×10^2 S/cm) lead specific capacitance of more than 600 F/g in acidic electrolytes[7,8]. Surface sites of ruthenium oxides are reversibly oxidized and reduced from Ru (II) to Ru (IV), and a simultaneous exchange of protons occurs within 1.2V in acidic solution (equation 1-3)[2]. However, specific capacitance show significant decrease at higher scan rates because of proton depletion, and high cost limits its application for ECs[7].

$$RuO_2 + xH^+ + xe^- \leftrightarrow RuO_{2-x}(OH)_x,\ 0 \le x \le 2. \qquad \text{Equation 1-3}^2$$

Low-cost manganese oxides (MnO_2) have attracted attention as promising pseudo-capacitive materials. The charge storage mechanism is reversible oxidation and reduction of

MnO_2 with simultaneous surface adsorption of electrolyte cations C^+ (K^+, Na^+) including protons (equation 1-4)[2,9]. Theoretical specific capacitance of MnO_2 is ~1370 F/g based on one-electron redox reaction per manganese[10]. However, this value can be achieved only for ultrathin (on the nanometer scale) film or nano-sized particles due to the limited insertion of cations on the surfaces. In addition, low electrical conductivity (10^{-5}~10^{-6} S/cm)[9] of MnO_2 can become rate-limiting for high power applications. Consequently, maximizing utilization of MnO_2 pseudocapacity and designing highly electrically conductive electrode microstructure is critical to realize MnO_2-based ECs.

$$MnO_2 + xC^+ + yH^+ + (x+y)e^- \leftrightarrow MnOOC_xH_y \qquad \text{Equation 1-4}^{2,9}$$

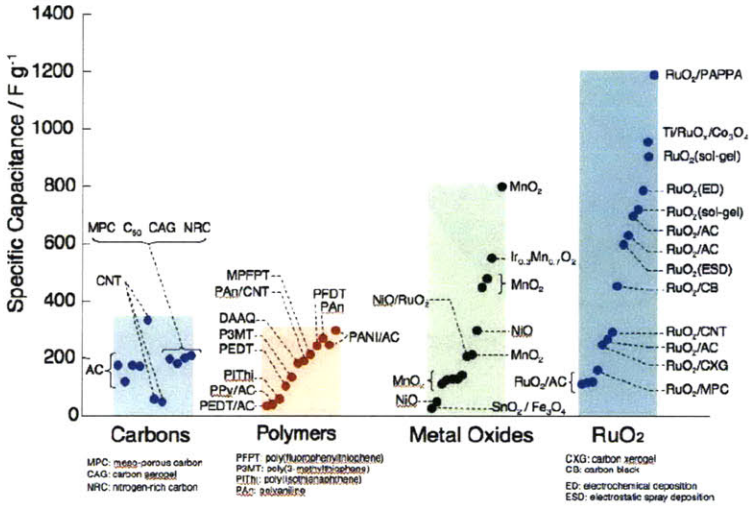

Figure 1-7. Specific capacitance of various materials for ECs in the Literature. Adapted from reference 7 (*The Electrochemical Society Interface* **17**, 34-37 (2008)).

One promising approach to improve the performance of pseudo-capacitive metal oxides is incorporating nano-sized materials into an electrically conductive carbon framework (Figure 1-8)[2], improving utilization of metal oxides and electrical conductivity of the electrode. These carbon matrix/metal oxide nano-composite electrodes have been

demonstrated with various kinds of carbons including carbon nanotubes,[11-14] carbon nanofoam,[15,16]and activated carbon,[17,18] showing significant increase in performance. For example, nano-sized RuO_2/carbon composite specific capacitance over 850 F/gRuO_2[19], and MnO_2/template mesoporous carbon exhibits ~600 F/gMnO_2[20]. The key issues of these composite electrodes are conformal coating of nano-sized metal oxides onto the carbon matrix, enabling fully utilization of metal oxides, and inter-connected 3D network structure including porosity ensuring fast electronic and ionic conduction trough the electrode. With only optimized nano-composite structures, we can fully utilize high energy density of metal oxides at high power density for real EC applications.

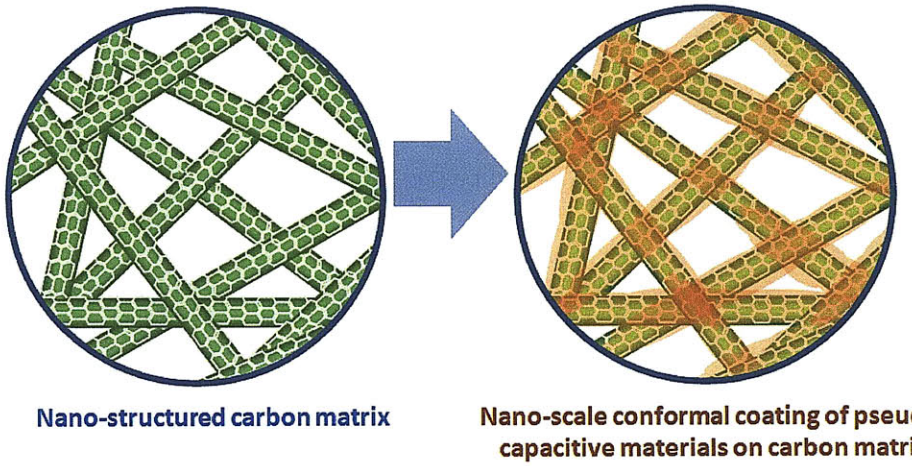

Figure 1-8. Strategy to improve both energy and power densities of electrochemical capacitors. Nano-scale conformal coating of pseudo-capacitive materials on nano-structured carbon matrix.

1.5 Layer-by-Layer Assembly

Layer-by-layer (LbL) assembly process[21] is thin film formation technique based on the alternating adsorption of positively and negatively charged species at ambient conditions, as illustrated schematically in Figure 1-9. Thin film characteristics can be controlled by deposition conditions such as pH of solutions and salt content, and post

treatments including heat-treatments and exposure to different pH condition. This LbL assembly technique is versatile, allowing the incorporation of a broad range of inorganic nano-objectives, metals and metal oxides as well as functional polymers. The LbL assembly can create dense, pin-hole free, and conformal thin films on various geometric supports at room conditions. These advantages make LBL multilayer films promising electrode materials for use in fuel cells, batteries, electrochemical capacitors, solar cells, and sensors.

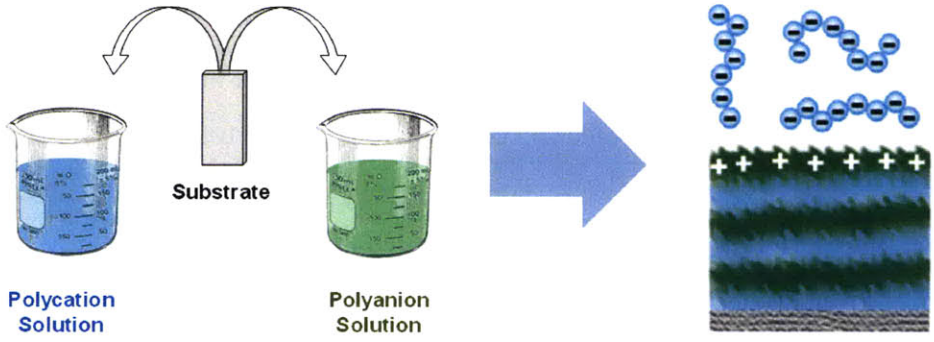

Figure 1-9. A schematic of alternating layer-by-layer assembly to create thin films on the substrates.

There are several specific advantages gained by the use of LbL assembly in the construction of the components for electrochemical devices. First of all, LbL assembly offers very simple water based dip-, roll-, and spray-coating processes to create the desired thin film electrodes or membranes on various kinds of substrates. A second advantage of LbL assembly is that extremely thin film electrodes or solid electrolytes can be fabricated with precise control of thickness. In addition, by applying the multilayer approach to the combining electrodes and solid electrolytes, it is possible to consider completely flexible thin film electrochemical devices. Moreover, patterning techniques developed for LbL assemblies allow extension of these concepts to micro-power geometries for MEMS (Micro-Electro-Mechanical Systems) and flexible electronics.

Finally, perhaps the most important contribution that this LbL technique can bring to the development of electrochemical systems is the ability to control the interface properties between the electrodes and electrolytes. As mentioned above, controlling electronic and ionic properties throughout the interface is the key technique to enhance energy and power performance of electrochemical systems. Since nano-objects including polymers and inorganic materials in the LbL thin films are highly interpenetrated, these LbL composite assemblies can be considered as nano-scale blend systems. When nano-objects of electrodes and polymers of electrolytes are incorporated into LbL assembly, nano-blended thin films allow maximization of interface area between electrodes and interfaces without phase separation. In addition, it is possible to systematically control porosities or introduce within specific regions of the film third materials including organic or inorganic elements, enhancing electron conductivity and ion transport.

1.5.1 Layer-by-Layer Assembly with Functionalized Carbon Nanotubes

Carbon nanotubes (CNT) are promising electrode materials for electrochemical systems such as fuel cells,[22-24] batteries[25-27] and supercapacitors[6,28,29], due to their unique physical properties, including high electrical conductivity, high specific surface area,[30,31] and superior chemical and mechanical stability. However, precipitation of CNTs into ropes or bundles due to strong van der Waals attraction between CNTs limits processibility of CNTs in solutions. To overcome these difficulties, various surface modifications of CNTs have been employed, including chemical functionalization using strong acids,[32,33] π-π stacking interactions between the side wall and aromatic groups,[34-36] and polymer wrapping of CNTs.[37-39] One simple and versatile method to assemble dispersed CNTs into thin-films is using LbL assembly.[21] Electrostatic LbL assembly in which functionalized CNTs have been alternated with polymer electrolytes[23,40,41] for various electrochemical systems been shown to exhibit improved network structures compared to conventional electrodes,[23,40,41] and increased mechanical strength by realizing uniform nano-scale blends without phase sepratoin.[42,43]

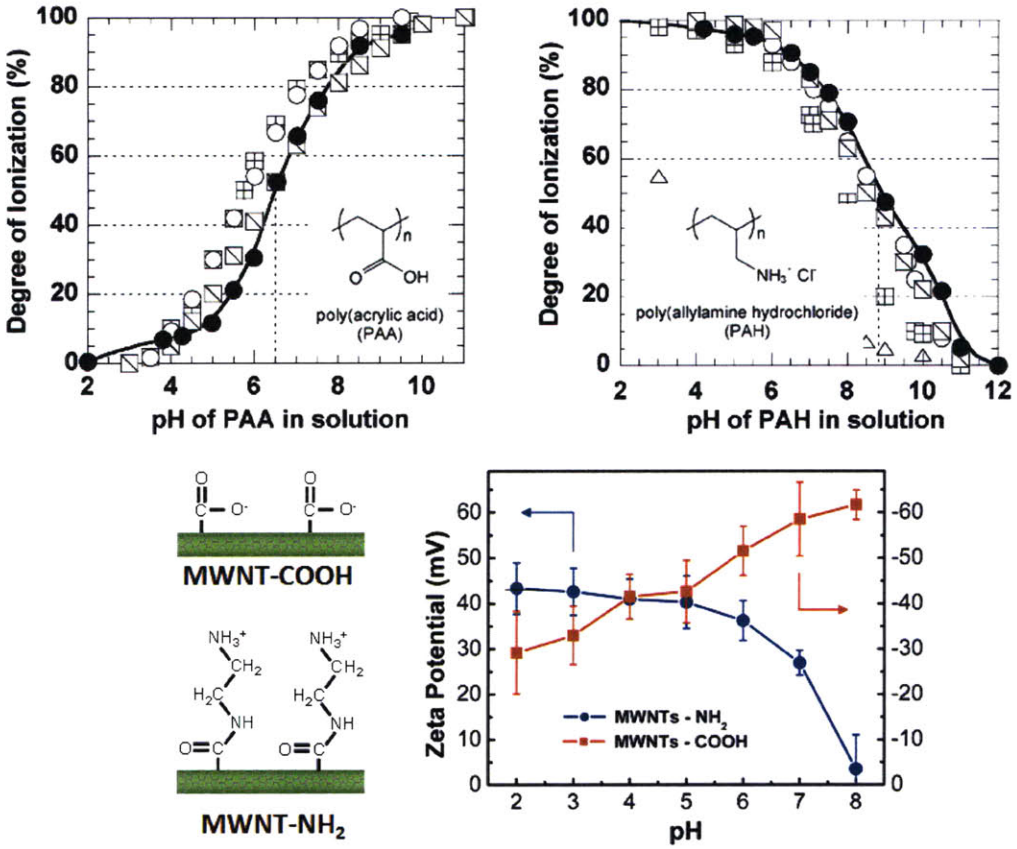

Figure 1-10. Degree of ionization of PAA (upper left) and PAH (upper right) in solution as a function of pH. Adapted from reference 46 (*Macromolecules* **38**, 116-124 (2005)). pH-dependent zeta potential of functionalized MWNTs (below). Adapted from reference 44 (*Journal of the American Chemical Society* **131**, 671-679 (2009)).

In this thesis, negatively and positively charged MWNTs were created via chemical functionalization of exterior surfaces to introduce MWNTs into an electrostatic LbL system.[44] The LbL assembly with weak polyelectrolytes such as poly(acrylic acid) (PAA) or poly(allylamine hydrochoride) (PAH) exhibit tunable thickness, composition ratio, and porosity by controlling the degree of ionization of polyelectrolytes with the pH of the assembly solution.[45-47] Functionalized MWNTs (MWNT-COOH and MWNT-NH_2) can be treated much like weak polyelectrolytes with similar pH dependent behaviors. For example, pH dependent zeta potential of MWNT-COOH and MWNT-NH_2 show analogy with pH

dependent degree of ionization of weak polyelectrolytes[46] such as PAA and PAH as compared at Figure 1-10. In addition, Figure 1-11 shows the analogy of pH dependent thickness behavior between weak polyelectrolytes[45] (PAA and PAH) and functionalized MWNTs (MWNT-COOH and MWNT-NH_2). Therefore, it is postulated that functionalized MWNTs can be directly incorporated into LbL multilayer films by electrostatic interactions (Figure 1-12), and the thickness and morphology of the LbL films can be controlled like weak polyelectrolytes by adjusting the assembly pH conditions. Unlike other LbL assemblies containing CNTs as one of two or more components, these all-MWNT systems incorporate MWNTs without including organic materials or polymer binders, resulting in the direct formation of porous, all-carbon nanostructures with high surface area.

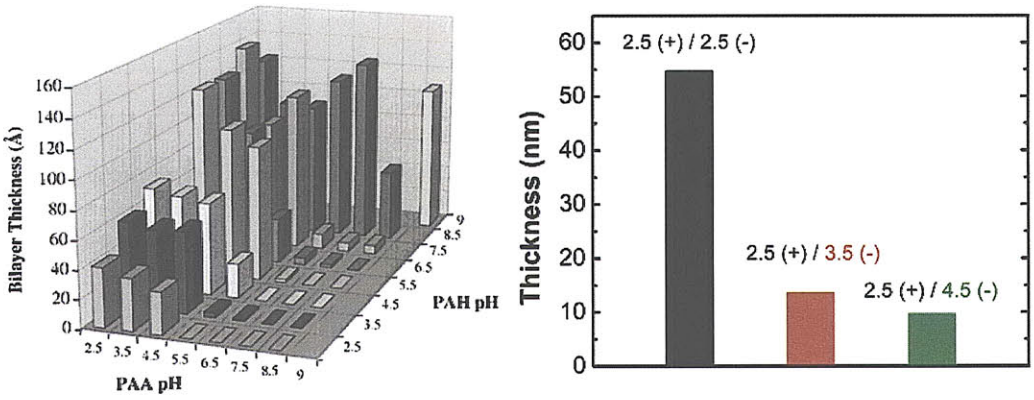

Figure 1-11. Complete pH matrix (Left) showing the average incremental thickness contributed by a PAH/PAA as a function of pH. Adapted from reference 45 (*Macromolecules* **38**, 116-124 (2005)). pH dependent average bilayer thicknesses of MWNT-NH_3^+/MWNT-COO^-. Adapted from reference 44 (*Journal of the American Chemical Society* **131**, 671-679 (2009)).

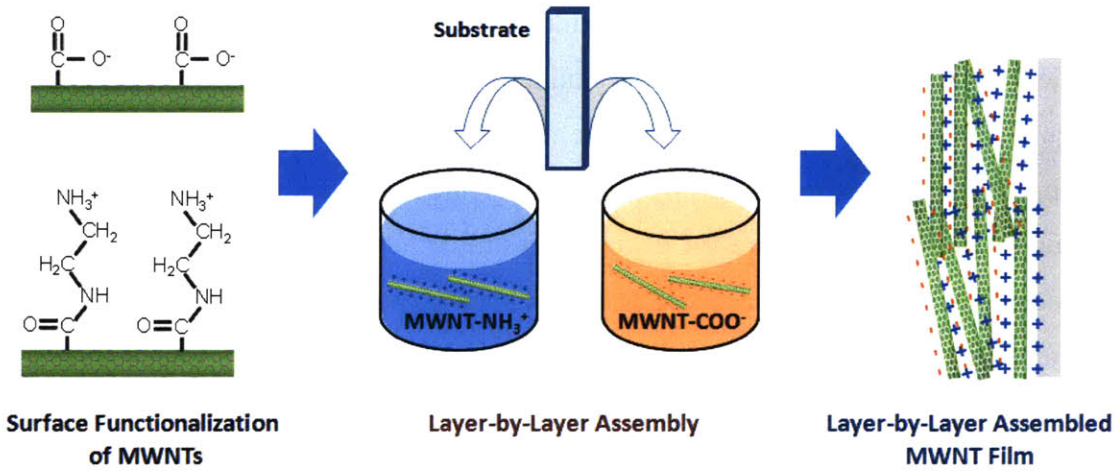

Figure 1-12. A schematic of layer-by-layer assembly of functionalized MWNTs. Modified from reference 44 (*Journal of the American Chemical Society* **131**, 671-679 (2009)).

1.6 Thesis Overview

In this thesis, electrodes for electrochemical energy storage and conversion devices are designed using MWNTs and metal oxides and metal electrocatalysts based on LbL assembly process. Nano-structured electrodes are systematically designed to control interface properties between electrodes and interfaces, and to facilitate ionic and electronic conduction throughout the electrodes. It will be demonstrated that these nano-structured electrodes have superior electrochemical performance by various electrochemical tests including cyclic voltammetry, charge/discharge test, rotating disk electrode test, and chronoamperometry test.

In Chapter 2, all-MWNT thin films are created by layer-by-layer (LbL) assembly of surface functionalized MWNTs. Negatively and positively charged MWNTs were prepared by surface functionalization, allowing the incorporation of MWNTs into highly tunable thin films via the LbL technique. Unlike other carbon nanotube/polymer multilayers and composites that have been reported, these systems consist entirely of MWNTs, enabling the creation of porous film morphologies with high surface area. The use of weak acid and base

groups on the MWNT surfaces enable manipulation of structure and film thickness with pH. Atomic force microscopy (AFM) and scanning electron microscopy (SEM) analysis show that surface topology and the inner structure of MWNT thin films are interconnected random network structures with physical entanglements, which is a promising ionic and electronic conducting structure for ECs. The resulting all-nanotube structures have unique electrochemical properties that scale linearly as a function of film thickness. An average volumetric capacitance of 132 ± 8 F/cm^3 in aqueous electrolytes was found; this value is considerably higher than those of vertically aligned CNTs[28] and conventional CNT electrodes[6] as a result of the high CNT densities in the LbL-MWNT thin films.

Chapter 3 focuses on examining the energy and power capabilities of LbL-MWNT electrodes in a nonaqueous solution of 1 M $LiPF_6$ in ethyl carbonate and dimethyl carbonate. With a lithium foil or a fully lithiated $Li_4Ti_5O_{12}$ composite as the negative electrode, it is shown that the Faradaic reactions of surface functional groups on LbL-MWNT electrodes can be better realized in wider voltage windows than in the aqueous solution to yield considerably higher energy and power capabilities. LbL-MWNT electrodes exhibit energy up to ~200 Wh/kg at very large power (100 kW/kg) in lithium cells, which have energy density comparable to lithium rechargeable batteries, yet with the kind of power density and lifetime associated with ECs. To avoid the safety issue of Li metal for practical applications, LbL electrodes were also evaluated with a fully lithiated $Li_4Ti_5O_{12}$ (LTO) composite in an asymmetric hybrid cell. Moreover, it is demonstrated that such high specific energy can be attributed to high packing density of nanotubes in the electrodes, and the Faradaic reactions of surface oxygen- and nitrogen-containing functional groups on MWNTs.

In chapters 4 and 5, pseudo-capacitive inorganic oxides such as MnO_2 and RuO_2 , electrocatalytic metal and metal alloys including Pt and Pt/Ru have been incorporated in LbL-MWNT electrodes using electroless redox deposition (Chatper 4) and square wave pulse potential deposition (Chapter 5) methods. LbL-MWNT/MnO_2 nano-composite ultrathin film electrodes are created by redox deposition of MnO_2 on LbL-MWNT matrix. SEM and TEM analysis show that LbL-MWNT/MnO_2 thin films have uniform conformal

coating of nano-sized MnO_2 on MWNT internetwork structure. These LbL-MWNT/MnO_2 electrodes show higher volumetric capacitance of 246 F/cm^3 with good capacity retention up to 1,000 mV/s due to fast access to electrons and ions throughout the electrodes. In addition, uniformly distributed nanosize RuO_2 were successfully introduced into LBL-MWNT films via square wave pulse potential cycling. Volumetric capacitance of LbL-MWNT/RuO_2 thin film electrodes was found to scale linearly as a function of the number of square wave potential cycles, reaching over ~1000 F/cm^3 in aqueous electrolytes. Moreover, nano-scale Pt and Pt/Ru electrocatalys were introduced into LbL-MWNT films using same method. These Pt/Ru nanoparticles inside LbL-MWNT electrode showed considerably higher specific activity for methanol oxidation than did a commercial, supported Pt catalyst (Tanaka Kikinzoku International, Inc.) of a comparable particle size and distribution.

Chapter 6 examines the role of surface steps on Pt nanoparticles for methanol oxidation reaction (MOR) and oxygen reduction reaction (ORR). The surface characteristics of Pt nanoparticles of very comparable sizes is controlled and correlated with the intrinsic activity for CO and methanol electro-oxidation. A linear relationship between the intrinsic activity for MOR and the amounts of surface steps on Pt nanoparticles is shown. Increasing step densities on Pt nanoparticles of ~2 nm can enhance specific activity based on Pt ESA up to 200% towards electro-oxidation of CO and methanol. On the other hand, ORR activity of Pt nanoparticles of ~2 nm is not influenced by surface steps in contrast to MOR activity. CO annealing experiment, used to reduce surface steps on Pt nanoparticles, does not affect ORR activity but considerably reduced MOR activity. It is hypothesized that minority sites associated with surface steps, do not govern ORR activity relative to majority terrace sites at high potentials relevant to ORR. This is in contrast to minority sites involving surface steps, which have preferential adsorption of oxygenated species at low potentials for MOR, dominate the MOR activity. The hypothesis is supported by in-situ X-ray adsorption measurements as a function of potential. This research suggests that strategies for increasing surface steps such as the n(111)×(111) type

on nanoparticles offer promise for finding new highly active electrocatalysts for electro-oxidation of small organic molecules.

Finally, conclusion and perspective of LbL-MWNTs as electrode materials of electrochemical systems are detailed in **Chapter 7.**

1.7 References

[1] Winter, M. and Brodd, R. J., What are batteries, fuel cells, and supercapacitors? *Chem. Rev.* **104**, 4245-4269 (2004).

[2] Simon, P. and Gogotsi, Y., Materials for electrochemical capacitors. *Nat. Mater.* **7**, 845-854 (2008).

[3] Miller, J. R. and Simon, P., Materials science - Electrochemical capacitors for energy management. *Science* **321**, 651-652 (2008).

[4] Miller, J. and Simon, P., Fundamental of electrochemical capacitor design and operation. *The Electrochemical Society Interface* **1**, 31-32 (2008).

[5] Simon, P. and Burke, A., Nanostructured carbons: double-layer capacitance and more. *The Electrochemical Society Interface* **17**, 49 (2008).

[6] Frackowiak, E. and Beguin, F., Carbon materials for the electrochemical storage of energy in capacitors. *Carbon* **39**, 937-950 (2001).

[7] Naoi, K. and Simon, P. , New materials and new configurations for advanced electrochemical capacitors. *The Electrochemical Society Interface* **17**, 34-37 (2008).

[8] Sugimoto, W. et al., Preparation of ruthenic acid nanosheets and utilization of its interlayer surface for electrochemical energy storage. *Angew. Chem.-Int. Edit.* **42**, 4092-4096 (2003).

[9] Bélanger, D., Brousse, T., and Long, J. W., Manganese oxides: battery materials make the leap to electrochemical capacitors. *The electrochemical Society Interface* **17**, 49-52 (2008).

[10] Toupin, M., Brousse, T., and Belanger, D., Charge storage mechanism of MnO2 electrode used in aqueous electrochemical capacitor. *Chem. Mat.* **16**, 3184-3190 (2004).

[11] Bordjiba, T. and Belanger, D., Direct Redox Deposition of Manganese Oxide on Multiscaled Carbon Nanotube/Microfiber Carbon Electrode for Electrochemical Capacitor. *J. Electrochem. Soc.* **156**, A378-A384 (2009).

[12] Ma, S. B. et al., Electrochemical properties of manganese oxide coated onto carbon nanotubes for energy-storage applications. *J. Power Sources* **178**, 483-489 (2008).

[13] Xie, X. F. and Gao, L., Characterization of a manganese dioxide/carbon nanotube composite fabricated using an in situ coating method. *Carbon* **45**, 2365-2373 (2007).

[14] Ma, S. B. et al., Synthesis and characterization of manganese dioxide spontaneously coated on carbon nanotubes. *Carbon* **45**, 375-382 (2007).

[15] Fischer, A. E. et al., Incorporation of homogeneous, nanoscale MnO2 within ultraporous carbon structures via self-limiting electroless deposition: Implications for electrochemical capacitors. *Nano Lett.* **7**, 281-286 (2007).

[16] Fischer, A. E. et al., Electroless deposition of nanoscale MnO2 on ultraporous carbon nanoarchitectures: Correlation of evolving pore-solid structure and electrochemical performance. *J. Electrochem. Soc.* **155**, A246-A252 (2008).

[17] Brousse, T., Toupin, M., and Belanger, D., A hybrid activated carbon-manganese dioxide capacitor using a mild aqueous electrolyte. *J. Electrochem. Soc.* **151**, A614-A622 (2004).

[18] Brousse, T. et al., Long-term cycling behavior of asymmetric activated carbon/MnO2 aqueous electrochemical supercapacitor. *J. Power Sources* **173**, 633-641 (2007).
[19] Hu, C. C., Chen, W. C., and Chang, K. H., How to achieve maximum utilization of hydrous ruthenium oxide for supercapacitors. *J. Electrochem. Soc.* **151**, A281-A290 (2004).
[20] Dong, X. P. et al., MnO2-embedded-in-mesoporous-carbon-wall structure for use as electrochemical capacitors. *J. Phys. Chem. B* **110**, 6015-6019 (2006).
[21] Decher, G., Fuzzy nanoassemblies: Toward layered polymeric multicomposites. *Science* **277**, 1232-1237 (1997).
[22] Wang, C. et al., Proton exchange membrane fuel cells with carbon nanotube based electrodes. *Nano Letters* **4**, 345-348 (2004).
[23] Michel, M. et al., High-performance nanostructured membrane electrode, assemblies for fuel cells made by layer-by-layer assembly of carbon nanocolloids. *Adv. Mater.* **19**, 3859-+ (2007).
[24] Li, W. Z. et al., Preparation and characterization of multiwalled carbon nanotube-supported platinum for cathode catalysts of direct methanol fuel cells. *J. Phys. Chem. B* **107**, 6292-6299 (2003).
[25] Frackowiak, E. et al., Electrochemical storage of lithium multiwalled carbon nanotubes. *Carbon* **37**, 61-69 (1999).
[26] Shimoda, H. et al., Lithium intercalation into opened single-wall carbon nanotubes: Storage capacity and electronic properties. *Phys. Rev. Lett.* **88** (2002).
[27] Morris, R. S. et al., High-energy, rechargeable Li-ion battery based on carbon nanotube technology. *Journal of Power Sources* **138**, 277-280 (2004).
[28] Futaba, D. N. et al., Shape-engineerable and highly densely packed single-walled carbon nanotubes and their application as super-capacitor electrodes. *Nature Materials* **5**, 987-994 (2006).
[29] Yoon, B. J. et al., Electrical properties of electrical double layer capacitors with integrated carbon nanotube electrodes. *Chemical Physics Letters* **388**, 170-174 (2004).
[30] Baughman, R. H., Zakhidov, A. A., and de Heer, W. A., Carbon nanotubes - the route toward applications. *Science* **297**, 787-792 (2002).
[31] Ajayan, P. M. and Zhou, O. Z., in *Carbon Nanotubes* (Springer-Verlag Berlin, Berlin, 2001), Vol. 80, pp. 391-425.
[32] Liu, J. et al., Fullerene pipes. *Science* **280**, 1253-1256 (1998).
[33] Esumi, K. et al., Chemical treatment of carbon nanotubes. *Carbon* **34**, 279-281 (1996).
[34] Chen, R. J., Zhang, Y. G., Wang, D. W., and Dai, H. J., Noncovalent sidewall functionalization of single-walled carbon nanotubes for protein immobilization. *Journal of the American Chemical Society* **123**, 3838-3839 (2001).
[35] Nakashima, N., Tomonari, Y., and Murakami, H., Water-soluble single-walled carbon nanotubes via noncovalent sidewall-functionalization with a pyrene-carrying ammonium ion. *Chem. Lett.*, 638-639 (2002).

[36] Paloniemi, H. et al., Layer-by-layer electrostatic self-assembly of single-wall carbon nanotube polyelectrolytes. *Langmuir* **22**, 74-83 (2006).
[37] O'Connell, M. J. et al., Reversible water-solubilization of single-walled carbon nanotubes by polymer wrapping. *Chemical Physics Letters* **342**, 265-271 (2001).
[38] Liu, P., Modifications of carbon nanotubes with polymers. *Eur. Polym. J.* **41**, 2693-2703 (2005).
[39] Satake, A., Miyajima, Y., and Kobuke, Y., Porphyrin - Carbon nanotube composites formed by noncovalent polymer wrapping. *Chem. Mat.* **17**, 716-724 (2005).
[40] Zhang, M. N. et al., Electrostatic layer-by-layer assembled carbon nanotube multilayer film and its electrocatalytic activity for O-2 reduction. *Langmuir* **20**, 8781-8785 (2004).
[41] Zhang, M. N., Su, L., and Mao, L. Q., Surfactant functionalization of carbon nanotubes (CNTs) for layer-by-layer assembling of CNT multi-layer films and fabrication of gold nanoparticle/CNT nanohybrid. *Carbon* **44**, 276-283 (2006).
[42] Mamedov, A. A. et al., Molecular design of strong single-wall carbon nanotube/polyelectrolyte multilayer composites. *Nat. Mater.* **1**, 190-194 (2002).
[43] Olek, M. et al., Layer-by-layer assembled composites from multiwall carbon nanotubes with different morphologies. *Nano Letters* **4**, 1889-1895 (2004).
[44] Lee, Seung Woo et al., Layer-by-Layer Assembly of All Carbon Nanotube Ultrathin Films for Electrochemical Applications. *Journal of the American Chemical Society* **131**, 671-679 (2009).
[45] Shiratori, S. S. and Rubner, M. F., pH-dependent thickness behavior of sequentially adsorbed layers of weak polyelectrolytes. *Macromolecules* **33**, 4213-4219 (2000).
[46] Choi, J. and Rubner, M. F., Influence of the degree of ionization on weak polyelectrolyte multilayer assembly. *Macromolecules* **38**, 116-124 (2005).
[47] Mendelsohn, J. D. et al., Fabrication of microporous thin films from polyelectrolyte multilayers. *Langmuir* **16**, 5017-5023 (2000).

Chapter 2. Layer-by-Layer Assembly of All Carbon Nanotube Ultrathin Films for Electrochemical Applications

Reproduced in part with permission from Seung Woo Lee, Byeong-Su Kim, Shuo Chen, Yang Shao-Horn, and Paula T. Hammond, *Layer-by-Layer Assembly of All Carbon Nanotube Ultrathin Films for Electrochemical Applications.* **J. AM. CHEM. SOC. 2009**, *131*, 671–679, Copyright 2009 American Chemical Society.

Abstract

All multiwall carbon nanotube (MWNT) thin films are created by layer-by-layer (LBL) assembly of surface functionalized MWNTs. Negatively and positively charged MWNTs were prepared by surface functionalization, allowing the incorporation of MWNTs into highly tunable thin films via the LBL technique. The pH dependent surface charge on the MWNTs gives this system the unique characteristics of LBL assembly of weak polyelectrolytes, controlling thickness and morphology with assembly pH conditions. We demonstrate that these MWNT thin films have randomly oriented interpenetrating network structure with well developed nanopores using AFM and SEM, which is an ideal structure of functional materials for various applications. In particular, electrochemical measurements of these all-MWNT thin film electrodes show high electronic conductivity in comparison with polymer composites with single wall nanotubes, and high capacitive behavior with precise control of capacity.

2.1 Introduction

Carbon nanotubes (CNT) are some of the most promising materials for the design of functional thin films, including those for catalytic membranes[1,2], actuation[3,4], and mechanical thin film applications[5], and perhaps most importantly for a range of electrochemical energy conversion and storage devices (such as fuel cells,[6-8] batteries[9-11] and supercapacitors[12-14]), due to their unique physical properties, including high electrical conductivity, superior chemical and mechanical stability, and large surface area.[15,16] Controlling the architecture of CNT thin films at the nanometer and micrometer-scale is critical to tailoring film properties and functionality[17]. For example, functional films of CNTs with vertically oriented geometries have been prepared using vapor deposition[12,18,19] and filtration,[20] but it is difficult to make dense films with low porosity with these methods. Nano-composites with polymer have been developed,[4,21] but limitations exist in the processibility of CNTs in solution, as CNTs precipitate into ropes or bundles due to strong van der Waals interactions between CNTs. Various surface modifications of CNTs have been employed to disperse CNTs, including chemical functionalization using strong acids,[22,23] π-π stacking interactions between the side wall and aromatic groups,[24-26] and polymer wrapping of nanotubes.[27-29]

One simple and versatile method to assemble dispersed CNTs into thin-films is using layer-by-layer (LBL) assembly,[30] which consists of the repeated, sequential immersion of a substrate into aqueous solutions of complementarily functionalized materials. This technique can produce conformal ultrathin films and highly tunable surfaces using various nanomaterials on geometric surfaces. Recently, electrostatic layer-by-layer (LBL) assembly in which CNTs have been alternated with polymers[7,31,32] for various energy storage and conversion devices been shown to exhibit improved networks for electrochemical energy applications relative to conventional electrodes,[7,31,32] and increased mechanical strength by preventing phase separation and realizing uniform nano-scale blends.[5,33].

In this work, we show, for the first time, the preparation of all MWNT thin films based on the LBL assembly method. Multiwall nanotubes (MWNTs) chemically modified to exhibit acid and base groups can be treated much like weak polyelectrolytes with

precisely controlled thickness. The LBL assembled thin films of weak polyelectrolytes such as poly(acrylic acid) or poly(allylamine hydrochoride) exhibit tunable thickness, composition ratio, and porosity by controlling the degree of ionization of polyelectrolytes with the pH of the assembly solution, which ultimately affects chain conformation within the film and film morphology.[34-36] Negatively and positively charged MWNTs have been created via chemical functionalization of exterior surfaces. Negatively and positively charged MWNTs have been functionalized on their exterior walls with carboxylic acid groups[23,37] yielding MWNT-COOH, and with amine groups [38,39] yielding MWNT-NH_2. LBL MWNT films, which consist of well-dispersed MWNTs, has been produced by LBL using stable dispersions of negatively and positively charged MWNTs (Scheme 2-1). Unlike other multilayer assemblies that contain CNTs as one of two or more components, these systems incorporate MWNTs without the incorporation of additional organic materials; this difference can enable the development of 100% CNT thin films with properties that can be manipulated using assembly conditions. In particular, the irregular shape of the CNTs enables the direct formation of porous, all-carbon nanostructures with high surface area. MWNT thin films show pH-dependent thickness and surface topology, which are characteristics of LBL thin films of weak polyelectrolytes. We demonstrate that the surface topology and the inner structure of MWNT thin films are interconnected random network structures with physical entanglements using atomic force microscopy (AFM), scanning electron microscopy (SEM), and swelling experiments. Sheet resistance and cyclic voltammetry measurements show that these MWNT thin films are promising electrode materials for high-power and high-energy electrochemical devices.

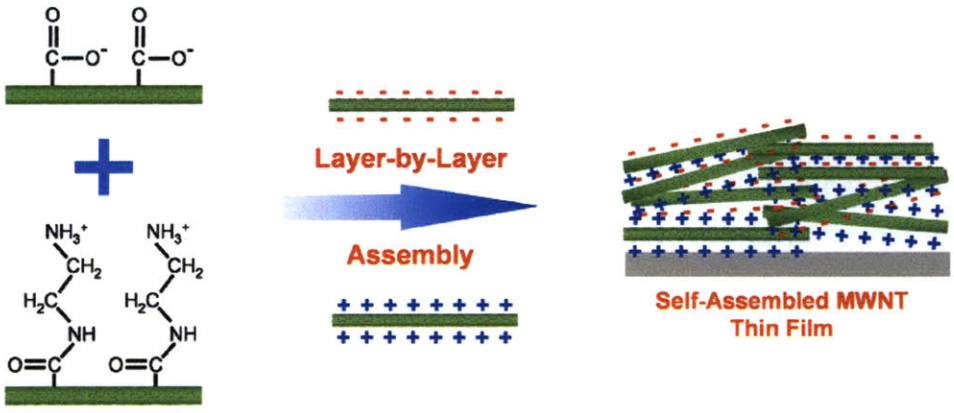

Scheme 2-1. Layer-by-layer assembled MWNT thin film with positively and negatively charged MWNTs

2.2 Experimental Section

Functionalization of Negatively and Positively Charged MWNTs (Scheme 2-2). MWNTs prepared by a conventional CVD method were purchased from NANOLAB (95% purity, length 1-5 μm, outer diameter 15 ± 5 nm). MWNTs were refluxed in concentrated H_2SO_4/HNO_3 (3/1 v/v, 96% and 70%, respectively) at 70 °C to prepare carboxylic acid functionalized MWNTs (MWNT-COOH), and then washed with deionized Milli-Q water (18 MΩ·cm) water several times using nylon membrane filter (0.2 μm). Dried carboxylated MWNTs were chlorinated by refluxing for 12 h with $SOCl_2$ (Sigma-Aldrich) at 70 °C. After evaporating any remaining $SOCl_2$, amine functionalized MWNTs (MWNT-NH_2) were obtained by reaction with $NH_2(CH_2)_2NH_2$ (Sigma-Aldrich) in dehydrated toluene (Aldrich) for 24 h at 70 °C. After washing with ethanol and deionized water several times, MWNT-NH_2 powder was obtained from drying at 50 °C in vacuum for 24 hr.

Layer-by-Layer Assembly of MWNT Thin Films. Dried MWNT-COOH and MWNT-NH_2 powders were sonicated using a Branson Bransonic 3510 ultrasonic cleaner (40 kHz) in Milli-Q water (18 MΩ·cm) for several hours to form stable dispersions. These solutions were subjected to dialysis against Milli-Q water for several days to remove any byproduct and residual during functionalization. The concentrations (0.5 mg/ml) and pHs of solutions were precisely adjusted after dialysis, and resulting solutions were sonicated briefly prior to

LBL assembly. MWNT films were fabricated with a modified Carl Zeiss DS50 programmable slide stainer on various substrates. Substrates were first dipped into a MWNT-NH_2 solution for 30 minutes, then three baths of Milli-Q water for 2, 1, 1 minutes each. The substrates were then exposed to a MWNT-COOH solution for 30 minutes, and washed in three baths of Milli-Q water for 2, 1, 1 minutes each. This cycle makes one bilayer of MWNT-NH_2 and MWNT-COOH, denoted (MWNT-NH_2/ MWNT-COOH). The cycle was repeated to reach the desired number of bilayers of MWNT thin films. To exclude the effect of gradual precipitation of MWNTs in the solutions after long timeframes (several days), a disk magnetic stirrer (VWR International) under the dipping bath was installed, which allowed the circulation of MWNT solution upon layering on the substrate and thus rendered uniform and high quality MWNT thin films on the substrate.

Characterization. The surface chemistry of functionalized MWNTs was analyzed using a Kratos AXIS Ultra Imaging X-ray photoelectron spectrometer (XPS). All spectra were calibrated with the C 1s photoemission peak for sp^2 hybridized carbons at 284.5 eV. Curve fitting of the photoemission spectra was done after a Shirley type background subtraction. The zeta potential as a function of pH was measured using a Zeta PALS (Brookhaven Instrument Corp.) to determine the effect of surface charge on MWNT dispersions. Thickness of MWNT thin films on silicone wafers was determined using a Tencor P-10 profilometer. Surface topology of MWNT thin films was examined using an AFM microscope (Digital Instruments EnviroScope, Veeco) in the tapping mode in the air. The root-mean-square (RMS) roughness of the LBL films was examined from AFM images with a size of $4 \times 4\ \mu m^2$. Surface morphology and interior structure of MWNT thin films were investigated using a scanning electron microscope (JEOL 6320 SEM) operating at 3.0 and 5.0 kV. Refractive indices of MWNT thin films were determined using a J.A.Woolham Co. VASE spectroscopic ellipsometer, and data fitting was performed with a Cauchy model using the WVASE32 software package. Sheet resistances were measured for films deposited on glass slides by using a standard four-point probe configuration (Signatone model S-302-4). A series of 3-4 measurements were taken on each film, and the measurements then were averaged to give the final reported value with the standard

deviation as an error range. A three-electrode cell was employed for electrochemical measurements, where a saturated calomel electrode (SCE) (Analytical Sensor, Inc.) and Pt wire were used as the reference and counter electrodes, respectively. MWNT thin films on ITO coated glass slides were used as the working electrode. Cyclic Voltammetry was performed between -0.25 and 0.80 V (SCE) at room temperature in 1.0 M H_2SO_4 solution using a bipotentiostat (PINE instrument).

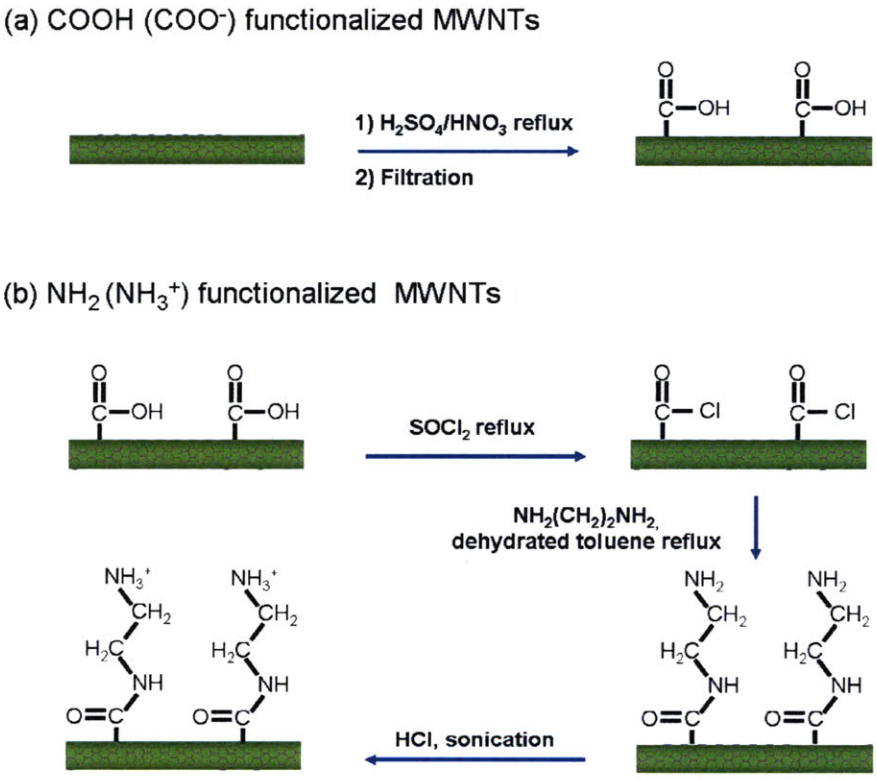

Scheme 2-2. Synthesis scheme of (a) COOH and (b) NH_2 functionalized MWNTs

2.3 Results and Discussion

To introduce MWNTs into an electrostatic LBL system, negatively and positively charged MWNTs were created via chemical functionalization of exterior surfaces. Negatively charged MWNTs were prepared by oxidation with extremely aggressive acids,

which could render oxygen-containing groups such as carboxylic acid groups on the MWNT surface (MWNT-COOH).[23,37] Carboxylic acid groups (COOH) on the surface of MWNTs exist as carboxylate anions (COO^-) in aqueous solution, yielding negatively charged MWNTs, (MWNT-COOH). Positively charged MWNTs were prepared by introducing amine groups (NH_2),[38,39] which could be protonated over a broad pH range, through the formation of amide bonds with COOH functionalized MWNTs and excess ethylene diamine.

2.3.1 XPS Results of Surface Functionalized MWNTs

X-ray photoemission spectroscopy (XPS) elemental analysis was performed to probe the surface functional groups on the modified MWNTs, as shown in Figure 2-1a. The O_{1s} photoemission peak was clearly observed on COOH functionalized MWNTs and amine functionalized MWNTs. The amount of surface oxygen-containing functional groups was found to increase with longer oxidation time, as indicated by the increase in the O_{1s} peak intensity from oxidation time from 1 hr to 2 hrs. The XPS analysis of C_{1s} spectra (Figure 2-1b-e) show detailed surface functional groups on the MWNTs. An asymmetric peak from sp^2 hybridized carbons centered at 284.5 eV with an extended tail at the higher energy region[40] was generated for raw MWNTs, and the same form of the asymmetric peak was used for all other fittings of the sp^2 hybridized graphite-like carbons. Using this asymmetric peak as a reference, the C_{1s} peak of the oxidized MWNTs was fitted to five Gaussian-Lorentzian shape peaks, which were attributed to sp^3 hybridized diamond-like carbons (285.2 ± 0.1 eV), C-O (286.2 ± 0.1 eV), carbonyls C=O (286.8 ± 0.2 eV), hydroxyls C-OH (287.5 ± 0.1 eV), and carboxyls O=C-OH (288.9 ± 0.2 eV).[41] The intensities of these peaks increased relative to sp^2 hybridized graphite-like carbons with oxidation time (Figures 2-1b and 2-1c). After 2 hrs of oxidation, the MWNT-COOH produced stable dispersions in water as a result of electrostatic repulsion between MWNTs (Figure 2-2a). In the case of the 1 hr oxidation MWNTs, a stable dispersion in water was not obtained, which could be the result of insufficient negative charges to prevent aggregation and gravitational precipitation of MWNTs due to van der Waals interaction

between MWNTs. The XPS analysis of C_{1s} and N_{1s} of MWNT-NH_2 (Figures 2-1e and 2-1f) suggests the presence of amide bonds N-C=O (287.9 eV in C_{1s} and 399.9 ± 0.1 eV in N_{1s}), and amines NH_2 (NH_3^+) (286.2 eV in C_{1s} and 401.8 ± 0.2 eV in N_{1s})[39], which indicate successful introduction of primary amine groups via the formation of amide bonds.

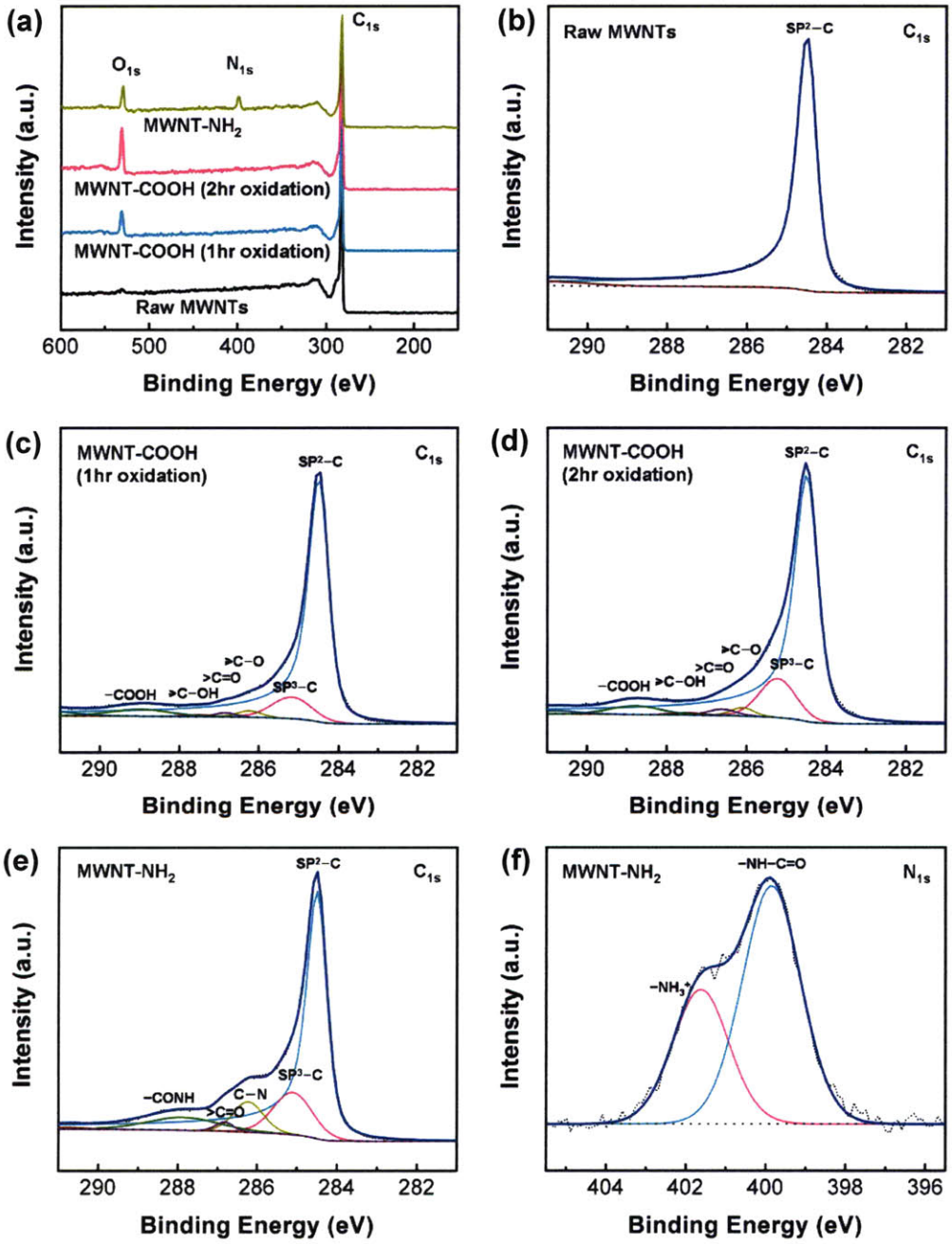

Figure 2-1. X-ray photoelectron spectroscopy (XPS) spectra of functionalized MWNTs. (a) Wide scan survey, (b) raw MWNTs C_{1s} spectra, (c) MWNT-COOH (1hr oxidation) C_{1s} spectra, (d) MWNT-COOH (2hr oxidation) C_{1s} spectra, (e) MWNT-NH_2 C_{1s} spectra, (f) MWNT-NH_2 N_{1s} spectra.

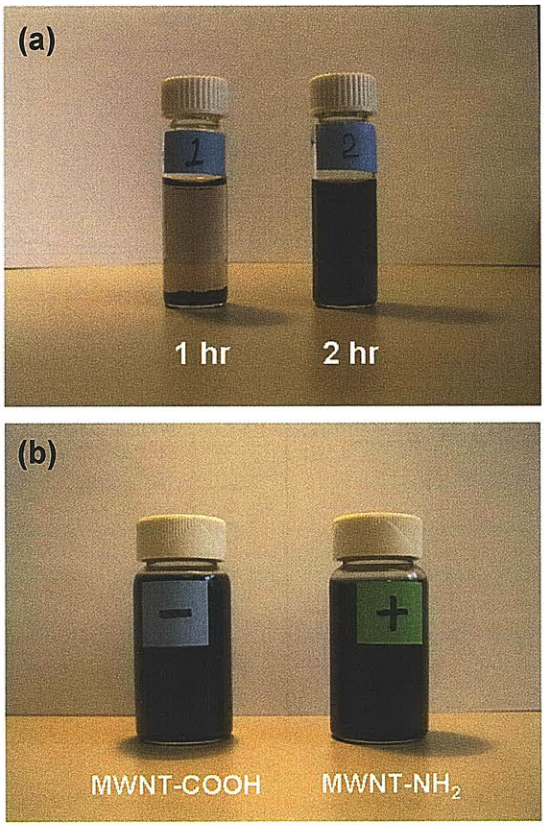

Figure 2-2. Optical images of (a) COOH(COO^-) functionalized MWNT solutions (1hr vs. 2hr oxidation). This picture was taken after 12 hours from sonication. (b) COOH(COO^-) functionalized MWNT solution (0.5 mg/ml) at pH 3.5 and $NH_2(NH_3^+)$ functionalized MWNT solution (0.5 mg/ml) at pH 2.5 in water. This picture was taken after 1 month from the pH adjustment.

Examples of the MWNT solutions used for LBL assembly are also pictured in Figure 2-2b. The pH of MWNT-COOH (0.5 mg/ml) and MWNT-NH_2 (0.5 mg/ml) solutions were adjusted to pH 3.5 and 2.5 respectively after dialysis. The solutions remained clearly dispersed even after one month following pH adjustment, suggesting that stable dispersions were achieved in the MWNT solutions. No precipitation of MWNTs was observed in the case of the MWNT-COOH solution, but some precipitation was noted for concentrated MWNT-NH_2 solutions in the bottom of the glass vial after several days. This suggests that the precipitation rate of positively charged MWNTs is much faster than negatively charged ones due to weak electrostatic repulsion between the MWNTs-NH_2.

2.3.2 Surface Charge and LBL Assembly of Functionalized MWNTs

The surface charges on MWNTs are not only key to creating stable colloidal dispersions, but are also required elements to achieving LBL assembled films. As shown in Figure 2-3, the zeta potential of the MWNT-COOH was found to decrease with decreasing pH due to the protonation of the COOH group on the MWNTs. On the other hand, the zeta potential of MWNT-NH_2 decreased as the pH was increased due to changes in the degree of ionization of the NH_2 group on MWNTs. This behavior is very similar to weak polyelectrolytes such as poly(acrylic acid) (PAA) and poly(allylamine hydrochloride) (PAH).[34] An interesting difference between PAA and MWNT-COOH is the difference in the degree of ionization observed at low pH. The degree of ionization of the PAA solution approaches zero,[35] but MWNT-COOH still has enough negative charge to maintain stable dispersions at pH 2 (approximately -30 mV). We speculate this difference comes from the different backbone structures to which the COOH groups are attached. The sp^2 hybridization character of the MWNT backbone can yield a much lower pK_a (pK_a of benzoic acid[42] : 4.19)compared to that of PAA (pK_a of propanoic acid[42] : 4.86), allowing higher degrees of ionization at lower pH. Therefore, it is postulated that MWNTs can be directly incorporated into multilayer films by electrostatic interactions (Scheme 2-1), and the thickness and morphology of the resulting LBL films can be controlled like weak polyelectrolytes by altering the assembly pH values.

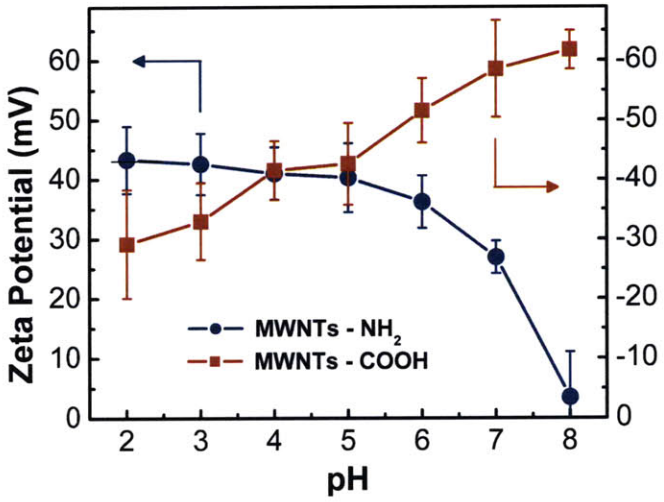

Figure 2-3. pH-dependent zeta potential of functionalized MWNTs. Each point of zeta potential value was obtained by more than 10 measurements and error bars show standard deviations.

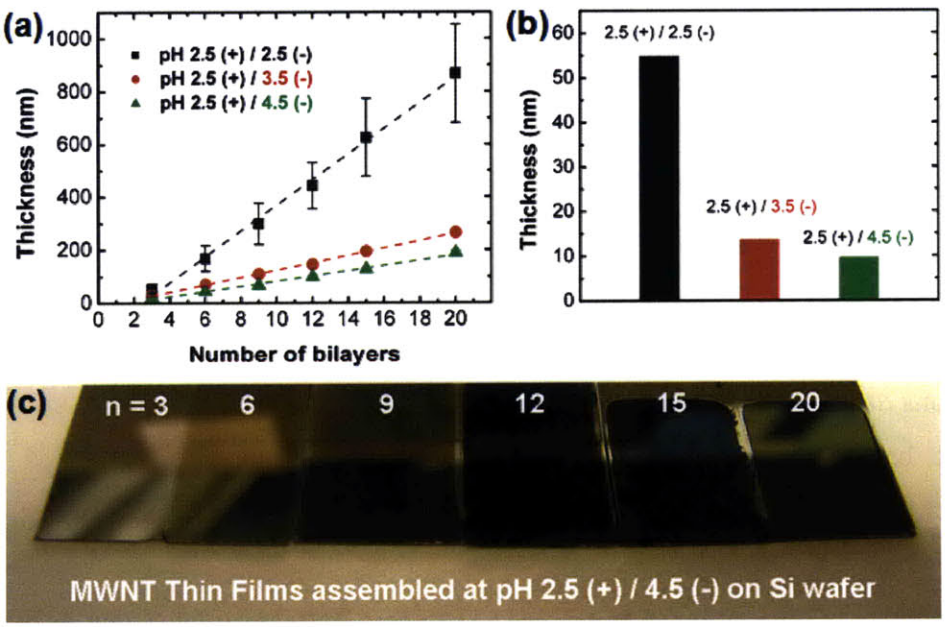

Figure 2-4. (a) Thickness of MWNT thin films under varying assembly pH conditions. The dashed lines are linear fit with standard deviations as error bars. pH 2.5 (+) / 2.5 (-)

indicates MWNT thin films assembled from MWNT-NH_2 at pH 2.5 and MWNT-COOH at pH 2.5. (b) pH dependent average bilayer thicknesses. (c) Representative digital picture image of assembled MWNT thin films on Si wafer from pH 2.5 (+) / 4.5 (-). Number on image indicates the number of bilayer (n) in (MWNT-NH_2 / MWNT-COOH)$_n$

Figure 2-4a shows the thickness of MWNT thin films at various pH conditions as a function of the number of bilayers. Figure 2-4b summarizes the averaged bilayer thickness for films assembled as a function of MWNT-COOH pH. Figure 2-4c shows representative optical images of MWNT thin films on Si wafer from pH 2.5 (+) / 4.5 (-), where each film has a characteristic reflective color corresponding to its thickness. The films darken with increasing thickness and appear black at a thickness greater than 300nm. For convenience of comparison, MWNT films assembled from MWNT-NH_2 at pH 2.5 and MWNT-COOH at pH 3.5 will be denoted as pH 2.5 (+) / 3.5 (-). The pH of MWNT-COOH was varied from 2.5 to 4.5 while fixing the pH of MWNT-NH_2 at 2.5 so as to maintain sufficient positive surface charge. The thickness per bilayer of the MWNTs films increases as the pH of the MWNT-COOH solution is decreased (Figure 2-4b). This increase in thickness from pH 4.5 to 2.5 is likely due to the significant charge decrease of carboxylic acid functionalized MWNTs from pH 4.5 to pH 2.5 as was proven by zeta potential measurements (Figure 2-3). The lowered degree of ionization on the nanotubes may require more adsorption of the negatively charged MWNTs to balance the positive charge for each bilayer. Interestingly, weak polyions show similar behavior in layer-by-layer assembly,[34,43] with bilayer thicknesses increasing when the degree of ionization of one of the polyelectrolytes is lowered; however, the behavior in weak polyions is due to changes in the conformation of polyelectrolyte chains from flat adsorbed coils to thick looped structures on the top surface. The rigidity of carbon nanotubes would preclude such changes in nanotube conformation on a molecular level; however, there may be differences in the degree of interpenetration between deposited nanotubes based on the nanotube charge density. The presence of fixed charges along the MWNT surface is influenced by the acid-base equilibria of the acid and amine groups, leading to strong charge regulation and an effective pKa that impacts shielding effects; however additional effects due to Van

der Waals interactions, excluded volume, and osmotic effects may also be important, as predicted theoretically for charged adsorbed layers.[44] In this case, one would anticipate higher degrees of nanotube interpenetration with increasing tube charge density, which could also lead to thinner films with somewhat denser packing between nanotubes. Finally, high charge densities may cause the nanotubes to adsorb in a slightly more flattened arrangement on the oppositely charged surface due to electrostatic forces, leading to thinner interpenetrated structures.

2.3.3 Microstructure of LBL Assembled, Surface Functionalized MWNT Thin Films.

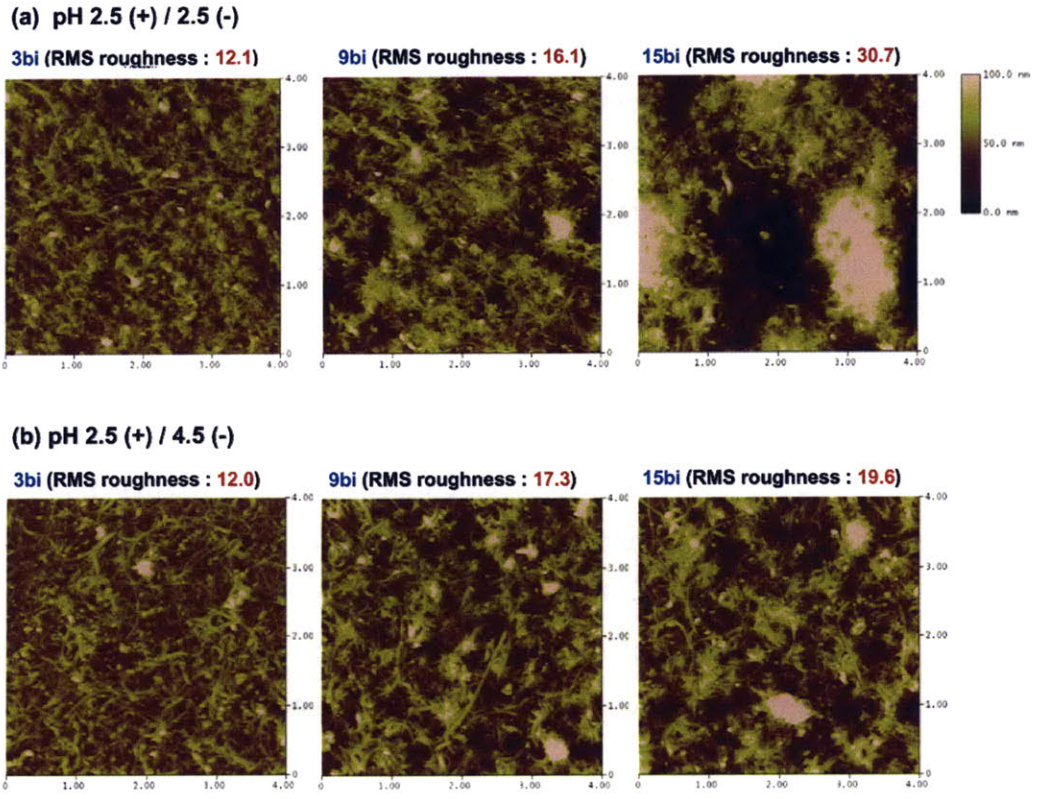

Figure 2-5. Atomic force microscopy (AFM) height images of (MWNT-NH_2/MWNT-COOH)n thin films deposited at different pH conditions. (a) pH 2.5 (+) / 2.5 (-), (b) pH 2.5 (+) / 4.5 (-). Size of each image is 4 μm × 4 μm.

Figure 2-5 shows tapping-mode AFM images of MWNT thin films assembled at different pH conditions with increasing number of bilayers. All AFM images clearly show that MWNT thin films have an interconnected network structure with separated individual MWNTs, which have an average diameter of 15 ± 5 nm. Root-mean-squared (RMS) roughness increases with the number of bilayers, showing similar behavior for different pH conditions at the beginning stages. However, assembly from pH 2.5 (+) / 2.5 (-) shows a steep increase of RMS roughness from 9 bilayers to 15 bilayers compared to other pH conditions. Images of pH 2.5 (+) / 3.5 (-) condition were not shown because of the resemblance of topography with the pH 2.5 (+) / 4.5 (-) condition. The higher roughness for the pH 2.5(-) films can be explained by the higher thickness of the films and the fact that the lowered surface charge density of the MWNT-COOH at pH 2.5 may lead to the looser adsorption of larger numbers of MWNTs, as discussed above, resulting in rougher surfaces, while the other two assemblies at higher MWNT-COOH pH show relatively uniform and somewhat more densely packed MWNT network structures.

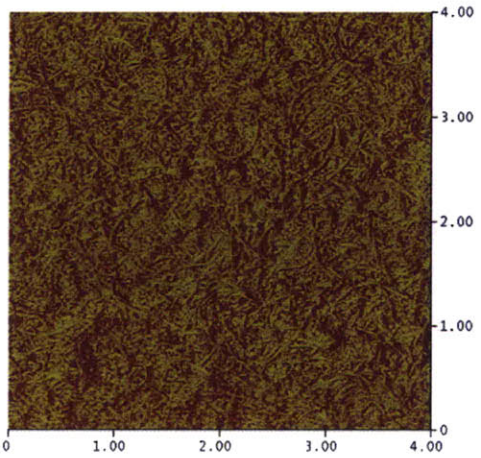

Figure 2-6. Representative atomic force microscopy (AFM) phase image of a MWNT thin film of 9 bilayers deposited at pH 2.5 (+) / 3.5 (-). Size of image is 4 μm × 4 μm.

The porous network structure of the LBL assembled MWNT thin films can be contrasted with simple cast films of raw MWNTs. Figure 2-7 shows comparison SEM top

view images of a cast film using raw MWNTs solution after 2 hours of sonication and a 20 bilayers MWNT thin film assembled at pH 2.5 (+) / 2.5 (-). The cast film of raw MWNTs shows aggregation and alignment of bundles of MWNTs due to van der Waals interactions and capillary forces. These films exhibit weak mechanical integrity, poor control of thickness and dense packing, leading to diminishment of the available surface area of the MWNTs. On the other hand, the LBL assembled MWNT films yield randomly oriented individual MWNTs with well developed nano-scale pores, making MWNT thin films an ideal electrode structure with mixed ionic/electronic conducting channels. These differences come from the electrostatic repulsion between nanotubes that act against van der Waals interactions that yield close packed aggregates, as well as the electrostatic cross-linking between positively and negatively charge MWNTs during the LBL process that lead to randomly oriented, kinetically driven CNT arrangements in the film. A cross-sectional view of a MWNT thin film (Figure 2-8a) demonstrates the conformal and uniform nature of the coating generated with LBL of MWNTs on silicon wafer, suggesting their application to substrates without any geometric constraint. A torn film shown in the Figure 6a insert reveals that most of the MWNTs in the film are not parallel with the substrate, but form an interpenetrated structure with random orientations of the nanotubes. An angled cross-sectional view was created by cutting films on a slant (Figure 2-8b); it more clearly shows the internal structure of the film, proving that a highly interpenetrated and porous structure is created. Since the MWNTs have intrinsically high electrical conductivity and higher surface area, these porous network structures can work as fast electronic and ionic conducting channels, providing the basis for design of the ideal matrix structure for energy conversion as well as energy storage devices.

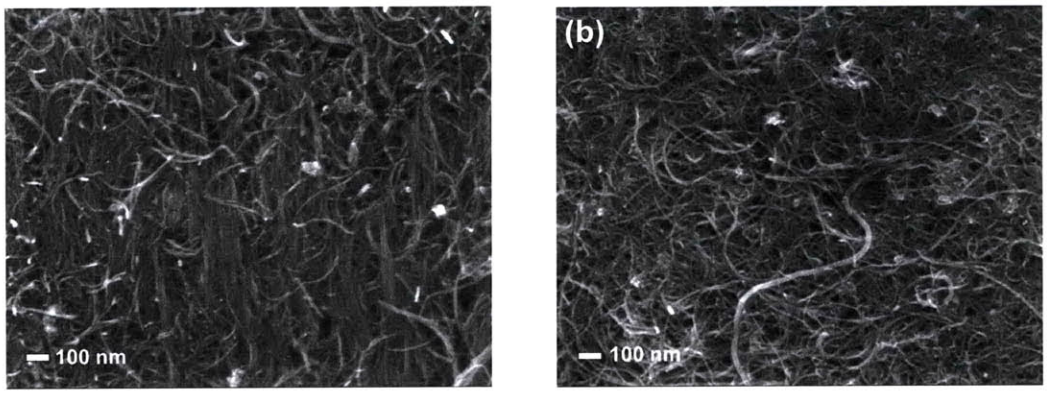

Figure 2-7. Comparison of the topology of MWNTs using scanning electron microscopy (SEM) images. (a) Deposition of raw MWNT solution on silicone wafer after 2 hr sonication. (b) LBL assembled MWNT thin film at (pH 2.5 (+) / 2.5 (-))$_{20}$.

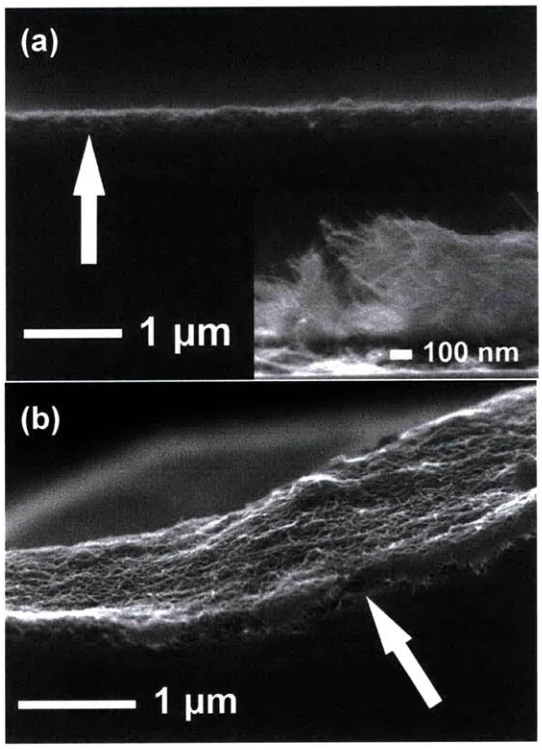

Figure 2-8. Scanning electron microscopy (SEM) images of MWNT thin films. (a) A cross-section view of 15 bilayers of MWNT film (pH 2.5 (+) / 3.5 (-)), and (b) a titled

cross-sectional view of a 20 bilayer MWNT film (pH 2.5 (+) / 4.5 (-)). White arrows indicate the interface between silicone substrate and MWNT thin films.

To measure the porosity of MWNT thin films, we used a recently developed model[45] by Lee and co-workers with ellipsometry, which allows the estimation of porosity from the refractive indices of materials in two different medium. MWNT thin films were cross-linked by amide bond formation by heat-treatment at 150 °C in vacuum, and the refractive index was measured in air and ethanol. To estimate the porosity we used the equation (equation 2-2) derived from the most frequently used Lorentz-Lorentz mixing rule of refractive index (equation 2-1). The estimated porosity range is about 35 ~ 43% depending on the sample and its thickness. Figure 2-9 shows representative refractive indices values in air and ethanol and the estimated porosity of MWNT thin films assembled at pH 2.5 (+) / 4.5 (-). There was some difficulty in measuring the refractive index accurately for the thicker samples assembled at lower pH, especially at pH 2.5 (+) / 2.5 (-) due to high surface roughnesses and absorption, making it difficult to determine the optical constant of thin films using spectroscopic ellipsometry.[46]

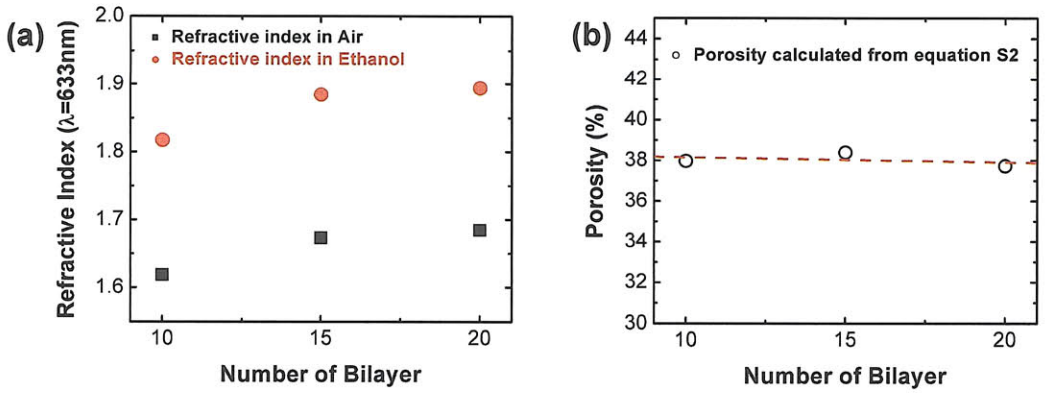

Figure 2-9. Representative refractive indices of MWNT thin films assembled at pH 2.5 (+) / 3.5 (-) in air and ethanol, and the porosity calculated from equation 2-2.

$$\frac{n_{12}^2 - 1}{n_{12}^2 + 2} = \varphi_1 \frac{n_1^2 - 1}{n_1^2 + 2} + \varphi_2 \frac{n_2^2 - 1}{n_2^2 + 2} \qquad \text{(2-1) Lorentz-Lorentz mixing rule}$$

$$P = \frac{\dfrac{n_{13}^2 - 1}{n_{13}^2 + 2} - \dfrac{n_{12}^2 - 1}{n_{12}^2 + 2}}{\dfrac{n_3^2 - 1}{n_3^2 + 2} - \dfrac{n_2^2 - 1}{n_2^2 + 2}} = \frac{\dfrac{n_{13}^2 - 1}{n_{13}^2 + 2} - \dfrac{n_{12}^2 - 1}{n_{12}^2 + 2}}{0.22} \qquad \text{(2-2)}$$

Here, n_{12} is the refractive index of the mixture of 1 and 2. n_1, n_2 and n_3 are the refractive indices of the MWNT thin films, air and ethanol respectively. φ_1 and φ_2 are volume fractions of each media.

2.3.4 Swelling Behavior and Mechanical Integrity of LBL Assembled, Surface Functionalized MWNT Thin Films

The time-dependent swelling behavior of the MWNT thin film in water was systematically investigated. When the thin film (156 ± 6 nm) was assembled at pH 2.5 (+) / 4.5 (-) on Si substrate was immersed in deionized water, small blisters were formed immediately in the center region of the film, then quickly grew and coalesced to large blisters which reached the boundary of substrate (Figure 2-10a-d). There is electrostatic repulsion between the negatively charged MWNTs in the film due to charge imbalances induced by a decrease in the degree of ionization of NH_2 (NH_3^+) groups, and increase of COOH (COO^-) groups in the water (pH 6.0), causing the film to swell. When the film is supported on a substrate and swollen in water, then the film can expand freely in the thickness direction, but it is confined laterally, creating strain in the lateral direction. Unlike polyelectrolyte-containing LBL films, rigid MWNT films cannot undergo high elastic strain to compensate for this stress. As a result, the generation of blisters and delamination of the film from the substrate begins from the point which has a larger strain energy compared to the adhesion energy between film and substrate to release excess strain energy in the film. Although individual MWNTs are quite elastic (bending modulus is

about 30 GPa[47]),[48] they cannot change their molecular conformations as polymers can due to rigidity; however, physical entanglements between nanotubes exist in the films due to their large aspect ratio and sinuous structure, allowing the film to maintain its mechanical integrity in spite of the detachment from the substrate (Figure 2-10d). This physical detachment from the substrate and expansion of the films via rearrangements of MWNTs in the film could be a mechanism of releasing strain energy in the film.[49] Gentle shaking of the substrate lead to the isolation of free-standing MWNT films due to their weak mechanical integrity. Part of the free-standing MWNT film was scooped from the water on a glass slide, and while maintaining the integrity of the film (Figure 2-10e). To increase the mechanical strength of the film and its adhesion to the substrate, thermally induced cross-linking (150°C in vacuum) of the MWNT thin film was conducted, which created amide bonds between the NH_3^+ and COO^- groups. XPS peaks of N_{1s} region (Figure 2-11) showed a significant decrease in the ammonium peak after the heat-treatment, which indicates the formation of amide bonds from charged ammonium groups.[50] Figure 2-10f shows that this cross-linked MWNT thin film is intact in water, which does not undergo swelling and preserves its original shape. Thus, thermal cross-linking of the MWNT films not only prevents swelling from electrolytes, but also provides mechanical strength and prevents lift-off and delamination from the substrate, which are required properties for real applications as electrodes for energy devices.

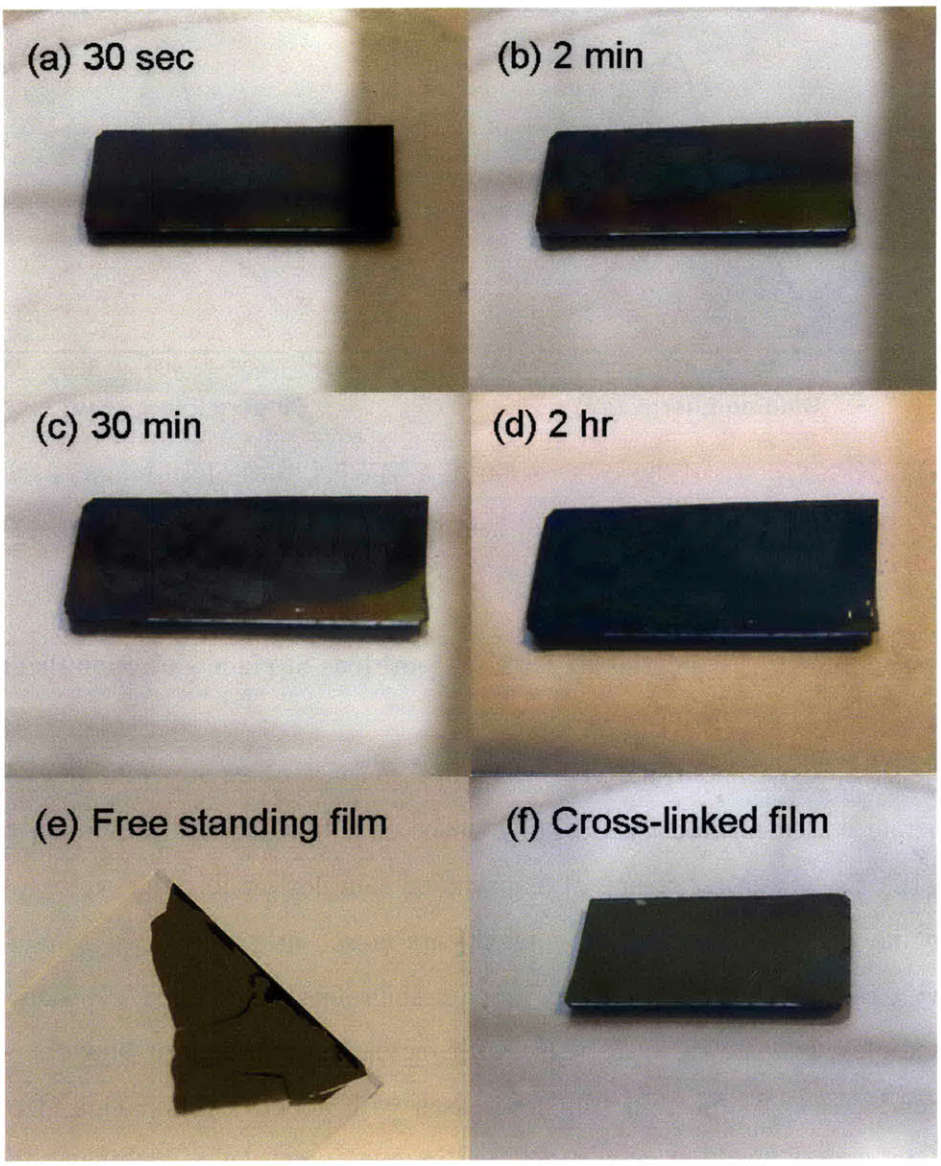

Figure 2-10. (a)-(d) Time-dependent water swelling behavior of MWNT thin film assembled at pH 2.5 / 4.5, (e) Free-standing film collected on a glass slide tip. (f) Thermally cross-linked film immersed after 24 hr in water. Note the structural integrity is maintained after cross-linking of the MWNT film at 150 °C in vacuum during overnight.

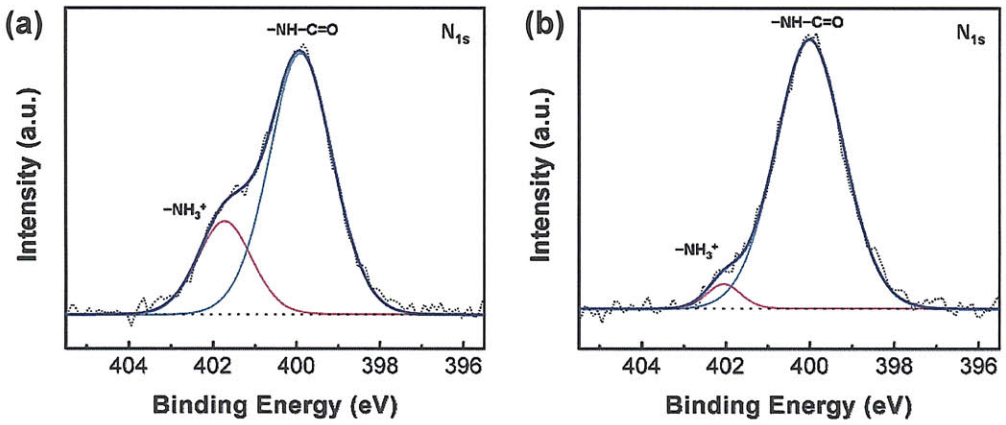

Figure 2-11. XPS spectra of the N1s region of a MWNT film of 10 bilayers assembled at pH 2.5 (+) / 3.5 (-) before (a) and after (b) heating at 150 °C under vacuum for 12 hours.

2.3.5 Electrochemical Properties of LBL Assembled, Surface Functionalized MWNT Thin Films.

The sheet resistance of the MWNTs thin films assembled at pH 2.5 (+) / 3.5 (-) on a glass substrate was measured by a 4-point probe as a function of the number of bilayers (Figure 2-12). The sheet resistance of as-prepared samples exhibit high values, thought to be due to the disruption of the conjugated carbon sp^2 orbitals on the MWNT exterior surface with the formation of surface functional groups. The sheet resistance of LBL MWNT samples was shown to decrease with increasing numbers of bilayers, suggesting that the conductivity of the thin films increases with added layers. This effect may be attributed to denser packing and more continuous intercolated pathways for electron transport in the thicker films. The heat-treatment at 150 °C in vacuum decreased the sheet resistance of LBL MWNT thin films roughly by one half, which could be attributed to facilitated electron flow between adjacent MWNTs cross-linked via amide formation. A subsequent heat-treatment at 300 °C in hydrogen atmosphere for 2 hr was used to burn off residual surface functional groups on the MWNTs, enabling direct contact was achieved between the electronically conducting MWNTs. This process led to a further decrease in the sheet resistance of the MWNT thin film, showing an average of an 82% reduction compared with as-assembled samples, as well as a film thickness that was slightly reduced

by about 10%. Further increases in electrical conductivity may be possible by higher temperature heat-treatments. To compare with other CNT electrodes reported previously, the all MWNT LBL electrodes were found to have sheet resistivity on the order of ~0.1 Ωcm (~10 S/cm) after heat treatments. Although this resistivity is higher than those of vertically oriented SWNT electrodes[12] (0.01 Ωcm, without surface functionalization) and ultrathin conductive SWNT films (1.5×10^{-4} Ωcm),[51] it is considerably lower than SWNT polymer composite electrodes (1 Ωcm).[52] Also the electrical conductivity of all MWNT LBL electrodes (Figure 2-12b) after heat-treatments is comparable or slightly higher than similar functionalized MWNTs capacitor,[53] which showed electrical conductivity (2~8 S/cm) as function of oxidation time, and ~3 S/cm at highest capacitance (~60 F/g). The high conductivity of the LBL electrodes can be attributed to the binder-free, all carbon nanotube composition of the multilayer film and its unique, highly interconnected morphology. These results show that heat-treatments of MWNT thin films after LBL assembly can increase their electrical conductivity as well as their mechanical integrity (Figure 2-10).

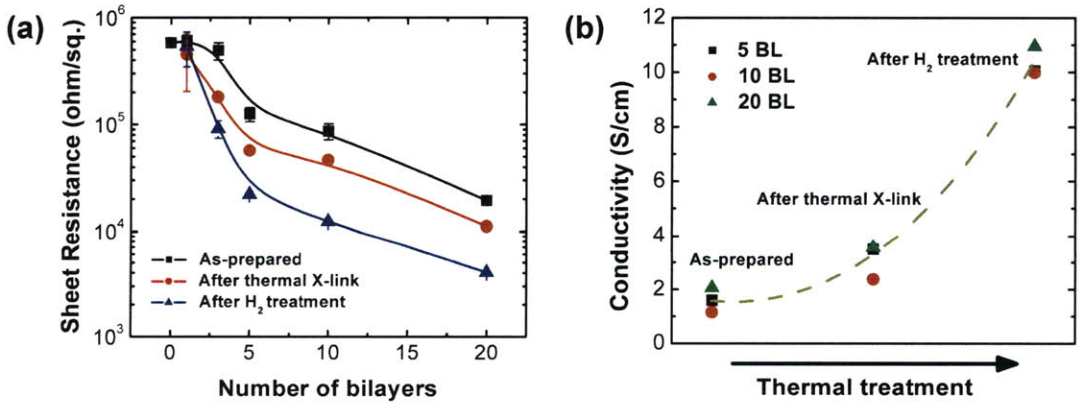

Figure 2-12. (a) Sheet resistance of the MWNT thin films. (square) as-assembled MWNT thin films assembled at pH 2.5 (+) / 3.5 (-). (circle) MWNT films after a thermal treatment at 150 °C in vacuum during overnight. (triangle) MWNT films after a second heat-

treatment at 300 °C in H_2 for 2 hours. (b) Corresponding electrical conductivity of the MWNT thin films in S/cm obtained from the data in (a), electrode thickness and area.

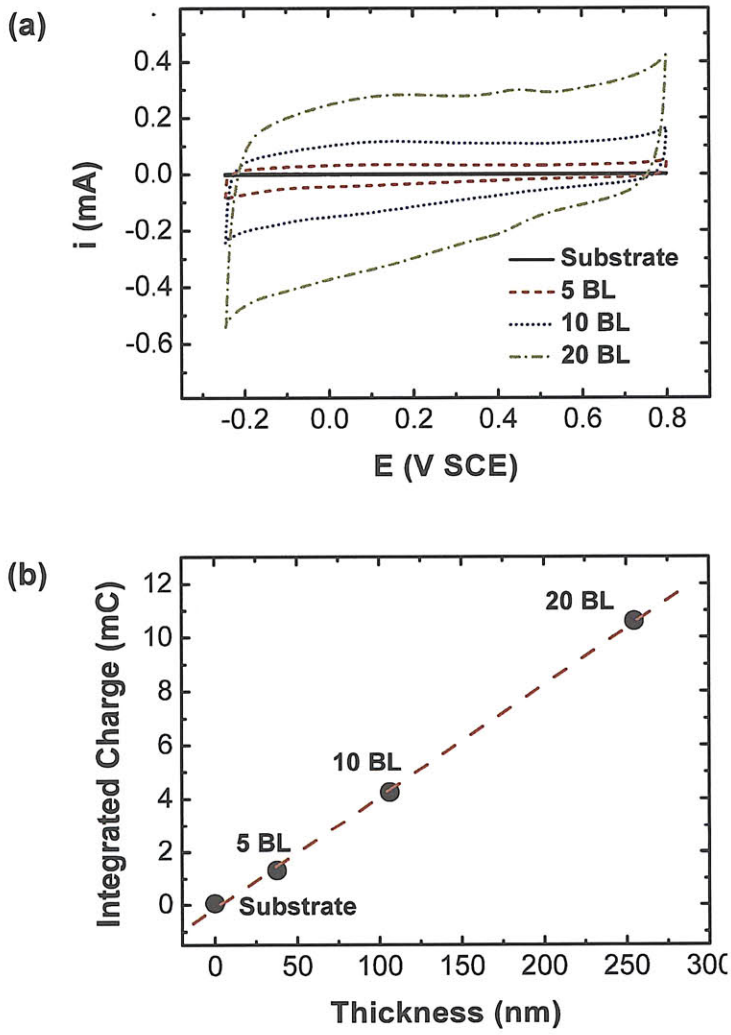

Figure 2-13. (a) Cyclic voltammograms obtained from MWNT thin films on ITO-coated glass electrode (after the second heat-treatment) in 1.0 M H_2SO_4 at room temperature. A scan rate of 50 mV/s was used. (b) Integrated charge from cyclic voltammograms vs. thickness of film measured from profilometer.

Cyclic voltammograms of heat-treated MWNT thin films (0.7 cm × 2 cm) on ITO-coated glass assembled at pH 2.5 (+) / 3.5 (-) were obtained in 1.0 M H_2SO_4 solution as a function of the number of bilayers (Figure 2-13a). The thickness dependent voltammetry curves showed considerably rectangular shapes, which is indicative of capacitive behavior of carbon materials.[14] Integrated surface charge from adsorbed and desorbed ions on MWNT thin film electrode was found to scale linearly as a function of film thickness (Figure 2-13b). An average capacitance of 132 ± 8 F/cm^3 (159 ± 10 F/g) was found and this value is considerably higher than those of vertically aligned CNTs[12] conventional CNT electrodes[14,53] as a result of the high CNT densities and well developed nanopores in the LBL MWNT thin films. This result indicates the potential to gain precise control of charge and energy storage in MWNT thin films by controlling the number of bilayers and film thickness in the LBL assembly.

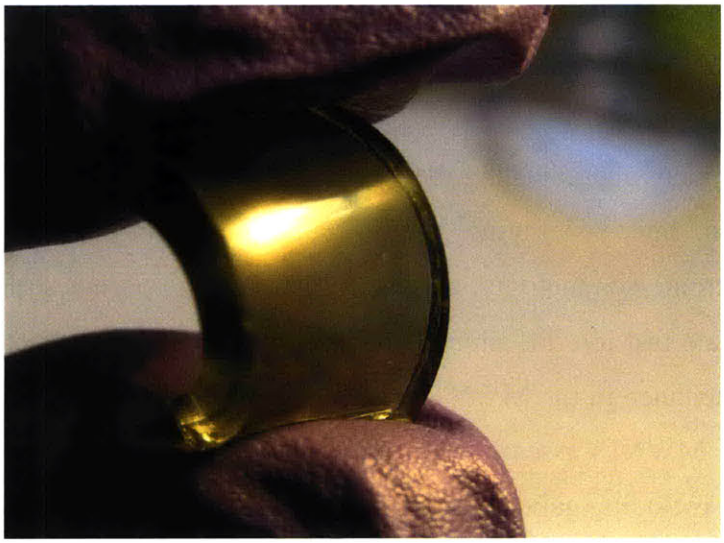

Figure 2-14. An optical image of a MWNT thin film of 10 bilayers assembled at pH 2.5 (+) / 3.5 (-) on PAH coated PDMS substrate.

Finally, to demonstrate the universality of the thin film application, a MWNT thin film was deposited on a flexible polydimethylsiloxane (PDMS) substrate. Figure 2-14

presents a 10 bilayer MWNT thin film assembled at pH 2.5 (+) / 3.5 (-) on PAH coated PDMS. Because of the ultrathin thickness of the MWNT film, the coating remains conformal and well-adhered even on a highly deformed PDMS substrate. This interesting result shows the possibility to design flexible energy storage and conversion devices[19] utilizing LBL assembled MWNTs as electrodes, electrical circuits, and current collectors.

2.4 Conclusions

Novel all-MWNT assemblies have been created through the alternation of surface functionalized positively and negatively charged MWNTs using the layer-by-layer technique. MWNT thin film assemblies show resemblance to LBL assembly from conventional weak polyelectrolytes such as PAA and PAH, which allow control of thickness and morphology by adjusting their conformation in the film via the manipulation of assembly pH conditions. Although MWNTs cannot change their molecular level conformation with changes in the local charge density due to their intrinsic rigidity, the surface charge density of MWNTs could play an important role in controlling film thickness and roughness by adjusting the charge reversal mechanism as well as the degree of interpenetration. Inter-penetrating MWNTs in the assembly make networks that can achieve high electronic conductivity, and the well-developed porous structures between the MWNTs may create fast ion diffusion channels to facilitate ion transport. The potential to achieve high capacitance in the MWNT thin films with precisely controlled capacity using LBL makes these MWNTs assemblies promising for supercapacitor electrodes. Capacitor performance tests including galvanostatic charge/discharge measurements and cycling tests are ongoing with various substrates and electrolytes for supercapacitor applications. We believe that these novel MWNT thin films fully utilize both advantages of intrinsic superior properties of functionalized MWNTs and precise control of the LBL system can be used to design ideal electrode materials for fuel cells, photoelectrochemical cells, batteries, supercapacitors, and gas and bio-sensors.

2.5 Reference

[1] Holt, J. K. et al., Fast mass transport through sub-2-nanometer carbon nanotubes. *Science* **312**, 1034-1037 (2006).

[2] Smajda, R., Kukovecz, A., Konya, Z., and Kiricsi, I., Structure and gas permeability of multi-wall carbon nanotube buckypapers. *Carbon* **45**, 1176-1184 (2007).

[3] Baughman, R. H. et al., Carbon nanotube actuators. *Science* **284**, 1340-1344 (1999).

[4] Landi, B. J. et al., Single wall carbon nanotube-Nafion composite actuators. *Nano Letters* **2**, 1329-1332 (2002).

[5] Mamedov, A. A. et al., Molecular design of strong single-wall carbon nanotube/polyelectrolyte multilayer composites. *Nat. Mater.* **1**, 190-194 (2002).

[6] Wang, C. et al., Proton exchange membrane fuel cells with carbon nanotube based electrodes. *Nano Letters* **4**, 345-348 (2004).

[7] Michel, M. et al., High-performance nanostructured membrane electrode, assemblies for fuel cells made by layer-by-layer assembly of carbon nanocolloids. *Adv. Mater.* **19**, 3859-+ (2007).

[8] Li, W. Z. et al., Preparation and characterization of multiwalled carbon nanotube-supported platinum for cathode catalysts of direct methanol fuel cells. *J. Phys. Chem. B* **107**, 6292-6299 (2003).

[9] Frackowiak, E. et al., Electrochemical storage of lithium multiwalled carbon nanotubes. *Carbon* **37**, 61-69 (1999).

[10] Shimoda, H. et al., Lithium intercalation into opened single-wall carbon nanotubes: Storage capacity and electronic properties. *Phys. Rev. Lett.* **88** (2002).

[11] Morris, R. S. et al., High-energy, rechargeable Li-ion battery based on carbon nanotube technology. *Journal of Power Sources* **138**, 277-280 (2004).

[12] Futaba, D. N. et al., Shape-engineerable and highly densely packed single-walled carbon nanotubes and their application as super-capacitor electrodes. *Nat. Mater.* **5**, 987-994 (2006).

[13] Yoon, B. J. et al., Electrical properties of electrical double layer capacitors with integrated carbon nanotube electrodes. *Chemical Physics Letters* **388**, 170-174 (2004).

[14] Frackowiak, E. and Beguin, F., Carbon materials for the electrochemical storage of energy in capacitors. *Carbon* **39**, 937-950 (2001).

[15] Baughman, R. H., Zakhidov, A. A., and de Heer, W. A., Carbon nanotubes - the route toward applications. *Science* **297**, 787-792 (2002).

[16] Ajayan, P. M. and Zhou, O. Z., in *Carbon Nanotubes* (Springer-Verlag Berlin, Berlin, 2001), Vol. 80, pp. 391-425.

[17] Arico, A. S. et al., Nanostructured materials for advanced energy conversion and storage devices. *Nat. Mater.* **4**, 366-377 (2005).

[18] Shaijumon, M. M., Ou, F. S., Ci, L. J., and Ajayan, P. M., Synthesis of hybrid nanowire arrays and their application as high power supercapacitor electrodes. *Chemical Communications*, 2373-2375 (2008).

[19] Pushparaj, V. L. et al., Flexible energy storage devices based on nanocomposite paper. *Proc. Natl. Acad. Sci. U. S. A.* **104**, 13574-13577 (2007).
[20] Li, W. Z. et al., Carbon nanotube film by filtration as cathode catalyst support for proton-exchange membrane fuel cell. *Langmuir* **21**, 9386-9389 (2005).
[21] An, K. H. et al., High-capacitance supercapacitor using a nanocomposite electrode of single-walled carbon nanotube and polypyrrole. *Journal of the Electrochemical Society* **149**, A1058-A1062 (2002).
[22] Liu, J. et al., Fullerene pipes. *Science* **280**, 1253-1256 (1998).
[23] Esumi, K. et al., Chemical treatment of carbon nanotubes. *Carbon* **34**, 279-281 (1996).
[24] Chen, R. J., Zhang, Y. G., Wang, D. W., and Dai, H. J., Noncovalent sidewall functionalization of single-walled carbon nanotubes for protein immobilization. *Journal of the American Chemical Society* **123**, 3838-3839 (2001).
[25] Nakashima, N., Tomonari, Y., and Murakami, H., Water-soluble single-walled carbon nanotubes via noncovalent sidewall-functionalization with a pyrene-carrying ammonium ion. *Chem. Lett.*, 638-639 (2002).
[26] Paloniemi, H. et al., Layer-by-layer electrostatic self-assembly of single-wall carbon nanotube polyelectrolytes. *Langmuir* **22**, 74-83 (2006).
[27] O'Connell, M. J. et al., Reversible water-solubilization of single-walled carbon nanotubes by polymer wrapping. *Chemical Physics Letters* **342**, 265-271 (2001).
[28] Liu, P., Modifications of carbon nanotubes with polymers. *Eur. Polym. J.* **41**, 2693-2703 (2005).
[29] Satake, A., Miyajima, Y., and Kobuke, Y., Porphyrin - Carbon nanotube composites formed by noncovalent polymer wrapping. *Chem. Mat.* **17**, 716-724 (2005).
[30] Decher, G., Fuzzy nanoassemblies: Toward layered polymeric multicomposites. *Science* **277**, 1232-1237 (1997).
[31] Zhang, M. N. et al., Electrostatic layer-by-layer assembled carbon nanotube multilayer film and its electrocatalytic activity for O-2 reduction. *Langmuir* **20**, 8781-8785 (2004).
[32] Zhang, M. N., Su, L., and Mao, L. Q., Surfactant functionalization of carbon nanotubes (CNTs) for layer-by-layer assembling of CNT multi-layer films and fabrication of gold nanoparticle/CNT nanohybrid. *Carbon* **44**, 276-283 (2006).
[33] Olek, M. et al., Layer-by-layer assembled composites from multiwall carbon nanotubes with different morphologies. *Nano Letters* **4**, 1889-1895 (2004).
[34] Shiratori, S. S. and Rubner, M. F., pH-dependent thickness behavior of sequentially adsorbed layers of weak polyelectrolytes. *Macromolecules* **33**, 4213-4219 (2000).
[35] Choi, J. and Rubner, M. F., Influence of the degree of ionization on weak polyelectrolyte multilayer assembly. *Macromolecules* **38**, 116-124 (2005).
[36] Mendelsohn, J. D. et al., Fabrication of microporous thin films from polyelectrolyte multilayers. *Langmuir* **16**, 5017-5023 (2000).
[37] Chen, J. et al., Solution properties of single-walled carbon nanotubes. *Science* **282**, 95-98 (1998).

[38] Baker, S. E. et al., Covalently bonded adducts of deoxyribonucleic acid (DNA) oligonucleotides with single-wall carbon nanotubes: Synthesis and hybridization. *Nano Letters* **2**, 1413-1417 (2002).

[39] Ramanathan, T., Fisher, F. T., Ruoff, R. S., and Brinson, L. C., Amino-functionalized carbon nanotubes for binding to polymers and biological systems. *Chem. Mat.* **17**, 1290-1295 (2005).

[40] Ago, H. et al., Work functions and surface functional groups of multiwall carbon nanotubes. *J. Phys. Chem. B* **103**, 8116-8121 (1999).

[41] Murphy, H., Papakonstantinou, P., and Okpalugo, T. I. T., Raman study of multiwalled carbon nanotubes functionalized with oxygen groups. *J. Vac. Sci. Technol. B* **24**, 715-720 (2006).

[42] *CRC Handbook of Chemistry and Physics*, 79 ed. (CRC Press, Boca Raton, 1998).

[43] Tagliazucchi, M., Williams, F. J., and Calvo, E. J., Effect of acid-base equilibria on the donnan potential of layer-by-layer redox polyelectrolyte multilayers. *J. Phys. Chem. B* **111**, 8105-8113 (2007).

[44] Tagliazucchi, M., Calvo, E. J., and Szleifer, I., Molecular theory of chemically modified electrodes by redox polyelectrolytes under equilibrium conditions: Comparison with experiment. *J. Phys. Chem. C* **112**, 458-471 (2008).

[45] Lee, D., Rubner, M. F., and Cohen, R. E., All-nanoparticle thin-film coatings. *Nano Letters* **6**, 2305-2312 (2006).

[46] Tompkins, Harland G.; Irene, Eugene A, *HANDBOOK OF ELLIPSOMETRY.* (William Andrew Publishing, New York, 2005).

[47] Ciocan, R., Gaillard, J., Skove, M. J., and Rao, A. M., Determination of the bending modulus of an individual multiwall carbon nanotube using an electric harmonic detection of resonance technique. *Nano Letters* **5**, 2389-2393 (2005).

[48] Bernholc, J. et al., Mechanical and electrical properties of nanotubes. *Annual Review of Materials Research* **32**, 347-375 (2002).

[49] Sharp, J. S. and Jones, R. A. L., Swelling-induced morphology in ultrathin supported films of poly(d,l-lactide). *Physical Review E* **66** (2002).

[50] Harris, J. J., DeRose, P. M., and Bruening, M. L., Synthesis of passivating, nylon-like coatings through cross-linking of ultrathin polyelectrolyte films. *Journal of the American Chemical Society* **121**, 1978-1979 (1999).

[51] Wu, Z. C. et al., Transparent, conductive carbon nanotube films. *Science* **305**, 1273-1276 (2004).

[52] Sung, J. et al., Transparent, low-electric-resistance nanocomposites of self-assembled block copolymers and SWNTs. *Adv. Mater.* **20**, 1505-+ (2008).

[53] Kim, Y. T. and Mitani, T., Competitive effect of carbon nanotubes oxidation on aqueous EDLC performance: Balancing hydrophilicity and conductivity. *Journal of Power Sources* **158**, 1517-1522 (2006)

Chapter 3. Functionalized Carbon Nanotube Electrodes for High-Power Energy Storage Applications

Portions of this chapter are reprinted from Seung Woo Lee, Naoaki Yabuuchi, Betar M. Gallant, Shuo Chen, Byeong-Su Kim, Paula T. Hammond and Yang Shao-Horn, *manuscript submitted.*

Abstract

An increasing number of applications such as microsystems, portable electronic devices, and load-leveling for hybrid vehicles, machineries and renewable energy require electrical energy storage with high power capability. Here we report the use of functionalized multiwall carbon nanotubes (MWNTs) in additive-free and high-packing-density electrodes with thicknesses of several microns in lithium batteries. These electrodes can store lithium up to a reversible gravimetric capacity of ~200 $mAh/g_{electrode}$ by utilizing the redox reactions of the surface functional groups on MWNT in the voltage range from 4.5 to 1.5 V vs. lithium. In addition, they show power capabilities and cycle life comparable to those of electrochemical capacitors. Combining the MWNTs as the positive electrode and a lithium titanium oxide negative electrode results in an electrochemical storage device with gravimetric energy ~5 times higher than conventional electrochemical capacitors.

3.1 Introduction

A major challenge in electrical energy storage is to bridge the performance gap between batteries and electrochemical capacitors by developing materials that can combine the advantages of batteries, which store high energy in the bulk of active particles but are

rate-limited, and electrochemical capacitors[1-3], which deliver high power at the cost of low energy storage by utilizing surface ion adsorption and surface redox reactions (referred to as pseudo-capacitance). Lithium rechargeable batteries (~150 Wh/kg_{cell} and ~1 kW/kg_{cell}) have higher gravimetric energy but lower power capability than electrochemical capacitors (~5 Wh/kg_{cell} and ~10 kW/kg_{cell})[1]. Power versatility in energy storage devices is crucial for hybrid applications[2]. For example, though conventional batteries have been used in light vehicles, hybrid platforms for heavy vehicles and machineries such as trucks demand delivery of much higher currents, where higher energy and comparable power capability relative to electrochemical capacitors is needed to meet this demand[1,2].

Considerable research efforts have been focused on increasing the power characteristics of lithium rechargeable batteries by reducing lithium storage material dimensions down to the nanometer scale[4-12], which reduces the time of lithium diffusion accompanying the Faradaic reactions of active particles. However, nanostructured lithium storage electrodes[5,13] still have lower power capability than electrochemical capacitor electrodes. On the other hand, workers have shown that the gravimetric energy of electrochemical capacitors can be increased by employing electrode materials with enhanced gravimetric capacitances (gravimetric charge storage per volt), which can result from utilizing carbon subnanometer pores for ion adsorption[1,14] or employing the pseudocapacitance of nanostructured transition metal oxides[15-17]. The high cost of Ru-based oxides is prohibitive for many applications while the cycling instability of Mn-based oxides[17-19] remains as a major technical challenge. Considering these developments, a promising approach is to utilize Faradaic reactions of surface functional groups on nanostructured carbon electrodes that would store more energy than surface ion adsorption on conventional capacitor electrodes[1] and also provide high-power capability.

3.2 Experimental Section

Materials. MWNTs prepared by chemical vapor deposition were purchased from NANOLAB (95% purity, outer diameter 15 ± 5 nm). Carboxylated MWNTs (MWNT-COOH) and amine functionalized MWNTs (MWNT-NH_2) were prepared and assembled

onto indium-tin oxide (ITO) coated glass slides using processes described in detail elsewhere[23]. The cross-sectional scanning electron microscope (SEM) images of MWNT electrodes after the heat-treatments were obtained with JEOL 6320 SEM operated at 5 kV.

Fabrication of Layer-by-Layer MWNT Electrodes. MWNT-COOH and MWNT-NH_2 powder samples were sonicated for several hours in Milli-Q water (18 MΩ·cm) to form a uniform dispersion, and this was followed by dialysis via Milli-Q water for several days, resulting in a stable dispersion of functionalized MWNTs solution (0.5 mg/ml). pH values of the solutions were adjusted to pH 2.5 (MWNT-NH_2) and pH 3.5 (MWNT-COOH) respectively, and the solutions were sonicated for 1 hour just before LBL assembly. All-MWNT electrodes were assembled with a modified Carl Zeiss DS50 programmable slide stainer. Details of LBL assembly of MWNT electrodes can be found elsewhere[23]. Assembled LBL-MWNT electrodes were dried in air, and these films were then heat-treated sequentially at 150 °C in vacuum for 12 hours, and at 300 °C in H_2 for 2 hours to increase mechanical stability.

X-ray Photoelectron Spectroscopy (XPS). A Kratos Axis Ultra XPS instrument (Kratos Analytical, Manchester) with a monochoromatized Al Kα X-ray source was used to analyze the surface chemistry of functionalized MWNTs and LBL-MWNT electrodes. The take-off angle relative to the sample substrate was 90°. Curve fitting of the photoemission spectra was performed following a Shirley type background subtraction. An asymmetric C1s peak from sp^2 hybridized carbons centered at 284.5 eV was generated for raw MWNTs. Using this asymmetric peak as a reference, all other peaks were fitted by the Gaussian-Lorentzian function. The experimental uncertainty on the XPS binding energy is ± 0.1 eV. Relative sensitivity factors used to scale the peaks of C 1s, O 1s, and N 1s were 0.278, 0.780, and 0.477, respectively.

Electrochemical measurements. Electrochemical measurements were conducted using a two-electrode electrochemical cell (Tomcell Co. Ltd., Japan), which consisted of an LBL-MWNT electrode on ITO coated glass, two sheets of microporous membrane (Celgard 2500, Celgard Inc., USA) and lithium foil as the counter electrode. LBL-MWNT electrode area of 100 and 50 mm^2 was used for electrochemical measurements with Li foil and fully

LTO negative electrodes, respectively. The weights of LBL-MWNT electrodes were determined from the area and the mass area density listed in SI information. The loading density of LBL-MWNT electrodes ranges from 0.025 ~ 0.25 mg/cm^2. A piece of aluminum foil (25 μm thick and with 1mm x 7mm area in contact with LBL-MWNT electrode) was attached to one edge and used as a current collector. The electrolyte solution was 1 M $LiPF_6$ dissolved in a mixture of ethylene carbonate (EC) and dimethyl carbonate (DMC) with a 3:7 volume ratio (3.5 ppm H_2O impurity, Kishida Chem. Corp. Ltd., Japan). The separators were wetted by the minimum amount of the electrolyte to reduce background current. Cyclic voltammetry and galvanostatic measurements of lithium cells were performed using a Solartron 4170 at room temperature.

Mass Determination of LBL-MWNT Electrodes. The area mass density (μg/cm^2) of LBL-MWNT electrodes after the heat-treatments was determined using a quartz crystal microbalance (Masscal G1 QCM/HCC), and the thickness was measured using a Tencor P-10 profilometer, from which electrode weight and volume were obtained. The mass density (0.83 g/cm^3) of the electrode was determined from the slope of the graph shown in Supplementary Fig. S1. The thickness of each LBL-MWNT electrode was determined by averaging the thickness at least three different locations on each electrode using the profilometer. The volume of each electrode was determined by multiplying the thickness and the geometric area of the electrode, and was converted to the mass using the density. The porosity of MWNT electrodes was estimated to be ~30% by considering a density of ~1.2 g/cm^3 for MWNT powder and a electrode density of 0.83 g/cm^3. The area mass density (μg/cm^2) of LBL-MWNT electrodes was determined using a quartz crystal microbalance (Masscal G1 QCM/HCC), and the thickness was measured using a Tencor P-10 profilometer.

Sample Preparation and Transmission Electron Microscopy (TEM). For MWNT powder sample preparation, raw and functionalized MWNTs were dispersed in Milli-Q water using a Branson Bransonic 3510 ultrasonic cleaner (40 kHz) for 30 minutes. To prepare LBL-MWNT electrodes for TEM observations, an LBL-MWNT electrode was scratched with a spatula in Milli-Q water, and was subsequently dispersed ultrasonically for

10 minutes. Well-dispersed MWNT solutions were deposited on a lacey carbon grid and dried in air for TEM observations. JEOL 2010 and JEOL 2010F electron microscopes were used for medium and high resolution imaging of the electrode samples. The JEOL 2010 uses a LaB_6 thermal emission electron gun and the JEOL 2010F uses a field emission gun. Both microscopes were operated at 200 kV and were able to ultimately achieve 0.19 nm point-to-point resolution.

$Li_4Ti_5O_{12}$ (LTO) Electrode Preparation. The $Li_4Ti_5O_{12}$ (LTO) was prepared using a solid-state method with of Li_2CO_3 (Alfa Aesar, 99.998%) and TiO_2 (Anataze, MTI Corporation, 99.99%, particle size:5-10 nm). Li_2CO_3 and TiO_2 were uniformly mixed (with a weight ratio of Li to Ti is 4.2/5.0), and the mixture was pre-heated at 600 °C for 1 hour in dry air. The product from the pre-heat-treatment was reground, pelletized, and then reheated up to 850 °C in dry air. To make the electrode, 80 wt% LTO was mixed with 10 wt% SUPER-P® carbon black and 10 wt% polyvinylidene fluoride (PVdF) in N-methyl-2-pyrrolidone (NMP). The mixture was cast on an aluminum foil with a doctor blade, which and was dried in a vacuum oven at 60 °C for 2 hours and then at 110 °C for 12 hours. LTO electrodes with an area of 2.36 cm^2 (Average weight: 9.24 mg) were prelithiated by Li metal prior to electrochemical testing with LBL-MWNT electrodes. After preconditioning LTO by repeating lithiation and delithiation several times at 0.2 C (35 mA/g), lithiation was stopped at about 70% of the full capacity for use in LTO/LBL-MWNT cells.

$LiNi_{0.5}Mn_{1.5}O_4$ (LNM) Electrode Preparation. The $LiNi_{0.5}Mn_{1.5}O_4$ (LNM) was prepared using two step solid-state method with of Li_2CO_3 and coprecipitated nickel manganese oxide (molar ratio Ni:Mn=1:3). Li_2CO_3 and nickel manganese oxide were uniformly mixed (Lithium 3% molar ratio rich), and the mixture was heated first step at 1000 °C for 30 min and was subsequently annealed at 700 °C for various times under atmospheric pressured dry air or pressurized oxygen condition (atmospheric, 100 kPa and 200 kPa). To make the electrode, 80 wt% LNM was mixed with 10 wt% SUPER-P® carbon black and 10 wt% polyvinylidene fluoride (PVdF) in N-methyl-2-pyrrolidone (NMP). The mixture was cast on an aluminum foil with a doctor blade, which and was dried in a vacuum oven at 60 °C for 2 hours and then at 110 °C for 12 hours.

Composite Functionalized MWNT Electrode Preparation. Functionalized MWNTs were mixed with PVdF dissolved in NMP at 50 °C. A black viscous slurry consisting of 80 wt % of MWNT and 20 wt % of PVdF was cast on an aluminum foil with a doctor blade. NMP was evaporated at 100 °C under vacuum for 12 hours. The electrodes were punched out into a disk with a diameter of 15 mm.

3.3 Results and Discussion

Here we report the use of an entirely different class of electrodes for lithium storage, which are based on functionalized multiwall carbon nanotubes (MWNTs) including stable pseudo-capacitive functional groups assembled using the layer-by-layer (LBL) technique[20]. These additive-free LBL-MWNT electrodes exhibit high gravimetric energy (200 $Wh/kg_{electrode}$) delivered at an exceptionally high power of 100 $kW/kg_{electrode}$ in Li/LBL-MWNT cells when normalized to the single electrode weight, with no loss noted up to thousands of cycles. LBL-MWNT electrodes show significantly higher gravimetric energy than not only electrochemical capacitor electrodes but also lithium battery electrodes at gravimetric power greater than ~10 $kW/kg_{electrode}$. In addition, cells (analogous to asymmetric electrochemical capacitors) consisting of LBL-MWNT and a lithiated $Li_4Ti_5O_{12}$ (LTO) negative electrode have comparable gravimetric energy to LTO/$LiNi_{0.5}Mn_{1.5}O_4$ cells[21] at low gravimetric power but can deliver much higher energy at higher power. Gravimetric energy and power at the cell level may be estimated by dividing these values based on LBL-MWNT weight only by a factor of ~5[22]. Furthermore, we show that Faradaic reactions between lithium ions and surface functional groups on MWNTs are responsible for high gravimetric energy found in Li/LBL-MWNT and LTO/LBL-MWNT cells.

3.3.1 Physical characteristics and surface chemistry of LBL-MWNT electrodes

Stable dispersions of negatively and positively charged MWNTs were obtained via functionalization of the exterior surfaces with carboxylic-acid (MWNT-COOH) and amine-containing (MWNT-NH_2) groups, respectively[23]. Uniform MWNT electrodes on indium tin oxide (ITO) coated glass (Fig. 3-1a) were assembled using alternate adsorption of charged

MWNTs[23]. The electrode thickness increases linearly with the number of positively and negatively charged layer pairs (bilayers), as shown in Fig. 3-1b. The transparency of the MWNT films decreased linearly with increasing thickness up to 0.3 m (Fig. 3-1b). The films were then heat-treated sequentially at 150 °C in vacuum for 12 hours, and at 300 °C in H_2 for 2 hours to increase film mechanical stability and electrical conductivity[23]. Combined profilometry and quartz crystal microbalance measurements give an electrode density of 0.83 g/cm^3 (Fig. 3-2) after the heat treatments, which is among the highest densities of CNT electrodes reported[24,25]. Cross-sectional scanning electron microscope (SEM) images showed that individual MWNTs are randomly distributed throughout the film thickness, and MWNT films are uniform and conformal on the substrate (Fig. 3-1c). Moreover, LBL-MWNT electrodes exhibit an interconnected network of individual MWNTs (Fig. 3-1c inset) with well-distributed pores of ~20 nm as revealed by transmission electron microscopy (TEM) imaging of an LBL-MWNT electrode slice (Fig. 3-1d).

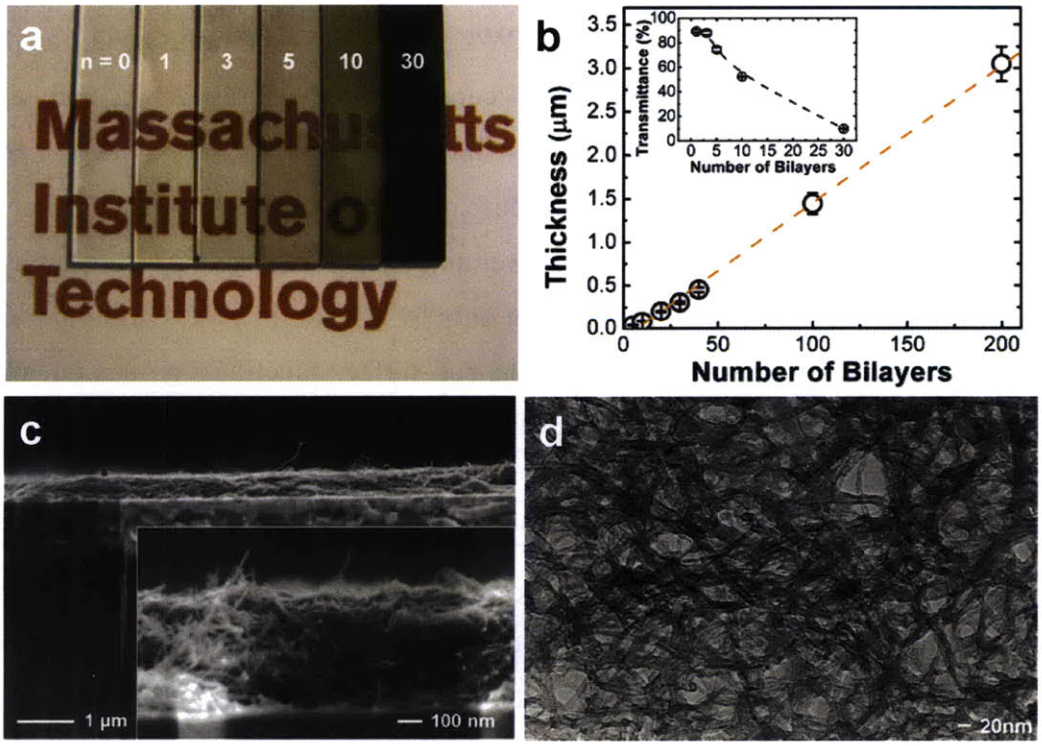

Figure 3-1. Physical characteristics of LBL-MWNT electrodes. a, A digital picture of representative MWNT electrodes on ITO coated glass slides. The number on each image indicates the number of bilayers (n) in $(MWNT\text{-}NH_2 / MWNT\text{-}COOH)_n$. **b,** Thickness of LBL-MWNT electrodes as a function of the number of bilayers. A linear relationship was shown for LBL-MWNT electrodes with thicknesses from 20 nm to 3 μm. Error bars show the standard deviation of thickness computed from 3 samples for each thickness. Transmittance measured at 550 nm as a function of the number of bilayers is shown in the figure inset. Error bars show the standard deviation of transmittance computed from 3 measurements. **c,** A SEM cross-sectional image of an LBL-MWNT electrode on ITO coated glass slide after the heat-treatments. A higher magnification image is shown in the figure inset, which reveals that MWNTs are inter-tangled in the direction perpendicular to the electrode surface. **d,** A TEM image of an LBL-MWNT electrode slice, which shows pore sizes on the order of ~20 nm.

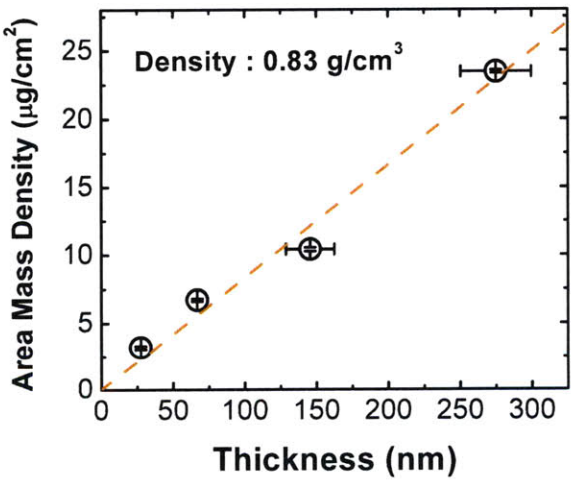

Figure 3-2. A plot of deposited area mass density ($\mu g/cm^2$) vs. thickness for LBL-MWNT electrodes on quartz crystal microbalance (QCM) substrates. The slope gives the mass density (0.83 g/cm^3) of MWNT electrodes. Each area mass density value was obtained by 3 measurements using QCM and error bars represent the standard deviations. 5-8 thickness measurements were taken at different positions of each sample using the profilometer.

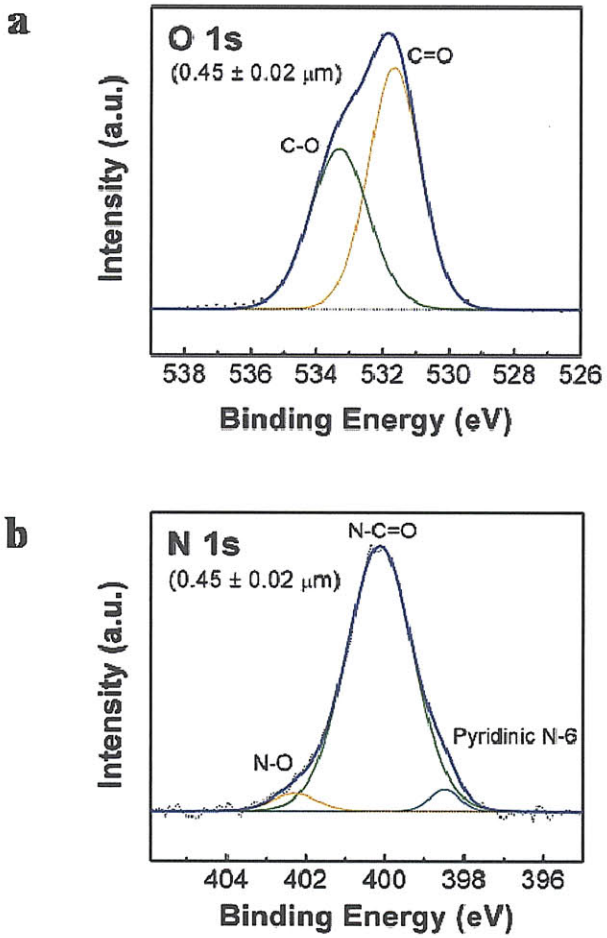

Figure 3-3. Surface chemistry of LBL-MWNT electrodes. a, XPS O 1s and **b,** N 1s spectra of a representative LBL-MWNT electrode after the heat-treatments. Two peaks (531.7 and 533.4 eV) were fitted in the O 1s spectrum, which could be attributed to oxygen atoms in the carbonyl groups and various other groups bound to the MWNT surface. The nitrogen atoms were mostly in the form of amide groups centered at 400.1 eV. Two small additional peaks suggest that some nitrogen atoms are pyridinic N-6 (398.5 eV) and tied in oxidized-nitrogen-containing functional groups (402.3 eV).

X-ray photoemission spectroscopy (XPS) analysis of LBL-MWNT electrodes after the heat-treatments revealed that significant amounts of oxygen-containing and nitrogen-

containing surface functional groups remained on the nanotube surface. The atomic composition of a representative LBL-MWNT electrode consists of 85.7% carbon, 10.6% oxygen, and 3.7% nitrogen. The presence of two distinct peaks (531.7 ± 0.1 eV and 533.4 ± 0.1 eV) in the O 1s spectrum (Fig. 3-3a) could be attributed to oxygen atoms in the carbonyl groups[26,27] and various other oxygen groups (Fig. 3-4) bound to the edges[26,28] of graphene sheets of MWNT side walls. This is in agreement with high-resolution TEM imaging of functionalized MWNTs, where many surface defects were found (Fig. 3-5). In addition, the chemical environment of the nitrogen atoms in the LBL-MWNT electrodes was mostly in the form of amide groups (Fig. 3-3b), as indicated by the N 1s peak centered at 400.1 eV[29]. Two small additional peaks in the N 1s spectrum suggest that some nitrogen atoms are pyridinic N-6[29] (398.5 ± 0.1 eV) and tied in oxidized nitrogen-containing functional groups (402.3 eV)[29].

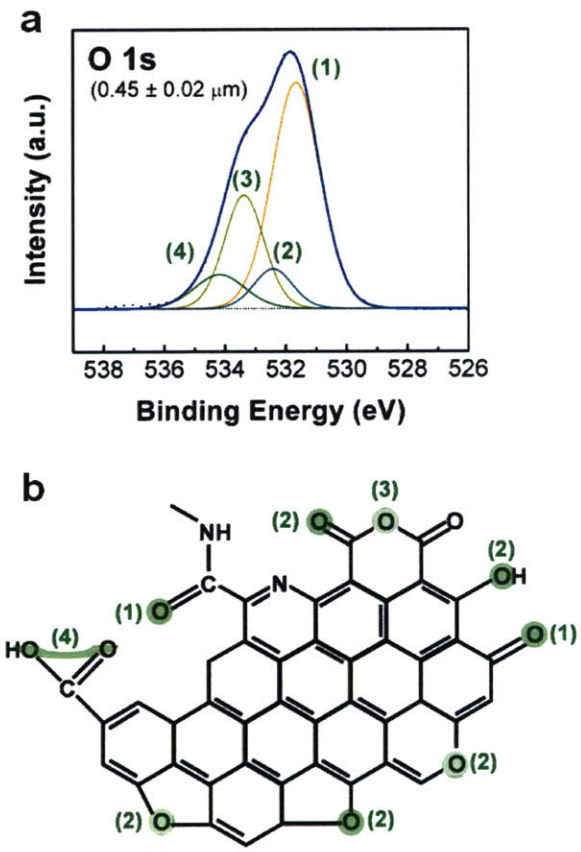

Figure 3-4. XPS O 1s spectra of a representative LBL-MWNT electrode after the heat-treatments. **a,** O 1s peaks were analyzed as following groups: carbonyl oxygen atoms in amide, ester, and anhydride groups at 531.7 eV (group 1), oxygen atoms in ether and hydroxyl groups at 532.4 eV (group 2), ether oxygen atoms in anhydride groups at 533.4 eV (group 3), and oxygen atoms in carboxylic acid groups at 534.2 eV (group 4). **b,** A schematic identifying possible surface functional groups on functionalized MWNTs.

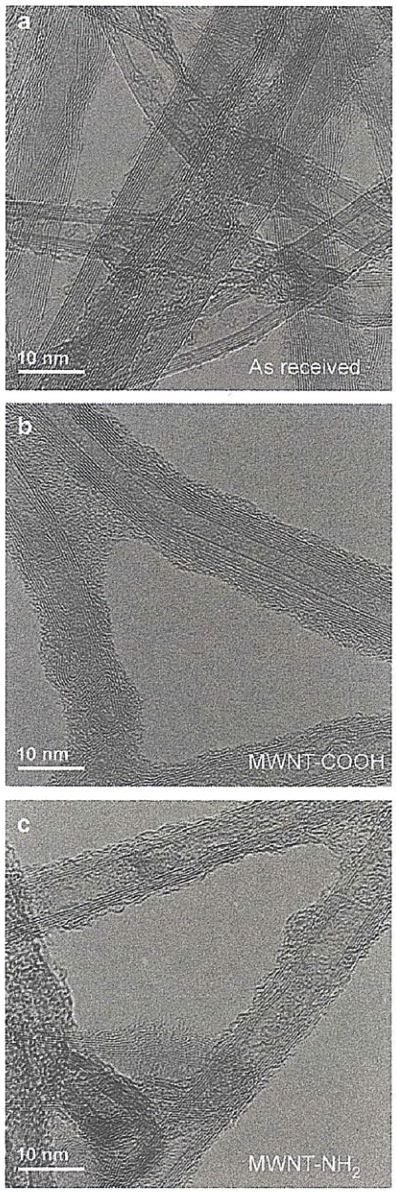

Figure 3-5. TEM images of the exterior wall structures of **a,** as-received MWNTs, and MWNTs functionalized with **b,** MWNT-COOH and **c,** MWNT-NH_2. Amorphous regions were observed on the surfaces of MWNT-COOH and MWNT-NH_2.

3.3.2 Electrochemical characteristics of LBL-MWNT electrodes

These surface functional groups can undergo Faradaic reactions as indicated by the potential-dependent gravimetric capacitance obtained from cyclic voltammetry measurements (Fig. 3-6a). Typical gravimetric capacitance of LBL-MWNT electrodes in the voltage range from 3 to 4.25 V vs. Li is ~125 F/g, which is comparable to values reported for functionalized MWNTs[23,30] and porous carbon materials[31,32] in aqueous solutions (with a comparable voltage scale of 0 to ~1.2 V vs. SHE). As LBL-MWNT electrodes have no additives, the gravimetric capacitance normalized to electrode weight is identical to that normalized to MWNT weight. Reducing the lower-potential limit from 3.0 to 1.5 V led to a significant increase in the gravimetric capacitance from ~125 to ~250 F/g measured at 4.0 and 2.5 V vs. Li, which is greater than those of conventional composite electrodes based on carbon[31,33] in organic electrolytes. More interestingly, the gravimetric capacitancies of LBL-MWNT electrodes in this study are comparable to those of electrodes consisting of nanostructured Mn-based oxides (~40 wt% oxides) used in the electrode composites despite the fact that higher capacitances normalized to active material mass (e.g. up to ~600 F/g_{MnO2})[34] are reported. Furthermore, considering the LBL-MWNT electrode density of 0.83 g/cm^3, we obtain a volumetric capacitance of ~180 F/cm^3 for LBL-MWNT electrodes. Very Few studies have reported volumetric capacitance of entire electrodes, and we note that this value is higher than that of nanostructured carbon (~50 F/cm^3) in organic electrolytes[31] and nanostructured MnO_2 electrodes (~150 F/cm^3) in aqueous electrolytes reported previously[16,35].

Recent studies have shown that carbonyl (C=O) groups can be reduced by Li^+ and reversibly oxidized in the voltage range from ~3.5 to ~1.5 V vs. Li in aromatic carbonyl derivative organic materials such as poly(2,5-dihydroxy-1,4-benzoquinone-3,6-methylene)[36] and $Li_2C_6O_6$[37]. Therefore, it is postulated that the doubled gravimetric

capacitance obtained from lowering the lower voltage limit of Li/LBL-MWNT cells (with open circuit voltages of ~3.2 V) from 3.0 to 1.5 V vs. Li can be attributed to the Faradaic reactions of surface oxygen on LBL-MWNTs, such as $C{=}O_{LBL\text{-}MWNT} + Li^+ + e^- \leftrightarrow C\text{-}OLi_{LBL\text{-}MWNT}$, which can become accessible at voltages lower than ~3 V vs. Li.

The contribution of surface functional groups to the high energy storage densities of LBL-MWNTs was further confirmed by comparing the specific capacitance of LBL-MWNTs before and after exposure to 4 % H_2 and 96 % Ar by volume at 500 °C for 10 hours. Gravimetric current and capacitance values of the LBL-MWNT electrode decreased considerably (by 40%) after this heat-treatment, as shown in Fig. 3-6b. XPS analysis showed that this high-temperature heat-treatment decreased the amount of surface oxygen and nitrogen functional groups on MWNTs.. The intensities of distinct C 1s peaks, which were assigned to carbon atoms in C-N[39] or C-O[38] centered at 285.9 ± 0.1 eV, carbonyl C=O[27,38] groups at 286.7 ± 0.1 eV, and amide N-C=O or carboxylic COOR groups at 288.4 ± 0.1 eV[39], was reduced greatly (by ~70 %) relative to those of sp^2 (284.5 eV) and sp^3 (285.2 eV) hybridized carbon[38] after the heat-treatment, as shown in Fig. 3-6c. Therefore, this experiment provides further evidence that the redox of surface oxygen and nitrogen functional groups with lithium ions are responsible for the large gravimetric capacitance of LBL-MWNT electrodes in organic electrolytes.

We show that MWNT surfaces and surface functional groups on MWNTs are better utilized in LBL-MWNT electrodes than composite electrodes. The capacitance normalized to MWNT weight for LBL-MWNT electrodes is 2.5 times higher than those of conventional composite electrodes consisting of 80 wt% functionalized MWNTs and 20 wt% binder, as shown in Fig. 3-6d. Considering MWNT-COOH and MWNT-NH_2 in the composite electrodes have similar ratios of carbon to oxygen atomic percentages to LBL electrodes (Table 6-1), this result suggests that LBL-MWNT electrodes can allow better utilization of MWNT surface relative to composite MWNT electrodes with binder, which can reduce ion adsorption and redox of surface functional groups by covering the surface of nanotubes. In addition, the gain in the capacitance normalized to electrode weight for LBL-MWNT (MWNT only) relative to composite electrodes is even higher (~3 times). More

interestingly, it should be mentioned that the advantage in the volumetric capacitance (~5 times) of LBL-MWNT electrodes over composite MWNT electrodes is far greater than that in gravimetric capacitance due to a higher electrode density (0.83 g/cm^3 for LBL-MWNT vs. 0.45 g/cm^3 for composite electrodes).

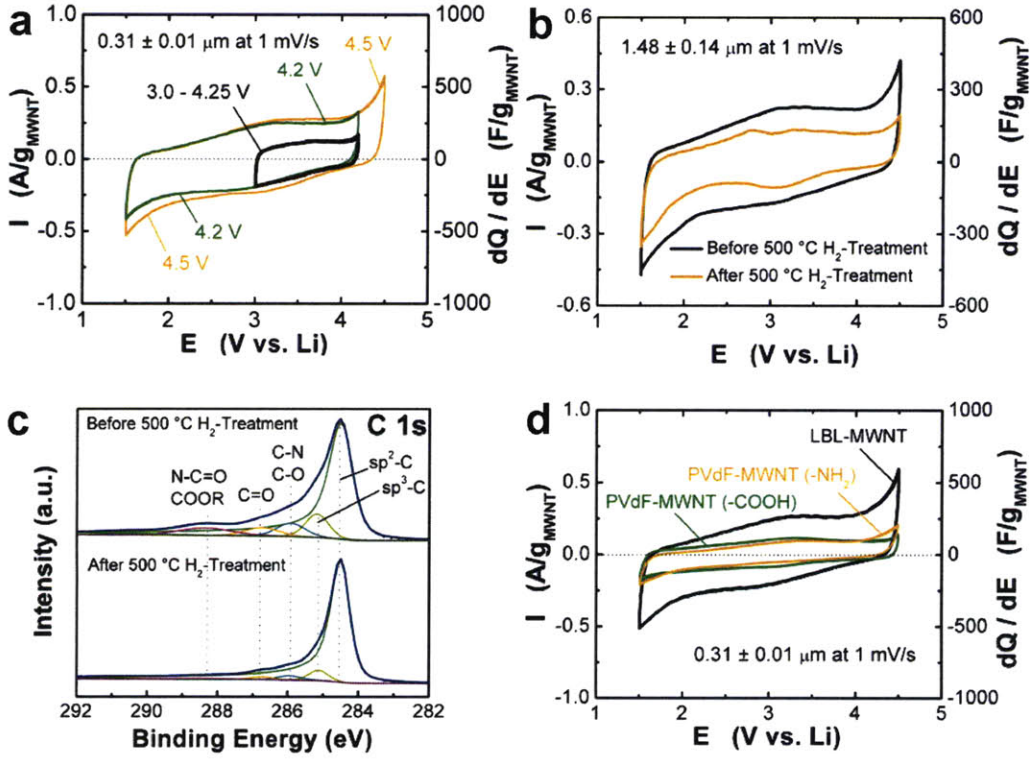

Figure 3-6. Potential-dependent electrochemical behavior of LBL-MWNT and functionalized MWNT composite electrodes measured in two-electrode lithium cells. a, Cyclic voltammogram data of an LBL-MWNT electrode obtained with different upper- and lower-potential limits. Reducing the lower-potential limit from 3 V to 1.5 V vs. Li resulted in increased current and gravimetric capacitance. **b,** Cyclic voltammogram data of an LBL-MWNT electrode before and after the 500 °C H_2-treatment in 4% H_2 and 96% Ar by volume for 10 hours. **c,** XPS C 1s spectra of an LBL-MWNT electrode before and after this additional heat-treatment, which is shown to remove a considerable amount of surface oxygen and nitrogen functional groups on the MWNT surface. **d,** Cyclic voltammogram

data of an LBL-MWNT electrode and composite electrodes of MWNT-COOH and MWNT-NH_2, where the LBL-MWNT electrode has higher current and capacitance normalized to the MWNT weight than composite electrodes. The composite electrodes consisted of 20 wt% PVDF and 80 wt% MWNT-COOH or MWNT-NH_2. Composite MWNT electrodes were prepared from slurry casting and dried at 100 °C for 12 hours under vacuum. The thickness of the LBL-MWNT electrode was 0.3 μm, and those of MWNT-COOH and MWNT-NH_2 composite electrodes are 50 and 30 μm, respectively. The density of composite electrodes was ~0.45 g/cm^3.

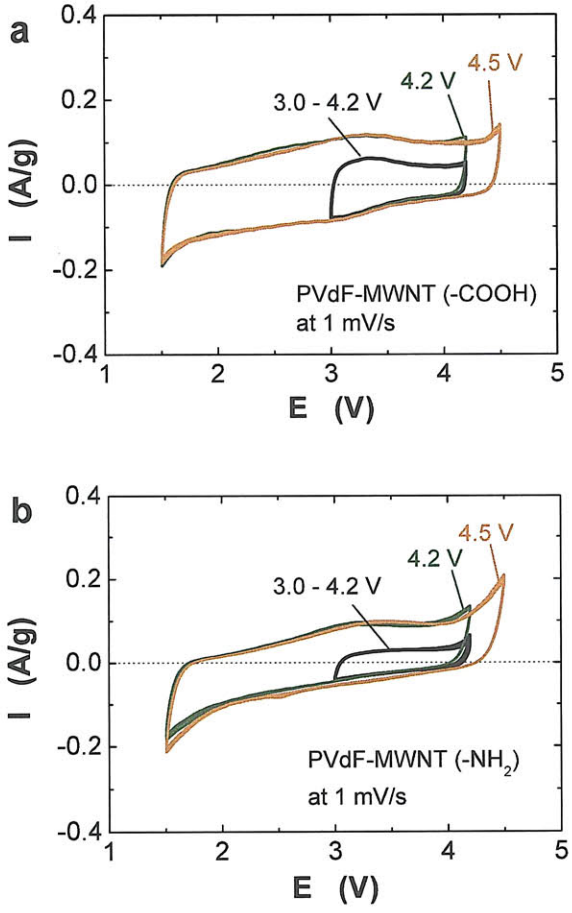

Figure 3-7. Cyclic voltammograms of conventional PVdF composite electrodes consisting of **a,** MWNT-COOH powder and **b,** MWNT-NH_2 powder collected at 1 mV/s

with different lower- and upper-potential limits. Similar to LBL-MWNT electrodes, narrowing the voltage window to 3.0 – 4.2 V vs. Li resulted in lower specific currents and capacitance values for composite MWNT-COOH and MWNT-NH_2 electrodes.

	Relative Atomic Ratio of C, O, and N		
	MWNT-COOH	**MWNT-NH_2**	**LBL Electrode**
O/C	**0.11**	**0.18**	**0.12**
N/C		**0.11**	**0.04**

Faradaic reactions of surface oxygen on LBL-MWNT: $C{=}O + Li^+ + e^- \leftrightarrow C\text{-}OLi$

Chemical composition of LBL Electrode: $C_{0.85}O_{0.11}N_{0.04}$

Estimated Capacity: $\frac{0.11 \times 96500(A \cdot \text{sec}/mol)}{12.52(g/mol) \times 3600(\text{sec}/hr)} = 236 mAh/g$

Table 3-1. Relative surface atomic ratio of C, O and N on functionalized MWNTs (MWNT-COOH and MWNT-NH_2) and a representative LBL-MWNT electrode after the heat-treatments, where were obtained from XPS data analysis. The estimated specific capacity based on the chemical formula ($C_{0.85}O_{0.11}N_{0.04}$) of LBL-MWNT and proposed Faradaic reactions betweens oxygen in the surface functional groups and Li ions is in good agreement with experimental results (Fig. 3-8c).

The energy stored in LBL-MWNT electrodes in lithium cells increases linearly with electrode thickness from increasing currents and charge from cyclic voltammetry measurements (Fig. 3-8a and inset). For a given thickness, the current at ~3 V was found to increase linearly with sweep rate, indicating a surface-redox limited process (Fig. 3-8b), which is in good agreement with the proposed mechanism of redox of functional groups and ion adsorption on MWNT surfaces. Storing energy on the surfaces of MWNTs enables

LBL-MWNT electrodes to have a high rate capability, which was demonstrated using galvanostatic measurements allowing direct comparison with the performance of high-power battery materials. Gravimetric capacity of 0.3 μm electrodes was ~200 mAh/g at low rates such as 0.4 A/g, which is in good agreement with the estimated capacity of LBL-MWNT electrodes based on the proposed Faradaic reaction between Li and surface oxygen ($C_{0.85}O_{0.11}N_{0.04}$) measured from XPS (Table 3-1). Half of the gravimetric capacity (100 mAh/g) was retained at exceptionally high discharge rates of ~180 A/g (corresponding to full discharge in less than 2 seconds), as shown in Fig. 3-8c.

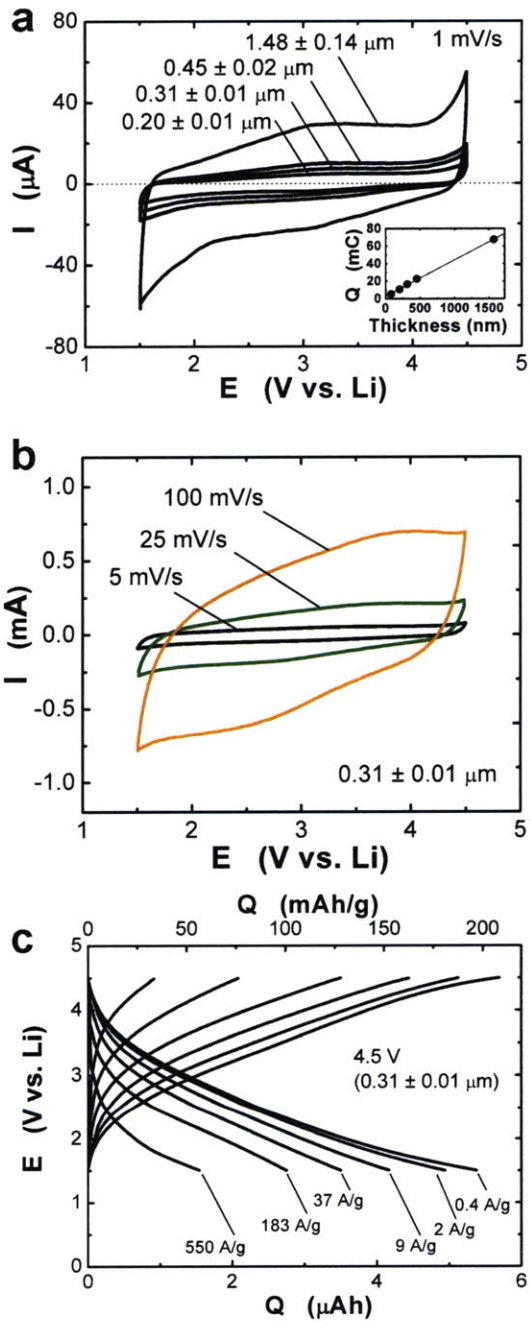

Figure 3-8. Electrochemical characteristics of LBL-MWNT electrodes in two-electrode lithium cells with 1 M $LiPF_6$ in a mixture of ethylene carbonate and dimethyl carbonate (volume ratio 3:7). a, Cyclic voltammogram data from electrodes with different thicknesses collected at a scanning rate of 1 mV/s in the voltage range from

1.5 to 4.5 V vs. Li. The integrated charge increases linearly with electrode thickness, as shown in the figure inset. **b,** Cyclic voltammogram data of a 0.3 μm LBL-MWNT electrode over a range of scan rates. **c,** Charge and discharge profiles of an electrode of 0.3 μm obtained over a wide range of gravimetric current densities between 1.5 V and 4.5 V vs. Li. Before each charge and discharge measurement for the data in Fig. 3-8c, cells were held at 1.5 V and 4.5 V for 30 min, respectively. It should be mentioned that the background current from the cell apparatus and ITO coated glass was found to be negligible in comparison to LBL-MWNT electrodes of 0.2 μm thick and greater (Fig. 3-10).

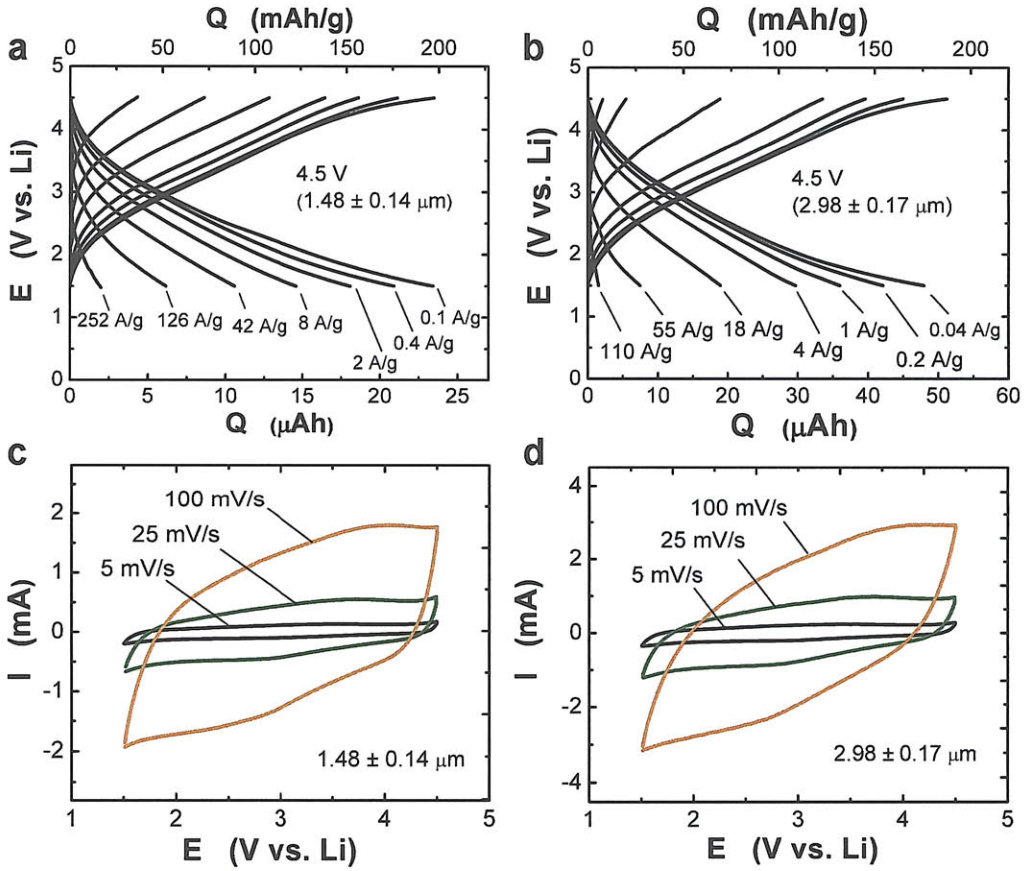

Figure 3-9. Charge and discharge voltages for **a,** 1.5 μm and **b,** 3.0 μm LBL-MWNT electrodes, respectively, obtained over a wide range of specific current densities in the voltage range from 1.5 V to 4.5 V vs. Li. Before each charge and discharge measurement,

cells were held at 1.5 V and 4.5 V for 30 min, respectively. Cyclic voltammogram data of **c,** 1.5 μm and **d,** 3.0 μm LBL-MWNT electrodes, respectively, over a range of scan rates.

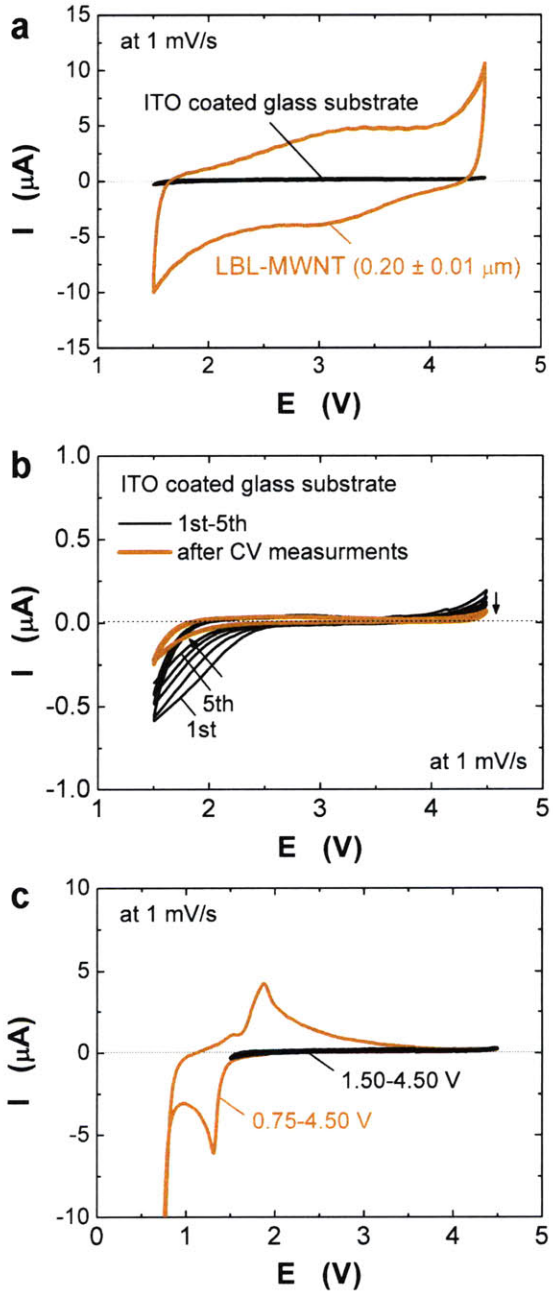

Figure 3-10. Background current of the cells with and without LBL-MWNT samples. **a,** Cyclic voltammogram data of ITO coated glass with and without an LBL-MWNT electrode (0.2 μm) collected at 1 mV/s, where significantly higher currents were noted for the LBL-

MWNT electrode. **b,** Background current of the Li/ITO-coated-on-glass cell was found to reduce during cycling at 1 mV/s. The data in orange are identical to the ITO-background current shown in Figure S8a. **c,** Electrochemical stability of ITO-coated glass measured in a two-electrode lithium cell with a Li foil as the counter electrode. The electrolyte was 1 M $LiPF_6$ in a mixture of EC and DMC (3:7 volume ratio). ITO can be reduced below 1.5 V vs. Li, and then be reversibly oxidized. In all of the electrochemical testing performed in this work, the lowest voltage has been set to be 1.5 V vs. Li to eliminate the reduction current from ITO substrate.

3.3.3 Gravimetric energy and power densities, and cycle life of LBL-MWNT

A Ragone plot in Fig. 3-11a shows the specific energy and power of LBL-MWNT electrodes with thicknesses up to 3.0 m, which were utilized in the 1.5 – 4.5 V range. Although the power capability of LBL-MWNT electrodes reduces somewhat with increasing thickness, electrodes of ~3.0 m can still deliver very high gravimetric energy of ~200 $Wh/kg_{electrode}$ at large gravimetric power of ~100 $kW/kg_{electrode}$, based on the single electrode weight alone. At low power, their gravimetric energy (~500 $Wh/kg_{electrode}$) approach those of $LiFePO_4$ and $LiCoO_2$[5,37,40]. At high power (greater than 10 $kW/kg_{electrode}$), LBL-MWNT electrodes show higher gravimetric energy than carbon-nanotube-based electrochemical capacitors (~70 $Wh/kg_{electrode}$ reported by Futeba et al.[25]), nanostructured lithium battery materials[5,13] and carbonyl derivative organic molecules[36,37] in the composite electrodes. Remarkably, at exceptionably high power greater than 100 $kW/kg_{electrode}$, LBL-MWNT electrodes exhibit higher energy than recently reported high-power lithium battery materials[4,41]. It is interesting to note that the volumetric energy densities of LBL-MWNT electrodes at high power (~80 $kW/l_{electrode}$ corresponding to 100 $kW/kg_{electrode}$) are on the order of ~200 $Wh/l_{electrode}$ (Fig. 3-12), which is higher than that of high-power lithium battery electrodes reported recently[4].

LBL-MWNT electrodes can be tested over 1000 cycles without any observable loss, as shown in Fig. 3-11b. Additional cycling of a ~1.5 μm LBL-MWNT electrode show no capacity loss up to 2500 cycles even after the cell was left open circuit for 30 days (Fig. 3-

13). Correspondingly, the voltage profiles in the 1st and 1000th cycles to 4.5 V are nearly unchanged (Figs. 3-11c and 3-14). TEM and XPS analysis of cycled electrodes (1000 cycles to 4.5 V, which was followed by additional 1000 cycles to 4.7 V vs. Li) provided further evidence for the cycling stability, as no distinctive change was noted in the surface atomic structure and surface functional groups after cycling (Fig. 3-15). The stability of functional groups on the MWNTs is remarkable in comparison to considerable losses of carbonyl derivative molecules within 50 to 100 cycles reported recently[36,37,42]. We hypothesize that the cycling stability of LBL-MWNT electrodes can be related to strong chemical covalent bonding of surface functional groups on MWNTs in contrast to gradual separation between active carbonyl groups and carbon additives in the composite electrodes during cycling.

Since a lithium negative electrode is not practical for real applications, we investigated the use of LBL-MWNT electrodes with a fully lithiated $Li_4Ti_5O_{12}$ (LTO) composite electrode. Although the electrode gravimetric energy and power in LTO/LBL-MWNT cells is decreased due to a lower cell voltage (Fig. 3-11d), the rate capability, gravimetric capacity and capacity retention is comparable to cells with the Li negative electrode (Fig. 3-16). More interestingly, while LTO/LBL-MWNT cells show comparable gravimetric energy to LTO/$LiNi_{0.5}Mn_{1.5}O_4$ (Supplementary Information) at low power but they exhibit significantly higher gravimetric energy at power greater than 10 $kW/kg_{electrode}$[21] (Fig. 3-11d and Fig. 3-17). Using a conservative assumption that the mass of the battery is 5 times greater than LBL-MWNT[22], which is higher than 2.5[4] typically used for conventional lithium rechargeable batteries due to reduced electrode thicknesses (such as 3 microns) demonstrated in this study, LTO/LBL-MWNT storage devices are expected to deliver ~30 Wh/kg_{cell} at ~5 kW/kg_{cell}. This value is significantly higher than that of current electrochemical capacitors with gravimetric energy of ~5 Wh/kg_{cell} at ~1 kW/kg_{cell}[1,31].

Finally, symmetrical LBL-MWNT/LBL-MWNT cells (cell voltage varied from 0 V to 3 V; with 1 M $LiPF_6$ in ethylene carbonate and dimethyl carbonate mixture of 3:7 by volume) show comparable power, but have much lower gravimetric energy than Li/LBL-MWNT and LTO/LBL-MWNT cells (Fig. 3-11d). This is expected as symmetric cells

utilize only electrical double-layer capacitance (~95 F/g found in this study, comparable with values of 70-120 F/g reported previously[43]) but cannot access charges associated with the Faradaic reactions of oxygen-and nitrogen-containing surface functional groups on functionalized MWNT.

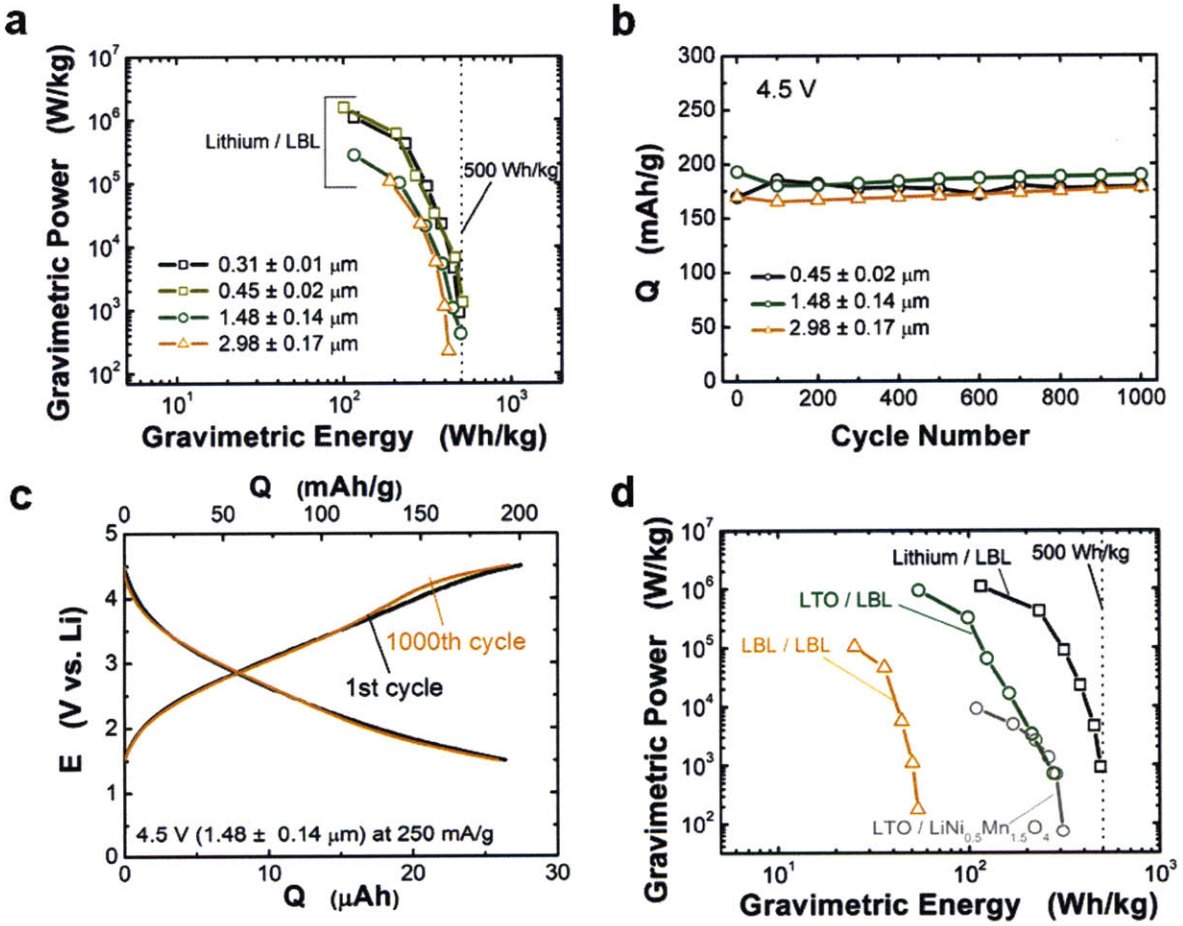

Figure 3-11. Gravimetric energy and power densities, and cycle life of LBL-MWNT electrodes obtained from measurements of two-electrode cells. a, A Ragone plot for Li/LBL-MWNT cells with different thicknesses (0.3 ~ 3.0 μm). Corresponding loading density of LBL-MWNT electrodes ranges from 0.025 ~ 0.25 mg/cm^2. Only the LBL-MWNT weight was considered in the gravimetric energy and power density calculations.

Gravimetric energy and maximum power densities were reduced for the LTO/LBL-MWNT cells subjected to the same testing conditions due to a lower cell voltage. **b,** Gravimetric capacities of a Li/LBL-MWNT cell as a function of cycle number, which were measured at a current density (~0.25 A/g) once every 100 cycles after voltage holds at the end of charge and discharge for 30 min. Within each 100 cycles, these cells were cycled under an accelerated rate of ~2.5 A/g. **c,** The voltage profiles of a 1.5 μm electrode in the 1st and 1000th cycles, where negligible changes were noted. **d,** A Ragone plot for Lithium/LBL-MWNT (black squares), LTO/LBL-MWNT (green circles), LTO/$LiNi_{0.5}Mn_{1.5}O_4$ (gray circles), and LBL-MWNT/LBL-MWNT (orange triangles) cells having 4.5 V vs. Li as the upper-potential limit. The thickness of the LBL-MWNT electrode was 0.3 μm for asymmetric Lithium/LBL-MWNT, LTO/LBL-MWNT, and 0.4 μm for symmetric LBL-MWNT/LBL-MWNT.

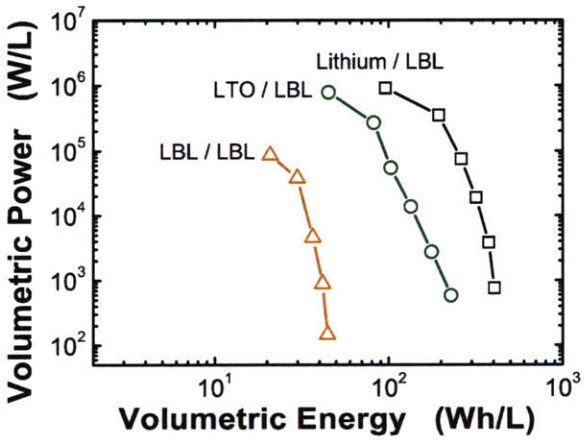

Figure 3-12. Ragone plot based on the unit volume of LBL-MWNT electrodes. The samples used in the graph are the same shown in Fig. 3-11a. It should be noted that the volumetric energy density of LBL-MWNT electrodes, is 2 to 5 times smaller than $LiFePO_4$ and $LiCoO_2$ electrodes due to a lower mass density (~0.8 g/cm^3 for LBL-MWNTs vs. ~4.0 g/cm^3 for composite $LiCoO_2$ electrodes)

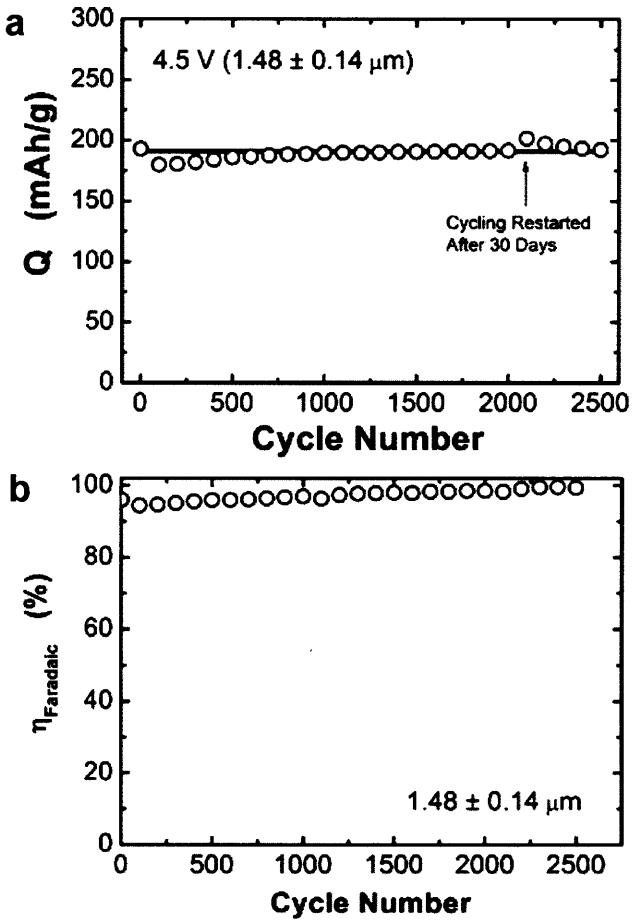

Figure 3-13. a, Cycling of a 1.48 μm LBL-MWNT electrode show that cycling is stable up to 2500 cycles, with no capacity loss even after the cell had been sitting for 30 days unused. **b,** Corresponding Faradaic efficiency (discharge capacity / charge capacity) as a function of cycle number. Capacities were measured at a current density (~0.25 A/g) once every 100 cycles after voltage holds at the end of charge and discharge for 30 min. Within each 100 cycles, these cells were cycled under an accelerated rate of ~2.5 A/g.

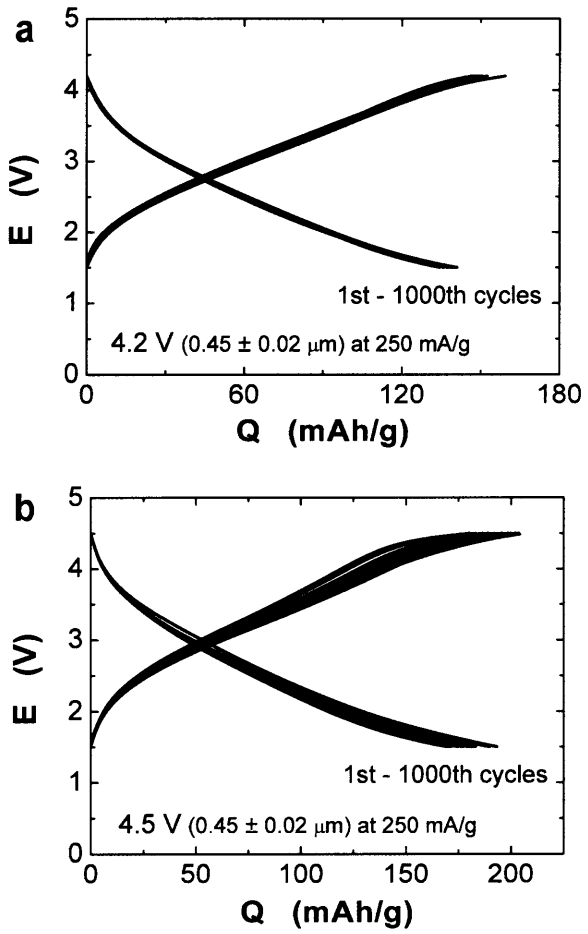

Figure 3-14. The change in the voltage profiles due to accelerated cycling at 2.5 A/g. Charge and discharge voltage curves of LBL-MWNT electrodes upon cycling within the voltage windows of **a,** 1.5 to 4.2 V and **b,** 1.5 to 4.5 V vs. Li. Measurements were obtained at a lower rate of 250 mA/g once every 100 cycles.

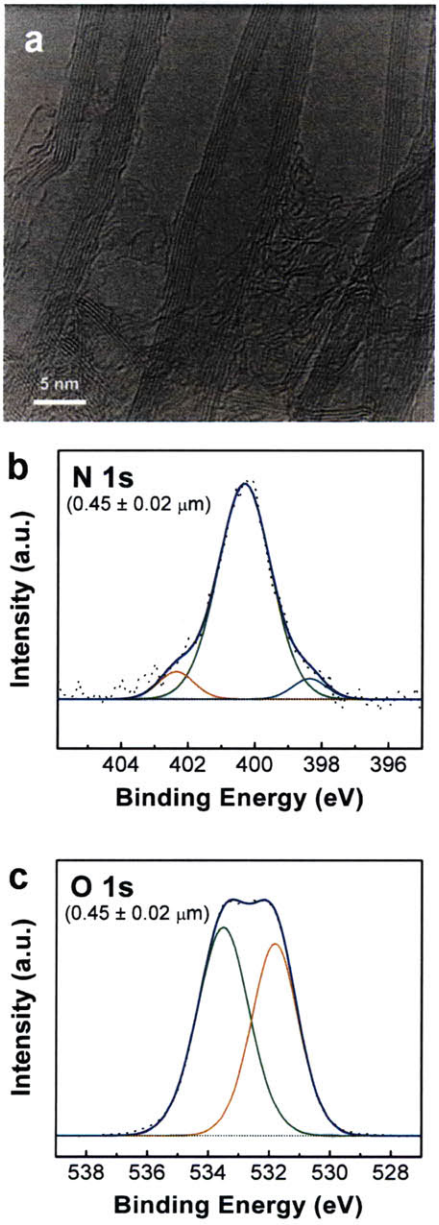

Figure 3-15. Surface morphology and surface functional groups of LBL-MWNT electrodes after cycling in lithium cells. **a,** TEM image, **b,** XPS N 1s and **c,** O 1s peaks of an LBL-MWNT electrode after 2000 cycles (1000 cycles in the region of 1.5 to 4.5 V,

followed by 1000 cycles from 1.5 to 4.7 V vs. Li). No visible change relative to LBL-MWNT electrodes before cycling (Fig. 3-1) was noted.

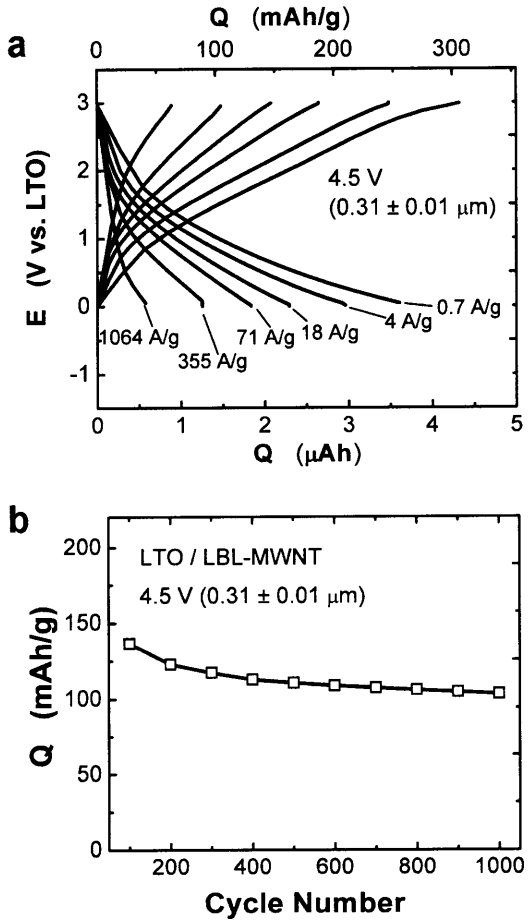

Figure 3-16. Rate capability of LTO/LBL-MWNT hybrid cells. **a,** Charge and discharge voltages were obtained over a wide range of specific current densities for LBL-MWNT electrode thicknesses of 0.3 μm. The voltage range of 0.0 – 3.0 V vs. LTO corresponds to 1.5 – 4.5 V vs. Li. **c,** Specific capacity as a function of cycle number, which was measured at a current density (~0.7 A/g) once every 100 cycles after voltage holds at the end of charge and discharge for 30 min. Within each 100 cycles, these cells were cycled under an accelerated rate of ~2.5 A/g.

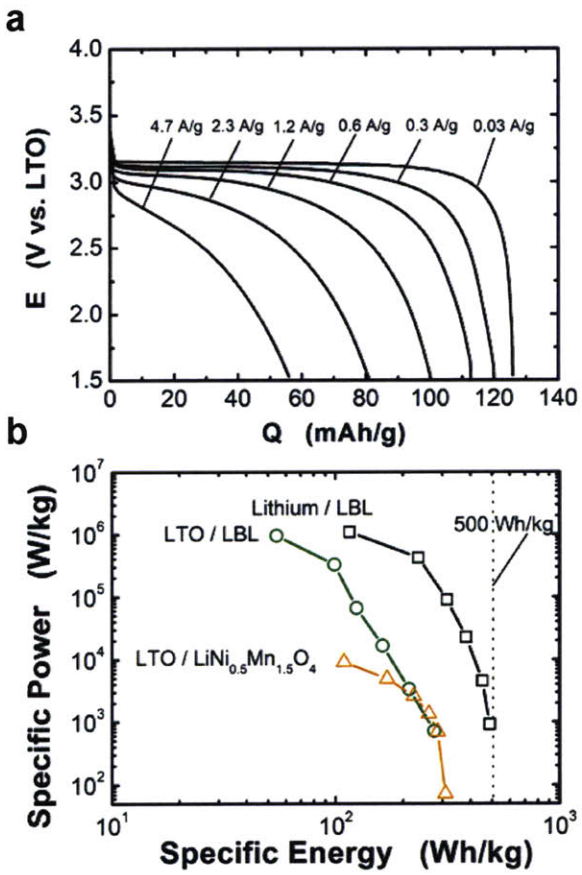

Figure 3-17. a, Charge and discharge profiles of an LTO/$LiNi_{0.5}Mn_{1.5}O_4$ cell obtained at various rates. The specific capacity is normalized to the weight of $LiNi_{0.5}Mn_{1.5}O_4$ as LTO has higher specific capacity (150 mAh/g) than $LiNi_{0.5}Mn_{1.5}O_4$ (~120 mAh/g), and cell capacity is limited by the capacity of $LiNi_{0.5}Mn_{1.5}O_4$. **b,** A Ragone plot for Li/LBL-MWNT (black squares), LTO/LBL-MWNT (green circles), and LTO/$LiNi_{0.5}Mn_{1.5}O_4$ (orange triangles) electrode. Only positive electrode weight was considered in the specific energy and power density calculations. The $LiNi_{0.5}Mn_{1.5}O_4$ electrode formulation is active material (80 wt%), SUPER-P® carbon black (10 wt%) and polyvinylidene fluoride (PVdF) binder (10 wt%). Specific power and energy is identical to gravimetric power and energy.

3.4 Conclusion

In summary, LBL-MWNT electrodes, which are conformal, densely packed and additive-free, can exhibit gravimetric energy up to ~200 $Wh/kg_{electrode}$ at gravimetric power of ~100 $kW/kg_{electrode}$, where gravimetric energy and power at the cell level can be estimated by dividing these values by a factor of ~5. The energy stored in the LBL-MWNT electrodes can be controlled by the electrode thickness (Figure 3-8a inset) and upper voltage limit (Figure 3-18). Lithium redox reactions with oxygen-and nitrogen-containing surface functional groups on functionalized MWNT electrodes in organic electrolytes are responsible for the observed high energy and power capabilities of LBL-MWNT electrodes. This is in agreement with the fact that symmetric LBL-MWNT/LBL-MWNT cells have relatively lower gravimetric energy, which is comparable to conventional electrochemical capacitors[1,31].

To explain the storage mechanism of LBL-MWNT electrodes at high power, we schematically illustrate the Faradaic reactions between surface oxygen functional species and Li ions on an HRTEM image of the LBL-MWNT electrodes in Fig. 3-19, where surface oxygen functional species can be accessed reversibly at high power as LBL-MWNT electrodes provide good electronic and ionic conduction, and high surface area. Energy and power capabilities of LBL-MWNT electrodes of a few microns in thickness demonstrated in this work open new opportunities for the development of high-performance electrical energy storage for microsystems, flexible and thin-film devices[22].

These LBL-MWNT electrodes could potentially find applications in heavy vehicles and heavy machineries, where the ability to deliver high energy at high power will be an enabling technological development. Large-scale thicker electrodes of tens of microns can be produced by a recently developed sprayed LBL system[44] that utilizes an automated process, which can reduce assembly time dramatically (about 70 times faster than the conventional dipping of LBL systems used in this study). Further research to the present work is needed, namely validating the reported energy and power capabilities of MWNT electrodes with thicknesses on the order of one hundred microns.

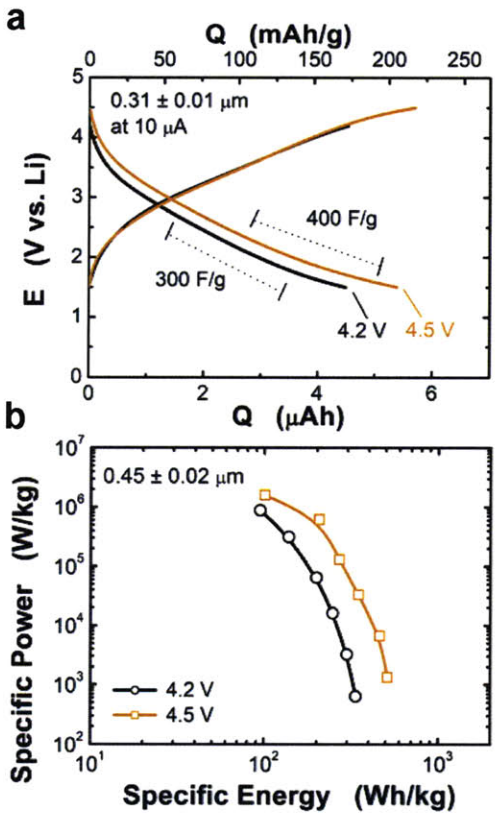

Figure 3-18. a, Charge and discharge voltage profiles of an electrode of 0.3 μm obtained with upper-voltage limits of 4.2 and 4.5 V vs. Li under constant current measurements. **b,** A Ragone plot of electrodes with thickness of 0.5 μm having 4.2 V or 4.5 V vs. Li as the upper-potential limit. Only the LBL-MWNT weight was considered in the specific energy and power calculations. Specific power and energy is identical to gravimetric power and energy.

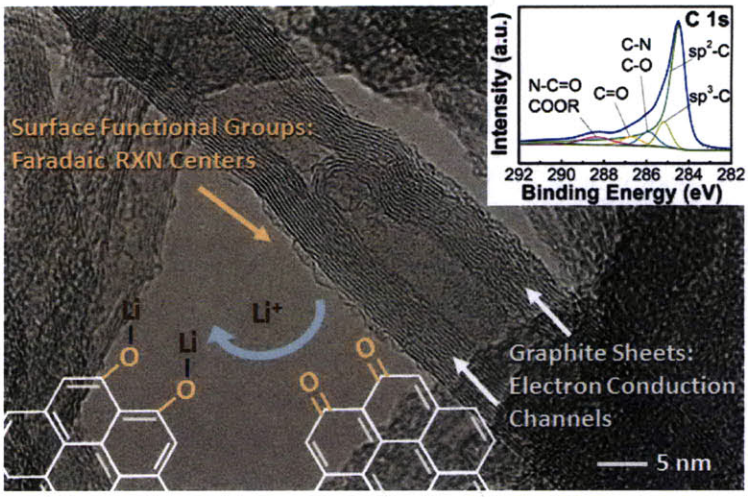

Figure 3-19. Schematic illustration of the energy storage mechanism of LBL-MWNT electrodes. Faradaic reactions between surface oxygen functional species (orange arrows) and Li were schematically illustrated on an HRTEM image of the LBL-MWNT electrodes. XPS C 1s spectra of the LBL-MWNT electrode is shown in the figure inset, which shows various oxygen and nitrogen functional groups on the MWNT surface. Intact graphite layers inside of the MWNTs (white arrows) were indicated as electron conduction channels.

3.5 References

[1] Simon, P. and Gogotsi, Y., Materials for electrochemical capacitors. *Nature Materials* 7, 845-854 (2008).

[2] Miller, J. R. and Simon, P., Materials science - Electrochemical capacitors for energy management. *Science* **321**, 651-652 (2008).

[3] Amatucci, G. G., Badway, F., Du Pasquier, A., and Zheng, T., An asymmetric hybrid nonaqueous energy storage cell. *Journal of the Electrochemical Society* **148**, A930-A939 (2001).

[4] Kang, B. and Ceder, G., Battery materials for ultrafast charging and discharging. *Nature* **458**, 190-193 (2009).

[5] Lee, Y. J. et al., Fabricating Genetically Engineered High-Power Lithium-Ion Batteries Using Multiple Virus Genes. *Science* **324**, 1051-1055 (2009).

[6] Nazar, L. F. et al., Nanostructured materials for energy storage. *International Journal of Inorganic Materials* **3**, 191-200 (2001).

[7] Arico, A. S. et al., Nanostructured materials for advanced energy conversion and storage devices. *Nature Materials* **4**, 366-377 (2005).

[8] Poizot, P. et al., Nano-sized transition-metaloxides as negative-electrode materials for lithium-ion batteries. *Nature* **407**, 496-499 (2000).

[9] Sides, C. R. et al., Nanoscale materials for lithium-ion batteries. *MRS Bulletin* **27**, 604-607 (2002).

[10] Bruce, P. G., Scrosati, B., and Tarascon, J. M., Nanomaterials for rechargeable lithium batteries. *Angewandte Chemie-International Edition* **47**, 2930-2946 (2008).

[11] Tarascon, J. M. and Armand, M., Issues and challenges facing rechargeable lithium batteries. *Nature* **414**, 359-367 (2001).

[12] Armand, M. and Tarascon, J. M., Building better batteries. *Nature* **451**, 652-657 (2008).

[13] Wu, X. L. et al., LiFePO4 Nanoparticles Embedded in a Nanoporous Carbon Matrix: Superior Cathode Material for Electrochemical Energy-Storage Devices. *Adv. Mater.* **21**, 2710-+ (2009).

[14] Chmiola, J. et al., Anomalous increase in carbon capacitance at pore sizes less than 1 nanometer. *Science* **313**, 1760-1763 (2006).

[15] Hu, C. C., Chen, W. C., and Chang, K. H., How to achieve maximum utilization of hydrous ruthenium oxide for supercapacitors. *Journal of the Electrochemical Society* **151**, A281-A290 (2004).

[16] Fischer, A. E. et al., Incorporation of homogeneous, nanoscale MnO2 within ultraporous carbon structures via self-limiting electroless deposition: Implications for electrochemical capacitors. *Nano Letters* **7**, 281-286 (2007).

[17] Reddy, A. L. M., Shaijumon, M. M., Gowda, S. R., and Ajayan, P. M., Coaxial MnO2/Carbon Nanotube Array Electrodes for High-Performance Lithium Batteries. *Nano Letters* **9**, 1002-1006 (2009).

[18] Kim, D. K. et al., Spinel LiMn2O4 Nanorods as Lithium Ion Battery Cathodes. *Nano Letters* **8**, 3948-3952 (2008).

[19] Bélanger, D., Brousse, T., and Long, J. W., Manganese oxides: battery materials make the leap to electrochemical capacitors. *The electrochemical Society Interface* **17**, 49 (2008).

[20] Decher, G., Fuzzy nanoassemblies: Toward layered polymeric multicomposites. *Science* **277**, 1232-1237 (1997).

[21] Xiang, H. F. et al., Effect of capacity matchup in the LiNi0.5Mn1.5O4/Li4Ti5O12 cells. *Journal of Power Sources* **183**, 355-360 (2008).

[22] Dudney, J. N., Thin film micro-batteries. *The Electrochemical Society Interface* **17**, 44 (2008).

[23] Lee, Seung Woo et al., Layer-by-Layer Assembly of All Carbon Nanotube Ultrathin Films for Electrochemical Applications. *Journal of the American Chemical Society* **131**, 671-679 (2009).

[24] Niu, C. M. et al., High power electrochemical capacitors based on carbon nanotube electrodes. *Appl. Phys. Lett.* **70**, 1480-1482 (1997).

[25] Futaba, D. N. et al., Shape-engineerable and highly densely packed single-walled carbon nanotubes and their application as super-capacitor electrodes. *Nature Materials* **5**, 987-994 (2006).

[26] Zielke, U., Huttinger, K. J., and Hoffman, W. P., Surface-oxidized carbon fibers .1. Surface structure and chemistry. *Carbon* **34**, 983-998 (1996).

[27] Kozlowski, C. and Sherwood, P. M. A., X-RAY PHOTOELECTRON-SPECTROSCOPIC STUDIES OF CARBON-FIBRE SURFACES .5. THE EFFECT OF PH ON SURFACE OXIDATION. *Journal of the Chemical Society-Faraday Transactions I* **81**, 2745-2756 (1985).

[28] Frackowiak, E. et al., Electrochemical storage of lithium multiwalled carbon nanotubes. *Carbon* **37**, 61-69 (1999).

[29] Burg, P. et al., The characterization of nitrogen-enriched activated carbons by IR, XPS and LSER methods. *Carbon* **40**, 1521-1531 (2002).

[30] Lota, G. et al., Effect of nitrogen in carbon electrode on the supercapacitor performance. *Chem. Phys. Lett.* **404**, 53-58 (2005).

[31] Simon, P. and Burke, A., Nanostructured carbons: double-layer capacitance and more. *The Electrochemical Society Interface* **17**, 49 (2008).

[32] Chmiola, J., Yushin, G., Dash, R., and Gogotsi, Y., Effect of pore size and surface area of carbide derived carbons on specific capacitance. *Journal of Power Sources* **158**, 765-772 (2006).

[33] Naoi, K. and Simon, P. , New materials and new configurations for advanced electrochemical capacitors. *The Electrochemical Society Interface* **17**, 34 (2008).

[34] Ma, S. B. et al., Electrochemical properties of manganese oxide coated onto carbon nanotubes for energy-storage applications. *Journal of Power Sources* **178**, 483-489 (2008).

[35] Fischer, A. E. et al., Electroless deposition of nanoscale MnO2 on ultraporous carbon nanoarchitectures: Correlation of evolving pore-solid structure and electrochemical performance. *Journal of the Electrochemical Society* **155**, A246-A252 (2008).

[36] Le Gall, T., Reiman, K. H., Grossel, M. C., and Owen, J. R., Poly(2,5-dihydroxy-1,4-benzoquinone-3,6-methylene): a new organic polymer as positive electrode material for rechargeable lithium batteries. *Journal of Power Sources* **119**, 316-320 (2003).

[37] Chen, H. et al., From biomass to a renewable LixC6O6 organic electrode for sustainable Li-ion batteries. *ChemSusChem* **1**, 348-355 (2008).

[38] Ago, H. et al., Work functions and surface functional groups of multiwall carbon nanotubes. *J. Phys. Chem. B* **103**, 8116-8121 (1999).

[39] Ramanathan, T., Fisher, F. T., Ruoff, R. S., and Brinson, L. C., Amino-functionalized carbon nanotubes for binding to polymers and biological systems. *Chem. Mat.* **17**, 1290-1295 (2005).

[40] Whittingham, M. S., Lithium batteries and cathode materials. *Chem. Rev.* **104**, 4271-4301 (2004).

[41] Kang, K. S. et al., Electrodes with high power and high capacity for rechargeable lithium batteries. *Science* **311**, 977-980 (2006).

[42] Chen, H. Y. et al., Lithium Salt of Tetrahydroxybenzoquinone: Toward the Development of a Sustainable Li-Ion Battery. *Journal of the American Chemical Society* **131**, 8984-8988 (2009).

[43] Frackowiak, E. and Beguin, F., Carbon materials for the electrochemical storage of energy in capacitors. *Carbon* **39**, 937-950 (2001).

[44] Krogman, K. C., Zacharia, N. S., Schroeder, S., and Hammond, P. T., Automated process for improved uniformity and versatility of layer-by-layer deposition. *Langmuir* **23**, 3137-3141 (2007).

Chapter 4. Carbon Nanotube/Manganese Oxide Ultrathin Film Electrodes for Electrochemical Capacitors

Portions of this chapter are reprinted from Seung Woo Lee, Junhyung Kim, Shuo Chen, Paula T. Hammond, Yang Shao-Horn, *manuscript in preparation.*

Abstract

Multiwall carbon nanotube (MWNT)/manganese oxide (MnO_2) nano-composite ultrathin film electrodes have been created via redox deposition of MnO_2 on layer-by-layer (LbL) assembled MWNT films. We demonstrate that these layer-by-layer assembled MWNT (LbL-MWNT)/MnO_2 thin films consist of a uniform coating of nano-sized MnO_2 on the MWNT network structure using SEM and TEM, which is a promising structure for electrochemical capacitor applications. LbL-MWNT/MnO_2 electrodes yield a significantly higher volumetric capacitance of 246 F/cm^3 with good capacity retention up to 1,000 mV/s due to rapid transport of electrons and ions within the electrodes. The electrodes are generated with two simple aqueous deposition processes: the layer-by-layer assembly of MWNTs followed by redox deposition of MnO_2 at ambient conditions, thus providing a straightforward approach to the fabrication of high power and energy electrochemical capacitors with precise control of electrode thickness at nano-meter scales.

4. 1 Introduction

Electrochemical capacitors (ECs), sometimes called supercapacitors or ultracapacitors, are electrical energy storage devices for various high power applications such as hybrid electric vehicles and load-leveling.[1, 2] Due to the fast charge storage mechanism of double layer capacitance, which is confined to the interface between the electrode and an electrolyte,

ECs have higher power density (~10 kw/kg), but exhibit a lower energy density (~5 wh/kg) than batteries[2]. However, applications such as hybrid electric vehicles and load-leveling demand significant increases in both energy and power density of electrochemical capacitors to meet their performance and cost requirements.[2, 3]

Conventional electrochemical capacitors generated with state-of-the-art electrode materials such as high surface area carbon[2, 4-6] including activated carbon, carbon aerogel, and carbon nanotubes[7] have stored energy densities measured in specific capacitance on the order of ~100 F/g and ~50 F/cm^3,[4, 8, 9] which linearly scales with electrical double layer capacitance (EDLC) in ~20 $microF/cm^2_{carbon}$ and electrochemically active surface area. It is very challenging to further increase the specific and volumetric capacitances of such electrodes due to difficulties in controlling pore size, electrochemically active surface area and surface chemistry. To increase the energy densities of electrochemical capacitorss, metal oxides that undergo fast surface redox (pseudo-capacitive) reactions are employed. Ruthenium oxide, RuO_2, shows a high specific capacitance of ~720 F/g[10, 11] in acidic electrolytes due to its high electrical conductivity and pseudocapacitance with protons; however, it also suffers from high cost. On the other hand, because of its low cost and toxicity, manganese oxides such as MnO_2, which have a long history as positive electrode materials for batteries,[12] have recently attracted attention as promising materials for the enhancement of the energy density of electrochemical capacitorss.[13] The theoretical specific capacitance of MnO_2 is ~1370 F/g_{MnO2} based on a one-electron redox reaction per manganese atom,[14] but this value can be achieved only for ultrathin (on the nanometer scale) films or nano-sized particles at the typical power required for electrochemical capacitor applications.[13, 14] However, getting sufficient electron access to MnO_2, with its low electrical conductivity (10^{-5}~10^{-6} S/cm)[13], can become rate-limiting for high power applications. Therefore, maximizing utilization of MnO_2 pseudocapacity and designing highly electrically conductive electrode microstructures is critical to realize MnO_2-based electrochemical capacitors.

One promising approach is the incorporation of nano-sized MnO_2 into an electrically conductive carbon framework,[2] improving the utilization of MnO_2 and

electrical conductivity of the electrode. These carbon matrix/metal oxide nano-composite electrodes have been demonstrated with various kinds of carbons, including carbon nanotubes,[15-20] carbon nanofoams,[21, 22]and activated carbon,[23, 24] showing a significant increase in performance. The key issues of carbon matrix/MnO_2 are conformal coatings of nano-sized MnO_2 onto a carbon matrix, enabling full utilization of MnO_2, and an inter-connected 3D porous network structure that ensures fast electronic and ionic conduction through the electrode. With optimized nano-composite structures, we can fully utilize the high energy density of MnO_2 at high power density for real electrochemical capacitor applications.

Previously, we have created ultrathin multiwall carbon nanotube films using layer-by-layer (LbL) assembly[25] with surface functionalized MWNTs.[26] These layer-by-layer assembled MWNT (LbL-MWNT) thin films have interconnected 3D porous network structures, and show high capacitance (~130 F/cm^3) in acidic electrolytes.[26] The porous structure of LbL-MWNT films allows further incorporation of electrochemically active nanomaterials that can increase energy density of electrochemical capacitors. In particular, this approach can significantly increase energy density based on volume when nano-scale materials are used to fill the void volume of the carbon matrix. However, generating a homogenous conformal coating of nano-scale materials within the compact ultrathin MWNT matrix can be challenging. In this study, we incorporate nano-scale MnO_2 films into LbL-MWNT films (Scheme 4-1), and the resulting LbL-MWNT/MnO_2 composite electrodes show a considerably high volumetric capacitance of ~246 F/cm^3 in neutral electrolytes. We show that the structure of the LbL-MWNT/MnO_2 composite electrodes consists of a nano-scale conformal coating of MnO_2 on interconnected MWNTs in a radom network structure using scanning electron microscopy (SEM), and high resolution transmission electron microscopy (TEM). Cyclic voltammetry measurements reveal that these LbL-MWNT/MnO_2 composite electrodes have high specific capacitance even at extremely high scan rates (up to 1,000 mV/s), which can be attributed to the presence of pseudo-capacitive MnO_2 nanoparticles connected to the electrically conductive MWNTs. Finally, we demonstrate the unique advantages of LbL processing, which include the

precise control of thickness on the nanometer scale, which enables pin point control of electrode capacity with thickness in the range of ~100 to ~350 nm.

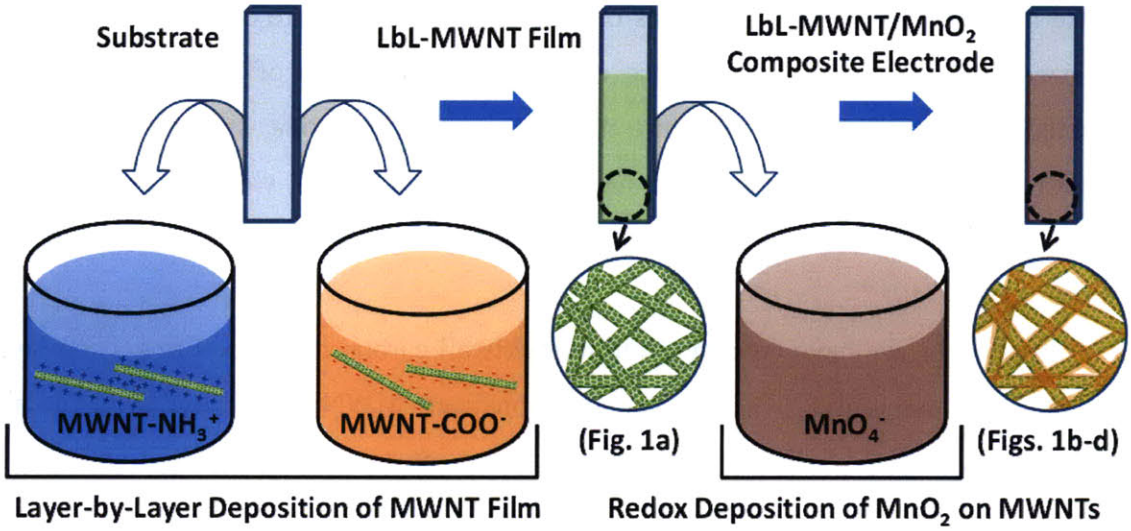

Scheme 4-1. Layer-by-layer assembly of MWNT (LbL-MWNT) film via alternative dipping of substrate into positively charged ($MWNT\text{-}NH_3^+$) and negatively charged ($MWNT\text{-}COO^-$) MWNTs, and process of LbL-MWNT/MnO_2 composite electrode though dipping of the LBLLbL-MWNT film into permanganate ion (MnO_4^-) solution.

4.2 Experimental Section

Layer-by-Layer Assembly of MWNT Thin Films. MWNTs were purchased from NANOLAB (95% purity, outer diameter 15 ± 5 nm, length 1~5 μm). Positively charged MWNTs ($MWNT\text{-}NH_3^+$) and negatively charged MWNTs ($MWNT\text{-}COO^-$) were prepared using surface functionalization processes described in previous research.[26] The LbL-MWNT films were fabricated with a modified Carl Zeiss DS50 programmable slide stainer on indium-tin oxide (ITO) coated glass slides (Delta Technologies). ITO coated glass slides were first dipped into a $MWNT\text{-}NH_3^+$ solution for 30 minutes, and washed in three baths of Milli-Q water for 2, 1, 1 minutes each to remove weakly adsorbed MWNTs. Then, the

substrates were dipped into a MWNT-COO^- solution for 30 minutes, and three baths of Milli-Q water for 2, 1, 1 minutes each. This cycle makes one bilayer of MWNT-NH_3^+/MWNT-COO^-, and the cycle was repeated to reach the desired thickness of MWNT thin films. In this study, we control the thickness of LbL-MWNT films from 110 nm to 350 nm. Detailed procedure and property of LbL-MWNT films can be found at previous research.[26]

Incorporation of MnO_2 into LbL-MWNT Films. Previous studies have showed that spontaneous redox deposition of MnO_2 on carbon materials is pH dependent.[18, 21] Reduction of permanganate ion (MnO_4^-) to MnO_2 on the carbon in acid can result in large agglomerated particles of MnO_2.[15, 21] On the other hand, thin films of MnO_2 can be obtained on the surface of carbon in neutral pHs, which show higher gravimetric capacitance compared to those of MnO_2 formed in acid.[21, 22] In this study, we dipped the LbL-MWNT films into 0.1 M K_2SO_4 (Sigma-Aldrich) + 0.1 M $KMnO_4$ (Sigma-Aldrich) solution from 10 to 60 minutes to incorporate MnO_2 in neutral condition. To facilitate MnO_4^- diffusion into the LbL-MWNT films, and solutions were stirred vigorously with magnetic stirrer.

Characterization. The thickness of electrodes was determined by averaging the thickness at least four different positions on each electrode using a Tencor P-10 profilometer. The volume of electrode was estimated by multiplying the geometric area of the electrode and measured average thickness. Inductively coupled plasma-atomic emission spectroscopy (ICP-AES) analysis was used to analyze the weight loading of MnO_2 on the MWNTs using a Horiba-Activa instrument; the measurements were made on emission peaks at 293.306 for Mn. The LbL-MWNT/MnO_2 film sample was dissolved in concentrated aqua regia and then diluted. The diluted solution was filtrated for analysis. Calibration curves were made from dissolved standards with concentrations from 0 to 25 ppm in the same acid matrix as the unknown. Micro-structure of LbL-MWNT/MnO_2 electrode was investigated using a scanning electron microscope (JEOL 6320 SEM) operating at 5.0 kV. For X-ray energy dispersive spectroscopy (EDS) with SEM, the accelerating voltage is set at 15.0 kV. The acquisition time is 354 s. Inner-structure of LbL-MWNT/MnO_2 electrode was examined

using a transmittance electron microscope (JEOL 2010F) for medium and high resolution imaging, as well as the select area electron diffraction (SAED) of the electrode samples. Scanning transmission electron microscopy mode is applied for EDS mapping. The acquisition time is 279 s. Oxygen K_{a1} (0.525 keV), carbon K_{a1} (0.285 keV), and manganese K_{a1} (5.899 keV) lines are used to generate the elemental maps of oxygen, carbon, and manganese, respectively. The surface chemistry of LbL-MWNT/MnO_2 electrode was investigated using a Kratos AXIS Ultra Imaging X-ray photoelectron spectrometer (XPS). Mn 3s and 2p spectra were calibrated with the C 1s photoemission peak for sp_2 hybridized carbons centered at 284.5 eV. The atomic ratio of manganese to carbon (Mn/C) was determined from XPS high resolution scan analysis. Electrochemical test of LbL-MWNT/MnO_2 electrode was measured at a three-electrode cell, using a saturated calomel electrode (SCE) (Analytical Sensor, Inc.) and Pt wire as the reference and counter electrodes, respectively. LbL-MWNT/MnO_2 electrodes were used as the working electrode in 0.1 M K_2SO_4 solution. Cyclic voltammetry was measured in the potential range between -0.5 and 0.8 V versus SCE at room temperature at various scan rates from 10 to 10,000 mV/s using a bipotentiostat (PINE instrument).

4.3 Results and Discussion

Ultrathin LbL-MWNT films were created by alternating adsorption of positively charged MWNTs (MWNT-NH_3^+) and negatively charged MWNTs (MWNT-COO^-) on ITO-coated glass substrates. By simply controlling the number of dipping cycles (the number of bilayers), we can precisely assemble pure MWNT films on the substrate with thicknesses in the range from 100 to 300 nm. To increase the mechanical stability and electrical conductivity of the electrodes, LbL-MWNTs were heat treated at 150 °C for 12 hr in vacuum[26] before the incorporation of MnO_2. Heat-treated LbL-MWNT films were dipped into a stirred 0.1 M $KMnO_4$/0.1 M K_2SO_4 solution for 10 ~ 60 min to incorporate MnO_2 at room temperature. When LbL-MWNT films were dipped into a solution of permanganate ions (MnO_4^-), a strong oxidizing agent, were spontaneously reduced to MnO_2 on the surface of MWNTs.[18, 21] Increases in both thickness and mass of the electrodes after

incorporation of MnO_2 were observed via profilometry and inductively coupled plasma-atomic emission spectroscopy (ICP-AES) analysis: ~10% of thickness (~17% of mass) after 30 min dipping and ~ 20% of thickness (~36% of mass) after 60 min dipping. Because the LbL assembly process is water-based assembly at ambient conditions, we can consider the spontaneous aqueous deposition of MnO_2 into LbL-MWNT films as a last step of the dipping process, which maintains the continuous nature of the film assembly process.

4.3.1 Microstructure of LbL-MWNT/MnO_2 composite electrodes

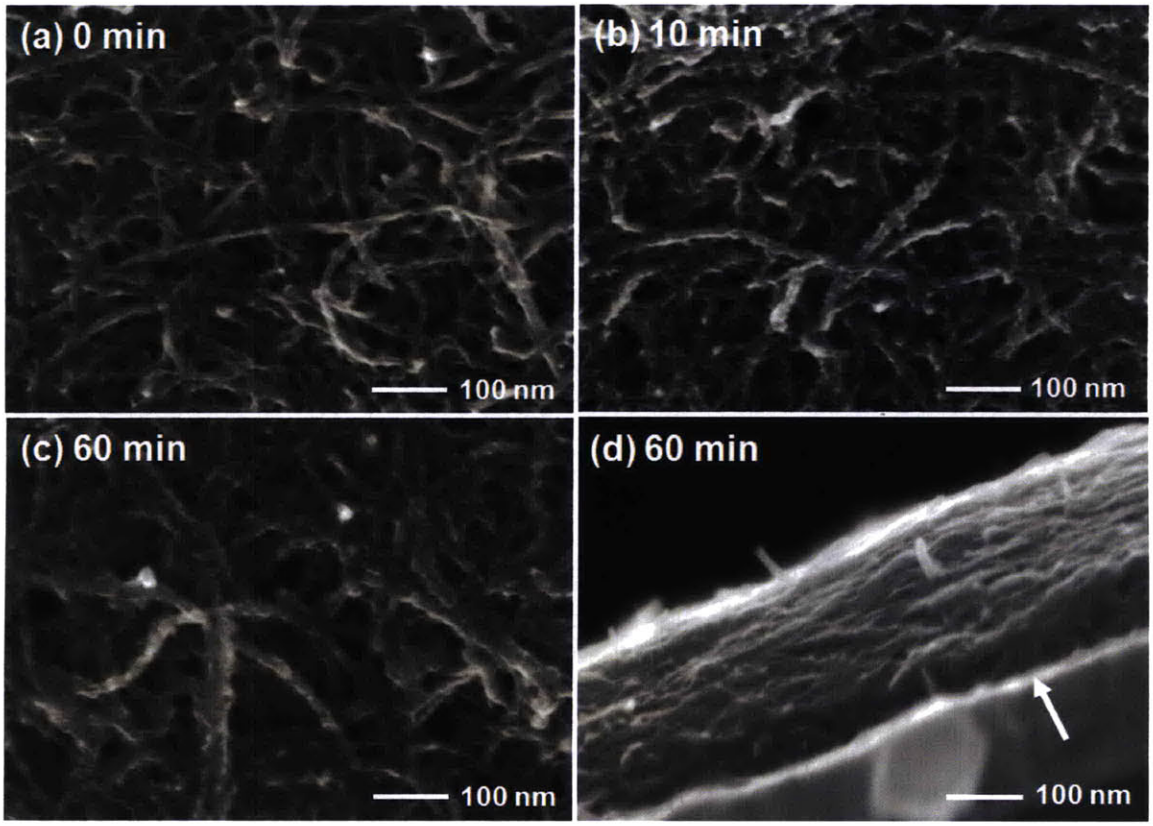

Figure 4-1. SEM images of (a) pristine LbL-MWNT electrode and (b-d) LbL-MWNT/MnO_2 composite electrodes prepared by dipping LbL-MWNT electrodes into 0.1 M $KMnO_4$/0.1 M K_2SO_4 solution at deposition time from 10 min to 60 min. (d) A cross-section view of an LbL-MWNT/MnO_2 composite electrode after 60min dipping. White arrow indicates the interface between the substrate and LbL-MWNT/MnO_2 composite film.

SEM images (Figure 4-1) show MnO_2-covered MWNTs created by the spontaneous reduction process, of LbL-MWNT films. As-assembled LbL-MWNT films have porous network structure of MWNTs (Figure 4-1a), where void volume within porous MWNT matrix allows MnO_4^- ions to diffuse into the films and be reduced to MnO_2 on the surface of MWNTs. From dipping of LbL-MWNT film into $KMnO_4$ solution for 10 min, we can clearly see a uniform coating of MnO_2 on the MWNT surfaces (Figure 4-1b), and the thickness of this MnO_2 coating increases as dipping time increases as indicated by the increasing tube diameters observed in SEM(Figures 4-1b-c). These SEM top-view images confirm that LbL-MWNT/MnO_2 electrodes have no large agglomerates or precipitation of MnO_2 on the exterior film surface, and still maintain a porous network structure after incorporation MnO_2 film into the inner network structure of LbL-MWNT. A cross-section SEM image (Figure 4-1d) reveals uniform thickness conformal nano-composite structure of LbL-MWNT/MnO_2 electrode on the substrate without phase segregation of MnO_2 within the electrode. More importantly, cross-sectional elemental mapping of Mn for LbL-MWNT/MnO_2 electrode (Figure 4-2) shows uniform distribution of Mn throughout the thickness direction, further confirming uniform introduction of MnO_2 into ultrathin LbL-MWNT electrode.

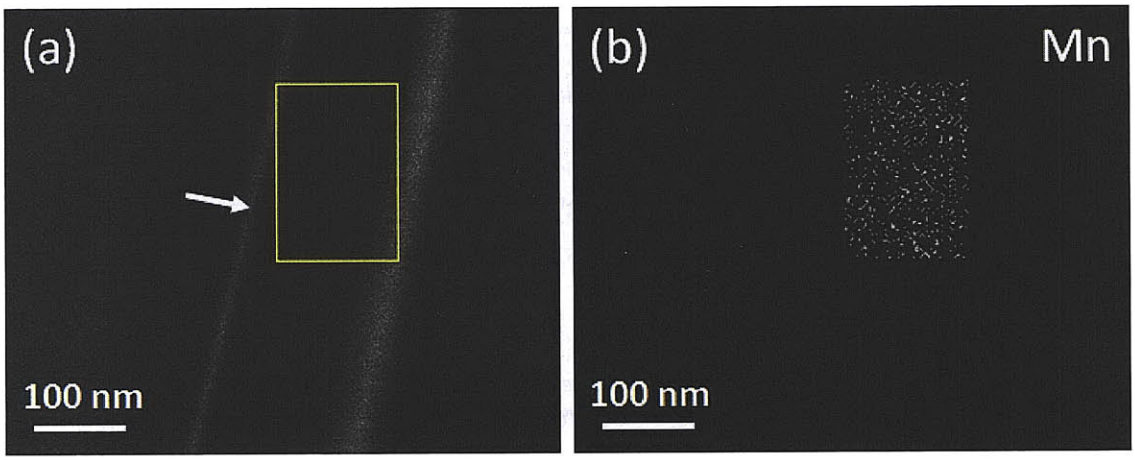

Figure 4-2. (a) A cross-section SEM image and (b) elemental mapping of Mn for an LbL-MWNT/MnO_2 composite electrode (60 min). White arrow indicates the interface between the substrate and LbL-MWNT/MnO_2 composite film.

TEM images with selected-area electron diffraction (SAED) analysis were used to determine the MnO_2 structure and microstructure of LbL-MWNT/MnO_2 electrodes, as shown in Figure 4-3. A representative TEM image with SAED for an LbL-MWNT electrode are presented in Figure 4-3a, showing a randomly oriented network structure of MWNTs with graphite characteristic planes of (002), (100), and (110), respectively. Previous research has shown that the redox deposition of MnO_2 on carbon forms a mixture of birnessite MnO_2 and the amorphous phase,[18, 21] and that longer deposition times can generate large size crystalline MnO_2.[22] However, the SAED of the composite electrode after 60 min dipping corresponds to the same highly disperse rings of graphite without characteristic diffractions from MnO_2, thus indicating the small volume and amorphous nature of MnO_2 films. MnO_2 films were found uniformly distributed throughout MWNT matrix, where MnO_2 on MWNTs was indicated by white arrows at Figure 4-3b. Elemental mapping in TEM images of the composite electrode (Figure 4-4) further confirm a homogenous coating of MnO_2 throughout the LbL-MWNT framework. These conformal coating of nano-scale MnO_2 on MWNTs suggest a promising nano-composite structure for energy storage application, where we can fully utilize high capacitance of MnO_2 through electrically conducting MWNT channels.

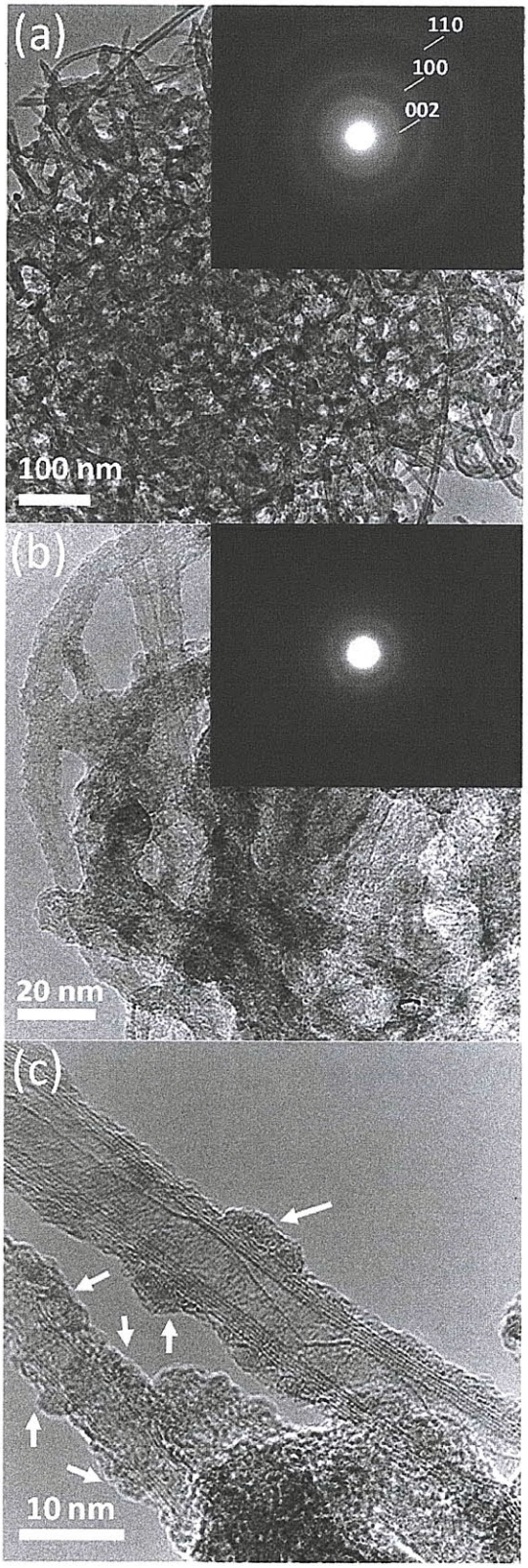
(a)
110
100
002
100 nm
(b)
20 nm
(c)
10 nm

Figure 4-3. TEM image with selected-area diffraction pattern (SAED) of (a) an LbL-MWNT and (b) an LbL-MWNT/MnO_2 composite electrode (60 min dipping). (c) High magnification image of an LbL-MWNT/MnO_2 composite electrode (60 min dipping). White arrows indicate nano-size MnO_2 coating on MWNTs.

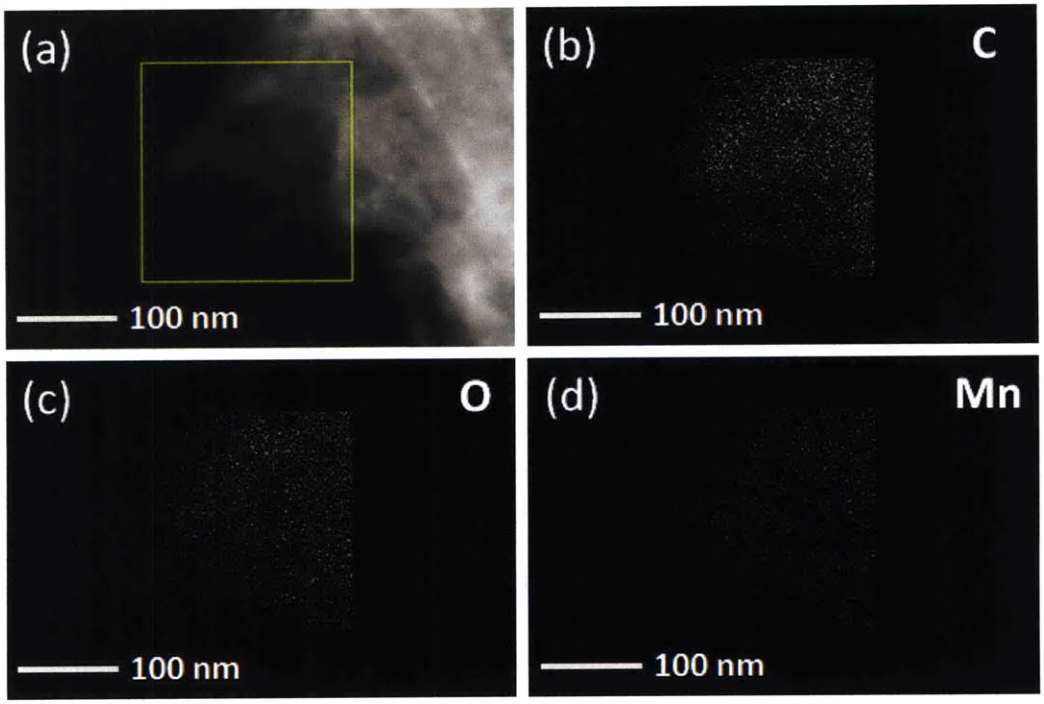

Figure 4-4. (a) TEM image with elemental mapping of (b) C, (c) O, and (d) Mn for an LbL-MWNT/MnO_2 composite electrode (60 min dipping).

X-ray photoelectron spectroscopy (XPS) spectra of the LbL-MWNT/MnO_2 composite electrodes were used to determine the oxidation state of as-synthesized MnO_2 within the LbL-MWNT film. Mn 2p spectra (Figure 4-5a) show that the binding energy of Mn 2p3/2 and Mn 2p1/2 is centered at 654.1 and 642.4 eV, respectively, which is in agreement with the binding energy of Mn $2p_{3/2}$ and the energy separation (11.8 eV) between 2p3/2 and 2p3/2 reported previously.[14, 27] Toupin, et al.[14] show the separation of peak energies (ΔE_b) between the two peaks of the Mn 3s components can be used as an

indicator of Mn oxidation state in manganese oxides, where Mn^{4+} and Mn^{3+} of MnO_2 have a peak separation of ~4.8 and ~5.3 eV, respectively.[14] The as-prepared LbL-MWNT/MnO_2 electrodes after 60 min dipping showed a separation energy of 4.93 eV for the Mn 3s doublet (Figure 4-5b), which suggest an intermediate oxidation state between Mn^{4+} and Mn^{3+}.

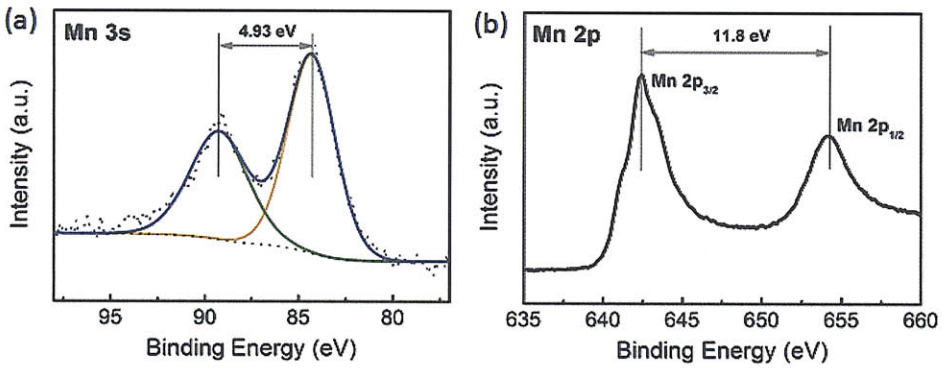

Figure 4-5. XPS spectra of LbL-MWNT/MnO_2 composite electrodes. (a) Atomic ratio of Mn/C as a function of dipping time, (b) Mn 2p spectra, and (c) Mn 3s spectra.

4.3.2 Electrochemical properties of LbL-MWNT/MnO_2 composite electrodes

Figure 4-6a shows the cyclic voltamogramm (CV) of LbL-MWNT/MnO_2 electrodes in 0.1 M K_2SO_4 at a scan rate of 50 mV/s as a function of dipping time. The potential window for cycling is confined between -0.5 V and 0.8 V versus SCE to avoid the oxygen evolution reaction at higher potentials and manganese dissolution at lower potentials.[13, 23, 24] The as-assembled LbL-MWNT electrode (0 min in Figure 4-6a) shows ~ 1.8 A/cm^3 based on EDLC of MWNTs. Volumetric currents of the LbL-MWNT/MnO_2 electrodes increase with dipping time due to increasing pseudocapacitive MnO_2, which results in increasing volumetric capacitance with dipping time (Figure 4-6b). Previous research[15, 28] has shown that crystalline MnO_2 in K_2SO_4 solution have redox peaks from the intercalation/deintercalation process of the cations. It is interesting that the LbL-

MWNT/MnO_2 electrodes have no such redox peaks, which can be related amorphous character of MnO_2 films on MWNT (Figure 4-4).

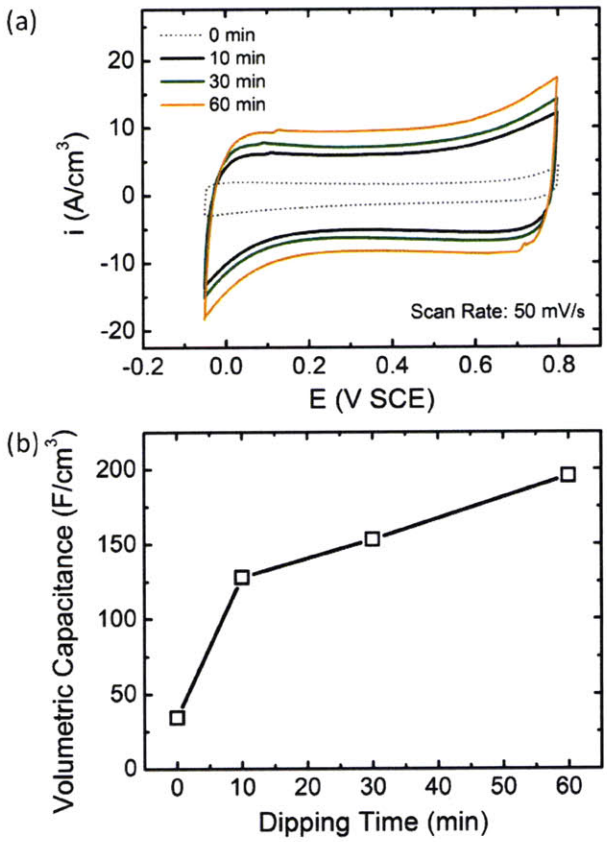

Figure 4-6. (a) Cyclic voltammograms for LbL-MWNT/MnO_2 composite films on ITO-coated glass electrodes in 0.1 K_2SO_4 at room temperature as a function of dipping time. A scan rate of 50 mV/s was used. 0 min indicates a pristine LbL-MWNT electrode (b) Volumetric capacitance as a function of dipping time. Capacitance was estimated from cyclic voltammograms with a scan rate of 50 mV/s (Fig. 4-6a).

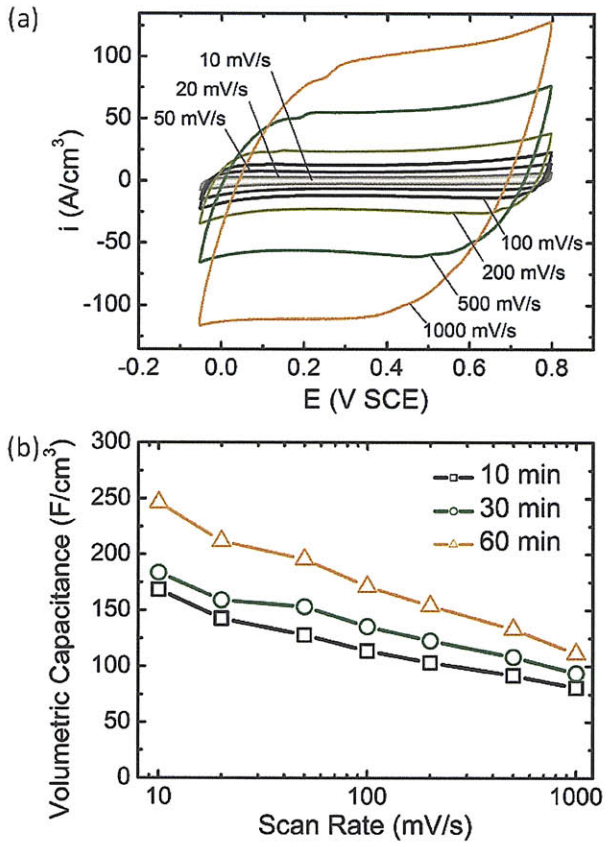

Figure 4-7. (a) Rate dependent Cyclic voltammograms of LbL-MWNT/MnO_2 composite electrodes at various scan rates (10 mV/s ~ 1,000 mV/s) (b) Volumetric capacitance (F/cm^3) obtained from LbL-MWNT/MnO_2 composite electrodes with dipping time as a function of scan rates (10 mV ~ 1,000 mV/s).

The rate-dependent CVs of LbL-MWNT/MnO_2 electrodes were investigated over a wide range of scan rates from 10 to 1,000 mV/s, as shown by Figure 4-7a. The rate capability of the LbL-MWNT/MnO_2 electrodes is remarkable, and they maintain a rectangular CV shape with only small distortions even at 1,000 mV/s, which results in only ~50% loss of capacitance compared to those measured at 10 mV/s (Figure 4-7b). This is in contrast to previous work, where the rectangular shape of the CV for MnO_2 electrodes[17] was found to distort considerably to a diamond shape as the scan rate increased and carbon

nanotube/carbon microfiber/MnO_2 electrodes[15] showed ~50% loss of capacitance from 10 mV/s to 200 mV/s. Moreover, LbL-MWNT/MnO_2 electrodes coated for 60 min show a significantly higher volumetric capacitance of 246 F/cm^3 at a scan rate of 10 mV/s compared to one of the highest reported values (156 F/cm^3)[22] for carbon/MnO_2 electrodes at a scan rate of 2 mV/s. The corresponding specific capacitance of the MWNT/MnO_2 electrodes is ~290 F/g(MWNT/MnO_2), with a specific capacitance of MnO_2 ~940 F/g(MnO_2); this number is significantly higher than the ~350 F/g previously reported for redox reduction in carbon nanofoam,[22] but lower than ~1370 F/g of the thin film form and the theoretical value of MnO_2.[14] The high volumetric capacitance and remarkable rate capability of LbL-MWNT/MnO_2 electrodes can be attributed to electrode microstructure, where nano-scale MnO_2 particles are supported on a high-packing-density, porous MWNT network with good access to electrons and ions in the electrolyte. In addition, the LbL-MWNT/MnO_2 electrodes show good cycling stability up to 1,000 cycles, as shown in Figure 4-8. Beyond this point, at a high scan rate of 200 mV/s, CVs of the electrode show a small decrease in current (Figure 4-8a), and capacity (~11.6% decay) (Figure 4-8b).

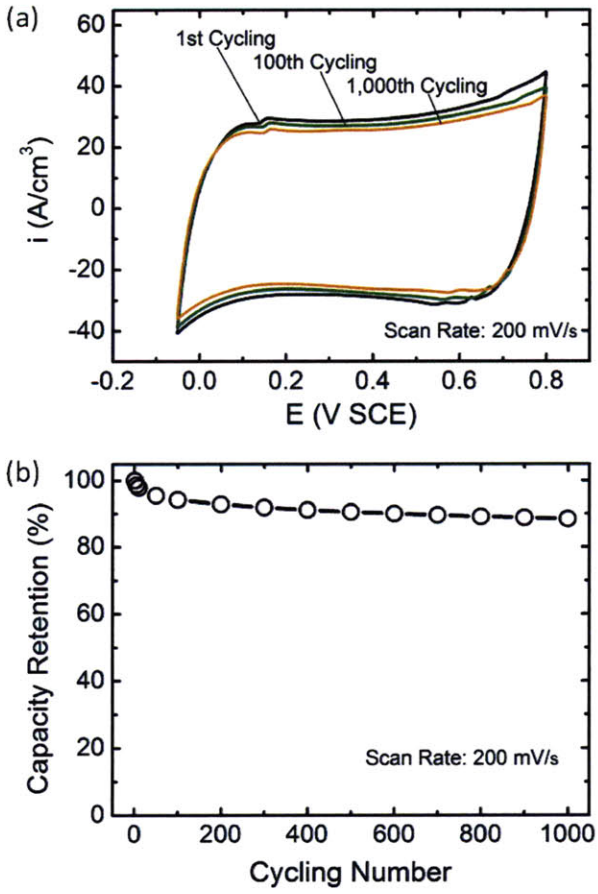

Figure 4-8. (a) Cyclic voltammograms obtained from LbL-MWNT/MnO_2 composite electrodes with different cycling numbers in 0.1 M K_2SO_4 at room temperature. A scan rate of 200 mV/s was used. (b) Capacity retention of from LbL-MWNT/MnO_2 composite electrodes as a function of cycling number.

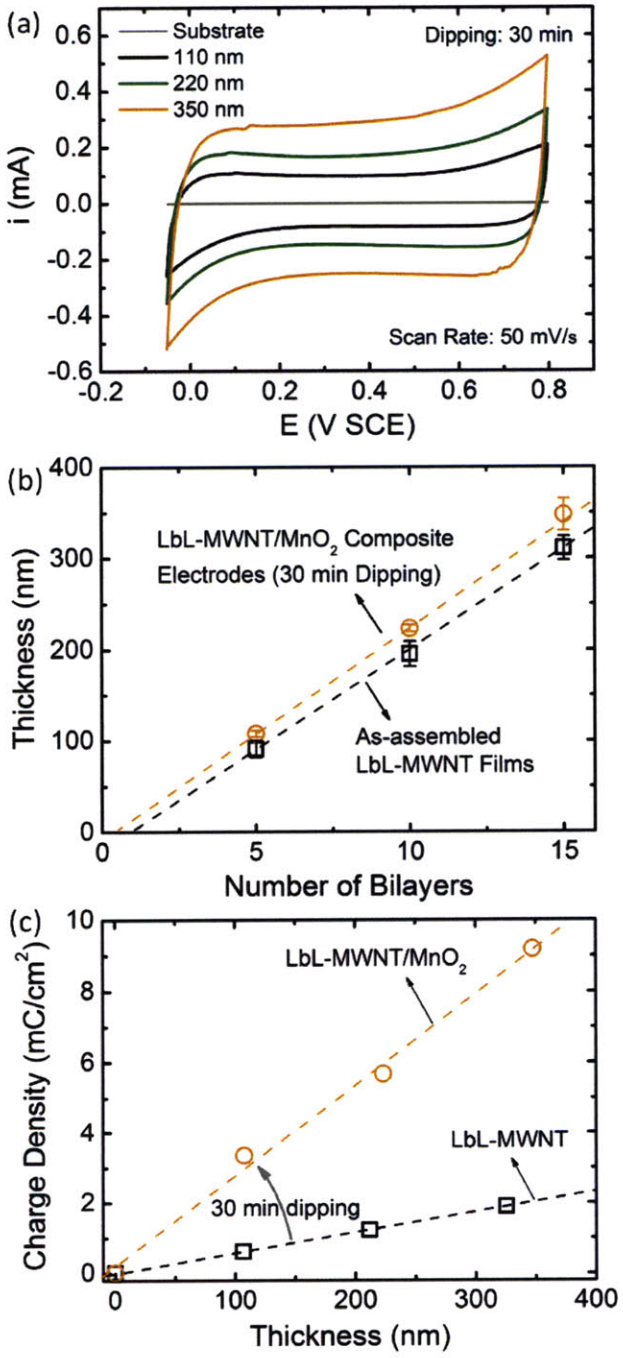

Figure 4-9. (a) Thickness of as-assembled MWNT thin films and LbL-MWNT/MnO_2 composite electrodes after 30 min dipping as a function of the number of bilayers. The dashed lines are linear fit with standard deviations as error bars. (b) Cyclic voltammograms

obtained from LbL-MWNT/MnO_2 composite electrodes with different thicknesses on ITO-coated glass electrode in 0.1 M K_2SO_4 at room temperature. A scan rate of 50 mV/s was used. (c) Charge density (measured from cyclic voltammograms and electrode area) vs. thickness of films from profilometry measurements.

Figure 4-9a shows a thickness-dependent CV of the MWNT/MnO_2 electrodes in the range from 110 nm to 350 nm at a scan rate of 50 mV/s. The thicknesses of LbL-MWNT/MnO_2 electrodes still scale with the number of bilayers after 30 min dipping was shown by Figure 4-9b, thus suggesting that the coverage of MnO_2 is uniform throughout the thickness of the LbL-MWNT films. Surface charge densities from the integration of CV curves were found to scale linearly with film thickness (Figure 4-9c) for both the LbL-MWNT films and the MWNT/MnO_2 electrodes, which suggest that MnO_2 in the LbL-MWNT electrodes is electrochemically active throughout the entire electrode thickness. Consequently, we can fully utilize the advantages of LbL process, enabling precise capacity control of the composite electrodes by controlling the thickness of LbL-MWNT films. In addition, versatile adaptability of the LbL technique on various kinds of substrates such as silicon, glass, and flexible substrates propose binder free MWNT/MnO_2 electrodes as promising electrodes for application of MEMS flexible electronics.[29]

4-4. Conclusions

In summary, we created LbL-MWNT/MnO_2 ultra thin film electrodes via an LbL assembly of functionalized MWNTs and continuous redox deposition of MnO_2 onto MWNTs. The porous MWNT network generated via alternating LbL assembly creates fast electronic and ionic conducting channels in the presence of electrolyte, and the conformal coating of MnO_2 on MWNTs provides high capacitance, which shows that these systems can provide a platform to design high-performance electrodes for EC applications. The ability to generate high electrode capacitances, and precise control of thickness and capacity from simple dipping processes at ambient conditions suggest a promising approach to the

creation of ultrathin electrodes in a controlled manner. We believe that these high-capacitance LbL-MWNT/MnO_2 film electrodes and the general approach to the fabrication of the composite electrodes can be applied to design novel electrode materials for EC and battery, and sensor applications.

4.5 References

1. Miller, J. R.; Simon, P., Materials science - Electrochemical capacitors for energy management. *Science* **2008,** *321*, 651-652.
2. Simon, P.; Gogotsi, Y., Materials for electrochemical capacitors. *Nat. Mater.* **2008,** *7*, 845-854.
3. Miller, J. R.; Burke, A., Electrochemical Capacitors: Challenges and Opportunities for Real-World Applications. *The Electrochemical Society Interface* **2008,** *17*, 53-57.
4. Frackowiak, E.; Beguin, F., Carbon materials for the electrochemical storage of energy in capacitors. *Carbon* **2001,** *39*, 937-950.
5. Simon, P.; Burke, A., Nanostructured carbons: double-layer capacitance and more. *The Electrochemical Society Interface* **2008,** *17*, 38-43.
6. Pandolfo, A. G.; Hollenkamp, A. F., Carbon properties and their role in supercapacitors. *J. Power Sources* **2006,** *157*, 11-27.
7. Futaba, D. N.; Hata, K.; Yamada, T.; Hiraoka, T.; Hayamizu, Y.; Kakudate, Y.; Tanaike, O.; Hatori, H.; Yumura, M.; Iijima, S., Shape-engineerable and highly densely packed single-walled carbon nanotubes and their application as super-capacitor electrodes. *Nat. Mater.* **2006,** *5*, 987-994.
8. Emmenegger, C.; Mauron, P.; Sudan, P.; Wenger, P.; Hermann, V.; Gallay, R.; Zuttel, A., Investigation of electrochemical double-layer (ECDL) capacitors electrodes based on carbon nanotubes and activated carbon materials. *J. Power Sources* **2003,** *124*, 321-329.
9. Kim, Y. J.; Abe, Y.; Yanaglura, T.; Park, K. C.; Shimizu, M.; Iwazaki, T.; Nakagawa, S.; Endo, M.; Dresselhaus, M. S., Easy preparation of nitrogen-enriched carbon materials from peptides of silk fibroins and their use to produce a high volumetric energy density in supercapacitors. *Carbon* **2007,** *45*, 2116-2125.
10. Zheng, J. P.; Cygan, P. J.; Jow, T. R., HYDROUS RUTHENIUM OXIDE AS AN ELECTRODE MATERIAL FOR ELECTROCHEMICAL CAPACITORS. *J. Electrochem. Soc.* **1995,** *142*, 2699-2703.
11. Zheng, J. P.; Jow, T. R., A NEW CHARGE STORAGE MECHANISM FOR ELECTROCHEMICAL CAPACITORS. *J. Electrochem. Soc.* **1995,** *142*, L6-L8.
12. Thackeray, M. M., Manganese oxides for lithium batteries. *Prog. Solid State Chem.* **1997,** *25*, 1-71.
13. Bélanger, D.; Brousse, T.; Long, J. W., Manganese oxides: battery materials make the leap to electrochemical capacitors. *The electrochemical Society Interface* **2008,** *17*, 49-52.
14. Toupin, M.; Brousse, T.; Belanger, D., Charge storage mechanism of MnO2 electrode used in aqueous electrochemical capacitor. *Chem. Mat.* **2004,** *16*, 3184-3190.
15. Bordjiba, T.; Belanger, D., Direct Redox Deposition of Manganese Oxide on Multiscaled Carbon Nanotube/Microfiber Carbon Electrode for Electrochemical Capacitor. *J. Electrochem. Soc.* **2009,** *156*, A378-A384.

16. Ma, S. B.; Nam, K. W.; Yoon, W. S.; Yang, X. Q.; Ahn, K. Y.; Oh, K. H.; Kim, K. B., Electrochemical properties of manganese oxide coated onto carbon nanotubes for energy-storage applications. *J. Power Sources* **2008,** *178*, 483-489.
17. Xie, X. F.; Gao, L., Characterization of a manganese dioxide/carbon nanotube composite fabricated using an in situ coating method. *Carbon* **2007,** *45*, 2365-2373.
18. Ma, S. B.; Ahn, K. Y.; Lee, E. S.; Oh, K. H.; Kim, K. B., Synthesis and characterization of manganese dioxide spontaneously coated on carbon nanotubes. *Carbon* **2007,** *45*, 375-382.
19. Fan, Z. J.; Qie, Z. W.; Wei, T.; Yan, J.; Wang, S. S., Preparation and characteristics of nanostructured MnO2/MWCNTs using microwave irradiation method. *Mater. Lett.* **2008,** *62*, 3345-3348.
20. Chou, S. L.; Wang, J. Z.; Chew, S. Y.; Liu, H. K.; Dou, S. X., Electrodeposition of MnO2 nanowires on carbon nanotube paper as free-standing, flexible electrode for supercapacitors. *Electrochem. Commun.* **2008,** *10*, 1724-1727.
21. Fischer, A. E.; Pettigrew, K. A.; Rolison, D. R.; Stroud, R. M.; Long, J. W., Incorporation of homogeneous, nanoscale MnO2 within ultraporous carbon structures via self-limiting electroless deposition: Implications for electrochemical capacitors. *Nano Lett.* **2007,** *7*, 281-286.
22. Fischer, A. E.; Saunders, M. P.; Pettigrew, K. A.; Rolison, D. R.; Long, J. W., Electroless deposition of nanoscale MnO2 on ultraporous carbon nanoarchitectures: Correlation of evolving pore-solid structure and electrochemical performance. *J. Electrochem. Soc.* **2008,** *155*, A246-A252.
23. Brousse, T.; Toupin, M.; Belanger, D., A hybrid activated carbon-manganese dioxide capacitor using a mild aqueous electrolyte. *J. Electrochem. Soc.* **2004,** *151*, A614-A622.
24. Brousse, T.; Taberna, P. L.; Crosnier, O.; Dugas, R.; Guillemet, P.; Scudeller, Y.; Zhou, Y.; Favier, F.; Belanger, D.; Simon, P., Long-term cycling behavior of asymmetric activated carbon/MnO2 aqueous electrochemical supercapacitor. *J. Power Sources* **2007,** *173*, 633-641.
25. Decher, G., Fuzzy nanoassemblies: Toward layered polymeric multicomposites. *Science* **1997,** *277*, 1232-1237.
26. Lee, S. W.; Kim, B. S.; Chen, S.; Shao-Horn, Y.; Hammond, P. T., Layer-by-Layer Assembly of All Carbon Nanotube Ultrathin Films for Electrochemical Applications. *Journal of the American Chemical Society* **2009,** *131*, 671-679.
27. Reddy, A. L. M.; Shaijumon, M. M.; Gowda, S. R.; Ajayan, P. M., Coaxial MnO2/Carbon Nanotube Array Electrodes for High-Performance Lithium Batteries. *Nano Lett.* **2009,** *9*, 1002-1006.
28. Brousse, T.; Toupin, M.; Dugas, R.; Athouel, L.; Crosnier, O.; Belanger, D., Crystalline MnO2 as possible alternatives to amorphous compounds in electrochemical supercapacitors. *J. Electrochem. Soc.* **2006,** *153*, A2171-A2180.
29. Gates, B. D., Flexible Electronics. *Science* **2009,** *323*, 1566-1567.

Chapter 5. Square-Wave Potential Electrodeposition of Nanoparticles into Carbon Nanotube Framework for Electrochemical Applications

Abstract

Recently, nano-scale materials have attracted great scientific and technological interest because of the unusual physical and chemical properties[1] compared to the bulk materials. These differences in nano-scale materials come from the geometric effects of a dramatic increase in the number of surface atoms relative bulk ones, and the electronic structure changes due to the delocalized electron states[1]. In particular, the properties of electrochemical reactions between nano-scale metal catalysts and small molecules are sensitive to the particle size, results in a significant change in intrinsic catalytic activities for oxygen reduction reaction (ORR)[2], CO[2] and methanol oxidation reaction (MOR)[3]. In addition, nano-structured energy storage materials such as metal oxides have significant advantages[4] because of their small dimension: nano-scale Li intercalation electrodes facilitate diffusion of Li into the materials, and nano-structured pseudo-capacitive materials[5,6] increase utilization of the Faradic reaction with electrolytes on the electrode surface. Because electrochemical properties are sensitive to dimension in nano-materials, controlling nano-architecture of the electrodes becomes a crucial issue for enhancing electrochemical performance for both energy conversion and storage devices. Here, we show a simple two-step nano-structured noble metal/carbon composite electrode preparation technique, consisting of the layer-by-layer assembly[7,8] of carbon nanotubes as a nano-framework and followed by the square-wave potential method (so called electropulse deposition) for deposition of capacitive RuO_2, monometallic and/or bimetallic electrocatalysts such as Pt and Pt/Ru alloy nanoparticles from aqueous precursors (i.e.

$RuCl_3$ and K_2PtCl_6). Using the two-step process, we can easily manipulate not only the electrode dimension to control electrochemical capacity, but also the metal composition into the nano-structured LbL film electrode for the superior electrochemical performances. The prepared RuO_2 nanoparticles within the LbL carbon nanotube film using this method enhanced the volumetric capacitance over 1,000 mV/cm^3 based on the volume of the electrode, which is one of highest volumetric capacitance for electrochemical capacitor materials[5,9-11]. Furthermore, the bimetallic electrocatalysts of Pt/Ru nanoparticles within the carbon nanotube framework show higher electrocatalytic activity in methanol oxidation than that of commercial TKK Pt nanoparticles with similar core size.

5.1 Introduction

Electroplating (or electrodeposition) is one of the traditional electrochemical methods to deposit thin layer of metals on the conductive substrates. The metal thin layers can be formed on substrates from the electrochemical reduction of metal cation precursors through constant high potential or current. Recently, several electrochemical potential deposition methods[12,13] have been applied for the synthesis of bulk- and nano-crystals (NCs). Sun et al.[13] showed the first electrochemical synthesis method for the high-index facet Pt NCs on a glassy carbon substrate using square-wave potential cycling. Interestingly, the high-index facet Pt NCs showed higher catalytic activity than conventional Pt nanoparticles for electro-oxidation of small organic molecules based on the electrochemically active surface area due to the unusual tetrahexahedral structure. However, the electrochemical synthesis method is rather limited to practical applications due to the small surface area of the glassy carbon substrate (1~2 cm^2) and low specific surface area of NCs with the large particle size (>100 nanometers). In order to enhance the electrochemically active surface area of electrocatalysts, nano-sized particles should be deposited on three dimensional (3D) high surface area substrates using the efficient electrochemical deposition method.

Electrochemical plating of Fe_3O_4 on 3D nano-structured substrate has been reported by Simon and co-workers[14] for battery applications. In this work[14], Cu nanorods (~200 nm)

as current collectors were electrochemically prepared using anodized alumina oxide (AAO) membrane as a template, and deposited Fe_3O_4 on the Cu nanorods exhibited six times improvement in power density over planar electrodes with similar energy density due to the enhanced kinetics with electrolytes. However, the limited dimension of the alumina oxide (AAO) membrane template, including pore-diameter and length, is still insufficient to maximize electrochemical performances.

Previously, we reported ultrathin multiwall carbon nanotube (MWNT) films via layer-by-layer (LbL) self assembly[7] with positively and negatively charged surface functionalized MWNTs[15]. The layer-by-layer assembled MWNT (LbL-MWNT) thin film electrodes have interconnected 3D porous network structures with closed packing density (~70%)[8]. Precise control of electochemical capacity by the film thickness on the various kinds of substrates suggests that the LbL-MWNT electrodes can be used as a promising nano-structured substrate for energy storage and conversion devices.

In this chapter, a simple electrochemical deposition method to incorporate electrochemically active noble metal nanoparticles into the nano-structured LbL-MWNT film substrate using square-wave pulse potential cycling will be described. Furthermore, the superior capacitance and electrocatalytic activity on the electrochemically synthesized RuO_2 and Pt/Ru alloy nanoparticles within the LbL-MWNT film will be discussed.

5.2 Experimental Section

Layer-by-layer assembly of MWNT electrodes. Pristine MWNTs were purchased from NANOLAB (95% purity, outer diameter 15 ± 5 nm, length 1~5 μm). Positively charged (MWNT-NH_3^+) and negatively charged (MWNT-COO^-) MWNTs were prepared through surface functionalization on the exterior walls, which is described in detail at previous research[15]. Briefly, the layer-by-layer assembled MWNT (LbL-MWNT) matrix was prepared with a modified Carl Zeiss DS50 programmable slide stainer on the indium-tin oxide (ITO) coated glass slides (Delta Technologies). The ITO coated glass slides were first dipped into the positively charged MWNT (MWNT-NH_3^+) solution for 30 minutes, and washed in three baths of Milli-Q water for 2, 1, 1 minutes each. Subsequently, the

substrates were dipped into the negatively charged MWNT (MWNT-COO^-) solution for 30 minutes, and placed in the three Milli-Q water washing baths for 2, 1, 1 minutes each to remove loosely bound positive and negative charged MWNTs. This process makes one bilayer of MWNT-NH_3^+/MWNT-COO^-, and the bilayer cycle was repeated to reach the desired thickness of the LbL-MWNT matrix. The prepared LbL-MWNT matrix electrodes were heat treated at 150 °C for 12 hr in vacuum before square-wave pulse electrodepostion to improve mechanical stability of the LbL MWNT film as well as the electrical conductivity of the electrodes.

Incorporation of noble metal nanoparticles into the LbL-MWNT matrix using square-wave potential method. All square-wave electrodepostion experiments were carried out in a three-electrode electrochemical cell by using a voltamaster potentiostat (Radiometer analytical, France).The working electrodes were the prepared LbL-MWNT thin film on the ITO coated glass slides. A platinum wire and a saturated calomel electrode (SCE) (Analytical Sensor, Inc.) were used as counter electrode and reference electrode, respectively. For the electropulse deposition, the LbL-MWNT electrodes were subjected to a potential cycles with lower potential (-0.10 V vs. SCE stayed for 0.02 sec) and higher potential (1.10 V vs. SCE stayed for 2 sec) in 50 mM metal precursors + 0.1 M $HClO_4$ solutions. For instance, 50 mM $RuCl_3$, 50 mM K_2PtCl_6, was used to prepare LbL-MWNT/RuO_2 and LbL-MWTN/Pt nanoparticles. In order to incorporate the bimetallic Pt/Ru alloy nanoparticles into the LbL-MWNT matrix, 25 mM $RuCl_3$ + 25 mM K_2PtCl_6 was prepared in the 0.1 M $HClO_4$ solution. The metal precursor solution was vigorously stirred by a magnetic stirrer during the electropulse deposition to maintain steady state diffusion of metal precursor ions into the LbL-MWNT film electrodes.

Characterization. The thickness of electrodes was determined by averaging thickness at least four different positions on each electrode by a Tencor P-16 profilometer. The volume of each electrode was measured by multiplying the geometric area of the electrode on the ITO coated glass and the thickness of electrode determined by profilometer. The core size and the distribution of the metal nanoparticle within the LbL-MWNT matrix were examined using a JEOL 2010F high resolution TEM (HRTEM). At least 100 randomly

selected nanoparticles from HRTEM images were used to present metal nanoparticle core size and distribution. From each distribution, the number-averaged diameter, d_n, was determined by $d_n = \frac{\sum_{i=1}^{n} d_i}{n}$. Energy dispersive X-ray (EDX) spectroscopy maps of the bimetallic Pt/Ru nanoparticles were made using aberration corrected TEM on a JEOL JEMS 2200 200 KeV microscope and a CEOS corrector at Oakridge National Laboratory as part of the High Temperature Materials Laboratory user Program. Electrochemical activity measurement of the noble metal nanoparticles within the LbL-MWNT film electrode was conducted in a three-electrode cell using a bipotentiostat (PINE instrument). The LbL-MWNT/metal nanoparticle electrodes were used as the working electrode with a saturated calomel electrode (SCE) (Analytical Sensor, Inc.) and Pt wire as the reference and counter electrodes, respectively. Cyclic voltammetry measurements of the LbL-MWNT/RuO_2 nanoparticle were performed from -0.192 to 0.850 V vs. SCE in 0.5 M H_2SO_4 electrolyte. Electrochemical surface area (ESA) of Pt was determined from the charge associated with hydrogen adsorption (210 C/cm^2_{Pt}) after double layer correction in the cyclic voltammetry data between 0.05 V and 0.35 V vs. RHE. Electrocatalytic methanol electro-oxidation activity of the LbL-MWNT/metal nanoparticles electrodes was measured at a scan rate of 50 mV/s in the potential range from 0.05 to 1.1 V vs. RHE in a N_2 saturated 1.0 M CH_3OH, in 0.1 M $HClO_4$ electrolyte at room temperature. The specific MOR activity of each metal nanoparticle was compared by plotting in the positive-going scan between ~ 0.3 V and 0.9 V vs. RHE after the subtraction of the double layer currents.

5.3 Results and Discussion

Introduction of nanoparticles into the LbL-MWNT film electrodes via square wave potential deposition is schematically shown in scheme 5-1, and the experimental details are described in the experimental section. The metal cations can be reduced within the LbL-MWNT film electrode during very short period time (~0.02 sec), thus allowing the formation of nano-size metal cluster without large aggregation at the low potential (-0.10 V)

(Figure 5-1a). On the other hand, at the high potential (1.10 V), reduced metal nanoparticles are oxidized as oxides form, and simultaneously metal cation precursors can diffuse into the porous LbL-MWNT film electrode. The given longer period oxidation time (~2 sec) at 1.10 V allows that the metal ion can completely diffuse into the several hundred nanometer film thickness electrode, and also can prevent localized reduction on the surface of the LbL-MWNT thin film electrode (Figure 5-1a). Figure 5-1b shows a representative current versus time plot during square-wave eletrodeposition, where cathodic and anodic currents clearly show the reduction and oxidation process of metal nanoparticles within the LbL-MWNT film electrode. By repeating these square-wave potential cycles, nano-sized metal clusters could form uniformly within the LbL-MWNT film electrode.

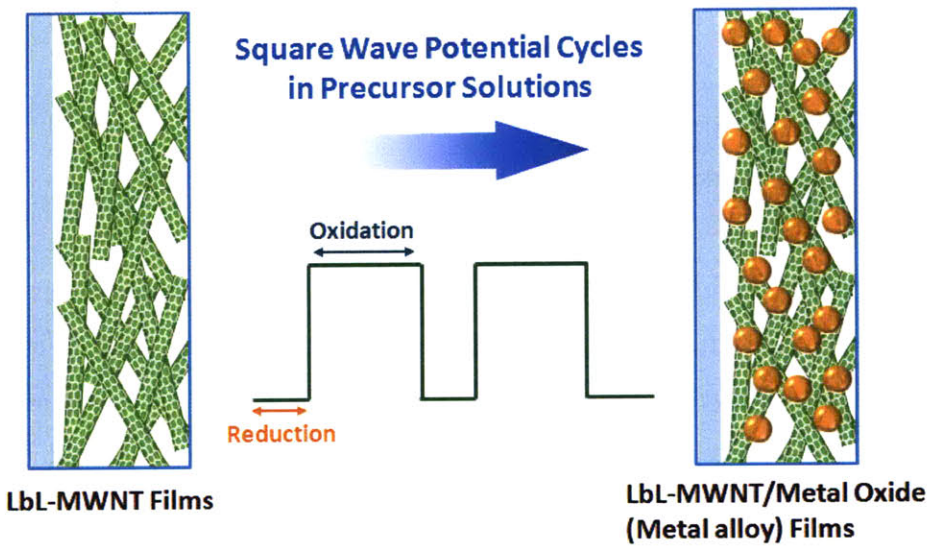

Scheme 5-1. Introduction of the metal oxide and the bimetallic nanoparticles into the layer-by-layer assembled multiwall carbon nanotube (LbL-MWNT) film electrode via square wave potential cycles in the metal precursor solution.

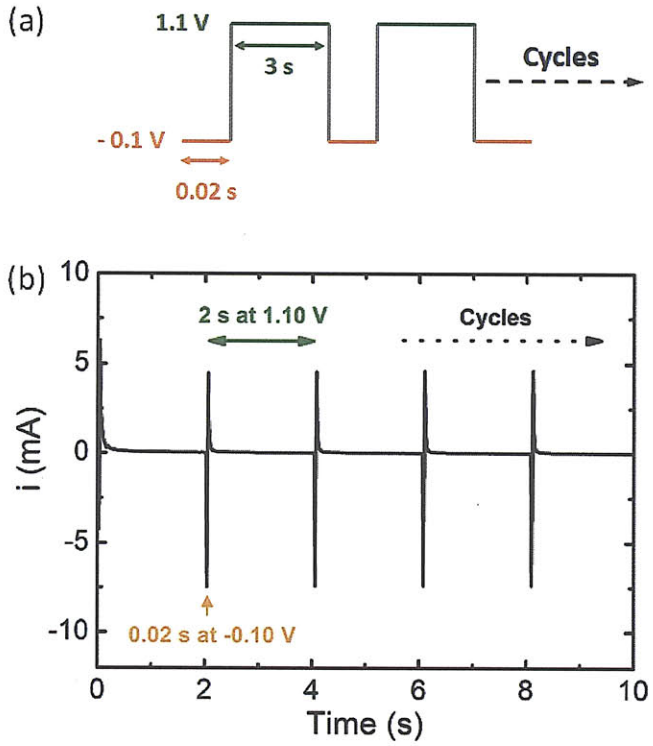

Figure 5-1. (a) Potential and time scales of square-wave potential cycles. (b) Representative current versus time plot during square-wave potential cycles.

5.3.1 Incorporation of RuO_2 nanoparticles into the LbL-MWNT electrodes

The first nanoparticles incorporated into the LbL-MWNT film electrodes using square-wave potential cycles are hydrous RuO_2, which is an electrochemically active material for electrochemical capacitor applications. Therefore, the prepared RuO_2 within the LbL-MWNT film electrode has pseudo-capacitive properties, very fast reversible redox reactions with electrolytes, due to fast mixed proton/electron conductivity. The calculated theoretical specific capacitance of the hydrous RuO_2 is 1368 F/g[6] based on reversible oxidation and reduction from Ru (II) to Ru (IV) and a simultaneous exchange of protons in acidic solution. However, this high capacitance is only available for nano-sized particles and/or nanometer scale ultrathin films[6] because pseudo-capacitive reactions are confined in the several nanometer thickness of hydrated cell. Therefore, synthesis of nano-scale RuO_2 is critical to fully utilize the pseudo-capacitance of the material. Figure 5-2a shows

representative low and high magnification TEM images and core size distribution of RuO_2 nanoparticles within the LbL-MWNT film electrodes after 400 square-wave potential cycles. The prepared RuO_2 particles were found uniformly distributed within the LbL-MWNT framework as shown in the low magnification TEM image. Moreover, the diameter size histogram (Figure 5-2b) of RuO_2 nanoparticles shows very narrow core size distribution in the LbL-MWNT film, which is 1.7 ± 0.3 nm.

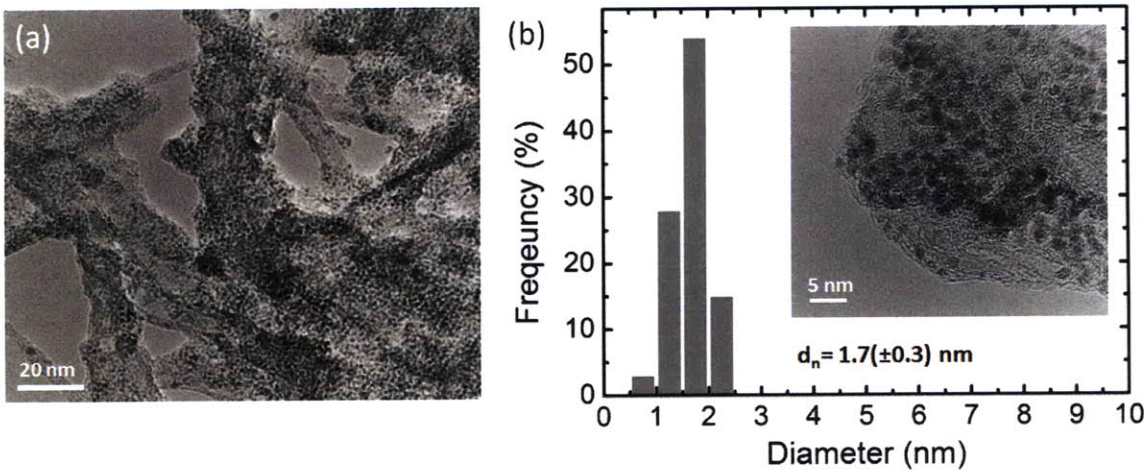

Figure 5-2. (a) A representative low-magnification TEM image of RuO_2 nanoparticles within the LbL-MWNT electrode after 400 cycles. (b) Histogram and high-magnification TEM image (inset) of RuO_2 nanoparticles within the LbL-MWNT film electrode after 400 cycles. Number-averaged diameter (d_n) and standard deviation of RuO_2 nanoparticles is indicated. At least 100 randomly selected nanoparticles were counted to present the histogram and d_n.

After thermal annealing process at 150 °C for 12 hr in air, cyclic voltamogramm (CV) measurement of the different number of electropulse deposition LbL-MWNT/RuO_2 electrodes were conducted in a 0.5 M H_2SO_4 solution at a scan rate of 50 mV/s as shown in Figure 5-3a. The LbL-MWNT framework with the thickness of 130 nm shows ~5 A/cm^3 based on mostly electrical double layer capacitance[9] of carbon nanotubes and partially

Faradaic redox reactions[16] on the surface functional groups[8]. Volumetric currents of the LbL-MWNT/RuO_2 electrodes increased with electropulse deposition cycle numbers owing to the increased pseudo-capacitive RuO_2 loading, which simultaneously increases volumetric capacitance with the electropulse deposition cycle number (Figure 5-3b). Volumetric capacitance of the LbL-MWNT/RuO_2 electrodes were found to scale linearly as a function of cycle number, and finally reached over 1000 $F/cm^3_{electrode}$ after 600 cycles (Figure 5-3b). To the best of our knowledge, this LbL-MWNT/RuO_2 electrode shows the highest volumetric capacitance among the carbon/pseudo-capacitive oxides composite electrodes[5,6] for electrochemical capacitors, based on the electrode volume including matrix and pseudo-capacitive materials. Moreover, it is important to note that uniformly distributed nano-size RuO_2 nanoparticles within the LbL-MWNT electrode increased capacitance without increasing the bulk volume of the LbL-MWNT framework.

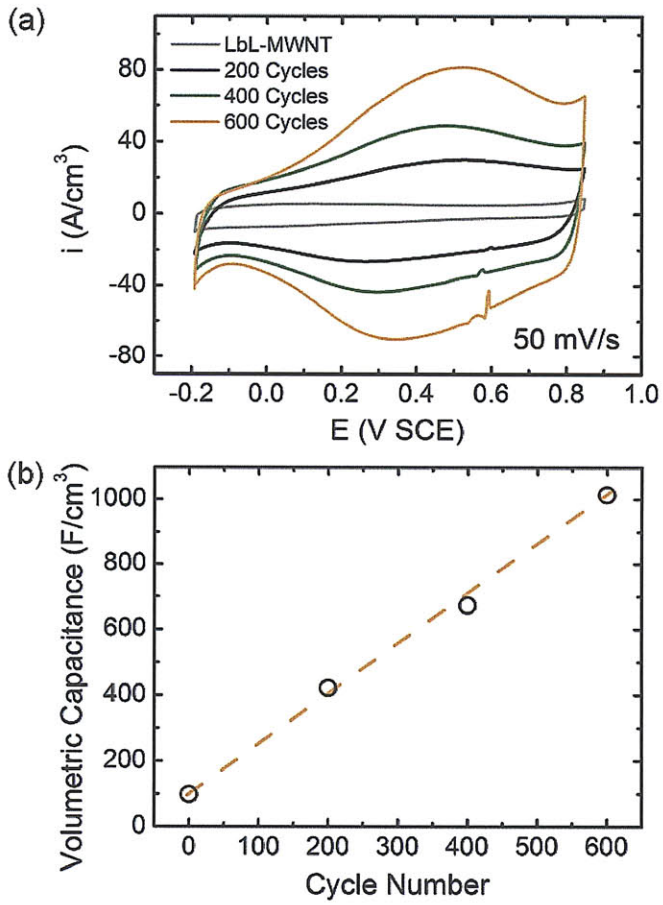

Figure 5-3. (a) Cyclic voltammograms for the different number of square-wave pulse cycle LbL-MWNT/RuO_2 composite electrodes on ITO-coated glass electrodes in a 0.5 M H_2SO_4 electrolyte at a scan rate of 50 mV/s at room temperature. (b) Comparison of volumetric capacitance as a function of electropulse deposition cycle number. Capacitance was estimated from the cyclic voltammograms at a scan rate of 50 mV/s (Fig. 5-3a).

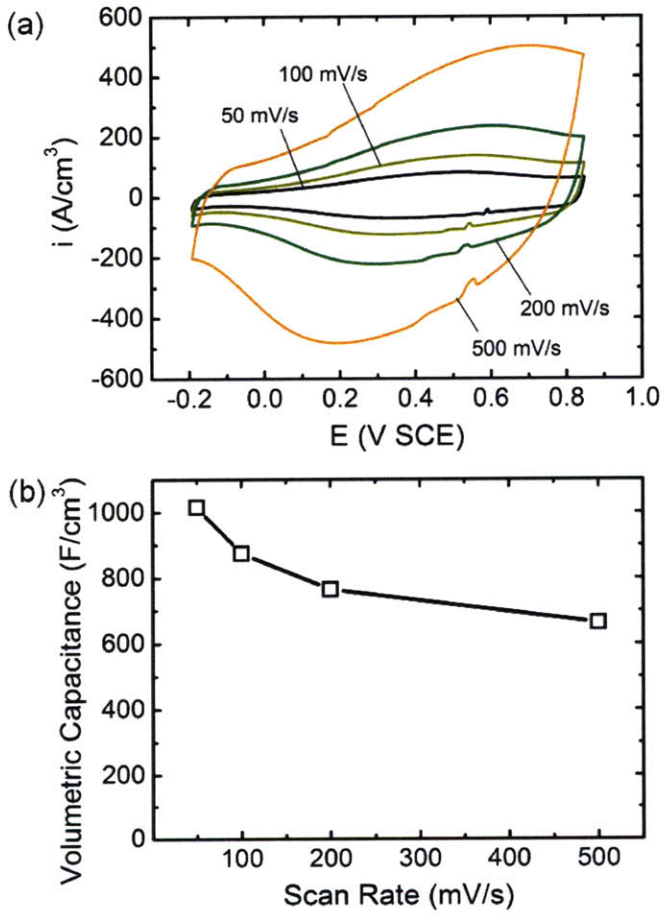

Figure 5-4. (a) Scan rate dependent cyclic voltammograms of the LbL-MWNT/RuO_2 composite electrode (600 cycles) at various scan rates (50 mV/s ~ 500 mV/s) (b) Volumetric capacitance (F/cm^3) obtained from the LbL-MWNT/RuO_2 composite electrode (600 cycles) as a function of scan rates (50 mV ~ 500 mV/s).

In general, the specific capacitance of RuO_2 significantly decreases at higher scan rates due to the electrical resistance and proton depletion. One of the advantages of the carbon matrix/RuO_2 composite electrodes is not only a mitigation of the kinetic loss at high scan rate from the utilization of the electrically conductive carbon framework[5]. Figure 5-4a shows scan rate-dependent of CVs on the LbL-MWNT/RuO_2 electrodes in the scan rate range from 50 to 500 mV/s. The CVs for the LbL-MWNT/RuO_2 electrodes maintain the similar shape until an extremely fast scan rate of 500 mV/s with small distortion, which results in only ~35% loss of the capacitance compared to that measured at 50 mV/s. High volumetric capacitance and the excellent rate capability of the LbL-MWNT/RuO_2 electrodes can be attributed to fully utilization of pseudo-capacitance of nano-size RuO_2 and inter-connected 3D porous network structure, where fast electron and ion transports are accessible throughout the electrodes.

5.3.2 Incorporation of Pt and Pt/Ru nanoparticles into the LbL-MWNT electrodes

This square-wave pulse potential deposition technique can be also extended to the synthesis monometallic Pt and bimetallic Pt/Ru alloy nanoparticles from the aqueous Pt precursor and the mixed Pt/Ru precursor solution. For this purpose we first prepared Pt and Pt/Ru alloy nanoparticles within the LbL-MWNT film electrode by using square wave potential cycles and then the prepared metal (oxide) electrode was further reduced at 200 °C for 2 hr in hydrogen atmosphere. Figure 5-5 shows size distributions and HRTEM images of the prepared Pt and Pt/Ru alloy nanoparticles within the LbL-MWNT film electrode after 400 cycles. Both Pt and Pt/Ru alloy nanoparticles show uniform and narrow core size distribution within the LbL-MWNT film electrode. The average core sizes of the Pt and Pt/Ru alloy nanoparticles are 2.1 ±0.6 nm and 2.2 ±0.6 nm, respectively. However, it is not clear that electrochemically synthesized alloy nanoparticles from the mixed Pt/Ru precursor are homogeneous alloy structures instead of a preferentially reduced one metal or a mixture of separated Pt and Ru nanoparticles from this TEM image.

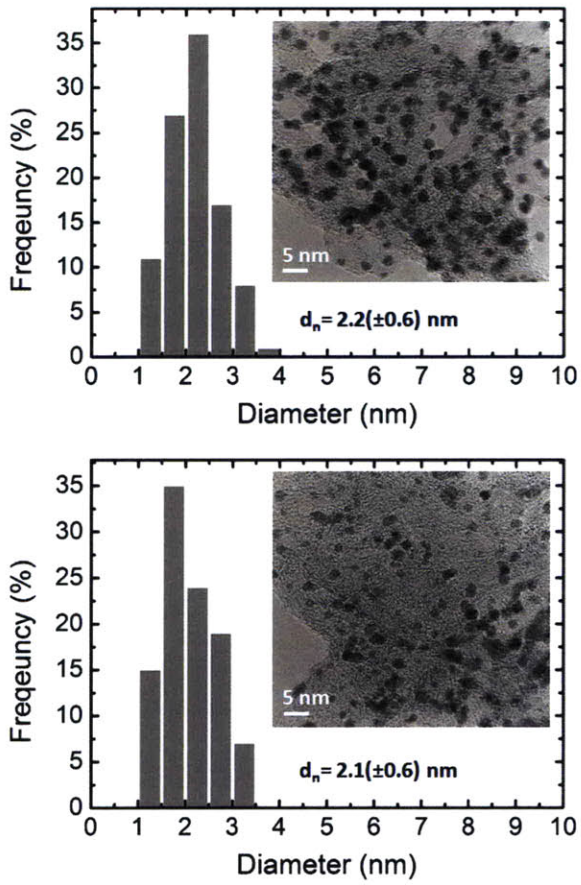

Figure 5-5. Histograms and representative HRTEM images of (a) Pt and (b) Pt/Ru alloy nanoparticle within the LbL-MWNT electrode after 400 cycles. Number-averaged diameter (d_n) and standard deviation of nanoparticles is indicated. At least 100 randomly selected nanoparticles were used to present histogram and d_n.

To clarify Pt/Ru alloy nanoparticle structure, energy dispersive X-ray (EDX) spectroscopy is applied for dispersed metal nanoparticles in the broad region (Figure 5-6a) and an individual nanoparticle (Figure 5-6b-d). Figure 5-6a shows a low-magnification image with an EDX spectroscopy for many Pt/Ru nanoparticles. In this region, the EDX spectroscopy shows 58.3 : 41.7 of the Pt : Ru atomic ratio, revealing co-reduction of both Pt and Ru precursor reduction instead of the preferential reduction of one metal. In addition, Pt and Ru EDX spectroscopy maps are applied for a randomly selected Pt/Ru alloy nanoparticle using aberration corrected TEM. Pt and Ru EDX map images for the selected

particle show uniform distribution of both Pt and Ru atoms on the entire area of the particle, confirming that the Pt/Ru alloy structured nanoparticles formed within the LbL-MWNT film using the electropulse deposition technique.

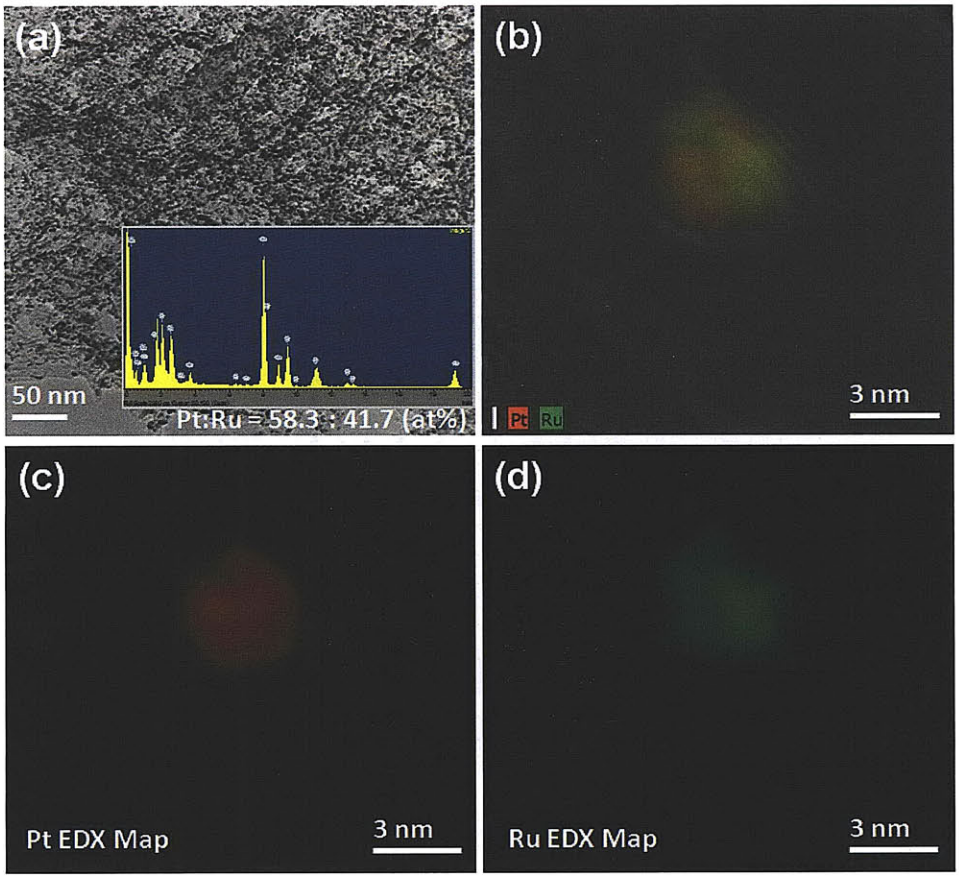

Figure 5-6. (a) A low-magnification image with an energy dispersive X-ray (EDX) spectroscopy of Pt/Ru nanoparticle within the LbL-MWNT film electrode after 400 cycles. Atomic ratio of Pt:Ru is indicated. (b-d) Pt and Ru EDX spectroscopy maps of randomly selected Pt/Ru nanoparticle using aberration corrected transmission electron microscopy (TEM).

Electrocatalytic methanol electro-oxidation activity of Pt and Pt/Ru alloy nanoparticles within the LbL-MWNT film electrodes were measured in Ar saturated 1.0 M

CH_3OH + 0.1 M $HClO_4$ using cyclic voltammograms (CVs). A representative cyclic voltammogram of Pt/Ru alloy nanoparticles for electro-oxidation of methanol is shown in Figure 5-7a, where the current is normalized by the electrochemical surface area (ESA) of Pt nanoparticles. Electrocatalytic methanol electro-oxidation activities were compared after double layer current correction, and the prepared Pt/Ru alloy nanoparticles in the LbL-MWNT film showed considerably higher specific activity than that of the prepared monometallic Pt nanoparticles and the commercial carbon supported Pt electocatalyst (Tanaka Kikinzoku International, Inc.). The High methanol oxidation reaction (MOR) activity of the Pt/Ru alloy nanoparticles can be explained by bi-functional mechanism[17], where Pt atoms adsorb and dissociate methanol into various residues including CO, and simultaneously Ru atoms dissociate water and oxidize adsorbed methanol residues at low potentials. Particularly, only Pt/Ru alloy nanoparticles show oxidizing currents at potential below 0.5 V since Ru atoms preferentially adsorb and dissociate water molecules, and oxidize adsorbed CO on the Pt atoms at lower potential region. Moreover, this bi-functional mechanism only works for randomly distributed Pt/Ru alloy nanoparticle surfaces, therefore, the enhanced MOR activity on the Pt/Ru alloy nanoparticles supports the uniform structure of the Pt/Ru alloy nanoparticles.

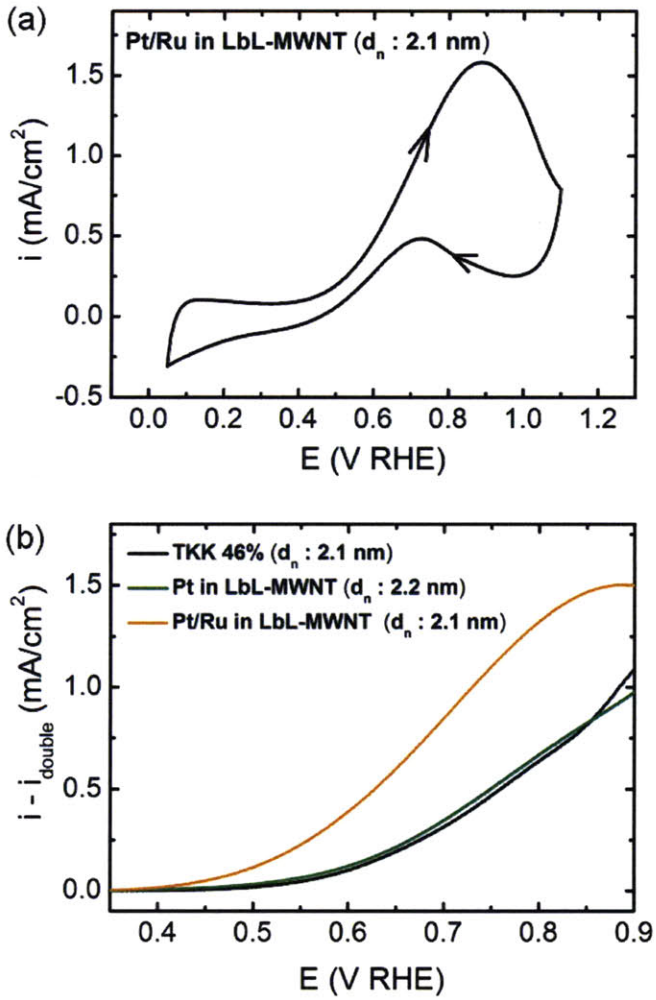

Figure 5-7. (a) Cyclic voltammograms of the methanol electro-oxidation on the Pt/Ru alloy nanoparticles within the LbL-MWNT film electrode, where the specific current is normalized by the ESA of Pt nanoparticles. The data were recorded at 50 mV/s from 0.05 to 1.10 V vs. RHE at room temperature. (b) Comparison of the methanol electro-oxidation activity on the Pt, Pt/Ru alloy nanoparticles within the LbL-MWNT film, and commercial carbon supported Pt nanoparticle electorocatalyst (TKK, d_n: 2.1nm). The specific currents normalized by the ESA of Pt nanoparticles were plotted thorough positive-going scan between ~0.3 V and 0.9 V vs. RHE after the subtraction of the double layer current.

5.4 Conclusions

A square-wave potential electrodeposition method was applied to produce noble metal/metal oxide nanoparticles within the LbL-MWNT films. This simple method showed the versatile fabrication of electrochemically active electrodes with well-controlled nanostructure and excellent electrochemical performances. This technique has many controllable factors such as dimension of the substrate, capacity, metal nanoparticle loading in the 3D substrate, and chemical composition, to maximize electrochemical performance of the electrode. In addition, the electrochemical synthetic process can be extended to the synthesis of non-noble metal and metal oxide nanoparticles including Co and Ni using non-aqueous solvent or ionic liquid, which have a wide available potential window. Finally, this general approach using electrodeposition would open new ways to synthesize various electrochemically active nano-size materials to design high energy and power density electrode for energy storage devices (i.e. electrochemical super capacitors and rechargeable batteries) and highly efficient electrocatalsyts for fuel cell applications.

5.5 References

[1] Roduner, E., Size matters: why nanomaterials are different. *Chem. Soc. Rev.* **35**, 583-592 (2006).

[2] Mayrhofer, K. J. J. et al., The impact of geometric and surface electronic properties of Pt-catalysts on the particle size effect in electocatalysis. *J. Phys. Chem. B* **109**, 14433-14440 (2005).

[3] Bergamaski, K., Pinheiro, A. L. N., Teixeira-Neto, E., and Nart, F. C., Nanoparticle size effects on methanol electrochemical oxidation on carbon supported platinum catalysts. *J. Phys. Chem. B* **110**, 19271-19279 (2006).

[4] Arico, A. S. et al., Nanostructured materials for advanced energy conversion and storage devices. *Nat. Mater.* **4**, 366-377 (2005).

[5] Simon, P. and Gogotsi, Y., Materials for electrochemical capacitors. *Nat. Mater.* **7**, 845-854 (2008).

[6] Naoi, K. and Simon, P. , New materials and new configurations for advanced electrochemical capacitors. *The Electrochemical Society Interface* **17**, 34-37 (2008).

[7] Decher, G., Fuzzy nanoassemblies: Toward layered polymeric multicomposites. *Science* **277**, 1232-1237 (1997).

[8] Lee, S. W. et al., Layer-by-Layer Assembly of All Carbon Nanotube Ultrathin Films for Electrochemical Applications. *Journal of the American Chemical Society* **131**, 671-679 (2009).

[9] Simon, P. and Burke, A., Nanostructured carbons: double-layer capacitance and more. *The Electrochemical Society Interface* **17**, 38-43 (2008).

[10] Miller, J. R. and Simon, P., Materials science - Electrochemical capacitors for energy management. *Science* **321**, 651-652 (2008).

[11] Miller, J. R. and Burke, A., Electrochemical Capacitors: Challenges and Opportunities for Real-World Applications. *The Electrochemical Society Interface* **17**, 53-57 (2008).

[12] Triaca, W. E., Kessler, T., Canullo, J. C., and Arvia, A. J., A STUDY OF THE OPTIMAL CONDITIONS FOR THE DEVELOPMENT OF PREFERRED ORIENTED PLATINUM SURFACES BY MEANS OF FAST SQUARE-WAVE POTENTIAL PERTURBATIONS. *J. Electrochem. Soc.* **134**, 1165-1172 (1987).

[13] Tian, N. et al., Synthesis of tetrahexahedral platinum nanocrystals with high-index facets and high electro-oxidation activity. *Science* **316**, 732-735 (2007).

[14] Taberna, L. et al., High rate capabilities Fe3O4-based Cu nano-architectured electrodes for lithium-ion battery applications. *Nat. Mater.* **5**, 567-573 (2006).

[15] Lee, Seung Woo et al., Layer-by-Layer Assembly of All Carbon Nanotube Ultrathin Films for Electrochemical Applications. *Journal of the American Chemical Society* **131**, 671-679 (2009).

[16] Frackowiak, E. and Beguin, F., Carbon materials for the electrochemical storage of energy in capacitors. *Carbon* **39**, 937-950 (2001).

[17] Iwasita, T., Electrocatalysis of methanol oxidation. *Electrochim. Acta* **47**, 3663-3674 (2002).

Chapter 6. Roles of Surface Steps on Pt Nanoparticles on the Electrochemical Activity for Electro-Oxidation of Carbon Monoxide and Methanol, and Oxygen Reduction Reaction

Reproduced in part with permission from Seung Woo Lee, Shuo Chen, Wenchao Sheng, Naoaki Yabuuchi, Yong-Tae Kim, Tadaoki Mitani, Elio Vescovo, and Yang Shao-Horn, *Roles of Surface Steps on Pt Nanoparticles in Electro-oxidation of Carbon Monoxide and Methanol.* **J. AM. CHEM. SOC.** 2009, *131*, 15669–15677, Copyright 2009 American Chemical Society.

Portions of this chapter are reprinted from Seung Woo Lee, Shuo Chen, Jin Suntivich, Kotaro Sasaki, Radoslav R. Adzic, and Yang Shao-Horn, *manuscript submitted.*

Abstract

Design of highly active nanoscale catalysts for electro-oxidation of small organic molecules and electro-reduction of oxygen molecules is of great importance to the development of efficient fuel cells. Increasing steps on single-crystal Pt surfaces is shown to enhance the activity of CO and methanol electro-oxidation up to several orders of magnitude. However, little is known about the surface atomic structure of nanoparticles with sizes of practical relevance, which limits the application of fundamental understanding in the reaction mechanisms established on single-crystal surfaces to development of active, nanoscale catalysts. In this study, we reveal the surface atomic structure of Pt nanoparticles supported on multiwall carbon nanotubes, from which the amount of high-index surface facets on Pt nanoparticles is quantified. Correlating the surface steps on Pt nanoparticles with the electrochemical activity and stability clearly show the significant role of surface steps in enhancing intrinsic activity for CO and methanol electro-oxidation. On the other hand, ORR activity of Pt nanoparticles is not influenced by surface steps in contrast to MOR activity. Here we show that increasing surface steps on Pt nanoparticles of ~2 nm can

lead to enhanced intrinsic activity up to ~200% (current normalized to Pt surface area) for electro-oxidation of methanol.

6. 1 Introduction

Studies on well-defined model systems such as single-crystal surfaces have led to determination of surface reaction mechanisms and identification of physical parameters such as electronic structure[1] and surface atomic structure[2] that govern activity. In particular, increasing steps and kinks on single-crystal Pt surfaces has shown to enhance the activity of electro-oxidation of carbon monoxide (CO) and methanol[3-6]. CO electro-oxidation can be catalyzed by preferential adsorption of oxygenated species on the under-coordinated sites[3] while methanol electro-oxidation can be assisted similarly by adsorbed oxygenated species in the indirect pathway, and via direct methanol oxidation[4] and methanol decomposition[7] at the step sites in the direct pathway. Extending electrochemical oxidation reaction mechanisms established on model single-crystal surfaces to design of active nanoscale catalysts[8] is not straightforward. Although high-index surfaces [(100) steps on (100) terraces] were shown to increase the activity of formic acid and ethanol oxidation on Pt nanoparticles of ~50 nm and larger[9], there is no previous experimental evidence to conclusively show the role of surface steps on Pt nanoparticles with sizes of practical relevance (typically ~5 nm) on the electro-oxidation activity of CO and methanol.

One of the intensively debated issues over the last two decades is centered on whether and how nanoparticle activity for MOR and ORR should be dependent on nanoparticle size and/or surface atomic structure. As only recent high-resolution transmission electron microscopy allows determination of surface structures on nanoparticles,[10] traditionally researchers have related nanoparticle sizes to electrochemical activity. However, both nanoparticle size and nanoparticle surface atomic structure can influence activity. Particle size reduction increases the density of surface under-coordinated sites as decreasing crystal size of a given particle shape such as truncated octahedron[11] increases the fractions of surface atoms on the corner and edge sites[12]. However, decreasing particle sizes does not always lead to higher intrinsic activity for nanoparticles as one would expect, to a first

approximation, based on stepped single-crystal Pt studies[6], where the underlying mechanism for this phenomenon is not understood. A number of studies have shown lower activity for adsorbed CO or methanol electro-oxidation on smaller Pt nanoparticles[13-19] while others report an opposite trend[8,12,20]. Kinoshita[12] have first showed that the intrinsic ORR activity in H_2SO_4 and H_3PO_4, having strong anion adsorption, decreases with increasing surface under-coordinated sites of smaller Pt nanoparticles (1.5 to 15 nm). Subsequently it is noted that decreasing Pt particle sizes (30 to 1 nm) also lowers ORR activity in $HClO_4$[18,21] having minimal anion adsorption, which is attributed to increasing surface oxygenated species with decreasing coordination of surface Pt atoms. However, this is in apparent disagreement with single-crystal studies, where adding {100} or {111} steps on the {111} terrace[22,23] to (lowering surface coordination) increases ORR in 0.1 M $HClO_4$. This discrepancy may be attributed to the hypothesis that the surface structures of nanoparticles in these previous studies, which are typically not characterized, may change with different sizes and influence activity to a greater extent than particle size reduction.

This work aims to bridge the gap in the fundamental understanding of the electro-catalytic activity for MOR and ORR between nanoparticles and single-crystal surfaces by correlating the surface structures of Pt nanoparticles and intrinsic electrocatalytic activities. In this study, we compare MOR and ORR activity of Pt nanoparticles of comparable sizes, where the amount of surface steps can be varied by heat-treatment temperature. Here we show that high-index surfaces, particularly steps on the (111) surfaces, can play a very important role in enhancing intrinsic activity for CO and methanol electrochemical oxidation on Pt nanoparticles of ~2 nm. On the other hand, We show that ORR activity is not influenced by surface steps on Pt nanoparticles of ~2 nm unlike MOR and CO oxidation.[24]

6.2 Experimental Section

High-resolution transmission electron microscopy. The size and distributions of Pt nanoparticles in Pt/MWNT samples were examined on a JEOL 2010F TEM operated at 200 kV with a point-to-point resolution of 0.19 nm. Pt/MWNT samples were first immersed in

Milli-Q 18 MΩ water and subsequently dispersed ultrasonically for 5 minutes. The suspension was then deposited on a lacey carbon grid and dried in air for TEM observations. At least 200 randomly selected nanoparticles from HRTEM images were used to produce each particle size distribution. For each distribution, the number-averaged diameter, d_n, was determined by $d_n = \frac{\sum_{i=1}^{n} d_i}{n}$. The error bars of d_n in Figure 6-1b are defined as the standard deviations of the mean (SDOM), $\sigma_x / \sqrt{N}$, where σ_x is the standard deviation of d_n in each sample, N is the number of particles in each histogram. The indexes of surface facets of Pt nanoparticles were determined from the HRTEM images. The FFT of a HRTEM image was performed with Digital Micrograph (Version 3.11.2, Gatan Inc., Pleasanton, CA). With the aid of Digital Micrograph, the interplanar distance and the angle between atomic planes were obtained from FFT images, which allowed indexing of lattice fringes and surface facets in the HRTEM images. The average fraction of high-index planes in each Pt/MWNT sample as a function of heat-treatment temperature was obtained by summing the product of average fraction of high-index surface within each bin (right axis) and the frequency (left axis) of the bin in the histogram of Figures 6-2a-d. The error bars in Figures 6-9a-b, σ_i, are defined as the standard deviations of the mean (SDOM), $\sigma_0 / \sqrt{N}$, where σ_0 is the standard deviations of the fraction of high-index planes in each bin and N is the number of particles in the bin. The error bars in Figure 6-1f are equal to $\left[\sum (\sigma_i f_i)^2\right]^{1/2}$, where f_i is the frequency (left axis) for each bin, and σ_i is the SDOM of the high-index plane fraction determined in the same bin. The fraction of high-index surface facets was obtained from analyzing at least 14 particles for each sample (Figures 6-1f and Figure 6-9).

In-situ X-ray absorption near edge structure measrumetns. In-situ X-ray absorption near edge structure measurements were carried out at the National Synchrotron Light Source (NSLS), Brookhaven National Laboratory (BNL) using beam lines X-19A. The electrochemical cell designed for passing X-ray beam was used for data collection in fluorescence mode, in which working and counter electrodes were separated by a Nafion®

membrane[25]. Data were collected at different electrode potentials in 1.0 M $HClO_4$ at room temperature.

Electrode Preparation. Pt/MWNT powder was well dispersed in Milli-Q 18 MΩ water using ultrasonicator (Sonics & Materials, Inc). 20 μL of suspension was dropped on the glassy carbon electrode (5 mm in diameter), resulting in Pt loading in the range of 10 to 30 $\mu g/cm^2_{electrode}$. Uniform, thin Pt/MWNT films were prepared by evaporation of the water, and followed by dropping 10 μL of a dilute Nafion® solution (0.025 wt%), which was prepared from 5 wt% Nafion® solution (Ion Power, Inc.). Only freshly prepared Pt/MWNT electrodes were used to measure electrochemical activity. A commercial Pt nanoscale catalyst sample supported on high surface area carbon [Tanaka Kikinzoku International, Inc.] with a metal loading of 46 wt%, which is commonly used in fuel cells[42], was used for comparison.

Electrochemical Measurements. All electrochemical measurements were performed in a three-electrode cell at room temperature. A Pt wire and a saturated calomel electrode (SCE) (Analytical Sensor, Inc.) were used as the counter and reference electrodes, respectively. SCE potential was calibrated to the RHE scale. Cyclic voltammetry measurements were performed in O_2-free 0.1 M $HClO_4$ electrolyte obtained by bubbling ultra high-purity N_2 gas (99.999%, Airgas) for at least 30 minutes. The electrodes were cycled with the potential range between 0.05 and 1.1 V (RHE) to reach steady-state cyclic voltammograms at a scan rate of 20 mV/s. Pt ESA was determined from the charge associated with hydrogen adsorption (210 $\mu C/cm^2_{Pt}$) after double layer correction in the cyclic voltammetry data between 0.05 V and 0.35 V vs. RHE. For CO stripping and CO chronoamperometric measurements, activity was measured in 0.1 M $HClO_4$ CO-free electrolyte with a scanning rate of 5 mV/s, which was obtained by bubbling ultra high purity N_2 gas (99.999%, Airgas) for at least 30 minutes, after complete adsorption of CO at a potential of 0.1 V (RHE). To prevent irreversible changes of Pt surface structure in CO atmosphere (typically referred to as CO annealing)[19], no electrochemical cycling of electrode in CO-saturated electrolyte was performed before any electrochemical measurements. To evaluate the activity of bulk CO electro-oxidation, current was obtained from scanning a RDE in a CO-saturated

solution as a function of potential vs. RHE (Figure 6-7). Current in the first cycle was recorded at 1600 rpm, which was used to calculate the specific activity in Figure 6-4c inset in order to minimize the effect of CO annealing on the surface atomic structure of Pt nanoparticles. CO-annealed Pt/MWNT samples were obtained after cycling in a CO-saturated 0.1 M $HClO_4$ solution from 0.1 to 1.1 V vs. RHE at a scan rate of 50 mV/s for 10 minutes. The activity of methanol electro-oxidation was evaluated by cyclic voltammetry in an N_2-saturated solution of 1 M CH_3OH in 0.1 M $HClO_4$ with a scanning rate of 50 mV/s. At least four experimental datasets were collected to generate the error bars in Figures 6-10b and 6-10d, which were defined as the standard deviations of specific current (normalized to Pt ESA). The charge associated with methanol oxidation in the positive-going scan of cyclic voltammogram data was calculated by the integration of the positive-going current between ~0.35 V and 1.1 V vs. RHE after subtraction of the double layer current, which was used to generate Figure 6-10d inset. Methanol electro-oxidation stability of Pt/MWNT samples were measured during cycles with 50 mV/s from 0.05 to 1.1 V vs. RHE in an N_2 saturated solution of 1 M CH_3OH in 0.1 M $HClO_4$ at room temperature. The oxygen reduction reaction (ORR) activity of Pt/MWNT samples was measured by sweep voltammetry in O_2 saturated $HClO_4$ using a rotating disk electrode at room temperature (Figure 6-13a). After the electrolyte was purged with pure oxygen (O_2) for at least half an hour, polarization curves were recorded between 0.05 and 1.0 V (RHE) under a voltage sweep rate of 10 mV/s at room temperature. The Pt specific kinetic activity (j_k / mA cm^{-2}_{Pt}) of Pt/MWNT samples was calculated from Koutecky-Levich equation and Pt ESA.

6.3 Results and Discussion Part 1: Roles of Surface Steps on Pt Nanoparticles in Electro-Oxidation of Carbon Monoxide and Methanol

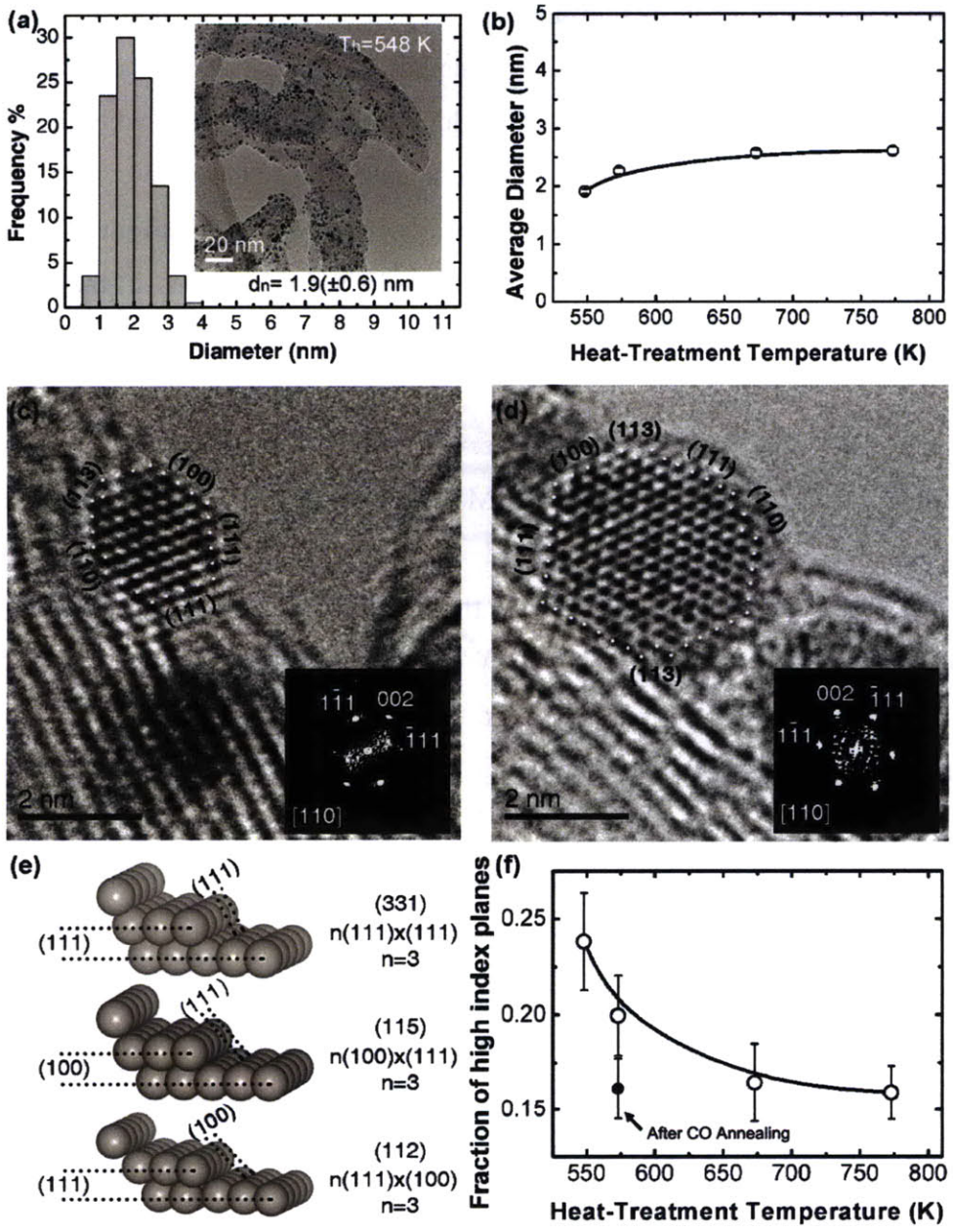

Figure 6-1. Particle sizes and surface atomic structure of Pt nanoparticles in the Pt/MWNT samples. (a) Histogram and typical TEM micrograph (inset) of a Pt/MWNT sample heat-treated at 548 K. (b) Number-averaged diameter (d_n) of Pt/MWNTs as a function of heat-treatment temperature. Standard deviation in d_n is ~1 nm and error bars in the graph are based on standard deviation of the mean by considering >200 Pt nanoparticles per sample.

(c) and (d) Typical HRTEM images and FFT results (inset) of Pt nanoparticles obtained from 573 K and 673 K, respectively. (e) Schematics of high-index planes observed on Pt nanoparticles. (f) Average area fractions of all high-index planes observed in the Pt/MWNT samples as a function of heat-treatment temperatures. The solid circle corresponds to the 573K sample that was cycled from 0.05 to 1.1 V vs. RHE in CO-saturated 0.1 M $HClO_4$ solution (CO annealing). The calculation of error bars can be found in the experimental section.

6.3.1 Surface Atomic Structure Characteristics of Pt Nanoparticles. Pt nanoparticles supported on multiwall carbon nanotubes (MWNTs) were prepared by the single atom to cluster (SAC) approach[26], which included 1) reduction of $H_2[PtCl_6]$ with $NaBH_4$ on thiolated MWNTs and 2) elimination of the thiol groups by a heat-treatment in H_2 to form Pt nanoparticles (the fraction of Pt in Pt/MWNTs is 20 wt%) in the range from 548 K to 773 K. Pt nanoparticles obtained from different temperatures were found dispersed uniformly on MWNTs (Figures 6-1 and 6-2). The number-averaged (d_n) particle diameters of Pt nanoparticles obtained from different heat-treatment temperatures in the range from 548 K to 773 K were found very similar, ~2 nm, as shown in Figure 6-1b. Combination of HRTEM images and their fast Fourier transforms (FFTs) allowed the identification of surface facets of Pt nanoparticles, and showed that Pt nanoparticles obtained at lower temperatures exhibited higher fractions of high-index surface facets. Representative HRTEM images and FFTs of Pt particles in the Pt/MWNT samples heat-treated at 573 K and 673 K are shown in Figures 6-1c and 6-1d, respectively, where surface atomic structures are revealed clearly. Not only were low-index surfaces found but also high-index surfaces in the groups of n(111)×(111), n(111)×(100), and n(100)×(111) were noted (Figures 6-1c-6-1e).

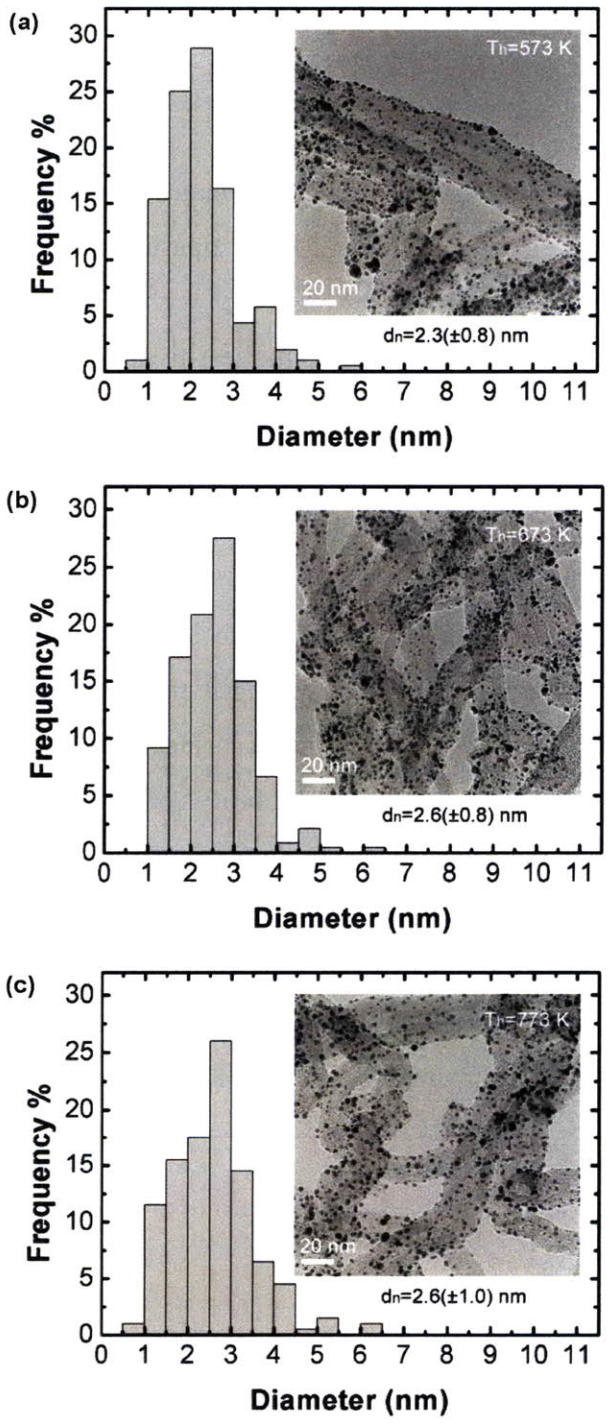

Figure 6-2. (a) to (c), Histograms and representative HRTEM micrographs of Pt/MWNT samples that were heat-treated at 573 K, 673 K, and 773 K, respectively. The histograms

were measured from at least 200 random selected particles of each sample. The number-averaged diameter and its standard deviation of Pt nanoparticles of each sample are shown.

The length fractions of low-index and high-index planes along the particle perimeter projected along the [110] zone axis of individual Pt nanoparticles could be measured from HRTEM images. The area fractions of all observed high-index surface facets of Pt nanoparticles were found to decrease with increasing heat-treatment temperature, as shown in Figure 6-1f. This trend was particularly notable for stepped surfaces on the (111) terrace, where the (111) and (100) steps were found to decrease considerably with increasing heat-treatment temperature (Figure 6-3). The observed changes in the surface atomic structure of Pt nanoparticles may be explained by considering the formation mechanism of Pt nanoparticles via single atom to cluster (SAC) approach[26]. It is hypothesized that Pt atoms do not have sufficient mobility nor time to fully reach the thermodynamically stable shape, namely truncated octahedron[11,27] with only low-index surfaces of (111) and (100), at lower heat-treatment temperatures while increasing mobility of Pt atoms at higher heat-temperatures can reduce and replace high-index surfaces with higher surface energy by low-index planes with lower surface energy[28,29]. Remarkably, we note that the area fraction of high-index planes on Pt nanoparticles can change up to 50% even though there is less than ~ 1 nm of difference in the number-averaged (d_n) particle diameters of Pt/MWNT samples obtained in the temperature from 548 K to 773 K in Figure 6-1f.

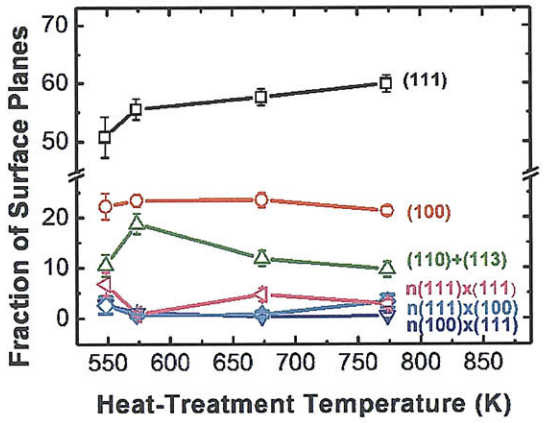

Figure 6-3. Fraction of low-index [(111) and (100)] and high-index surface planes as a function of the heat-treatment temperature. The high-index planes are divided into 1) steps on the (111) terrace, which includes n(111)×(100) and n(111)×(111) having n equal or greater than 2; 2) steps on the (100) terrace, which contains n(100)×(111) having n greater than 2.

6.3.2 Intrinsic Activity of Pt Nanoparticles for CO Electro-Oxidation. We first analyzed the electro-oxidation activity of CO on Pt/MWNT samples as CO commonly serves a model system to understand the electrocatalysis of small organic molecules[6,19,30,31] such as methanol. The intrinsic electro-oxidation activity of adsorbed CO (CO_{ad}) on Pt/MWNT samples was found to increase with decreasing heat-treatment temperature. Figures 6-4 and 6-5 show specific activity, defined as current normalized to electrochemical surface area (ESA) of Pt, as a function of potential versus reversible hydrogen electrode (RHE). The onset and peak oxidation potentials of CO_{ad} on the Pt/MWNT samples shift to lower potentials with decreasing heat-treatment temperature. Further experimental evidence of enhanced CO_{ad} electro-oxidation kinetics with decreasing heat-treatment temperature is provided by chronoamperometric measurements, where the characteristic time to reach the current maximum can be related to the reciprocal of the reaction rate constant. With increasing potentials, shorter time was required to reach the current maximum and to complete CO oxidation, which could be attributed to increasing adsorption of oxygenated species at higher voltages similar to those reported previously[3,19] (Figure 6-6). More importantly, the characteristic time to reach current maximum at a given potential decreased considerably for Pt/MWNT samples with decreasing heat-treatment temperature, indicating faster oxidation kinetics. Specific current transients of Pt/MWNT samples obtained from 548 K and 773 K at 0.73 V are compared in Figure 6-4b, where the time to reach the current maximum for the 773 K sample is ~4 times longer than that of the 548 K sample, and the 773 K sample showed 40% oxidation of CO_{ad} in comparison to 80% oxidation for the 548 K sample after 30 s.

The enhanced specific activity for electro-oxidation of CO_{ad} on Pt nanoparticles obtained from lower temperatures (Figure 6-4) can be attributed to increasing and preferential adsorption of oxygen species associated with water dissociation on higher fractions of high-index surface facets (Figures 6-1f and 6-2). Oxidation of CO_{ad} in acid is known to proceed by the Langmuir-Hinshelwood reaction echanism[32], where CO_{ad} reacts with adsorbed oxygenated species to form CO_2. Although Arenz et al.[19] suggest that surface defect sites can influence CO_{ad} electro-oxidation of Pt nanoparticles, this study, for the first time, reveals and quantifies surface under-coordinated sites, namely, high-index surface facets such as the (111) steps on the (111) surfaces in Figures 6-1f and 6-2, which can be correlated with enhanced intrinsic activity of CO_{ad} oxidation on Pt nanoparticles. Our results are in good agreement with the findings reported for the electro-oxidation activity of CO_{ad} on single-crystal Pt stepped (111) surfaces, where the intrinsic activity is enhanced significantly with increasing (111) step density[3]. It should be pointed out that the proposed physical origin of activity enhancement of electro-oxidation of CO_{ad} in the Pt/MWNT samples are different from some previous studies of Pt nanoparticles[14,15], where decreasing activity with smaller particle sizes has been attributed to reduced mobility of CO_{ad} as a result of stronger adsorption of CO on Pt sites with lower coordination.

Intrinsic activity of bulk CO electro-oxidation was also found to increase on Pt/MWNT samples with decreasing heat-treatment temperatures. Current was obtained from scanning a rotating disk electrode (RDE) in a CO-saturated solution as a function of potential (Figure 6-7). Geometric current densities (normalized to RDE area) of Pt/MWNT samples heat-treated at 573 K and 773 K are compared in Figure 6-4c. Specific CO oxidation activity on the oxidized Pt surface in the negative-going scan, which is normalized to the Pt ESA, was found to increase with decreasing heat-treatment temperature, as shown in Figure 3c inset. At a potential of 0.7 V vs. RHE, the specific current of the 573 K sample is 0.13 mA/cm^2_{Pt} as compared to 0.03 mA/cm^2_{Pt} for the 773 K sample, indicating higher activity for the samples heat-treated at lower temperatures. In addition, it is interesting to note that the Pt/MWNT sample obtained at 573 K with a d_n of ~2 nm, exhibits much higher specific activity (1 mA/cm^2_{Pt} at 0.8 V vs. RHE) than a CO

annealed, commercial Pt catalyst sample with a smaller diameter having d_n of ~1 nm (~0.05 mA/cm^2_{Pt} at 0.8 V vs. RHE) reported previously[18]. This observation suggests that factors beyond particle size are important, and knowing the surface atomic structure and chemistry of nanoparticles is essential to understand, predict and enhance the electro-oxidation activity of CO on Pt.

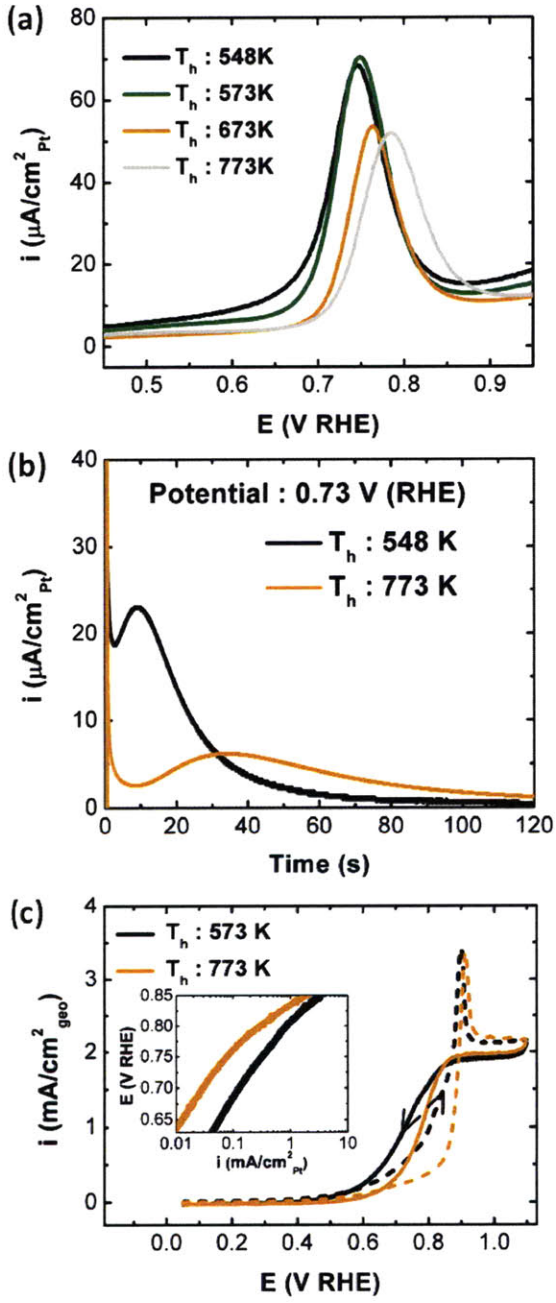

Figure 6-4. CO electro-oxidation activity on Pt/MWNT samples measured at room temperature. (a) Specific oxidation current (normalized to Pt ESA) of CO_{ad} on Pt/MWNT samples in 0.1 M $HClO_4$ with 5 mV/s. (b) Specific current transients (normalized to Pt ESA) of the oxidation of CO_{ad} after the potential was stepped from 0.1 to 0.73 V vs. RHE. (c) RDE current density (normalized to RDE geometric area) of CO bulk oxidation at 1600 rpm, where the specific activity (normalized to Pt ESA) calculated from current in the negative potential sweep with 5 mV/s is shown in the figure inset.

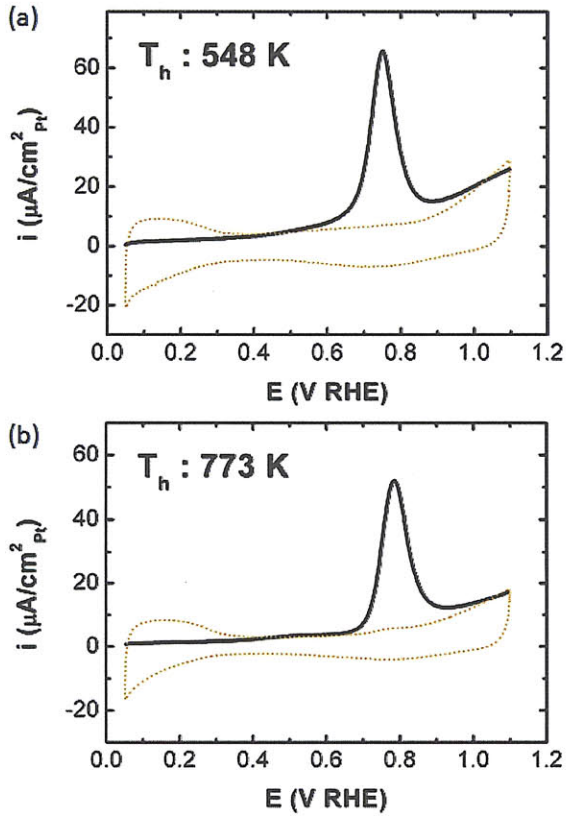

Figure 6-5. CO stripping voltammetry of Pt/MWNTs obtained at (a) T_h : 548 K and (b) T_h : 773 K with a scanning rate of 5 mV/s at room temperature. Data include voltammogram of adsorbed CO oxidation (solid line) recorded in 0.1M $HClO_4$ purged after CO adsorption with nitrogen for 30 minutes at 0.1 V vs. RHE, and base voltammogram data (dotted line) after CO oxidation.

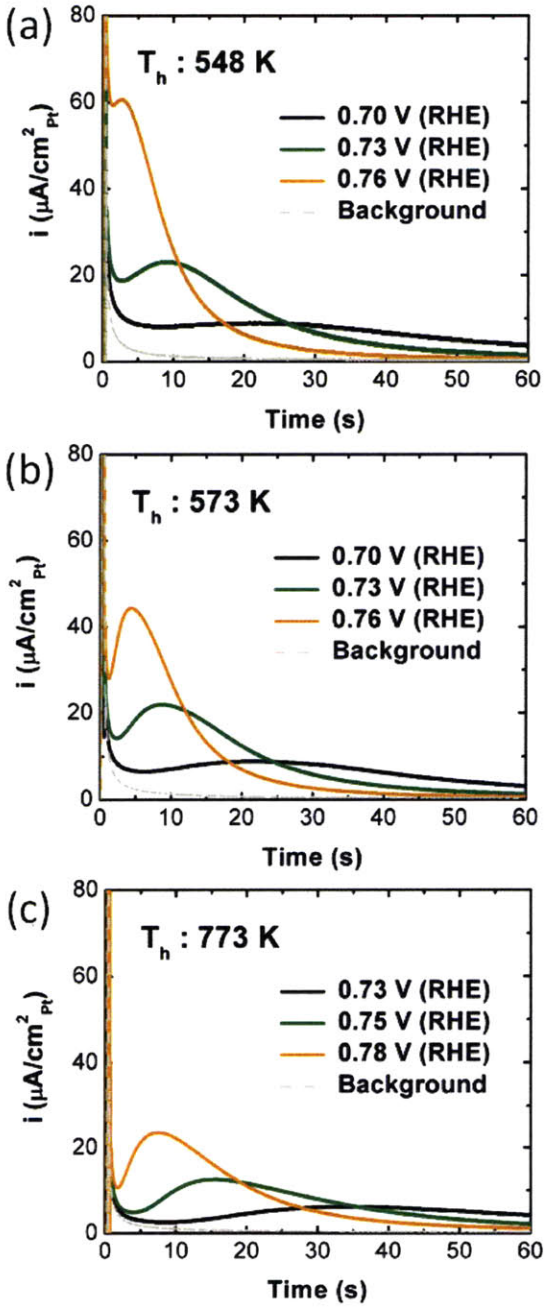

Figure 6-6. Current transients of the oxidation of CO adlayer obtained at (a) T_h : 548 K, (b) T_h : 573 K, (c) T_h : 773 K. The potential was stepped from 0.1 V vs. RHE to three potentials near the CO stripping peak potential.

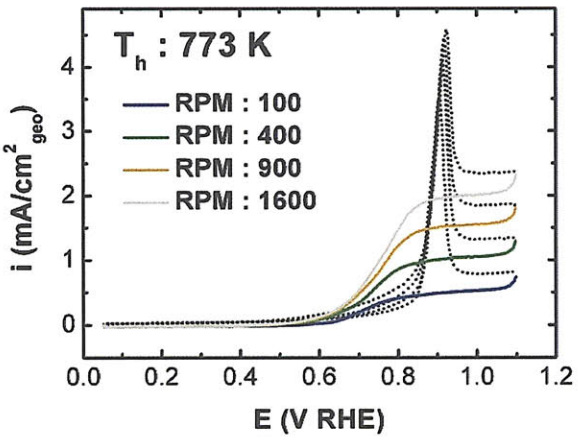

Figure 6-7. CO bulk oxidation of Pt/MWNTs obtained at 773 K at rotation rates of 100, 400, 900, and 1600 rpm using a rotation disk electrode. The potential region was from 0.5 to 1.1 V vs. RHE at a scanning rate of 5 mV/s in 0.1M $HClO_4$.

A very recent study of Pt single-crystal surfaces[31] has shown that even a modest number of potential cycling in CO-saturated solution (CO annealing[19]) can dramatically reduce surface adislands and decrease CO electro-oxidation activity. In addition, CO annealing has shown to decrease CO electro-oxidation activity of Pt nanoparticles[18]. However, correlation between such a structure change and CO electro-oxidation activity on Pt nanoparticles during CO annealing have not yet been investigated, in spite of significant technical importance. Pt/MWNT sample obtained at 573 K was cycled in a CO-saturated solution from 0.1 to 1.1 V vs. RHE at a scan rate of 50 mV/s for 10 minutes (CO annealing). Intrinsic activity for electro-oxidation of CO_{ad} (CO stripping data in Figure 6-8a and chronoamperometric data in Figure 6-8b) and for bulk CO-electro-oxidation (Figure 6-8c) decreased considerably on Pt/MWNT sample obtained at 573 K after CO annealing. The number-averaged (d_n) particle diameters of Pt/MWNTs heat-treated at 573 K before and after CO annealing were found comparable, ~2.5 nm, as shown in Figures 6-9a and 6-9b. Two representative HRTEM images of Pt nanoparticles in the Pt/MWNTs after CO annealing are shown in Figures 6-9c and 6-9d, which reveal that the nanoparticle surface is covered largely by the (111) and (100) facets. After analyzing HRTEM images of 22

particles within each sample, the fractions of high-index surface facets of Pt nanoparticles in Pt/MWNTs heat-treated at 573 K were found to decrease after CO annealing, as shown in Figure 6-1f. Earlier work on single-crystal Pt surfaces[31] has suggested that CO_{ad} can assist the diffusion of Pt adatoms and incorporation into step edges of low-index planes during the CO annealing. Such a process may result in decreased fraction of high-index surface facets on Pt nanoparticles during CO annealing, which presumably diminishes the density of active sites for adsorption of oxygen species and thus reduce CO electro-oxidation activity.

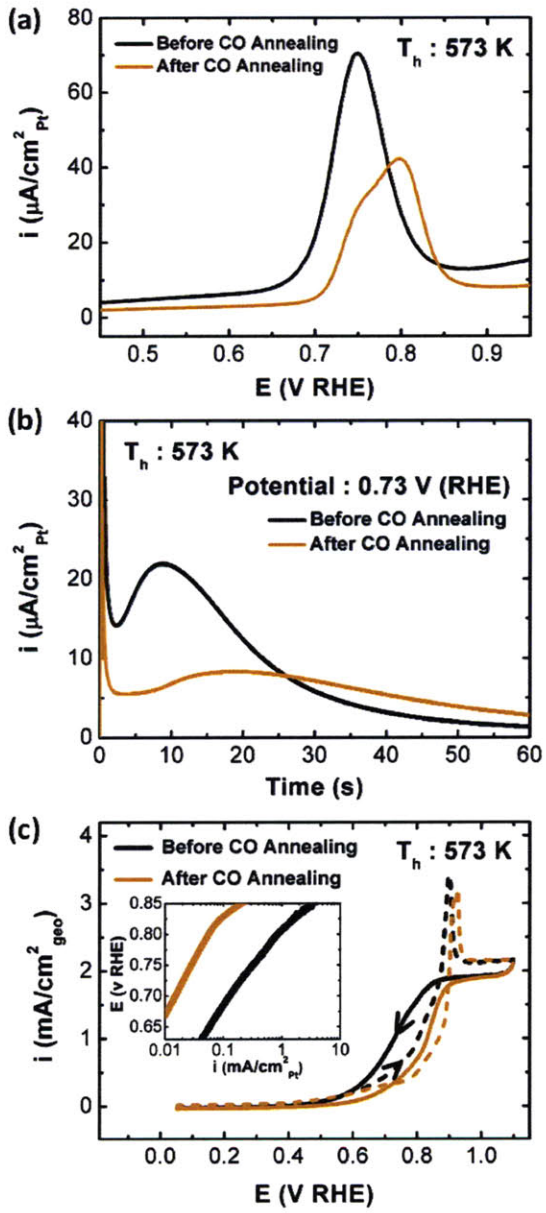

Figure 6-8. Comparison of CO electro-oxidation activity on Pt/MWNTs of 573 K before and after CO annealing. (a) Specific oxidation current (normalized to Pt ESA) of CO_{ad} on Pt/MWNT sample in 0.1 M $HClO_4$ with 5 mV/s. (b) Specific current transients (normalized to Pt ESA) of the oxidation of CO_{ad} after the potential was stepped from 0.1 to 0.73 V vs. RHE. (c) RDE geometric current density of CO bulk oxidation at 1600 rpm, where the

specific activity (normalized to Pt ESA) calculated from current in the negative potential sweep with 5 mV/s is shown in the figure inset.

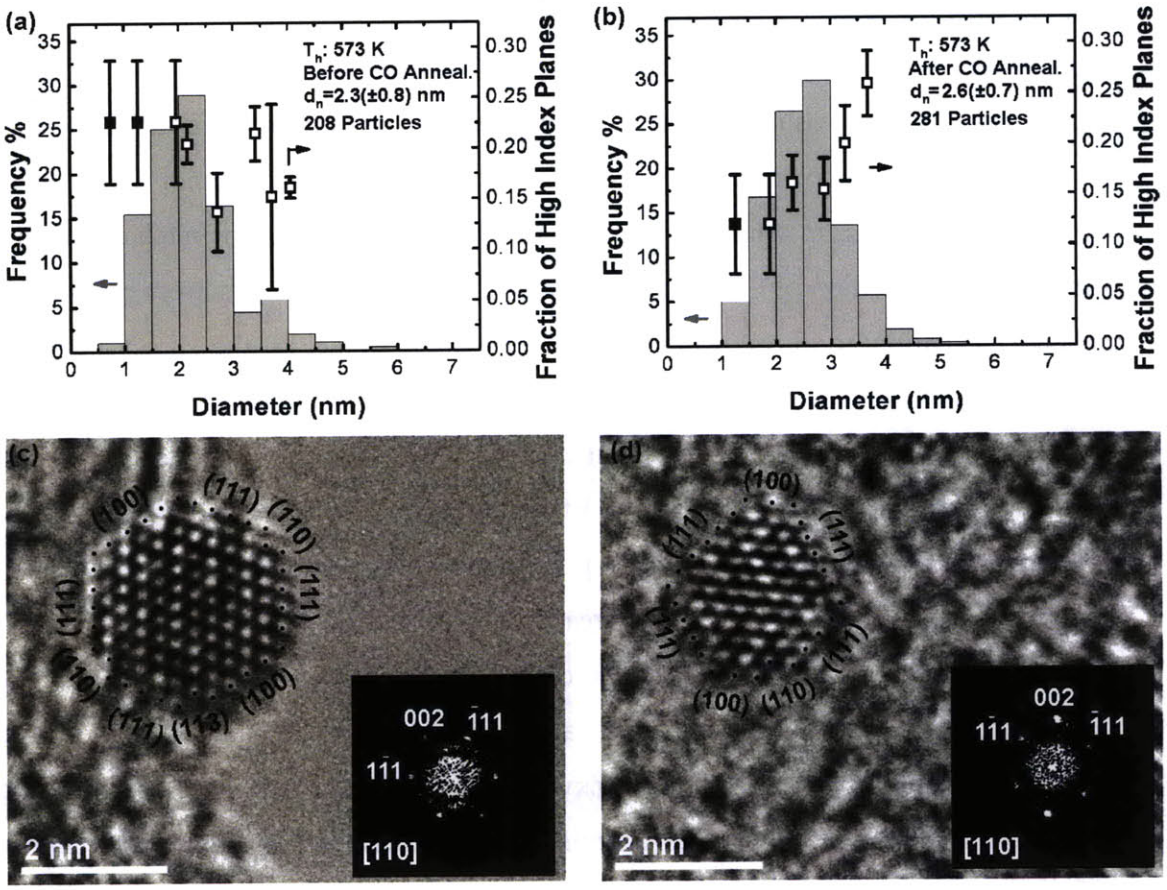

Figure 6-9. Pt particle size distribution (left axis) and area fraction of high-index planes (right axis) in Pt/MWNTs heat treated at 573 K before (a) and after (b) CO annealing, respectively. (c) and (d) Typical HRTEM image and FFT of a Pt nanoparticle in the Pt/MWNT sample after CO annealing. The calculation of error bars can be found in the Experimental section.

6.3.3 Intrinsic Activity of Pt Nanoparticles for Methanol Electro-Oxidation.

The specific (Pt-ESA-normalized) activity of methanol electro-oxidation of Pt/MWNT

samples was found to increase on Pt nanoparticles obtained from decreasing heat-treatment temperature, as shown in both positive-going and negative-going cyclic voltammetry data in Figure 6-10a. Cyclic voltammograms of Pt/MWNT samples shown in Figure 6-10a were recorded typically after 3-5 cycles and the data no longer changed with subsequent cycling (Figure 6-11). The cyclic voltammogram data of methanol oxidation on Pt/MWNTs can be explained qualitatively using the following mechanistic understanding established on bulk Pt surfaces. It is well known that the electrochemical oxidation of methanol follows through two parallel reactions, in which successive dissociative adsorption of methanol to finally form CO_{ad} and oxidation of CO_{ad} on the surface is recognized as the indirect pathway while methanol oxidation to form soluble intermediates is called as the direct pathway[6,33]. Adsorption of methanol first occurs, and continuous dehydrogenation and formation of adsorbed CO is followed as the potential increases[34]. With further increasing potential in the positive-going scan, the dissociation of water begins, which provides the oxygenated species for the Langmuir-Hinshelwood type reaction[6] with adsorbed CO to form CO_2. This reaction rate increases as potential increases until the surface becomes "poisoned" by surface oxygenated species (the coverage of oxygenated species is too high to obtain the maximum reaction rate), which leads to a characteristic oxidation peak in the positive-going scan. At the negative-going scan, oxygenated species are dominant on the surface at the high potential region, and the reaction rate increases with reduction or removal of surface oxygenated species and re-adsorption of methanol and carbonaceous intermediates with decreasing potential. Eventually the surface becomes "poisoned" by carbonaceous species such as CO as the potential decreases, which gives rise to a characteristic oxidation peak in the negative-going direction.

Specific currents (based on Pt ESA) at 0.5, 0.6 and 0.7 V vs. RHE in the positive-going scan of Pt/MWNT samples were found to increase with decreasing heat-treatment temperature in Figure 6-10b, indicating higher activity for Pt nanoparticles obtained from lower temperatures (e.g., ~80 and ~600 $\mu A/cm^2_{Pt}$ for the 548 K sample vs. ~50 and ~300 $\mu A/cm^2_{Pt}$ for the 773 K sample at 0.5 and 0.7 V, respectively). Further evidence for enhanced specific activity for methanol electro-oxidation on Pt nanoparticles of lower heat-

treatment temperatures is provided in the chronoamperometric measurements. When the potential was stepped from 0.1 V to 0.7 V (RHE), the specific current was found to decrease sharply in the first 0.1 s and gradually approach a steady-state value at longer times, as shown in Figure 6-10c. The Pt/MWNT sample of 573 K, which had a higher fraction of high-index surface facets, was found to have a steady-state specific current after 900 s, which is ~200% that of the 773 K sample, as shown in Figure 6-10c inset. It should be noted that the specific current values of Pt/MWNTs after 900 s are comparable to those from cyclic voltammetry data at 0.7 V vs. RHE (Figure 6-10b), which indicates that Pt nanoparticles of ~2 nm in this study are reasonably stable for methanol oxidation, and our cyclic voltammetry data are representative of those under steady-state conditions.

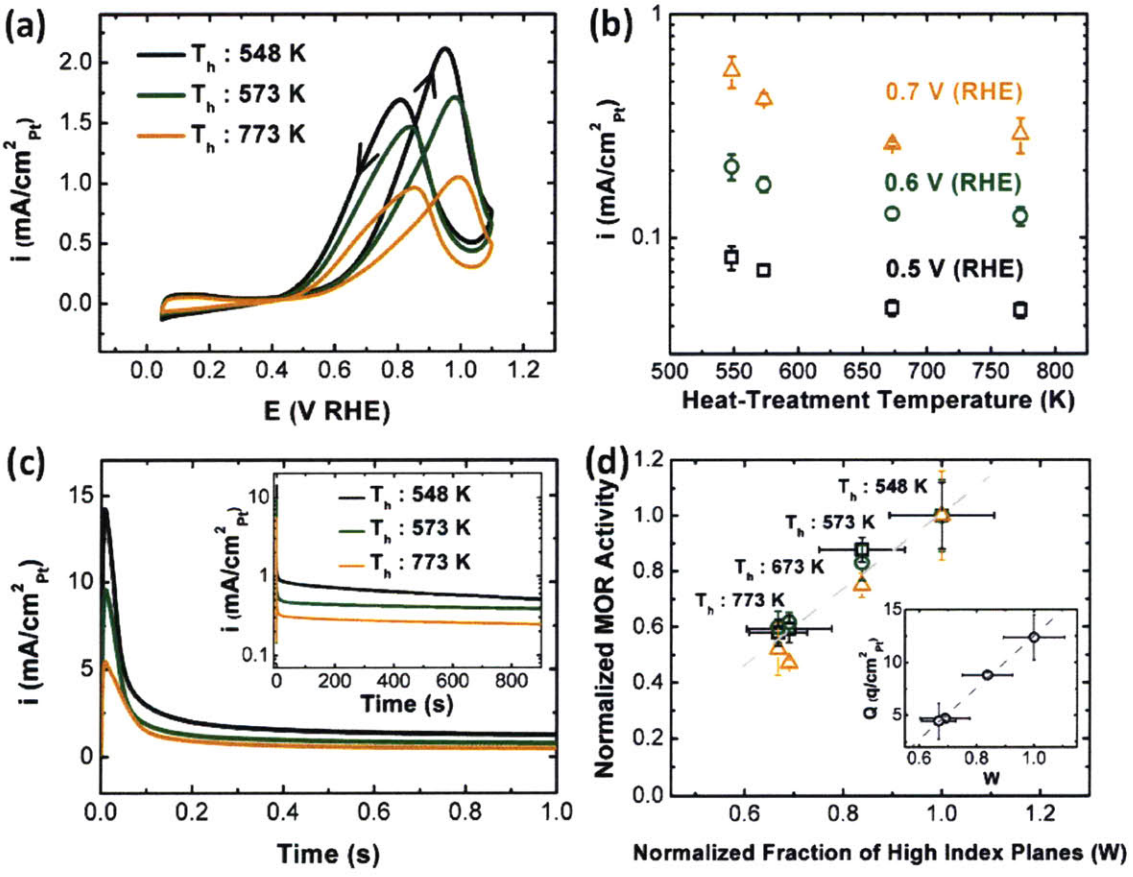

Figure 6-10. Methanol electro-oxidation activity on Pt/MWNT samples measured at room temperature. (a) Cyclic voltammograms for methanol electro-oxidation of Pt/MWNT samples, where specific current is normalized to the Pt ESA. The data were recorded with 50 mV/s from 0.05 to 1.1 V vs. RHE. (b) Specific currents (normalized to Pt ESA) at different potentials (RHE) in cyclic voltammograms. (c) Specific current transients (normalized to Pt ESA) of the electro-oxidation of methanol in the first second, and of the long-time response to 900 s in the inset, which were recorded upon imposing a voltage step from 0.1 to 0.7 V vs. RHE. Measurements were conducted in an N_2 saturated solution of 1 M CH_3OH in 0.1 M $HClO_4$. (d) Intrinsic methanol oxidation activity as a function of area fraction of high-index planes normalized to the 548 K sample. Inset compares specific methanol oxidation charge in the positive-going scan of cyclic voltammogram with the area fraction of high-index planes normalized to the 548 K sample. The calculation of error bars can be found in the Experimental section.

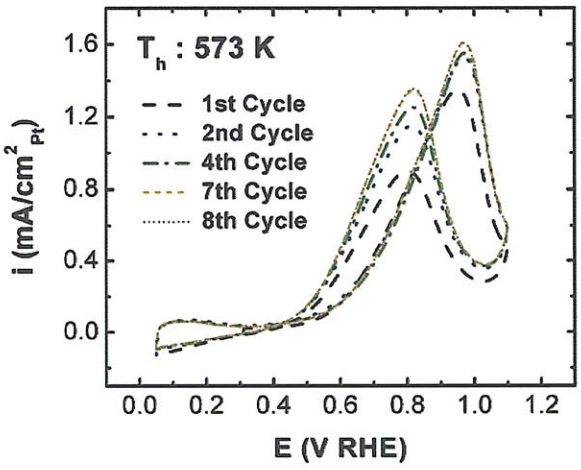

Figure 6-11. Cyclic voltammograms for methanol oxidation reaction for Pt/MWNTs obtained at 573 K. The potential cycles were recorded at a scan rate of 50 mV/s from 0.05 to 1.1 V (RHE) in N_2 saturated a solution of 1M CH_3OH in 0.1 M $HClO_4$ at room temperature. Steady-state cyclic voltammetry curves are reached typically after ~5 cycles.

Increasing the electro-oxidation activity of methanol on Pt nanoparticles in the Pt/MWNT samples obtained at lower heat-treatment temperatures in Figures 6-10a-c can be attributed largely to higher fractions of surface steps shown in Figure 6-1f. As Pt surface step sites can promote dissociative chemisorption of methanol to form CO_{ad}[7], increased electro-oxidation activity of CO_{ad} observed on Pt nanoparticles obtained from lower temperatures (Figure 6-4) suggests enhanced reaction kinetics for indirect methanol oxidation. In addition, surface steps on single-crystal surfaces[4] are shown to promote the kinetics of direct methanol oxidation. Therefore, enhanced reaction kinetics for direct methanol oxidation on surface under-coordinated sites of Pt nanoparticles can also contribute to the enhanced intrinsic activity of methanol oxidation on Pt/MWNTs obtained from lower heat-treatment temperatures. In order to quantify the influence of high-index surface facets of Pt nanoparticles on the intrinsic activity of methanol oxidation, specific current of methanol oxidation in the positive-going cyclic voltammetry scan of Pt/MWNT samples, which was normalized to that of 548 K, is plotted as a function of area fraction of high-index planes normalized to that of 548 K, as shown in Figure 6-10d. A linear correlation exists between normalized, specific activity for methanol oxidation and normalized area fraction of high-index surface facets for current collected at 0.5, 0.6 and 0.7 V vs. RHE. In addition, the specific charge (based on Pt ESA) associated with methanol electro-oxidation in the positive-going scan showed a linear trend with the normalized area fraction of high-index planes, as shown in Figure 6-10d inset.

It should be pointed out that the Pt/MWNT sample of 548 K was found to have considerably higher specific activity (up to an increase of ~200% at 0.5 V vs. RHE) for methanol oxidation than a commercial, supported Pt catalyst (Tanaka Kikinzoku International, Inc.)[35] of a comparable particle size and distribution (Figure 6-12a). These results show that increasing step densities on Pt nanoparticles of very comparable sizes and size distributions can greatly enhance the intrinsic activity for methanol electro-oxidation, and the magnitude of activity enhancement can be correlated with the amount of surface steps on nanoparticles. In addition, Pt/MWNTs obtained at 573 K showed no loss of activity for methanol electro-oxidation in the potential region from 0.5 to 0.7 V vs. RHE

during potential cycling from 0.05 to 1.1 V vs. RHE in an N_2 saturated solution of 1 M CH_3OH in 0.1 M $HClO_4$ (methanol annealing) up to 250 cycles, as shown in Figure 6-12b. This result suggests that surface structural changes of Pt nanoparticles associated with methanol electro-oxidation are not significant. It is interesting to contrast that CO annealing leads to significant reduction in the surface step density and activity for CO electro-oxidation while methanol annealing appears to have no effect on either the surface atomic structure nor activity for methanol electro-oxidation. As previous studies have suggested that CO_{ad} can facilitate surface Pt atom diffusion[31], greater stability for the methanol electro-oxidation activity on Pt/MWNTs during cycling in a methanol solution than CO electro-oxidation in a CO saturated solution may be attributed to lower surface CO_{ad} on Pt nanoparticles in methanol at high potentials, where further studies are needed to provide details. This finding suggests that Pt nanoparticles with increasing surface steps can have long-term activity enhancement and stability for methanol electro-oxidation.

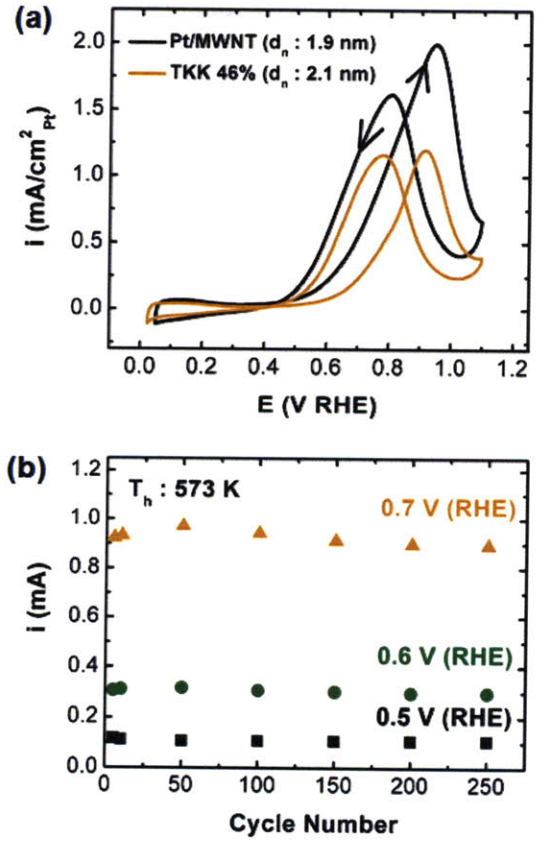

Figure 6-12. (a) Cyclic voltammograms for methanol electro-oxidation for Pt/MWNTs obtained at 548 K (d_n: 1.9 nm) and a TKK Pt 46 wt% (d_n: 2.1 nm) sample that is commonly used in fuel cells. The potential cycles were recorded at a scan rate of 50 mV/s from 0.05 to 1.1 V (RHE) in N_2 saturated a solution of 1M CH_3OH in 0.1 M $HClO_4$ at room temperature. (b) Methanol electro-oxidation current of Pt/MWNTs of 573 K as a function of cycle number, which were measured at different potentials (RHE) in the postive-going sweep. The currents were recorded during potential cycling with 50 mV/s from 0.05 to 1.1 V vs. RHE in an N_2 saturated solution of 1 M CH_3OH in 0.1 M $HClO_4$ at room temperature.

6.4 Results and Discuss Part 2: Comparing the Role of Surface Steps of Pt Nanoparticles on the Electrochemical Activity for Oxygen Reduction and Methanol Oxidation

ORR activity of Pt/MWNT samples was measured using a rotating disk electrode (RDE) and linear sweep voltammetry in O_2-saturated $HClO_4$ electrolyte (Figure 6-13a). The electrochemical surface area (ESA) of Pt nanoparticles was obtained from integrating the charge associated with hydrogen desorption in the O_2-free electrolyte (Figure 6-14). Specific ORR activity normalized to the Pt ESA is independent of heat-treatment temperature in Figure 6-13b, which indicates that surface steps on Pt nanoparticles do not greatly influence intrinsic ORR activity. Specific ORR activity of Pt nanoparticles at 0.9 V vs. RHE is ~200 A/cm^2_{Pt}, which is in good accordance with reported specific activity for Pt nanoparticles of comparable sizes in $HClO_4$.[18,21,35]

It is interesting to compare the role of surface steps on Pt nanoparticles on the intrinsic activity of ORR with that of MOR. Specific ORR activity at 0.85 V and specific MOR activity at 0.5 V (current density in the positive-going cyclic voltammetry)[24] is plotted as a function of area fraction of surface steps normalized to that of 548 K (Figure 6-15). Specific ORR activity at 0.85 V is independent of normalized area fraction of stepped surfaces while MOR activity linearly increases with the amount of stepped surfaces on Pt nanoparticles.

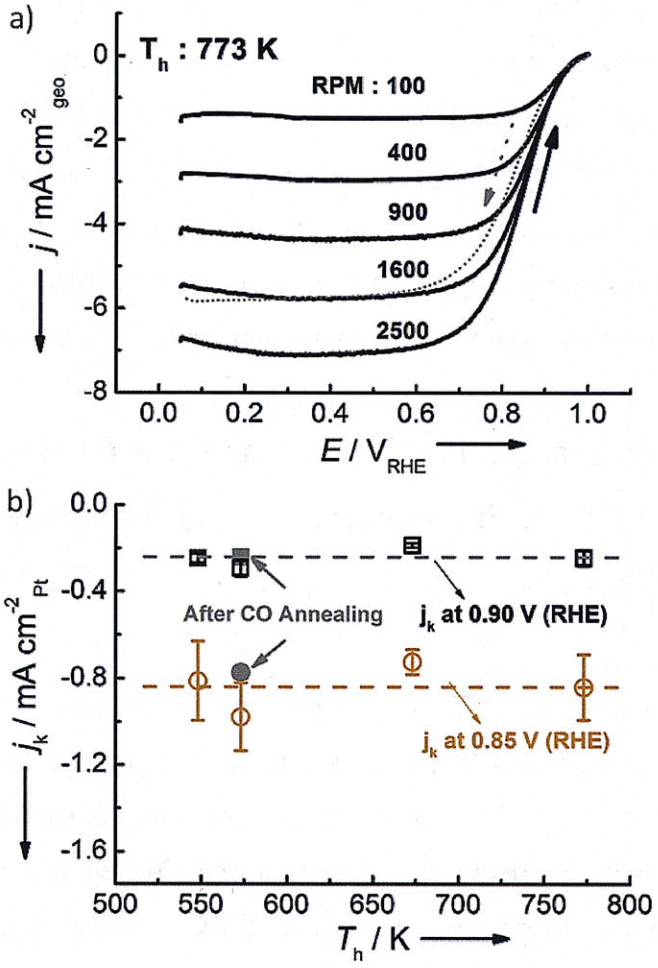

Figure 6-13. a) ORR polarization curves of a Pt/MWNT sample heat-treated at 773 K (denoted as Pt/MWNT-773 K). Experiments were conducted in O_2 saturated 0.1 M $HClO_4$, with a scan rate of 10 mV/s. b) Specific ORR activity of Pt/MWNT samples at 0.85 V and 0.9 V vs. RHE as a function of heat-treatment temperature, which was obtained from the positive-going scan at 1600 rotation per minute (rpm).

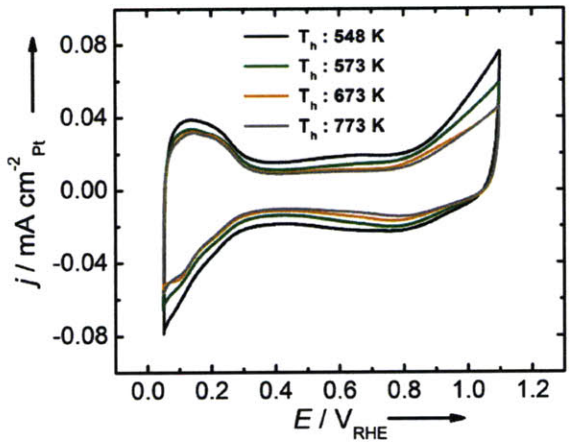

Figure 6-14. Cyclic voltammograms of Pt nanoparticles obtained from different heat-treatment temperature in 0.1M $HClO_4$ at a sweep rate of 20 mV/s at room temperature.

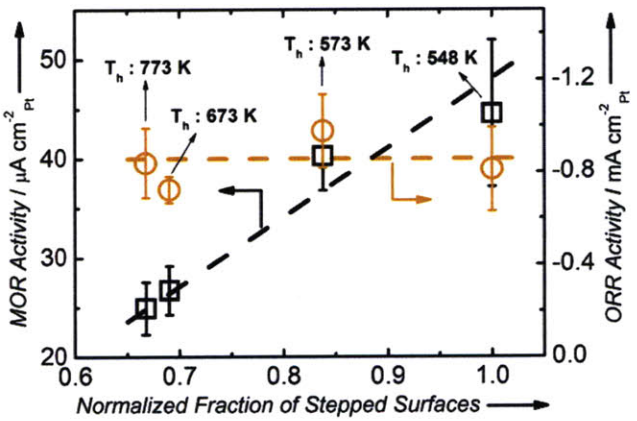

Figure 6-15. Specific MOR (left axis) and ORR activity (right axis) as a function of area fraction of stepped surfaces normalized to the 548 K sample. Specific MOR activity was measured at 0.5 V vs. RHE after subtraction of the double layer current. Specific ORR activity was measured at 0.85 V vs. RHE at 1600 rpm.

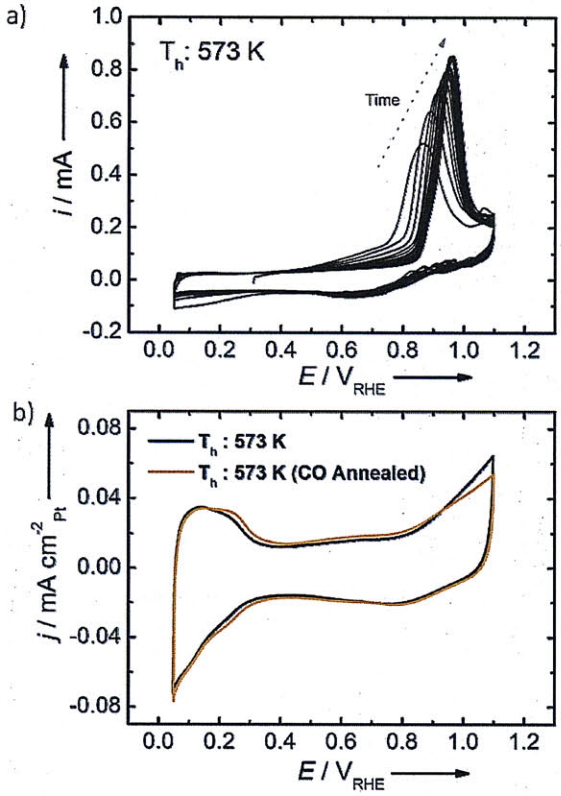

Figure 6-16 a) Cyclic voltammograms during potential cycling on Pt/MWNT-573 K in a CO-saturated 0.1 M $HClO_4$ solution from 0.1 to 1.1 V vs. RHE at a scan rate of 50 mV/s for 10 minutes (CO annealing) at room temperature. b) Comparison of cyclic voltammograms on Pt/MWNT-573 K before and after CO annealing. The potential cycles were recorded at a scan rate of 20 mV/s from 0.05 to 1.1 V (RHE) in an N_2 saturated 0.1 M $HClO_4$ at room temperature.

Conducting a CO annealing experiment can further contrast the role of surfaces steps on the ORR and MOR activity of Pt nanoparticles as CO annealing[19] is shown to reduce adislands and stepped surfaces on Pt single-crystals[31] and Pt nanoparticles.[24] Cyclic voltammetry of Pt/MWNT-573 K was cycled in a CO-saturated solution (CO annealing) from 0.1 to 1.1 V vs. RHE at a scan rate of 50 mV/s for 10 minutes (Figure 6-16), which was shown to reduce surface steps on Pt nanoparticles.[24] There was a negligible change in the specific ORR activity of Pt/MWNT-573 K after CO annealing (Figures 6-13b and 6-17),

further confirming that intrinsic ORR activity on Pt nanoparticles is insensitive to surface steps. On the other hand, a considerable decrease in MOR activity after CO annealing was noted (Figure 6-18), clearly showing strong dependence of intrinsic MOR activity on the surface steps. This result can be explained by previous single-crystal studies, where surface steps are shown to promote the MOR activity by providing active sites for the dissociative chemisorption of methanol to form adsorbed CO, further assisting the Langmuir-Hinshelwood type reaction[32] between adsorbed CO and oxygenated species, and enhancing direct oxidation of various intermediates of methanol.[4] Therefore, a small increase in the amount of surface steps on Pt nanoparticles can enhance MOR activity considerably but not ORR activity.

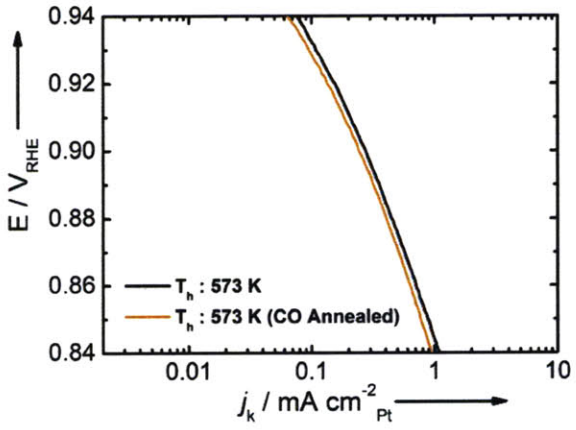

Figure 6-17. Comparison of Tafel plots of ORR specific activity on Pt/MWNT-573 K before and after CO annealing at room temperature. Tafel plots were obtained from the polarization curves in the positive-going scans at 1600 rpm, which was normalized to Pt electrochemical surface area (Figure 6-14).

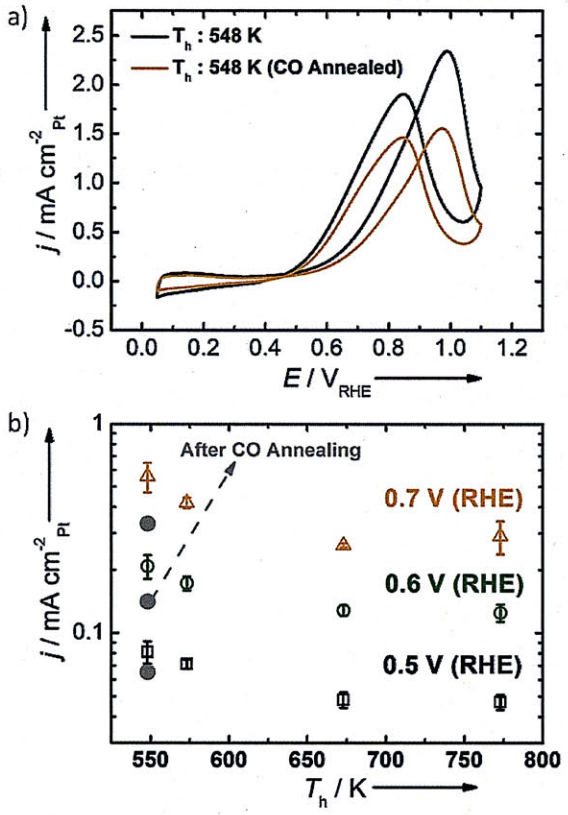

Figure 6-18 a) Comparison of cyclic voltammograms for methanol oxidation activity on Pt/MWNT-548 K before and after CO annealing at room temperature. The potential cycles were recorded at a scan rate of 50 mV/s from 0.05 to 1.1 V (RHE) in N_2 saturated a solution of 1M CH_3OH in 0.1 M $HClO_4$ at room temperature. b) Specific currents (normalized to Pt ESA) at different potentials (RHE) in cyclic voltammograms.

Previous work has suggested that increasing coverage of surface oxygenated species on Pt nanoparticles can reduce ORR activity[18] at high potentials but increase MOR activity[4,6] at low potentials. First-principle studies have shown stronger binding of oxygenated species[36] on the surface steps (with upshifted d band center relative to the Fermi-level[37,38]). To provide further insights to the surface coverage of oxygenated species on Pt nanoparticles with different amounts of surface steps, we examine normalized Pt L_3-edge X-ray absorption near edge structure (XANES) spectra of Pt/MWNT-573 K and 773 K, which were collected in-situ in an electrochemical cell[25] as a function of potential

(Figures 6-19a and 6-20). First to note is that the white line intensity increases with electrode potential. Chemical adsorption of oxygenated species such as OH and O[39,40] on Pt can lead to the appearance of unoccupied antibonding states above the Fermi level, and thus an increase in the L_3 X-ray absorption edge can be attributed to higher coverage of adsorbed oxygenated species on nanoparticle surfaces. Second, the difference in the values of Pt L_3 edges of the Pt/MWNT-573 K and 773 K diminishes with increasing potential, as shown in Figure 6-19b. Higher value of Pt/MWNT-573 K compared to 773 K at lower potential region (< ~0.5 vs. RHE, Figure 6-20b) can be contributed to preferential adsorption of oxygenated species on surface steps, which can explain higher MOR activity of Pt/MWNT samples with more step sites. On the other hand, similar values for Pt/MWNT-573 K and 773 K at high potential region (> ~0.8 V vs. RHE) reflect comparable coverage of oxygenated species (per Pt atom) on Pt nanoparticles. As the fraction of atoms on the terrace sites is much greater than that associated with stepped surfaces (< ~20%, Figure 6-3) for all Pt/MWNT samples, coverage of oxygenated species on major surface sites - terrace sites would dominate the values from XANES measurements. Comparable values of Pt/MWNT-573 K and 773 K at high potentials suggest that the coverage of surface oxygenated species associated with surface steps were not markedly higher than those of terrace sites.

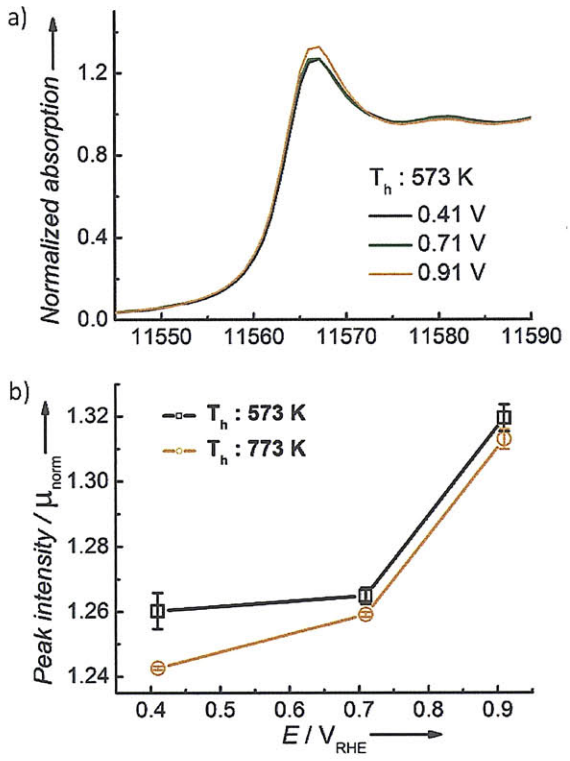

Figure 6-19. a) XANES spectra obtained with the Pt/MWNT-573 K at the Pt L_3 edge at three different potentials. b) Comparison of values extracted from the XANES spectra for Pt/MWNT-573 K and 773 K as a function of potential in 1 M $HClO_4$.

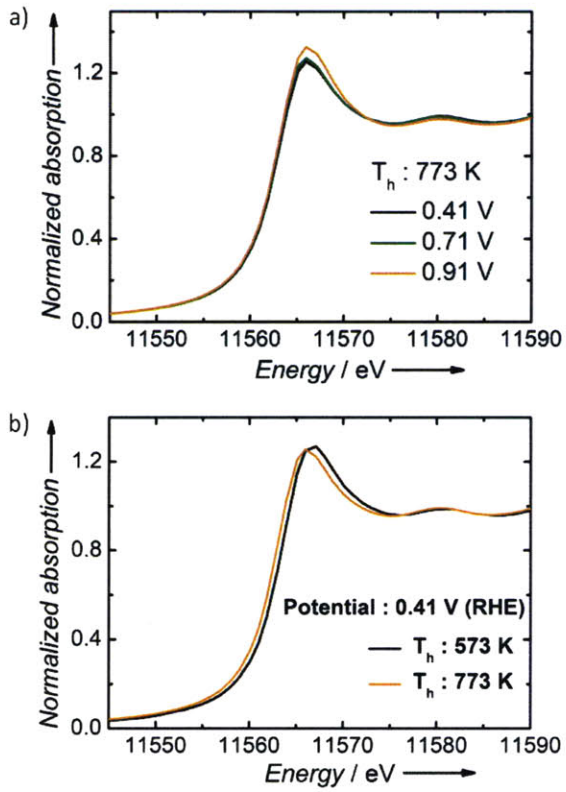

Figure 6-20 (a) XANES spectra obtained with the Pt/MWNT-773 K at the Pt L_3 edge at four different potentials. (b) Comparison of XANEs spectra for Pt/MWNT-573 K and 773 K at 0.41 V vs. RHE. Data were collected in fluorescence mode with the in-situ electrochemical cell[25] at different electrode potentials in 1.0 M $HClO_4$ at room temperature.

Surface steps do not appear to govern ORR activity of nanoparticles of ~2 nm (Figure 6-21). Considering experimental findings[21,35] of an order of magnitude drop in ORR activity from bulk to nanoparticle (~2 nm) surfaces and computational results of a 4-time reduction in ORR activity from 10 nm to 2 nm,[41] the sizes of the {111} and {100} terraces may greatly influence the ORR activity. In contrast, minority sites involving surface steps, which have higher oxygenated species at low potentials (Figure 6-19b) and markedly enhanced activity for MOR, dominate the intrinsic MOR activity of nanoparticles.

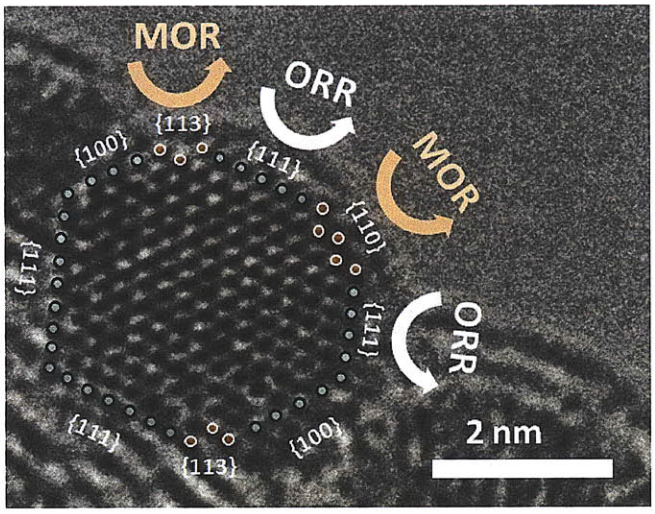

Figure 6-21. HRTEM image of a Pt nanoparticle in Pt/MWNT-673 K. Active sites on the nanoparticle terraces dominate ORR activity while active sites involving surface steps governs MOR activity at low potentials.

6.5 Conclusions

This work, for the first time, characterizes and quantifies the role of surface steps on Pt nanoparticles in electro-oxidation of CO and methanol with sizes of practical relevance. This study demonstrates that insights from single crystal studies are significantly relevant for understanding the behavior of small nanoparticles. A linear relationship between the intrinsic activity (Pt ESA normalized current) and the amounts of surface steps is shown. The CO oxidation activity, together with the incidence of high-index facets on Pt nanoparticles, is reduced after extensive cycling in CO-saturated solution (CO annealing). Interestingly, a corresponding decrease for methanol oxidation activity is not observed upon cycling in methanol. Increasing step densities on Pt nanoparticles of ~2 nm can enhance specific activity based on Pt ESA up to 200% towards electro-oxidation of carbon monoxide and methanol. The enhanced intrinsic activity for methanol electro-oxidation observed in these Pt/MWNT catalysts can translate to reduction of Pt weight up to 200% for a given fuel cell current output. Of significance, this research suggests that strategies to

increasing surface steps such as the n(111)×(111) type on nanoparticles offer promise for finding new highly active electrocatalysts for electro-oxidation of small organic molecules.

In addition, we show ORR activity of Pt/MWNTs independent of the fraction of surface steps on Pt nanoparticles of ~2 nm. This is in contrast to a linear relationship between the fraction of surface steps on nanoparticles and MOR activity, which highlights the significant role of surface steps in enhancing intrinsic activity of MOR. This study contrasts the influence of surface steps on Pt nanoparticles for ORR and MOR by extending the insights from single crystal studies onto nanoparticles. The understanding can be directly utilized to design highly active ORR and MOR novel electrocatalysts for energy conversion and storage devices.

6.6 Reference

[1] Stamenkovic, V. R. et al., Improved oxygen reduction activity on $Pt_3Ni(111)$ via increased surface site availability. *Science* **315**, 493-497 (2007).

[2] Jaramillo, T. F. et al., Identification of active edge sites for electrochemical H-2 evolution from MoS2 nanocatalysts. *Science* **317**, 100-102 (2007).

[3] Lebedeva, N. P., Koper, M. T. M., Feliu, J. M., and van Santen, R. A., Role of crystalline defects in electrocatalysis: Mechanism and kinetics of CO adlayer oxidation on stepped platinum electrodes. *Journal of Physical Chemistry B* **106**, 12938-12947 (2002).

[4] Housmans, T. H. M. and Koper, M. T. M., Methanol oxidation on stepped Pt[n(111) x (110)] electrodes: A chronoamperometric study. *J. Phys. Chem. B* **107**, 8557-8567 (2003).

[5] Adzic, R., in *Modern Aspects of Electrochemistry*, edited by J.O.M. Bockris, B.E. Conway, and R.E. White (1990), Vol. 21, pp. 163-236.

[6] Lai, S. C. S., Lebedeva, N. P., Housmans, T. H. M., and Koper, M. T. M., Mechanisms of carbon monoxide and methanol oxidation at single-crystal electrodes. *Topics in Catalysis* **46**, 320-333 (2007).

[7] Shin, J. W. and Korzeniewski, C., Infrared Spectroscopic Detection of Co Formed at Step and Terrace Sites on a Corrugated Electrode Surface Plane During Methanol Oxidation. *Journal of Physical Chemistry* **99**, 3419-3422 (1995).

[8] Wieckowski, A., Savinowa, E., and Vayenas, C.G. eds., *Catalysis and Electrocatalysis at Nanoparticle Surfaces*. (Marcel Dekker, Inc., New York, 2003).

[9] Tian, N. et al., Synthesis of tetrahexahedral platinum nanocrystals with high-index facets and high electro-oxidation activity. *Science* **316**, 732-735 (2007).

[10] Gontard, L. C. et al., Aberration-corrected imaging of active sites on industrial catalyst nanoparticles. *Angew. Chem.-Int. Edit.* **46**, 3683-3685 (2007).

[11] Frenken, J. W. M. and Stoltze, P., Are vicinal metal surfaces stable? *Physical Review Letters* **82**, 3500-3503 (1999).

[12] Kinoshita, K., Particle-Size Effects for Oxygen Reduction on Highly Dispersed Platinum in Acid Electrolytes. *Journal of the Electrochemical Society* **137**, 845-848 (1990).

[13] Park, S., Xie, Y., and Weaver, M. J., Electrocatalytic pathways on carbon-supported platinum nanoparticles: Comparison of particle-size-dependent rates of methanol, formic acid, and formaldehyde electrooxidation. *Langmuir* **18**, 5792-5798 (2002).

[14] Maillard, F., Savinova, E. R., and Stimming, U., CO monolayer oxidation on Pt nanoparticles: Further insights into the particle size effects. *Journal of Electroanalytical Chemistry* **599**, 221-232 (2007).

[15] Maillard, F. et al., Size effects on reactivity of Pt nanoparticles in CO monolayer oxidation: The role of surface mobility. *Faraday Discussions* **125**, 357-377 (2004).

[16] Mayrhofer, K. J. J. et al., CO surface electrochemistry on Pt-nanoparticles: A selective review. *Electrochim. Acta* **50**, 5144-5154 (2005).

[17] Frelink, T., Visscher, W., and Vanveen, J. A. R., Particle-Size Effect of Carbon-Supported Platinum Catalysts for the Electrooxidation of Methanol. *Journal of Electroanalytical Chemistry* **382**, 65-72 (1995).

[18] Mayrhofer, K. J. J. et al., The impact of geometric and surface electronic properties of Pt-catalysts on the particle size effect in electocatalysis. *J. Phys. Chem. B* **109**, 14433-14440 (2005).

[19] Arenz, M. et al., The effect of the particle size on the kinetics of CO electrooxidation on high surface area Pt catalysts. *Journal of the American Chemical Society* **127**, 6819-6829 (2005).

[20] Chen, L. and Lu, G. X., Hydrothermal synthesis of size-dependent Pt in Pt/MWCNTs nanocomposites for methanol electro-oxidation. *Electrochim. Acta* **53**, 4316-4323 (2008).

[21] Mayrhofer, K. J. J. et al., Measurement of oxygen reduction activities via the rotating disc electrode method: From Pt model surfaces to carbon-supported high surface area catalysts. *Electrochim. Acta* **53**, 3181-3188 (2008).

[22] Macia, M. D., Campina, J. M., Herrero, E., and Feliu, J. M., On the kinetics of oxygen reduction on platinum stepped surfaces in acidic media. *J. Electroanal. Chem.* **564**, 141-150 (2004).

[23] Kuzume, A., Herrero, E., and Feliu, J. M., Oxygen reduction on stepped platinum surfaces in acidic media. *J. Electroanal. Chem.* **599**, 333-343 (2007).

[24] Lee, Seung Woo et al., Roles of Surface Steps on Pt Nanoparticles in Electro-oxidation of Carbon Monoxide and Methanol. *J. Am. Chem. Soc.* **131**, 15669 (2009).

[25] Zhang, J., Sasaki, K., Sutter, E., and Adzic, R. R., Stabilization of platinum oxygen-reduction electrocatalysts using gold clusters. *Science* **315**, 220-222 (2007).

[26] Kim, Y. T. et al., Fine size control of platinum on carbon nanotubes: From single atoms to clusters. *Angewandte Chemie-International Edition* **45**, 407-411 (2006).

[27] Ferreira, P. J. and Shao-Horn, Y., Formation mechanism of Pt single-crystal nanoparticles in proton exchange membrane fuel cells. *Electrochem. Solid State Lett.* **10**, B60-B63 (2007).

[28] Foiles, S. M., Baskes, M. I., and Daw, M. S., Embedded-Atom-Method Functions for the Fcc Metals Cu, Ag, Au, Ni, Pd, Pt, and Their Alloys. *Phys. Rev. B* **33**, 7983-7991 (1986).

[29] Skriver, H. L. and Rosengaard, N. M., Surface-Energy and Work Function of Elemental Metals. *Phys. Rev. B* **46**, 7157-7168 (1992).

[30] Markovic, N. M. and Ross, P. N., Surface science studies of model fuel cell electrocatalysts. *Surf. Sci. Rep.* **45**, 121-229 (2002).

[31] Strmcnik, D. S. et al., Unique Activity of Platinum Adislands in the CO Electrooxidation Reaction. *J. Am. Chem. Soc.* **130**, 15332-15339 (2008).

[32] Gilman, S., The Mechanism of Electrochemical Oxidation of Carbon Monoxide and Methanol on Platinum. II. The "Reactant-Pair" Mechanism for Electrochemical Oxidation of Carbon Monoxide and Methanol. *Journal of Physical Chemistry* **68**, 70-80 (1964).

[33] Parsons, R. and Vandernoot, T., The Oxidation of Small Organic-Molecules - a Survey of Recent Fuel-Cell Related Research. *Journal of Electroanalytical Chemistry* **257**, 9-45 (1988).

[34] Iwasita, T., Electrocatalysis of methanol oxidation. *Electrochimica Acta* **47**, 3663-3674 (2002).

[35] Gasteiger, H. A., Kocha, S. S., Sompalli, B., and Wagner, F. T., Activity benchmarks and requirements for Pt, Pt-alloy, and non-Pt oxygen reduction catalysts for PEMFCs. *Applied Catalysis B-Environmental* **56**, 9-35 (2005).

[36] Han, B. C., Miranda, C. R., and Ceder, G., Effect of particle size and surface structure on adsorption of O and OH on platinum nanoparticles: A first-principles study. *Phys. Rev. B* 77, 075410 (2008).

[37] Norskov, J. K., CHEMISORPTION ON METAL-SURFACES. *Rep. Prog. Phys.* **53**, 1253-1295 (1990).

[38] Hammer, B., Nielsen, O. H., and Norskov, J. K., Structure sensitivity in adsorption: CO interaction with stepped and reconstructed Pt surfaces. *Catalysis Letters* **46**, 31-35 (1997).

[39] Lytle, F. W. et al., EFFECT OF CHEMICAL ENVIRONMENT ON MAGNITUDE OF X-RAY ABSORPTION RESONANCE AT LLLL EDGES - STUDIES ON METALLIC ELEMENTS, COMPOUNDS, AND CATALYSTS. *J. Chem. Phys.* **70**, 4849-4855 (1979).

[40] Mukerjee, S. and McBreen, J., Effect of particle size on the electrocatalysis by carbon-supported Pt electrocatalysts: an in situ XAS investigation. *J. Electroanal. Chem.* **448**, 163-171 (1998).

[41] Greeley, J., Rossmeisl, J., Hellman, A., and Norskov, J. K., Theoretical trends in particle size effects for the oxygen reduction reaction. *Z. Phys. Chemie-Int. J. Res. Phys. Chem. Chem. Phys.* **221**, 1209-1220 (2007).

Chapter 7. Conclusion and Perspective

In this thesis, layer-by-layer (LbL) assembled multiwall carbon nanotube (MWNT) electrodes were designed for energy storage and conversion devices. The novel LbL-MWNT electrodes consist of repeated, sequential immersion of substrates into positively and negatively charged MWNT aqueous solutions. LbL-MWNT electrodes[1] have an inter-penetrating network structures that can achieve high electronic conductivity, and the well-developed porous structures between the MWNTs could create fast ion diffusion channels to facilitate ion transport. In addition, LbL-MWNT assembly is additive-free carbon electrode that contains no insulating polymer binders allowing fast electron transport to the entire electrode structure. These electrodes were observed to have mass density of 0.83 g/cm^3 after heat treatment, which is among the highest reported for carbon electrodes, and high volumetric capacitance (132 F/cm^3) in aqueous electrolyte (1M H_2SO_4),[1] which is higher than conventional carbon electrodes.[2-4]

Further increases in the capacitance of the LbL-MWNT electrodes were achieved via the incorporation of nanoscale inorganic oxides or organic molecules with pseudocapacitive properties. Inorganic oxides such as MnO_2 and RuO_2 have been incorporated to increase volumetric capacitance in LbL-MWNT electrodes using electroless redox deposition[5] and square-wave pulse potential deposition methods. Figure 7-1 shows that the volumetric capacitances of LbL-MWNT/MnO_2 and LbL-MWNT/RuO_2 composite electrodes increase up to 1000 F/cm^3 in aqueous electrolytes. It was examined the electrochemical characteristics of such composite LbL electrodes in aqueous electrolytes as the electrodes of electrochemical capacitors, where it is possible to precisely control both the capacity and the capacitance of the electrodes. It will be interesting to explore the energy and power characteristics of such composite LbL electrodes in lithium nonaqueous cells as asymmetric electrochemical capacitors, where it could potentially increase the energy and power densities of LbL-MWNT electrodes.

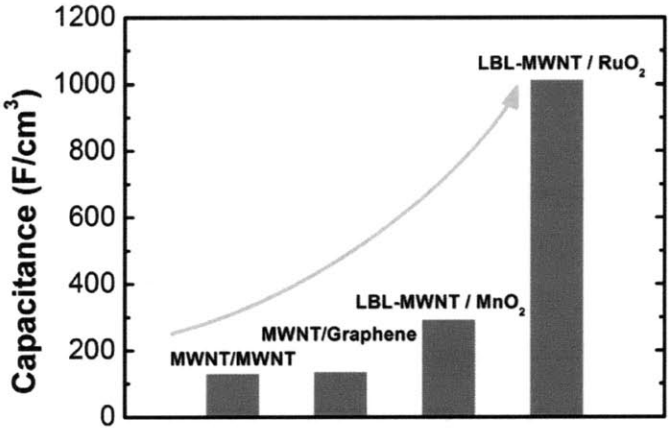

Figure 7-1. Comparison of the volumetric capacitance (F/cm^3) in aqueous electrolytes for various LbL assembled electrodes.

An asymmetric electrochemical capacitor, also referred to as a hybrid electrochemical capacitor, combines a battery-like electrode with a capacitor-like electrode, bridging the energy and power performance gap between batteries and electrochemical capacitors. Recent review papers[2,6] proposed this technology as a promising and new energy storage system that combines the high energy density of batteries with the high power and long cycle lifetime of electrochemical capacitors. In this thesis, it was shown that high energy densities (200 Wh/kg) of MWNT electrodes in lithium cells at exceptional power (100 kW/kg). The high energy densities of LbL-MWNT electrodes can be attributed to the Faradaic reactions between lithium ions and surface functional groups on MWNT electrodes (rending high pseudo-capacitance), which can be accessed in the voltage window from 1.5 V vs. 4.5 V vs. Li in a nonaqueous electrolyte (not accessible in aqueous electrolytes). In addition, these LbL-MWNT electrodes were assembled and evaluated in a lithium-metal-free, asymmetric cell, which showed much higher energy densities with comparable power and cycle life relative to conventional symmetrical and asymmetrical electrochemical capacitors.

The LbL-MWNT electrodes in lithium cell have higher energy densities to conventional lithium storage electrode materials at high power demands. If we compare

MWNT electrodes with the state-of-the-art high-power lithium storage technologies, MWNT electrodes reported herein can deliver considerably higher power (~200 Wh/kg at ~100 kW/kg) than high-power $LiFePO_4$ lithium battery electrodes[7,8] reported very recently. Energy, power and lifetime characteristics of MWNT electrodes were further evaluated in a lithium-metal-free cell for completeness and safety considerations for practical applications, where the lithium metal counter electrode was replaced with *a lithiated titanium oxide* $Li_4Ti_5O_{12}$ (LTO) electrode. Using a conservative assumption that the packaged specific energy of practical devices to roughly 1/5 of electrode specific energy, specific energy of LTO/LbL-MWNT storage devices can be estimated to be ~30 Wh/kg_{cell}, which is significantly higher than that of current electrochemical capacitors (~ 5 Wh/kg_{cell}).[2] Utilizing Faradaic reactions of functional groups on carbon surfaces for energy storage is a promising approach to develop electrode materials for high-power and high-energy storage devices. Estimated packaged gravimetric energy densities of Li/LbL-MWNT and LTO/LbL-MWNT devices (based on the assumption that packaged gravimetric energy density of practical devices is roughly 1/5 of gravimetric electrode energy density) was compared and overlaid with those of electrochemical capacitor, Ni-MH and Li-ion batteries in the following Ragone plot shown in Figure 7-2,[2] which was published recently in Nature Materials 2008. It is evident that Li/MWNT and LTO/MWNT devices (blue circular regions in the graph) can potentially provide higher packaged gravimetric energy densities at higher gravimetric power relative to Li-ion batteries while they provide much higher gravimetric energy densities at comparable gravimetric power to electrochemical capacitors.

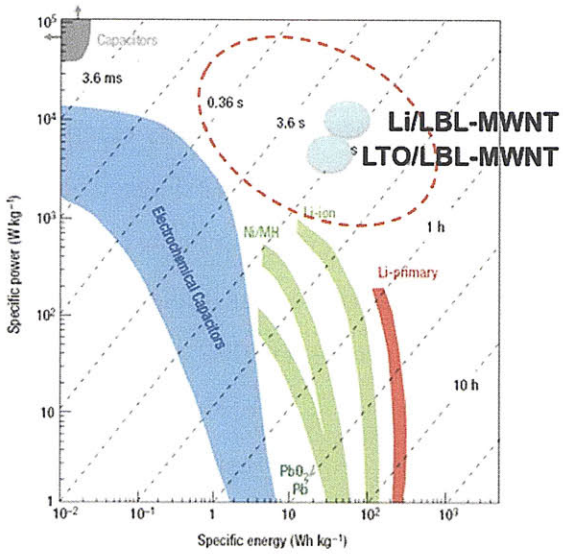

Figure 7-2. Blue circular regions show estimated gravimetric energy and power density of an asymmetric EC device assembled with LBL-MWNT for positive and Li or LTO for negative electrode. Higher power density for LBL-MWNT devices are observed over Li-ion batteries at comparable energy density. Red dashed area is expected range of future development in EC devices using LbL approach. Adapted from Ref. 2 (*Nature Materials* 7, 845-854 (2008)).

With regard to the practicality of this LbL technique, unlike Langmuir-Blodgett techniques based on assembly of surface-active materials on a trough, the electrostatic layer-by-layer assembly process requires no specialized equipment, is highly stable and can be used to generate films with great ease under common conditions. Although the LbL process has traditionally been implemented in many laboratories via automated programmed dipping processes with cycle times on the order of several minutes, automated misting LbL methods that involve the alternate spraying of positively and negatively charged species onto the substrate have been demonstrated in many groups, including our own[9]. To decrease electrode fabrication time as well as increase LbL electrode thickness (>10 μm) and area (>1 cm^2), it will be employ a rapid and potentially lower cost fabrication process by using a newly developed and patented automated spraying system for LbL

electrodes, as shown in Figure 7-3. Uniform LbL films similar to those created with dipping are generated using off-the-shelf, common commercial equipment, and nanomaterials can be incorporated into LbL films quite rapidly and over very large areas using adaptations of this method. The automated spray process utilizes cycle times as short as 2 seconds, and cuts down the processing time by as much as 70 to 100 time[9]. Notably, the high surface area, chemical functionality and high porosity, combined with the absence of CNT aggregation and lack of binder in these systems yield materials that outperform other systems significantly in electrochemical properties while maintaining a simple and easily implemented water-based process of controlled assembly.

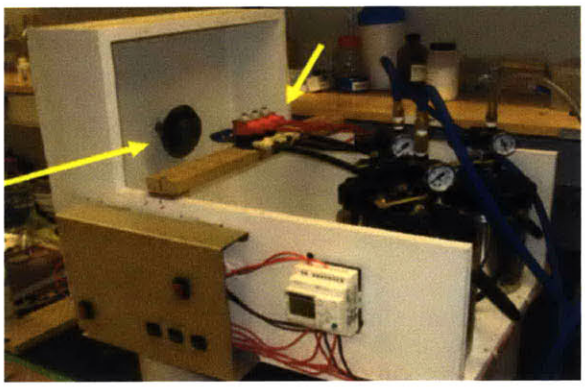

Figure 7-3. Automated mister for constructed for spray-LBL in the Hammond laboratory at MIT capable of fabricating ~100 cm^2 electrodes. Arrows indicate mist jets (right) and target (left).

Finally, there are a large number of applications that require microscale energy storage such as Micro-electro-mechanical systems (MEMS) devices, energy harvesting microsystems, and sensors[10]. Conformal coating of LbL-MWNT electrodes can be deposited on various 2D or 3D substrates, including silicon or silicon carbide wafers, glass, polymers, for the development of high-energy and high-power density thin-film electrochemical capacitors. It was demonstrated that patterned LbL-MWNT electrodes can be deposited on a silicon wafer and flexible ITO-coated PET film as shown at Figure 7-4.

(Manuscript (Byeong-Su Kim, Seung Woo Lee, Hyeonseok Yoon, Michael S. Strano, Yang Shao-Horn, and Paula T. Hammond) including the Figure was submitted). The LbL-MWNT electrodes of this work are also suitable for energy capturing and storage associated with MEMS and Microsystems, transparent thin film electrodes (below 100 nm), photovoltaic devices, and thin film flexible energy storage devices[4] such as smart cards and e-books.

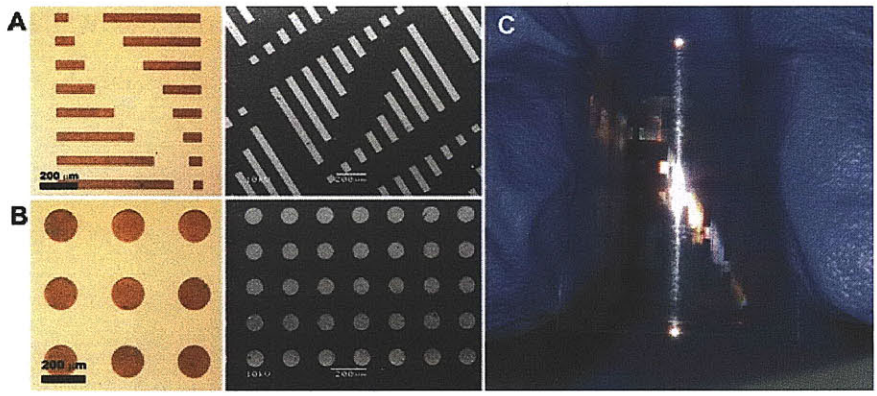

Figure 7-4. (a, b) Representative (left) optical microscope and (right) SEM images of patterned MWNT multilayer film on a silicon wafer, (c) photograph of MWNT pattern transferred on a flexible ITO-coated PET film. All are 5 bilayers of MWNT film. Manuscript (Byeong-Su Kim, Seung Woo Lee, Hyeonseok Yoon, Michael S. Strano, Yang Shao-Horn, and Paula T. Hammond) including the Figure was submitted.

In conclusion, I strongly believe that interest in the LbL process will continue to grow as it allows a "bottom-up" synthesis technique in which electrode properties can be engineered and fine-tuned at the most fundamental level. Furthermore, novel LbL-MWNT electrodes tackle one of the grand challenges in electrochemical energy storage technology, which is improving energy storage to meet the requirements of new transportation technologies, increase the functionality of portable electronics and provide load-leveling for solar and stationary power applications.

References

[1] Lee, Seung Woo et al., Layer-by-Layer Assembly of All Carbon Nanotube Ultrathin Films for Electrochemical Applications. *Journal of the American Chemical Society* **131**, 671-679 (2009).

[2] Simon, P. and Gogotsi, Y., Materials for electrochemical capacitors. *Nature Materials* 7, 845-854 (2008).

[3] Simon, P. and Burke, A., Nanostructured carbons: double-layer capacitance and more. *The Electrochemical Society Interface* **17**, 49 (2008).

[4] Frackowiak, E. and Beguin, F., Carbon materials for the electrochemical storage of energy in capacitors. *Carbon* **39**, 937-950 (2001).

[5] Fischer, A. E. et al., Incorporation of homogeneous, nanoscale MnO2 within ultraporous carbon structures via self-limiting electroless deposition: Implications for electrochemical capacitors. *Nano Letters* 7, 281-286 (2007).

[6] Miller, J. R. and Simon, P., Materials science - Electrochemical capacitors for energy management. *Science* **321**, 651-652 (2008).

[7] Lee, Y. J. et al., Fabricating Genetically Engineered High-Power Lithium-Ion Batteries Using Multiple Virus Genes. *Science* **324**, 1051-1055 (2009).

[8] Kang, B. and Ceder, G., Battery materials for ultrafast charging and discharging. *Nature* **458**, 190-193 (2009).

[9] Krogman, K. C., Zacharia, N. S., Schroeder, S., and Hammond, P. T., Automated process for improved uniformity and versatility of layer-by-layer deposition. *Langmuir* **23**, 3137-3141 (2007).

[10] Dudney, J. N., Thin film micro-batteries. *The Electrochemical Society Interface* **17**, 44 (2008).